STRATOSPHERIC AEROSOL EXTINCTION RETRIEVED FROM SCIAMACHY MEASUREMENTS IN LIMB GEOMETRY

STEFFEN DÖRNER

THESIS PRESENTED TO THE MAX PLANCK GRADUATE CENTER FOR THE ACADEMIC DEGREE OF DOCTOR RERUM NATURALIUM (DR. RER. NAT.)

Max Planck Graduate Center
mit der Johannes Gutenberg-Universität Mainz

Max Planck Institute for Chemistry
Satellite Remote Sensing Group

Steffen Dörner: *Stratospheric Aerosol Extinction Retrieved From SCIAMACHY Measurements In Limb Geometry,* © March 2015

Day of examination: 29th May 2015

PHD ADVISORY COMMITEE:

LOCATION:
Mainz

ABSTRACT

Particles in the stratosphere, although usually undetectable by the human eye, influence climate and atmospheric composition significantly. Continuous data sets of stratospheric aerosol extinction profiles with good spatial and temporal coverage therefore provide essential information for the investigation of the radiative effect of aerosol particles as well as their role in heterogeneous chemistry. Already in 1978, measurements of the second Stratospheric Aerosol Measurement (SAM II) instrument formed the start of a data set that is continued to the present day by instruments like the second Stratospheric Aerosol and Gas Experiment (SAGE II), the SCanning Imaging Absorption spectroMeter for Atmospheric CHartographY (SCIAMACHY), the Optical Spectrograph and InfraRed Imaging System (OSIRIS) and the Ozone Mapping and Profile Suite (OMPS).

This thesis introduces a newly developed retrieval algorithm which applies an onion peeling approach to gain aerosol extinction profiles between 12 and 33 km. The algorithm is applied to radiances at individual wavelengths measured by the SCIAMACHY instrument. SCIAMACHY's unique capability of alternating measurements in limb and nadir geometry provides collocated information with good vertical and horizontal resolution, respectively. This information can be used to improve the retrieval of volcanic plumes or polar stratospheric clouds. If for such plumes or clouds one-dimensional retrieval algorithms are used which assume a horizontal homogeneous distribution, the retrieved profiles would underestimate optical thickness and altitude. In this work three-dimensional radiative transfer simulations with horizontally resolved data sets account for horizontal gradients along the line of sight.

Comparison studies with SAGE II occultation measurements and balloon borne in-situ measurements with an optical particle counter indicate that the algorithm is very well capable of retrieving extinction profiles of stratospheric particles. Case studies on volcanic eruptions and polar stratospheric clouds show that the application of the three-dimensional correction method improves the retrieval results significantly.

ZUSAMMENFASSUNG

Stratosphärische Partikel sind typischerweise mit dem bloßen Auge nicht wahrnehmbar. Dennoch haben sie einen signifikanten Einfluss auf die Strahlungsbilanz der Erde und die heteorogene Chemie in der Stratosphäre. Kontinuierliche, vertikal aufgelöste, globale Datensätze sind daher essenziell für das Verständnis physikalischer und chemischer Prozesse in diesem Teil der Atmosphäre. Beginnend mit den Messungen des zweiten Stratospheric Aerosol Measurement (SAM II) Instruments im Jahre 1978 existiert eine kontinuierliche Zeitreihe für stratosphärische Aerosol-Extinktionsprofile, welche von Messinstrumenten wie dem zweiten Stratospheric Aerosol and Gas Experiment (SAGE II), dem SCanning Imaging Absorption spectroMeter for Atmospheric CHartographY (SCIAMACHY), dem Optical Spectrograph and InfraRed Imaging System (OSIRIS) und dem Ozone Mapping and Profile Suite (OMPS) bis heute fortgeführt wird.

In dieser Arbeit wird ein neu entwickelter Algorithmus vorgestellt, der das sogenannte „Zwiebel-Schäl Prinzip" verwendet, um Extinktionsprofile zwischen 12 und 33 km zu berechnen. Dafür wird der Algorithmus auf Radianzprofile einzelner Wellenlängen angewandt, die von SCIAMACHY in der Limb-Geometrie gemessen wurden. SCIAMACHY's einzigartige Methode abwechselnder Limb- und Nadir-Messungen bietet den Vorteil, hochaufgelöste vertikale und horizontale Messungen mit zeitlicher und räumlicher Koinzidenz durchführen zu können. Die dadurch erlangten Zusatzinformationen können verwendet werden, um die Effekte von horizontalen Gradienten entlang der Sichtlinie des Messinstruments zu korrigieren, welche vor allem kurz nach Vulkanausbrüchen und für polare Stratosphärenwolken beobachtet werden. Wenn diese Gradienten für die Berechnung von Extinktionsprofilen nicht beachtet werden, so kann dies dazu führen, dass sowohl die optischen Dicke als auch die Höhe von Vulkanfahnen oder polarer Stratosphärenwolken unterschätzt werden. In dieser Arbeit wird ein Verfahren vorgestellt, welches mit Hilfe von dreidimensionalen Strahlungstransportsimulationen und horizontal aufgelösten Datensätzen die berechneten Extinktionsprofile korrigiert.

Vergleichsstudien mit den Ergebnissen von Satelliten- (SAGE II) und Ballonmessungen zeigen, dass Extinktionsprofile von stratosphärischen Partikeln mit Hilfe des neu entwickelten Algorithmus berechnet werden können und gut mit bestehenden Datensätzen übereinstimmen. Untersuchungen des Nabro Vulkanausbruchs 2011 und des Auftretens von polaren Stratosphärenwolken in der südlichen Hemisphäre zeigen, dass das Korrekturverfahren für horizontale Gradienten die berechneten Extinktionsprofile deutlich verbessert.

CONTENTS

LIST OF FIGURES

LIST OF TABLES

ACRONYMS

AOT aerosol optical thickness

CI color index

ECMWF European Center for Medium-Range Weather Forecast

ENVISAT ENVIronmental SATellite

ERBS Earth Radiation Budget Satellite

FOV field of view

HALOE	Halogen Occultation Experiment
LOS	line of sight
LUT	look up table
MERRA	Modern-ERa Retrospective Analysis model
MODIS	MODerate resolution Imaging Spectroradiometer
NASA	National Aeronautics and Space Administration
NAT	Nitric Acid Trihydrate
NIR	near-infra-red
OMPS	Ozone Mapping and Profile Suite
OPC	opticle particle counter
OSIRIS	Optical Spectrograph and InfraRed Imaging System
PSC	polar stratospheric cloud
RTM	radiative transfer model
SAA	solar azimuth angle
SAGE II	second Stratospheric Aerosol and Gas Experiment
SAGE III	third Stratospheric Aerosol and Gas Experiment
SAM II	second Stratospheric Aerosol Measurement
SEVIRI	Spinning Enhanced Visible and InfraRed Imager
SCIAMACHY	SCanning Imaging Absorption spectroMeter for Atmospheric CHartographY
SNR	signal to noise ratio
SRAA	solar relative azimuth angle
SSA	single scattering albedo
STS	Supercooled Ternary Solution
Suomi NPP	Suomi National Polar-orbiting Partnership
SZA	solar zenith angle
TH	tangent height
TP	tangent point

UTC	universal time code
UV	ultra-violet
VCD	vertical column density
VIS	visible
VOS	volume of sensitivity

SYMBOLS

α	Ångström exponent		Eqn. 4.9
β	Aerosol extinction	(km^{-1})	Eqn. 4.8
c	Spatial straylight correction factor		Eqn. 6.26
$\bar{c}$	Averaged values of c as used for the LUT		Fig. 6.18a
D	Mean deviation for all tangent heights		Eqn. 6.23
γ	Radiance-extinction gradient	(km)	Eqn. 6.6
h_{Sat}	Satellite altitude	(km)	Sect. 4.2
I_{sim}	Simulated radiance (normalized)		Eqn. 6.5
I_{meas}	Measured radiance	$\left(\frac{\text{Photons}}{\text{s cm}^2\,\text{nm sr}}\right)$	Eqn. 6.5
i	Tangent height index		Fig. 6.3
j	Altitude index		Fig. 6.2
k	Iteration index		Eqn. 6.13
λ	Wavelength	(nm)	
m	Refractive index		
$n(r)$	Number size distribution		Eqn. 2.1
ω_{eff}	Effective albedo		Eqn. 6.1
$P(\xi)$	Scattering phase function		Eqn. 4.4
φ	Azimuth angle	(°)	Sect. 4.2
R	Color Index		Eqn. 5.1
r	Particle radius	(nm)	
R_{Earth}	Earth radius	(km)	Sect. 4.2
r_m	Mean mode radius of log-normal size distribution	(nm)	Eqn. 2.1
S	Spatial straylight contribution		Eqn. 6.25

SAA	Solar azimuth angle	(°)	Sect. 4.2
SRAA	Solar relative azimuth angle	(°)	Sect. 4.2
SZA	Solar zenith angle	(°)	Sect. 4.2
σ	Mode width of log-normal size distribution		Eqn. 2.1
TH	Tangent height	(km)	Fig. 3.1a
Θ	Color index ratio		Eqn. 5.2
ϑ	Elevation angle	(°)	Sect. 4.2
ξ	Single scattering angle	(°)	Sect. 4.2

Part I

INTRODUCTION

1

MOTIVATION

Three years after the successful launch of Sputnik I in 1957, the era of satellite remote sensing of the atmosphere began with cloud imagery on the first Television and Infra-Red Observation Satellite (TIROS). During the first 15 years, instrumental capabilities restricted satellite borne measurements to nadir geometry, looking straight down to earth. Satellite imagery in nadir geometry provided horizontally resolved information with unprecedented temporal or global coverage depending on the respective orbit configuration. Experiments like the Backscatter Ultraviolet (BUV) on the Nimbus-4 satellite provided information on the global distribution of ozone. At the same time the understanding of ozone chemistry in the lower to middle stratosphere was improved. Theoretical and technical advancements showed that information with improved vertical resolution was required for better scientific understanding of the upper atmosphere. Since then, new measurement methods using limb scatter and solar occultation were developed and implemented on the Limb Radiance Inversion Radiometer on Nimbus-6 in 1975 and the Stratospheric Aerosol Monitor on Nimbus-7 in 1978, respectively. Solar occultation measurements provide vertically resolved information with high precision and a comparatively simple measurement geometry, but are restricted to sunrise and sunset. Measurements in limb geometry can be performed globally on the sunlit half of the Earth, but usually have a reduced signal to noise ratio.

Nowadays, scientific questions concerning the stratosphere are related to the recovery of the ozone layer, the influence of climate change on stratospheric chemistry and dynamics, and detailed information on the radiation budget of the upper atmosphere. All of these questions are related to the abundance and properties of stratospheric aerosols as they increase the reaction surface for heterogeneous chemistry and reflect sunlight back into space. The stratospheric aerosol particle concentration and their microphysical properties are strongly interlinked with stratospheric dynamics affecting particle formation, growth, sedimentation and evaporation.

In satellite remote sensing, microphysical properties like size and refractive index of stratospheric particles are not measured directly. Instead they have to be retrieved from spectrally resolved radiances. In order to interpret the complex relationship between measurements in limb geometry and the atmospheric state, the application of radiative transfer models is required. Assumptions and approximations are necessary to solve this underdetermined problem. As novel satellite measurements provide data sets with increasing spectral, spatial and temporal resolution, radiative transfer models and retrieval algorithms are under continuous development in terms of computational efficiency and full description of the physical theory.

In this thesis a method to retrieve stratospheric aerosol extinction from satellite measurements in limb geometry using the onion peeling method is developed and applied to measurements by the SCanning Imaging Absorption spectroMeter for Atmospheric CHartographY (SCIAMACHY) on board of the ENVIronmental SATellite (ENVISAT), see figure 1.1. Chapters 2 to 4 will give a basic introduction on particles in the stratosphere, satellite measurements and radiative transfer. The color index method will be explained and applied to SCIAMACHY measurements in chapter 5. The retrieval method and implementation will be discussed in chapter 6. Retrieved aerosol extinction profiles for the lower to middle stratosphere between 12 and 33 km are compared to results from the SAGE II and balloon soundings in chapter 7. Case studies of volcanic plumes and polar stratospheric clouds will show that the newly developed three-dimensional correction improves retrieval results for horizontally inhomogeneous particle layers. Method and application of the three-dimensional correction will be presented in chapter 8. After the findings of this thesis will be summarized and discussed in chapter 9, technical improvements and retrieval applications will be proposed in chapter 10.

Figure 1.1: An artistic view of ENVISAT [European Space Agency, 2010].

2

PARTICLES IN THE STRATOSPHERE

Aerosol particles in the stratosphere play an important role for chemical reactions and radiative transfer: In heterogeneous chemistry, reaction rates of catalytic cycles, which affect ozone chemistry, increase when aerosol particle concentration and therefore reaction surface is increasing. Thus, variations of the ozone profile are connected to the variability of the aerosol particle abundance and the occurrence of polar stratospheric clouds (PSCs). In addition, stratospheric aerosol particles are capable of cooling the atmosphere by reflecting short wave solar radiation [Humphreys, 1940]. Particles in the stratosphere can be categorized into three major groups summarized in figure 2.1:

- Background aerosol also known as the Junge layer [Junge and Manson, 1961]
- Tropospheric intrusions like volcanic eruptions or large convective biomass burning events (pyro-convection)
- Polar stratospheric clouds

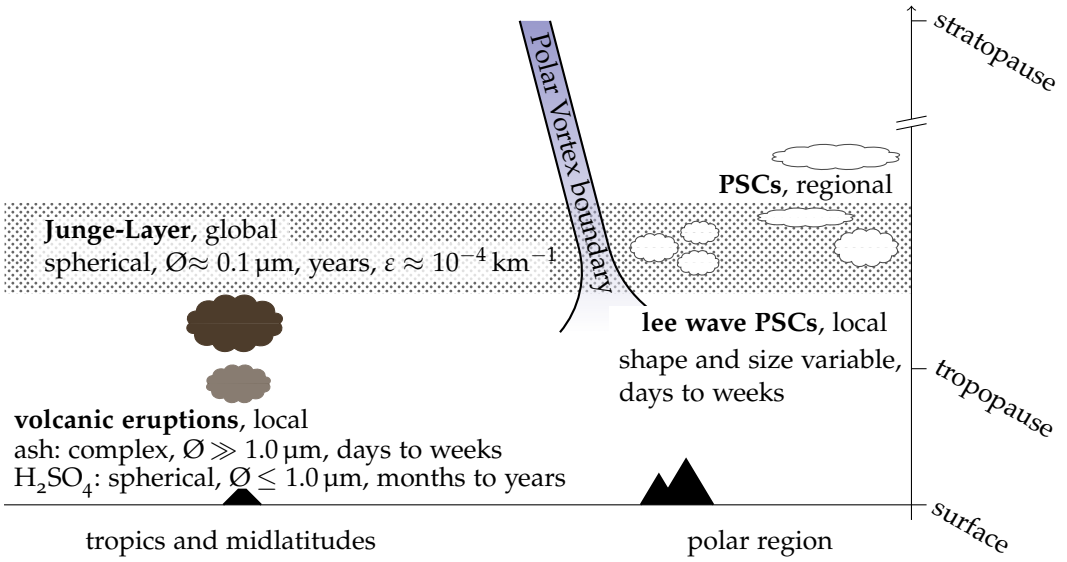

Figure 2.1: Main characteristic features for three types of stratospheric particles discussed in this section: Background aerosol, volcanic plumes and polar stratospheric clouds. Sources for particle sizes/life times: Kirner et al. [2011] and SPARC/ASAP [2006]

In the following section properties of these three particle types are described in detail. Other types like aviation induced-aerosol or meteorite dust will not be

discussed, since they are not detected by the satellite measurements shown in this thesis. However, studies show that small particles with meteoritic origin affect particle nucleation inside the polar vortex [Hunten et al., 1980; Curtius et al., 2005] and the formation of PSCs [Engel et al., 2013; Hoyle et al., 2013].

2.1 BACKGROUND AEROSOL LAYER

In the lower stratosphere around 16 to 20 km, droplets containing sulfuric acid (H_2SO_4) and water (H_2O) form the Junge layer. Above 30 km aerosol particles become much less abundant. This was confirmed for the first time by a high altitude balloon experiment in 1959 [Junge and Manson, 1961]. Source gases like carbonyl sulfide (OCS, natural) and sulfur dioxide (SO_2, natural and anthropogenic) typically enter the stratosphere in the tropics and form H_2SO_4 through oxidation and photolysis. Sulfate aerosol then formed via heterogeneous nucleation on existing nuclei like stratospheric Aitken particles [Cadle and Kiang, 1977], meteorite dust [Hunten et al., 1980] or via homogeneous nucleation [Brock et al., 1995]. Strong zonal winds in the lower tropical stratosphere keep most of the aerosol particles in the low latitudes [Trepte and Hitchman, 1992], until they are either picked up by the Brewer-Dobson circulation or leaking into the lower subtropical stratosphere as described by the "leaky pipe model" [Shia et al., 1998; Neu and Plumb, 1999].

Stratospheric background aerosol is assumed to be of spherical shape with the size often being parameterized by an unimodal lognormal distribution:

$$n(r) = \frac{N_0}{r \cdot \ln\sigma \cdot \sqrt{2\pi}} \cdot \exp\left(\frac{\ln r - \ln r_m}{2 \cdot \ln\sigma}\right) dr \tag{2.1}$$

with the particle radius r, the number concentration $n(r)$, the total particle concentration N_0, the median radius r_m and the width of the distribution σ. Typical atmospheric values for an altitude around 21 km are $N_0 = 5 - 10\,\mathrm{cm}^{-3}$, $r_m = 70\,\mathrm{nm}$ and σ between 1.6 and 1.8 [SPARC/ASAP, 2006].

2.2 VOLCANIC ERUPTIONS

Volcanic eruptions occur frequently around the globe, causing impacts on local to regional scale in most cases. This changes if the eruption is powerful enough to reach the stratosphere. Strong eruptions like Krakatoa (1883), Pinatubo (1991) and to a lesser extent Nabro (2011) caused significant disturbances in the stratospheric aerosol layer that lasted for several months or even a few years. Depending on the eruption H_2O, CO_2, SO_2 and ash will be injected into the stratosphere. While large particles like ash or ice will sediment relatively fast, SO_2 is transformed into sulfate aerosol on timescales between hours and weeks and resides within the stratosphere for several months. The newly formed aerosol usually consists of particles that are larger than the background aerosol. This disturbance can be described by a second lognormal mode with a particle radius of about 200 nm [Deshler, 2008].

Similar to strong volcanic eruptions, large biomass burning events can also reach the stratosphere. Since the plumes of these pyro-convective events mainly contain ash, effects can only be observed on the regional scale for a time scale of days to weeks [Fromm et al., 2005; Trentmann et al., 2006].

2.3 POLAR STRATOSPHERIC CLOUDS

In polar regions of the winter hemisphere clouds can form at altitudes around 15 to 25 km. At this height they are still scattering sunlight while the sun has already disappeared on ground level causing them to be well recognizable [Larden, 1884]. Aside from well noticed Mother-of-Pearl clouds [Mohn, 1893] additional types were identified during the past century. Nowadays, three main types of polar stratospheric clouds (PSCs) are distinguished based on their particle composition as shown in the following figure.

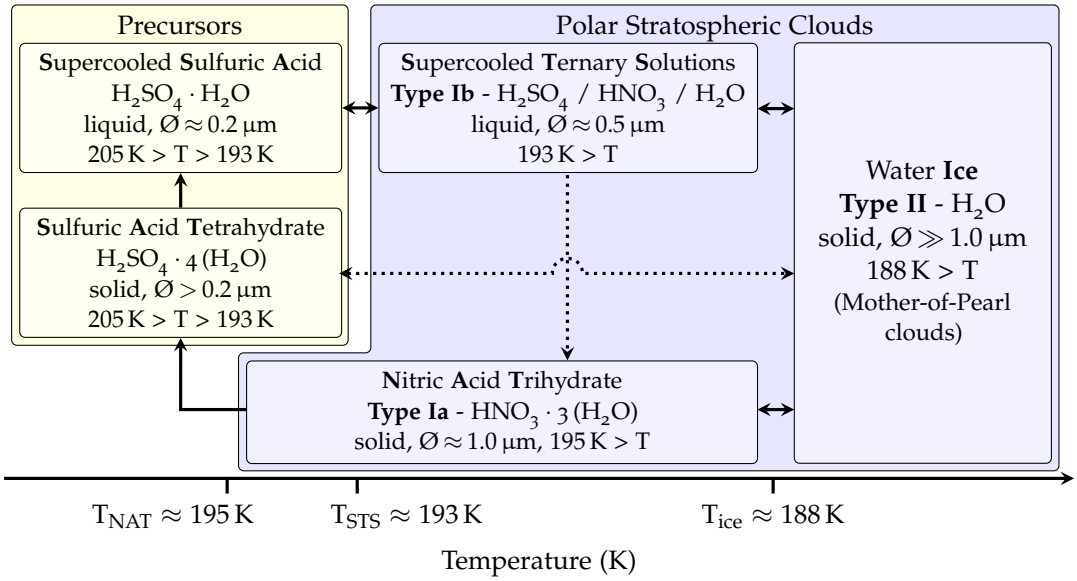

Figure 2.2: A scheme of polar stratospheric cloud development including characteristic features like size, state of matter and temperature requirements of the three main cloud types based on the studies of Tabazadeh et al. [1994], Bertram et al. [1996], Lowe and MacKenzie [2008] and Kirner et al. [2011]. The arrows show possible transitions between different compositions (bi-directional or one-way), with dashed lines indicating less important path ways.

TYPE IA Nitric Acid Trihydrate (NAT) clouds are mainly formed by heterogeneous nucleation on water ice particles (Type II PSCs) or to a lesser extent by freezing of supercooled ternary solution droplets (Type Ib PSCs). Recent studies show that meteoritic dust might also play an important role in the heterogeneous formation of NAT particles [Hoyle et al., 2013]. The solid particles with radii

of about 1 µm evaporate at about 195 K. They can be found as a remnant of water ice clouds on the lee side of mountain ridges (lee wave PSCs) like the Antarctic Peninsula in the south or the Scandinavian Mountains in the north [Meilinger et al., 1995].

TYPE IB Supercooled Ternary Solution (STS) droplets can form without nucleation by uptake of gaseous HNO_3 in sulfate aerosol starting at temperatures of around 193 K [Tabazadeh et al., 1994]. Droplets of STSs are typically larger than typical sulfate aerosol with about 0.5 µm, but remain liquid and are therefore spherically shaped.

TYPE II Water ice clouds can nucleate homogeneously at temperatures below 188 K [Koop et al., 2000]. In addition, similar to the nucleation of NAT particles, recent studies show that meteoritic dust particles can serve as ice nuclei in the polar stratosphere during winter season [Engel et al., 2013]. Water ice particles are typically larger than 1 µm and have complex shapes. These PSCs are frequently found in lee wave PSCs east of the Antarctic peninsula or the Scandinavian mountains.

PSCs are formed frequently above Antarctica (southern polar region) where temperatures are below 188 K consistently each winter season (Figure 2.3a). In the northern hemisphere PSCs are less frequent due to the different characteristic stratospheric temperature regime (Figure 2.3b).

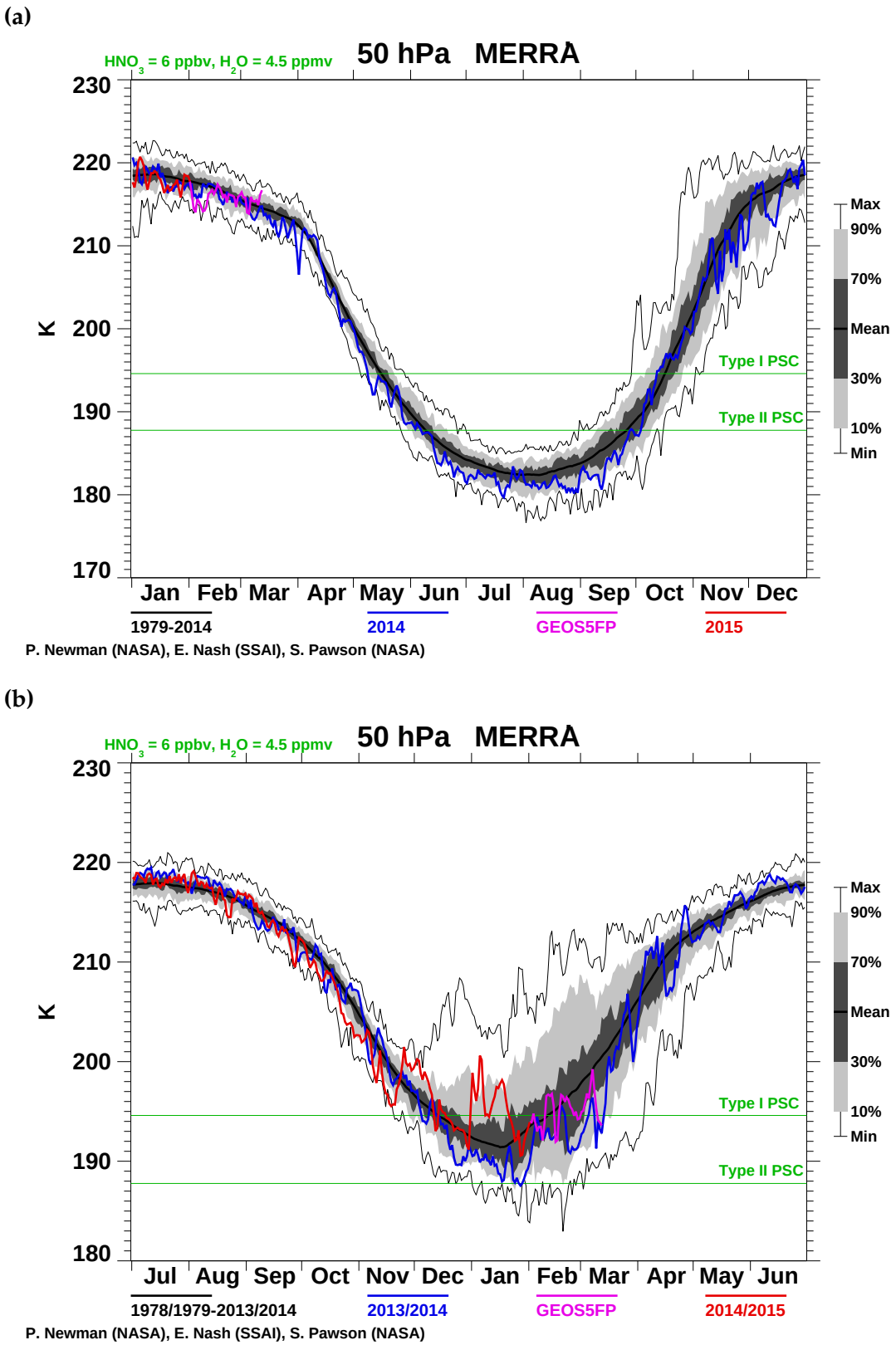

Figure 2.3: Development of the minimum temperature for the southern (a) and northern (b) polar stratosphere on the 50 hPa surface between 50° and 90° latitude of the respective hemisphere during 2014 and 2015. Most recent winter seasons (colored lines) are compared to the climatological mean of the years between 1979 and 2014 (black line) as simulated by the Modern-ERa Retrospective Analysis model (MERRA) [Newman et al., 2015]. Also shown are the threshold temperatures for the formation of PSCs of type I and II calculated with constant mixing ratios for HNO_3 (6 ppb) and H_2O (4.5 ppm).

3

SATELLITE MEASUREMENTS

The era of satellite remote sensing began after the successful launch of Sputnik I in 1957. Ever since, satellite measurements complement more traditional measurement platforms like balloons, weather stations and aircrafts, especially in remote regions like the atmosphere above the tropopause. Typical tasks of satellite missions changed over the course of time and became more and more specific. The Television and Infra-Red Observation Satellite (TIROS-1) is the first satellite which provided radiance spectra in order to describe Earth's cloud coverage and albedo [Conover, 1965]. It had a total mass of 129 kg and was designed with a life time in the order of months [OSCAR, 2015]. Nowadays, it is possible to design satellite programs with multiple specific tasks, longer presumed lifetimes and a significantly larger variety of carried instruments resulting in a much heavier payload ranging from 1200 to 2500 kg. For example, the Sentinel 3 satellite is equipped with 5 instruments and designed for a lifetime of over 7 years [Berger et al., 2012]. In this chapter, after a general introduction to satellite measurement geometries, two instruments of successful satellite missions will be explained in more detail as they provide the main data sets used in this thesis:

- SCanning Imaging Absorption spectroMeter for Atmospheric CHartographY (SCIAMACHY) on board of the ENVIronmental SATellite (ENVISAT) operating between 2002 and 2012
- Second Stratospheric Aerosol and Gas Experiment (SAGE II) on board of the Earth Radiation Budget Satellite (ERBS) operating between 1984 and 2005

3.1 MEASUREMENT GEOMETRIES IN SATELLITE REMOTE SENSING

Passive satellite remote sensing measurements are performed without using an active light source. Instead, measurements rely on scattered, reflected or direct light from sources like the Sun, the Moon, the Earth or stars with sufficient brightness. This observation type is generally categorized in three geometries: occultation, limb and nadir. This section explains these geometries and presents typical applications.

In **limb** geometry the telescope is looking tangential to the Earth's surface. The tangent height (TH) is defined as the shortest distance between the Earth's surface and the line of sight (LOS) located at the tangent point (TP) as shown in figure 3.1a. Due to the viewing geometry, the LOS has the highest sensitivity to an altitude region around the TH determined by the aperture angle. This type of measurement provides height resolved spectra but lacks in horizontal resolution along the line of sight. Since this measurement geometry highly depends on particles/molecules scattering light into the LOS, signal to noise ratio (SNR) worsens for high altitudes

due to decreasing number of molecules or long wavelengths due to decreasing scattering efficiency of molecules and aerosol particles. The SNR improves significantly for altitudes with increased number of stratospheric aerosol particles or towards lower altitudes where air density and therefore the number concentration of air molecules increases. However, depending on parameters like wavelength and cloud coverage, the optical thickness along the light path is strongly enhanced for lower tangent heights limiting the possibilities to retrieve information on the mid to lower troposphere. Measurements in limb geometry are typically used for deriving information on profiles of stratospheric molecules (e.g. Ozone) and particles (e.g. sulfuric acid droplets).

The **occultation** geometry (Fig. 3.1b) is a special case of limb geometry with the instrument pointing directly towards the light source. It is known for a high signal to noise ratio. Measured radiances are dominated by the light source while being reduced by absorption and scattering processes along the line of sight. This type of geometry was used since 1975 (SAM I) to measure vertically resolved spectra in order to determine ozone concentration and aerosol extinction profiles with high precision. The major disadvantage of this method is the restriction to locations from which the instrument can directly look into the light source, i.e. during rise or set of the light source.

In "near" **nadir** geometry (Fig. 3.1c) the field of view of the telescope covers the Earth's atmosphere around the nadir location. Despite the name of this measurement geometry, the telescope is not looking perpendicular to the Earth's surface for the full width of a swath. The nadir viewing direction is only reached at the center of the swath. This measurement geometry is sensitive to the troposphere and the planetary boundary layer due to enhanced light path lengths. Especially for bright surfaces measurements in nadir geometry usually have a good signal to noise ratio. At the same time measurements are able to cover a large fraction of the sunlit half of the Earth's surface. While providing an improved horizontal resolution, the vertically resolved information is more difficult to retrieve.

3.2 SCIAMACHY INSTRUMENT ON ENVISAT

In March 2002 the SCanning Imaging Absorption spectroMeter for Atmospheric CHartographY (SCIAMACHY) was launched on board of the polar orbiting, sun-synchronous ENVIronmental SATellite (ENVISAT). SCIAMACHY provided passive measurements in the spectral range between 240 and 1700 nm and a few selected regions up to 2380 nm until April 2012 [European Space Agency, 2010]. The full wavelength range of the instrument is subdivided into channels with different spectral resolutions ranging from 0.2 to 1.5 nm. For the description of measurements by SCIAMACHY the following list of terms is frequently used:

ORBIT describes a full track of the satellite around the globe.

(a) Measurement in limb geometry

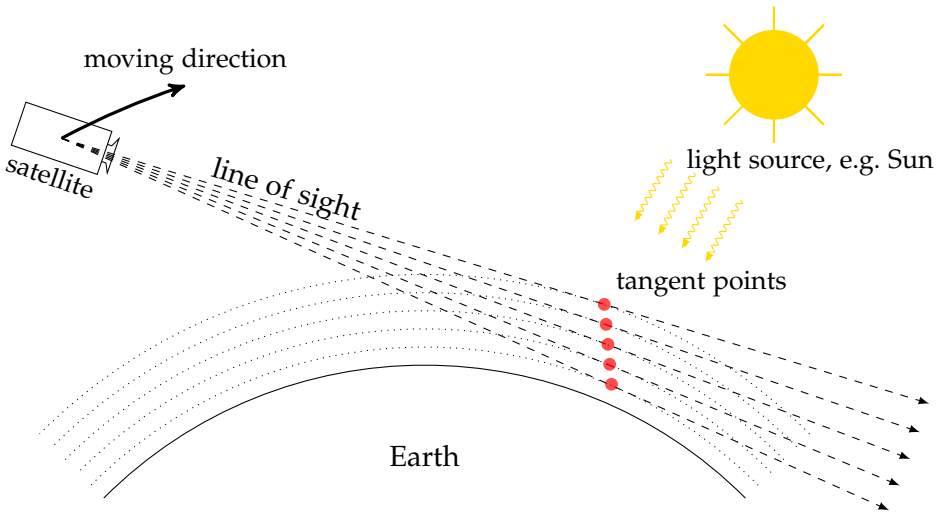

(b) Measurement in occultation geometry

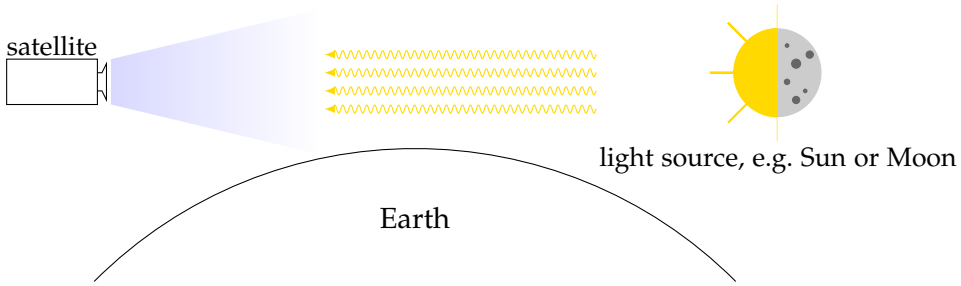

(c) Measurement in nadir geometry

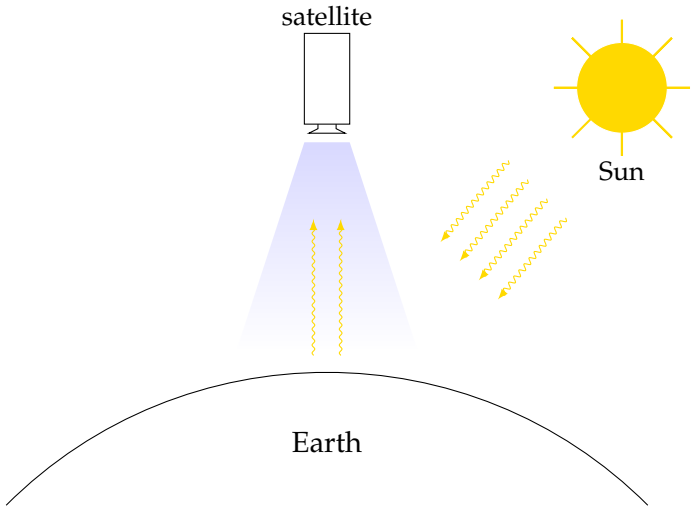

Figure 3.1: Three different measurement geometries are typically used in passive satellite remote sensing: (a) limb, (b) occultation and (c) nadir. Measurements in limb and occultation geometry are used to gain information on the vertical distribution of trace gases and particles. In occultation geometry the telescope is directly looking into a light source (Sun, Moon, Earth or other celestial objects). Measurements in nadir geometry provide improved horizontal resolution at the expense of vertically resolved information.

DESCENDING NODE is the part of the ENVISAT track that is on the day side of the Earth, see figure 3.2. Flight direction is from north to south. Accordingly, the ascending node is on the night side of the Earth.

STATE describes a cluster of measurements with the same geometry. As shown in figure 3.2, SCIAMACHY alternates between measurement states in limb and nadir geometry for the main part of the descending node. In addition, a solar occultation measurement is performed in the north and a lunar occultation measurement is performed in the south.

PIXEL is the single measurement at a specific location. The pixel size depends on measurement geometry and is determined by integration time and aperture angle. In nadir geometry, SCIAMACHY provides a horizontal resolution of 30 km along track and 60 km across track. In limb geometry the resolution is between 240 and 960 km across track and 3.3 km vertically at the tangent point location, compare figure 3.3.

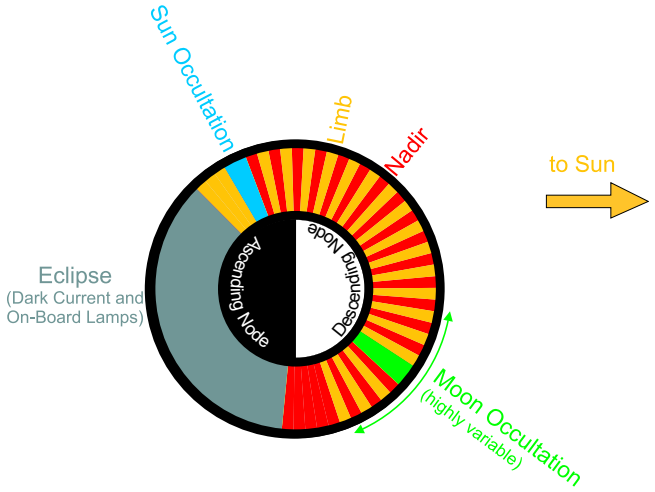

Figure 3.2: Measurement geometries that are performed on each orbit of the SCIAMACHY instrument. The orbit is subdivided into limb and nadir states and two occultation measurements which are mainly measured on the descending node. This figure is adapted from [Noël et al., 1999].

The ENVISAT orbit is slightly tilted. Thus, satellite measurements in limb geometry are only available for latitudes below 86° in the respective hemisphere. Each limb state after the measurements in occultation geometry spatially overlaps with its corresponding nadir state. This configuration can be used to apply a stratospheric correction to measurements in nadir geometry [Heue et al., 2005] or to gain additional information by applying tomographic techniques [Puķīte et al., 2008; Beirle et al., 2010; Hilboll et al., 2013]. In this work, nadir measurements are used to retrieve information on the effective albedo, which accounts for the effects of surface albedo and tropospheric clouds. In addition, SO_2 vertical column densitys retrieved from nadir measurements are used as proxy data of the horizontal extent of aerosol

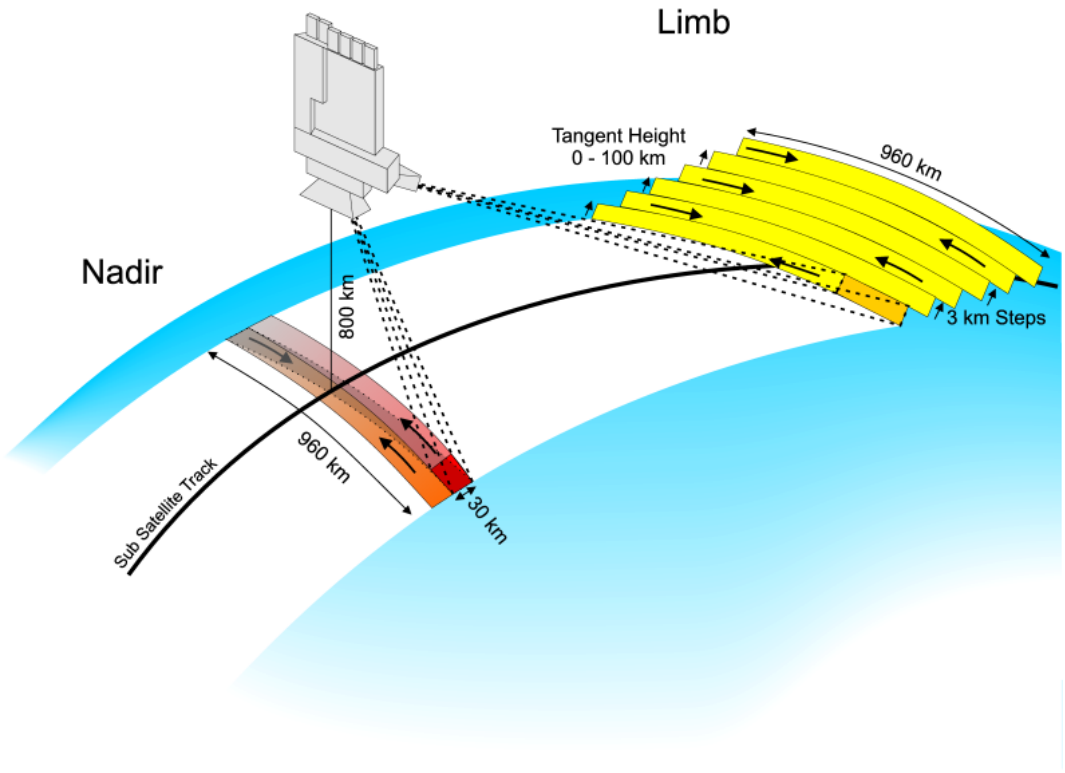

Figure 3.3: SCIAMACHY pixel sizes of measurements in limb and nadir geometry, from Noël et al. [2000].

plumes. Figure 3.4 shows an example of an ENVISAT orbit with locations of limb and nadir states on the 31st December 2010 (Orbit 46209).

The ENVISAT orbit is sun-synchronous crossing the equator at 10:00 am local time. The local time of each SCIAMACHY measurement varies with latitude and pixel number (viewing direction) and deviates from the equator crossing time by up to 60 minutes. Solar zenith angle (SZA) and solar azimuth angle (SAA) of each measurement depend on latitude and time of the year, creating a typical annual cycle for SCIAMACHY measurements in limb geometry. As shown in figure 3.5, typical regions with a backscatter geometry are located in the southern hemisphere and regions with a forward scatter geometry are located in the northern hemisphere, respectively. SCIAMACHY is a passive instrument and requires sunlight for the signal to noise ratio of measurements to be high enough for retrieval applications. Thus, measurements at high latitudes with a SZA larger than 93° are usually not used for the retrieval of aerosol extinction.

In a work by Soest [2005] evidence of residual grooves in the outer mirror of SCIAMACHY was found which diffract light into the instrument optics and broaden of the effective field of view. This causes an additional measurement signal that is referred to as spatial straylight. This work will review the investigations of spatial straylight for its altitude dependency in section 6.3.3.

(a) SCIAMACHY limb states

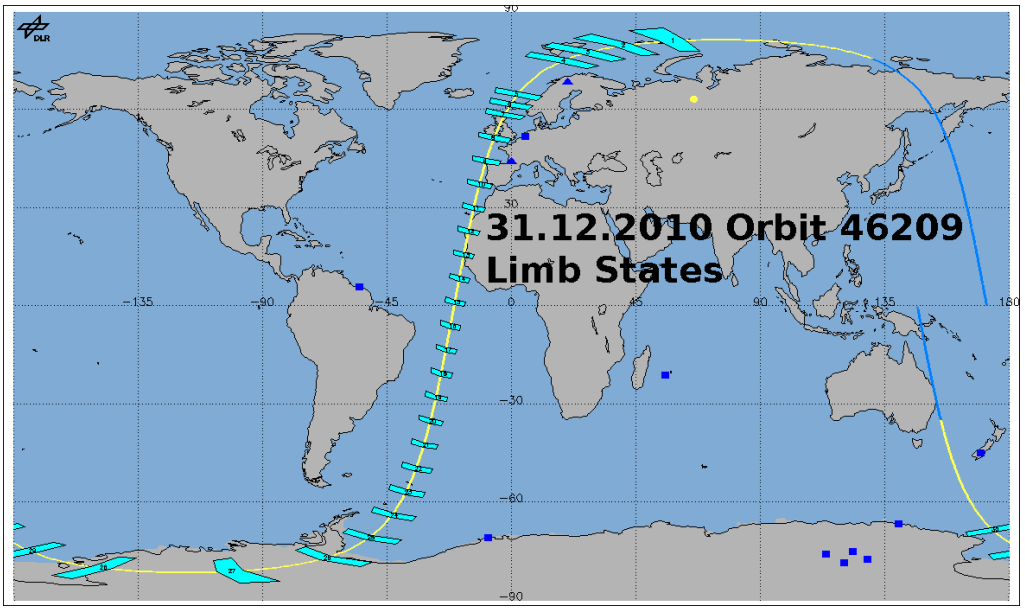

(b) SCIAMACHY nadir states

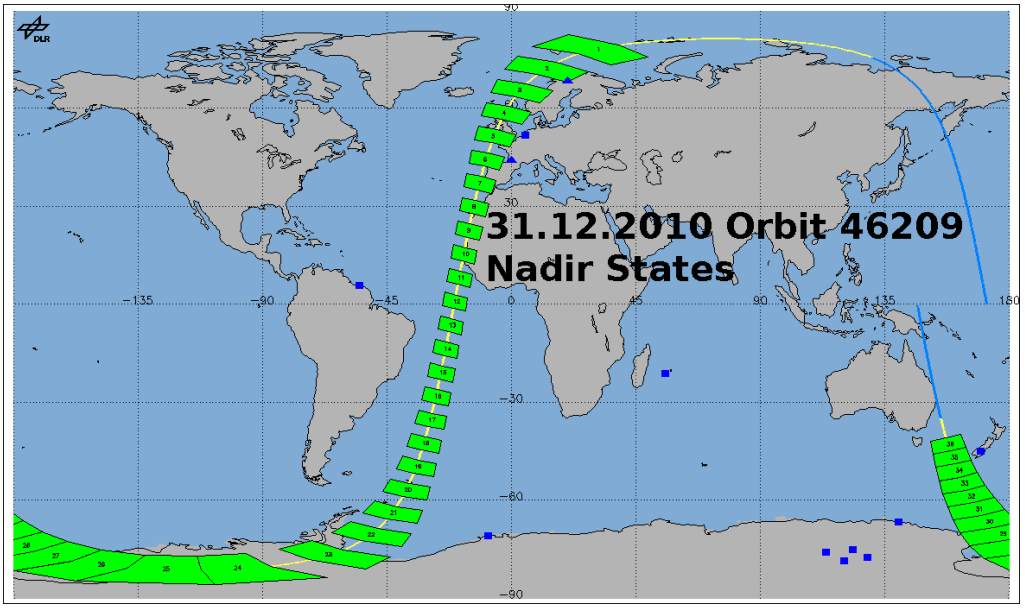

Figure 3.4: Example for the descending node of an ENVISAT orbit on 31st December 2010. Cyan boxes in 3.4a indicate the tangent points of SCIAMACHY measurements in limb geometry and green boxes in 3.4b show the footprint of a measurement in nadir geometry. This figure is adapted from [SCIAMACHY Operations Support Team, 2010].

(a) Annual Cycle of the Solar Zenith Angle

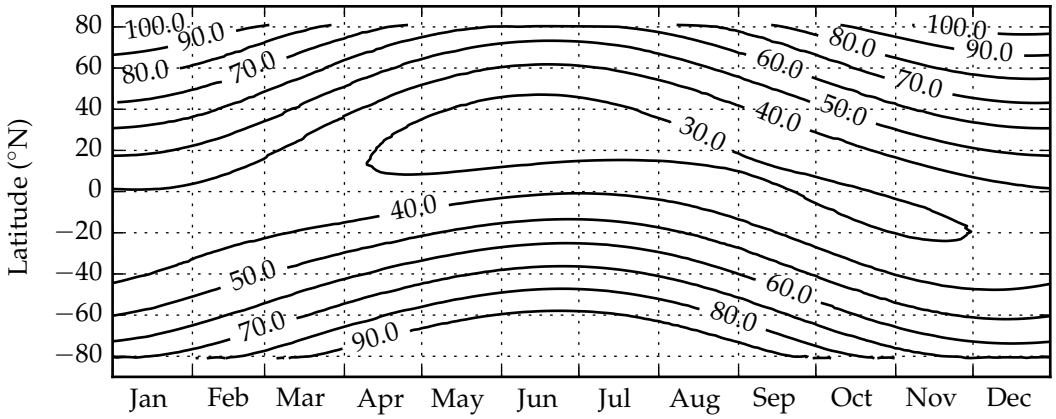

(b) Annual Cycle of the Solar Relative Azimuth Angle

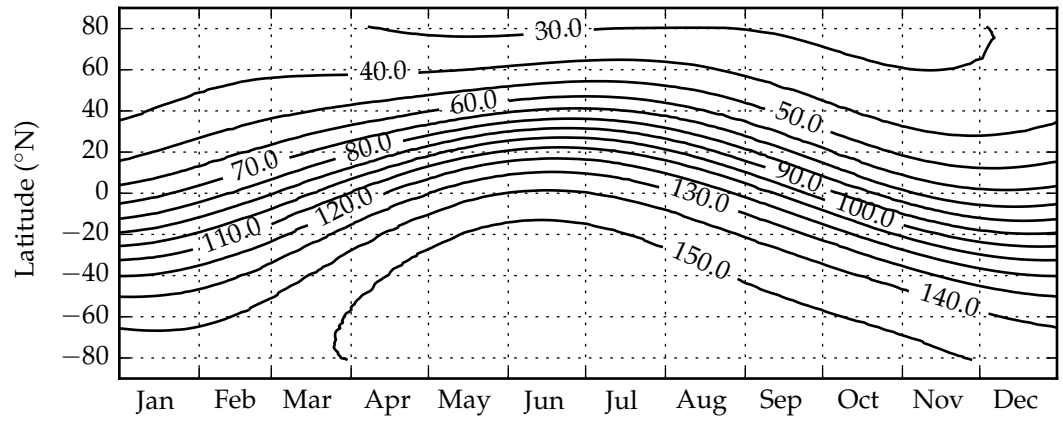

(c) Annual Cycle of the Single Scattering Angle ξ

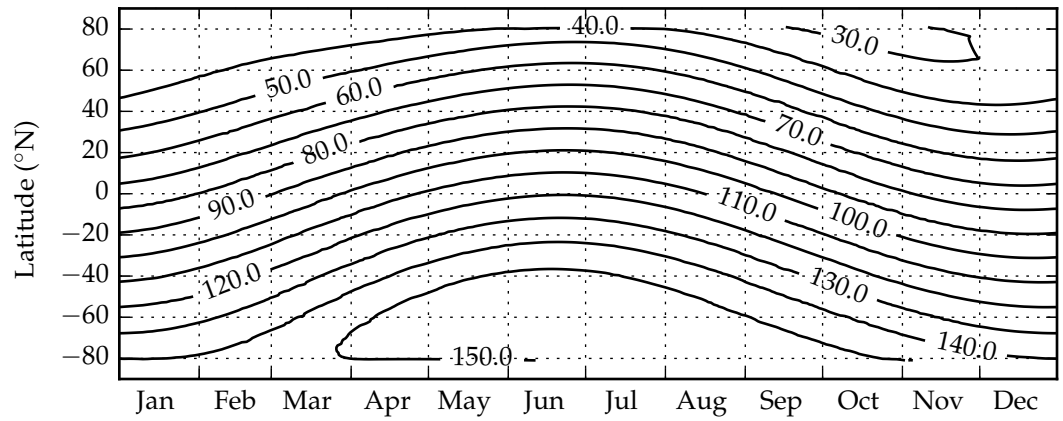

Figure 3.5: The annual variation of the relative sun position at the center of each SCIAMACHY limb state displayed by: (a) solar zenith angle, (b) solar relative azimuth angle and (c) single scattering angle ξ.

3.3 SAGE II INSTRUMENT ON ERBS

The second generation of the second Stratospheric Aerosol and Gas Experiment (SAGE II) on the Earth Radiation Budget Satellite (ERBS) was initially planned with a lifetime of two years when it was deployed from the Space Shuttle Challenger in October 1984. It exceeded its lifetime by far until it was shut down on 22nd August 2005 after 21 years of consistent measurements. SAGE II recorded direct sunlight in occultation geometry at seven wavelengths ranging from 382 to 1020 nm during fifteen sunrises and fifteen sunsets each day. ERBS was on a drifting orbit with an inclination of 57°. Therefore, SAGE II measurements were performed every 24° of longitude mainly covering northern and southern high latitudes as shown in figure 3.6. The instrument viewing direction of SAGE II changes between east-to-west for sunsets and west-to-east for sunrises by turning a telescope mirror.

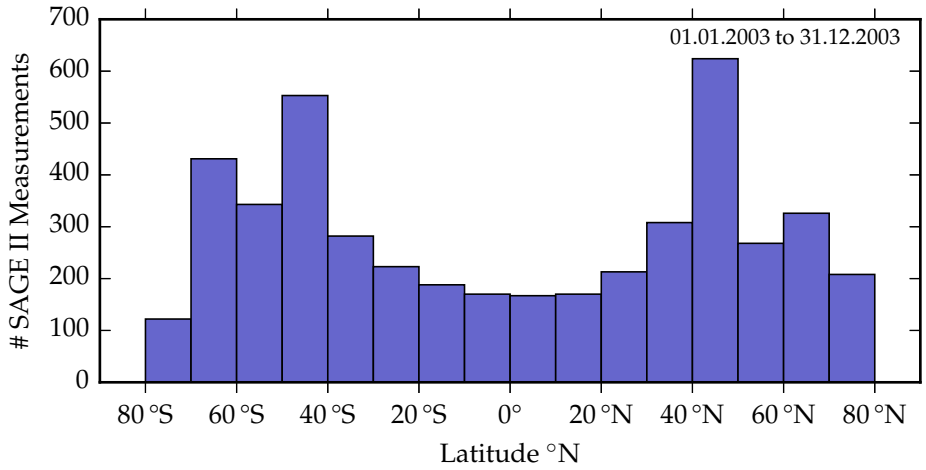

Figure 3.6: Latitudinal distribution of SAGE II measurements in 2003. With occultation measurements for sunrise and sunset the instrument mainly covers the high latitudes between 40 and 70° of each hemisphere.

From measured sunlight that is reduced by scattering and absorption of trace gases and aerosols, vertical profiles of the following quantities are retrieved between 10 and 40 km with a resolution of 0.5 km: ozone, water vapor, chlorine monoxide, nitrogen dioxide, bromine monoxide, sulfur dioxide and aerosol size, extinction and concentration. In this thesis the SAGE II version 6.2 data set are used for initial assumptions in the retrieval algorithm and for the determination of spatial straylight (see section 6.1.2 and 6.3.3).

4

RADIATIVE TRANSFER SIMULATION

Radiative transfer simulations are a key technique in retrieving information on aerosol particles from measured radiance profiles at various wavelengths. This section provides an introduction on particle properties and equations used in this thesis. Detailed configurations of the radiative transfer model (RTM) will be explained together with retrieval methods in chapter 6.

4.1 INTRODUCTION TO MCARTIM

The Monte Carlo atmospheric radiative transfer model McArtim developed by Deutschmann [2014] is used in this thesis. It supports the following features that are essential for the methods used in the stratospheric aerosol retrieval algorithm:

- The simulation of light paths on a spherical, three dimensional grid for a given atmospheric configuration.
- An effective simulation method ("importance sampling", Deutschmann [2014]) that optimizes the computational effort for each simulation.
- The possibility to include prescribed phase functions for any type of scattering particles.

McArtim was being constantly developed during the last three years. The version of 21st April 2014, that is used for the simulations in the retrieval algorithm, was compared other radiative transfer models (RTMs), following the comparison study performed by Wagner et al. [2007]. In this study, simulated normalized radiances are compared for wavelengths between 310 and 577 nm for a ground based instrument setup at various elevation angles, solar relative azimuth angles and solar zenith angles for an atmosphere with and without aerosol layer. The version of McArtim used in this study compares well against from the results of other RTM showed in this study.

4.2 SATELLITE GEOMETRY CONFIGURATION

Since multiple definitions of relative sun position and viewing geometry exist, the following list explains the conventions used in this thesis. The definitions are separated by tangent point location and sub-satellite location since both locations are typically multiple thousand kilometer apart and have therefore different relative sun positions as shown in figure 4.1.

VIEWING GEOMETRY: The viewing geometry is described by elevation angle (ϑ) and line of sight azimuth angle (φ), both defined at the sub-satellite location. The elevation angle ϑ is defined as (90° − zenith viewing angle) typically ranging from 90° (zenith) over 0° (horizon) to −90° (nadir). In this thesis the elevation angle is usually expressed as tangent height (TH). This is the shortest distance between the line of sight with an elevation angle ϑ and Earth's surface as shown in figure 4.1:

$$TH = \cos(\vartheta) \cdot (R_{\text{Earth}} + h_{\text{Sat}}) - R_{\text{Earth}} \tag{4.1}$$

with Earth's radius R_{Earth} and the altitude of the satellite h_{Sat}. In McArtim the line of sight azimuth angle is 0° for the north direction and increases for a counter clockwise rotation towards the west.

SUN POSITION: The position of the Sun is typically described either absolutely by latitude and longitude coordinates of the location, where the sun is in zenith position, or relative by solar zenith angle (SZA) and solar azimuth angle (SAA). For the configuration of McArtim the relative description at the position of the SCIAMACHY satellite is used. The solar zenith angle ranges from 0° with sun in zenith position over 90° with the sun at the horizon (sunrise/sunset) to 180° with the sun in zenith at the other side of the Earth. The solar azimuth angle is 0° for the north direction and increases for a clockwise rotation towards east. For the relative description of the solar position in McArtim the solar relative azimuth angle (SRAA) at the satellite location is used. With the definitions of SAA and line of sight azimuth angle (φ) the SRAA is derived following figure 4.2:

$$\text{SRAA} = 360 - \text{SAA} + \varphi \tag{4.2}$$

The solar position differs significantly between satellite and tangent point location. Therefore, solar zenith and azimuth angle are also determined at the tangent point location. The solar relative azimuth angle is then calculated like at the satellite position but with a different φ. For the calculation of the bearing of the shortest distance between to locations on Earth, the viewing azimuth from tangent point to satellite is not the same as the viewing azimuth from satellite to tangent point − 180°.

SINGLE SCATTERING ANGLE: The solid angle determined by SZA and SRAA is called the single scattering angle ξ. It is used to approximate the scattering direction at the TP location in an optically thin atmosphere. Note, that the elevation angle is 0° at the TP location and is therefore not considered in the following equation:

$$\xi = \arccos\left[\sin(\text{SZA}) \cdot \cos(\text{SRAA})\right] \tag{4.3}$$

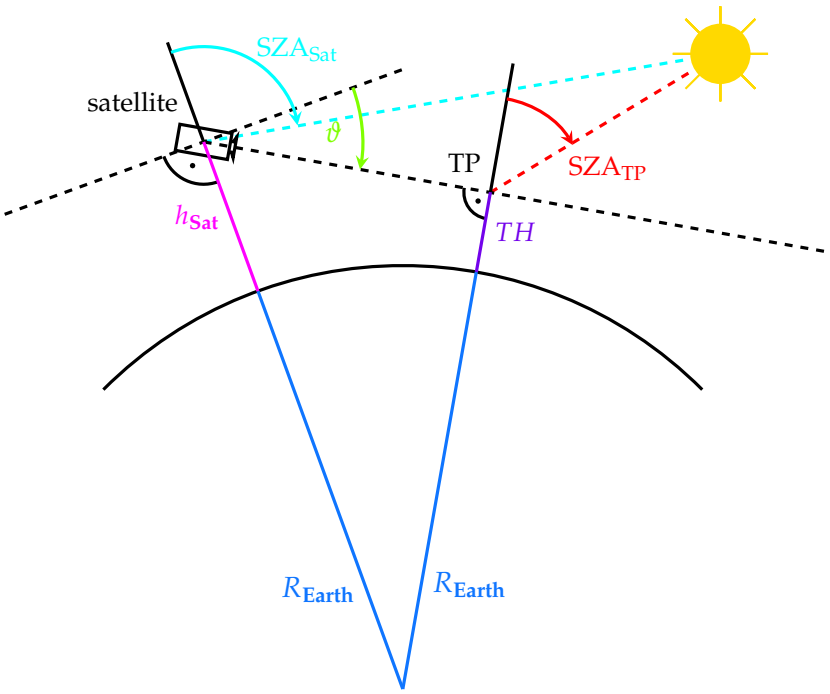

Figure 4.1: Tangent point (TP) and tangent height (TH, violet) are defined by satellite height h_{Sat} (magenta), elevation angle ϑ (green) and Earth radius R_{Earth} (blue). The solar zenith angle (SZA) at the satellite (cyan) differs from the SZA at the TP (red). This sketch is not according to scale.

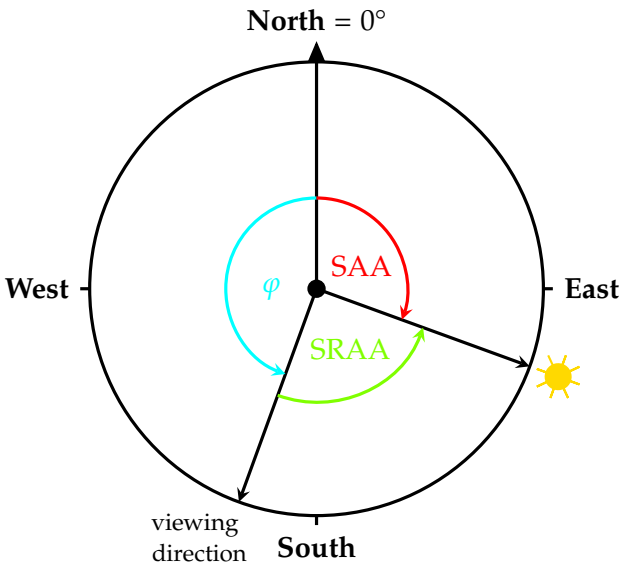

Figure 4.2: Azimuth angle definitions of line of sight (φ, cyan), the solar position (SAA, red) and the solar relative azimuth angle (SRAA, green) as used in this thesis. In the center of this horizontal projection is either the satellite or the tangent point.

4.3 SCATTERING PHASE FUNCTION

The scattering phase function describes the probability $P(\xi_{\text{out}})$ that a photon's direction of propagation is changed to a specific scattering angle ξ_{out} relative to the incident direction after interacting with a particle. For a full description of light scattering on aerosol particles with radii in the same order of magnitude as wavelengths in the visible (VIS) and near-infra-red (NIR) spectral range, Mie theory needs to be applied [Mie, 1908]. According to this theory, the scattering phase function of monodisperse particles can be derived from the complex refractive index and the size parameter of the spherical particle:

$$P = P(\xi, x, m) \tag{4.4}$$

$$x = \frac{2\pi \cdot r}{\lambda} = 2\pi \cdot k \cdot r \tag{4.5}$$

with phase function P, scattering angle ξ, size parameter x, refractive index m, particle radius r, wavelength λ and wave number k. Accordingly, the phase function for a particle size distribution $n(r)$ is derived as the normalized weighted sum of monodisperse scattering phase functions:

$$P[\xi, n(r), \lambda, m] = \sum_{r=r_l}^{r_u} P(\xi, \lambda, r, m) \cdot \frac{n(r)}{N} \tag{4.6}$$

$$N = \int_{r_l}^{r_u} n(r)\, dr \tag{4.7}$$

with the total number of particles N in the radius interval $[r_l, r_u]$. Lower and upper border of this interval have to be selected such that they represent the full size distribution ($n(r_l) \approx 0$ and $n(r_u) \approx 0$). For this work a single mode log-normal size distribution from equation 2.1 is chosen. Therefore, the scattering phase function P is described by wavelength λ, median radius r_m, distribution width σ and refractive index m. An example for very small particles $r \ll \lambda$ and typical size distributions for stratospheric aerosol is given in figure 4.3b. The phase function converges towards the phase function of the Rayleigh approximation when the particle radius decreases, as shown in this example for a wavelength of 1090 nm. The algorithm used in this thesis to calculate Mie phase functions is provided by the Earth Observation Data Group [McGarragh, 2015].

The refractive index that is used for the Mie calculations, depends on wavelength and the concentration of solved H_2SO_4 within the sulfate aerosol droplet. For varying compositions of the solution, the real part of the refractive index varies between 1.38 and 1.50. For the wavelengths used in this thesis, the composition of the sulfate aerosol affects the value of m stronger than the wavelength. Therefore, the refractive index is set to a constant value of $m = 1.405 + 0.000i$ according to in

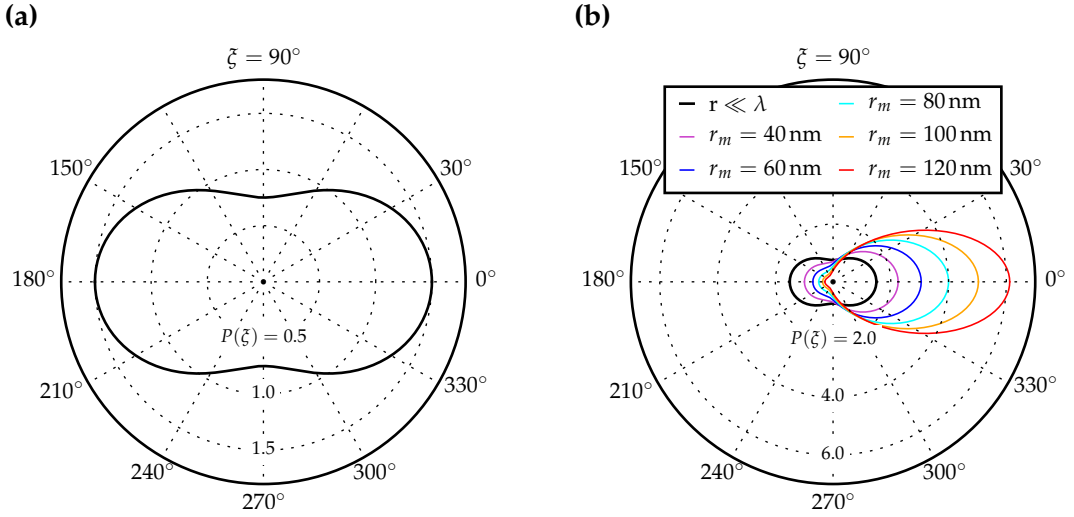

Figure 4.3: (a) Aerosol scattering phase function $P(\xi)$ for a particle radius of $r = 1\,\text{nm}$ at a wavelength of $\lambda = 1090\,\text{nm}$ (Rayleigh approximation) varying with scattering angle ξ with a linear scale for $P(\xi)$. (b) $P(\xi)$ is determined from Mie theory assuming a lognormal aerosol size distribution with $\sigma = 1.6$, various values for the mean radius r and a wavelength of $\lambda = 1090\,\text{nm}$ (colored lines). The different phase functions are compared against the Rayleigh phase function (black).

situ measurements of stratospheric aerosol particles with the high altitude aircraft ER-2 Baumgardner et al. [1996].

4.4 EXTINCTION COEFFICIENT

Scattering and absorption by particles in the atmosphere is generally described by the extinction coefficient β. Extinction describes the sum of absorption and scattering by particles or molecules. Wendisch and Yang [2012] define β as:

$$\beta = \int C_{\text{ext}}(\lambda, m, r') \cdot \frac{dn}{d\log r}(r')\, d\log r' \tag{4.8}$$

with number size distribution $n(r)$, particle radius r and the extinction cross-section C_{ext} which depends on wavelength λ, particle radius r' and refractive index m. In this thesis, the refractive index is assumed to be $m = 1.405 + 0.000i$ as described in the previous section. In this case the absorption cross-section becomes $C_{\text{abs}} = 0$ and the extinction cross-section equals the scattering cross-section.

4.5 ÅNGSTRÖM EXPONENT

Ångström [1930] introduced the parameter of atmospheric turbidity α is introduced:

$$\frac{\beta_1}{\beta_2} = \left(\frac{\log \lambda_2}{\log \lambda_1}\right)^{\alpha} \tag{4.9}$$

with wavelength λ and aerosol extinction β at the respective wavelength. Nowadays α is known as the Ångström exponent. Anders Ångström found it to be closely linked to the size of aerosol particles: Typical values of α range from 0.0 for very large particles (no wavelength dependency of aerosol extinction as for example in white clouds) to 4.0 for particles that can be described by Rayleigh Theory ($r \ll \lambda$, blue sky). For tropospheric aerosol particles α is found to be between 1.0 and 1.5. For strong volcanic eruptions α decreases to values of 0.5 or less [Ångström, 1930]. For stratospheric background aerosol typical values around 2.0 are found [Schuster et al., 2006]. In more recent studies the Ångström exponent is used to determine microphysical properties of aerosol particles [Gobbi et al., 2007]. In this work α is used to interpolate the aerosol extinction from SAGE II from given wavelengths 525 and 1020 nm to the wavelengths used in the retrieval algorithm: 525, 750, 870 and 1090 nm as follows: First, the aerosol extinction β measured at the wavelengths 525 and 1020 nm is used to derive the Ångström exponent α as

$$\alpha = \log\left(\frac{\beta_{525\,\mathrm{nm}}}{\beta_{1020\,\mathrm{nm}}}\right) \Big/ \log\left(\frac{525\,\mathrm{nm}}{1020\,\mathrm{nm}}\right). \tag{4.10}$$

The derived value for α is then used to derive the aerosol extinction at other wavelengths according to equation 4.9:

$$\beta_{750\,\mathrm{nm}} = \beta_{525\,\mathrm{nm}} \cdot \left(\frac{\log 525}{\log 750}\right)^{\alpha} \tag{4.11}$$

$$\beta_{870\,\mathrm{nm}} = \beta_{525\,\mathrm{nm}} \cdot \left(\frac{\log 525}{\log 870}\right)^{\alpha} \tag{4.12}$$

$$\beta_{1090\,\mathrm{nm}} = \beta_{1020\,\mathrm{nm}} \cdot \left(\frac{\log 1020}{\log 1090}\right)^{\alpha} \tag{4.13}$$

Part II

STRATOSPHERIC AEROSOL RETRIEVAL

5

COLOR INDEX METHOD

Scattering by molecules (Rayleigh approximation) and larger particles for instance in clouds or aerosol are distinguished by characteristic wavelength dependencies. These differences can be expressed by a ratio of radiances at two wavelengths that are not influenced by molecular absorption, to identify particle scattering along the light path of measured spectra. In Savigny et al. [2005] a ratio of radiances at two wavelengths $I_{750\,\mathrm{nm}}$ and $I_{1090\,\mathrm{nm}}$, called color index (CI), is defined as:

$$R(TH) = \frac{I_{1090\,\mathrm{nm}}(TH)}{I_{750\,\mathrm{nm}}(TH)} \tag{5.1}$$

with color index R, tangent height TH and measured radiance I_λ at $\lambda = 750\,\mathrm{nm}$ and $\lambda = 1090\,\mathrm{nm}$, respectively. It is shown that by applying this method to SCIAMACHY measurements in limb geometry, polar stratospheric clouds (PSCs) can be detected.

In case of molecular scattering the measured radiance is decreasing proportional to λ^{-4} according to the Rayleigh approximation: In an atmosphere without aerosol $I_{1090\,\mathrm{nm}}$ is smaller than $I_{750\,\mathrm{nm}}$ by about a factor of 4.5 if the incoming radiance is assumed to be constant, resulting in $R \approx 0.2$. Particles with radii $r \gg \lambda$ like cloud droplets reduce the wavelength dependency depending on the number of particles which affect the measurement and therefore increase the color index R. While this simple method lacks information about vertical extent or particle quantity, it is capable of identifying air masses with enhanced particle concentration in the stratosphere such as PSCs, volcanic eruptions or pyro-convective plumes strong enough to cross the tropopause.

Figure 5.1 shows the color index retrieved from SCIAMACHY measurements in January 2005 during a stable polar vortex period. Temperature contours at an altitude of 18.5 km are derived from the ERA Interim model data set provided by the European Center for Medium-Range Weather Forecast (ECMWF). Enhanced values of the color index indicate that measurements at a tangent height of 18.5 km are affected by enhanced particle scattering. For the shown measurements, the CI is only increased within a region where the temperature is below 195 K and therefore hints to PSCs, according to the scheme presented in figure 2.2.

In figure 5.2 the color index shows the influence of the Nabro eruption on stratospheric particle abundance within the first two days after the eruption. Correlated to a significant increase in SO_2 vertical column density (VCD), the color index proves the existence of particles in altitudes around 18.5 km, that are larger as the typical background aerosol described in section 2. Determining the particle type (i.e. volcanic ash, water ice or sulfate aerosol) is not possible using only the color index. The comparison to other proxy data like SO_2 helps to interpret color index

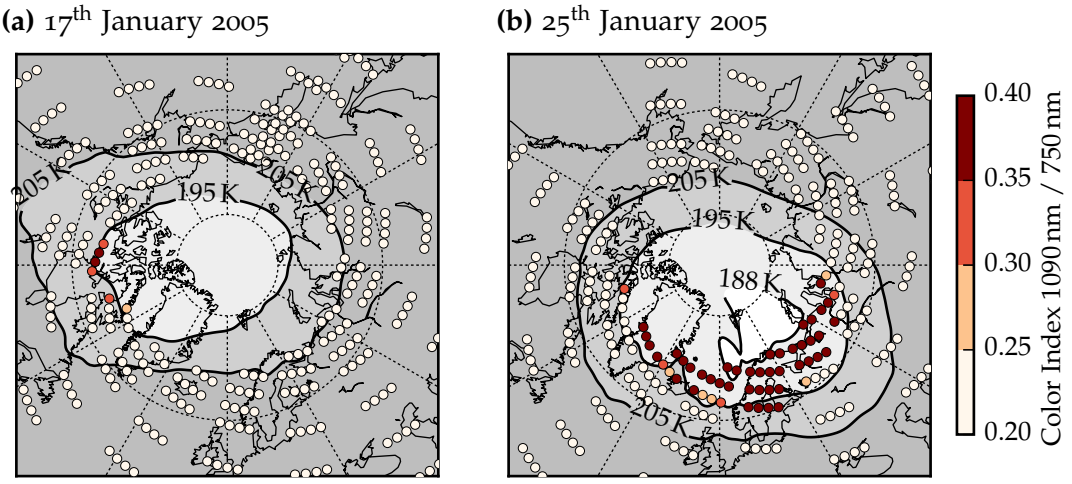

Figure 5.1: Color Index measured by SCIAMACHY in January 2005 displayed as colored circles at the tangent point location at a tangent height of 18.5 km for the Arctic region. Contour lines and gray shades show the ECMWF ERA-Interim temperature interpolated to an altitude of 18.5 km. The color index significantly increases for very cold polar regions indicating particles involved in the process of PSC formation.

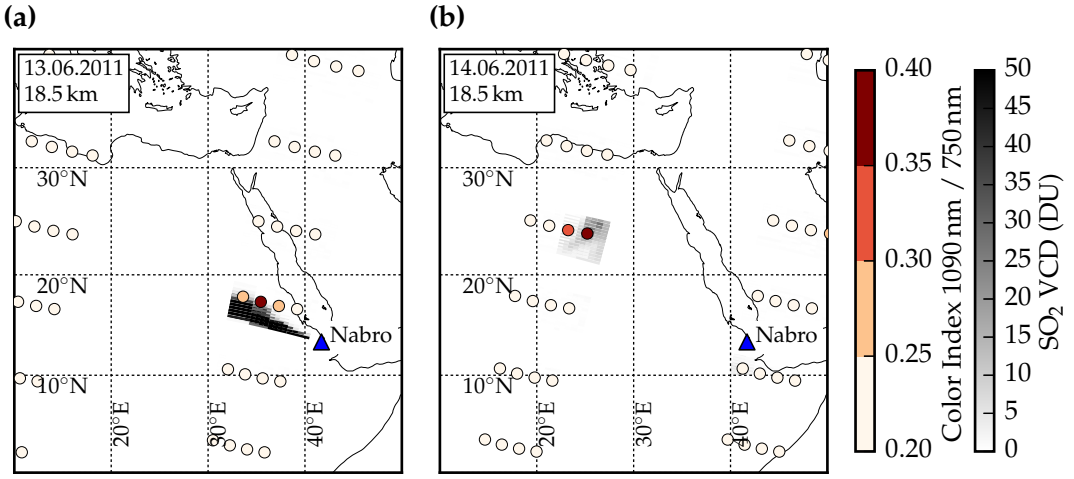

Figure 5.2: Color Index measured by SCIAMACHY in June 2011 at a tangent height of 18.5 km. Gray shaded boxes show SCIAMACHY VCD of SO_2. In this case the color index significantly increases for regions with an increased SO_2 VCD marking the plume of the Nabro eruption on 13th June 2011 (a) and 14th June 2011 (a).

values, but is not always unambiguous as shown in figure 5.3. While SO_2 VCDs are a vertically integrated quantities, CI values are shown for a specific tangent height integrated along a slant light path in limb geometry. Thus, SO_2 VCDs can be increased without a correlated enhancement of the CI if the plume is located below

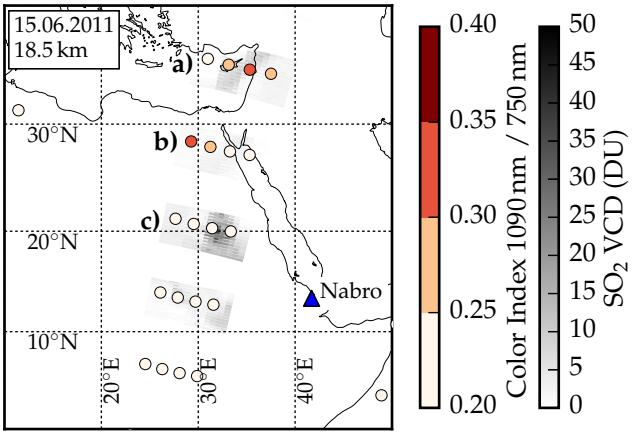

Figure 5.3: As figure 5.2 but for the 15th June 2011. This plot shows the three typical cases for the comparison of the color index (CI) with other data sets: In state a) both data sets are correlated. In state b) CI values are enhanced for regions with a few DU of SO_2. State c) shows no enhancement for CI values despite the increase in SO_2 VCD (see text).

an altitude of 18.5 km as in figure 5.3 state c). In addition, correlation characteristics vary for different parts of the volcanic plume as shown in figure 5.3 state b) where CI values are enhance for regions where increases in SO_2 VCDs are less pronounced.

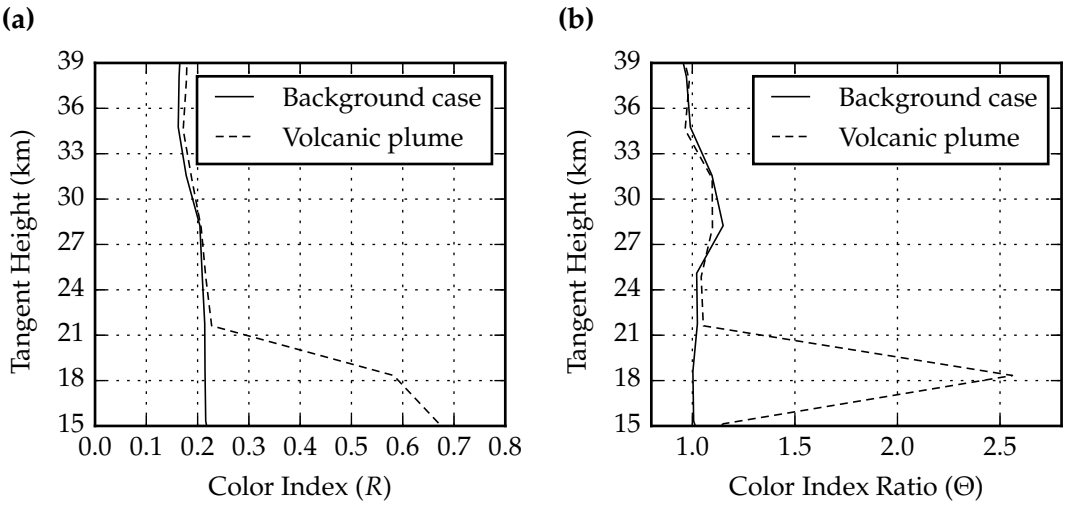

Figure 5.4: Example for color index and color index ratio (Θ) for two measurements on the 14th June 2011. Solid lines show the profile of CI (a) and Θ (b) for background conditions. Dashed lines indicate a profile that is influenced by a volcanic plume of the Nabro eruption.

The color index is sufficient to describe horizontal regions of enhanced particle scattering qualitatively. However, the measured radiance in limb geometry at a specific tangent height is also influenced by scattering processes that occur above

the respective altitude. Thus, CI values remain high for tangent height (TH) below the altitude region affected by particle scattering. The color index ratio (Θ) on the other hand focuses on the CI change from one tangent height to the next enhancing the signal at the top of layers with increased particle abundance. It is defined as

$$\Theta(TH) = \frac{R(TH)}{R(TH + \Delta TH)} \tag{5.2}$$

Figure 5.4 shows that Θ strongly increases at the top of the volcanic plume and also shows slightly elevated values around 30 km. Hence, this method not only identifies polar stratospheric clouds as intended in the work of Savigny et al. [2005], but also other types of increased particle scattering.

Additional examples for the spatial and temporal variation of Θ are given in the following.

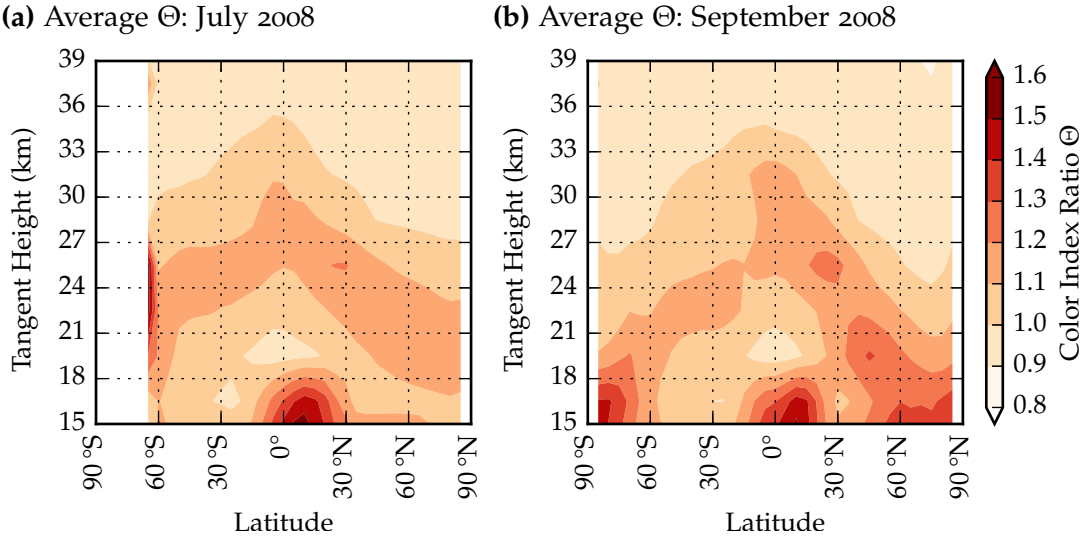

Figure 5.5: Monthly and longitudinally averaged color index ratio Θ profiles calculated from SCIAMACHY measurements with a solar zenith angle smaller than 90° in July 5.5a and September 5.5b of 2008.

Figure 5.5 shows monthly and longitudinally averaged variations of Θ for an altitude range between 15 and 39 km in July and September 2008. The following list shows main sources of variability in stratospheric aerosol particle abundance identified by Θ:

- The stratospheric aerosol background layer (Junge layer) varies both temporally, roughly following the latitude region of strongest incoming solar radiation, and latitudinally from tropics to high latitudes between 21 and 27 km.
- Tropical convective clouds reach up to an altitude of 18 km at around 10 °N.
- Polar stratospheric clouds above Antarctica (around 80 °S) descend from about 24 km in July to about 15 km in September 2008.

- Mt. Kasatochi eruption on 08.08.2008 influences the stratospheric aerosol layer around 50 °N up to an altitude of 21 km.

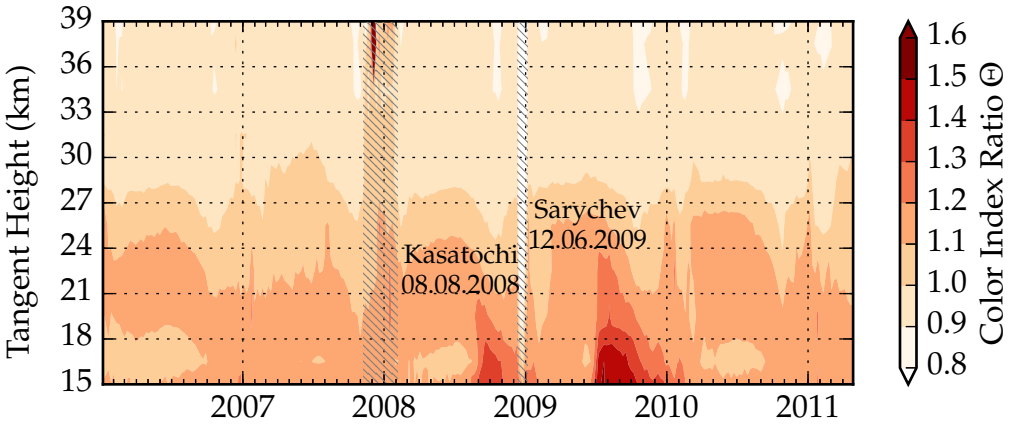

Figure 5.6: Color index ratio Θ profiles calculated from SCIAMACHY measurements for the time range from January 2006 to April 2011. Hatched gray areas indicate time ranges with measurement problems in 2008 and 2009. Shown values are averaged over five days between 55 °N to 65 °N.

Rise and decay of increased particle scattering induced by volcanic eruptions of Mt. Kasatochi in August 2008 and Mt. Sarychev in June 2009 are shown in figure 5.6. In addition, seasonal and annual variations of the stratospheric background aerosol layer between 55 °N to 65 °N can be identified.

The given examples indicate the potential information on aerosol particles contained in SCIAMACHY limb geometry measurements. In order to gain more detailed information on particle properties and quantity, radiative transfer simulations have to be applied. In the following chapters the retrieval of stratospheric aerosol extinction using individual wavelengths will be explained and investigated. The color index is used in sensitivity studies shown in chapter 8 for the identification of measurements which are affected by enhanced particle scattering.

6

STRATOSPHERIC AEROSOL EXTINCTION RETRIEVAL

High precision in-situ measurements of stratospheric aerosol properties taken by high altitude aircrafts like the ER-2 [Drdla et al., 1994] or weather balloons [Deshler et al., 2006] are only performed for distinct locations and times. Remote sensing from satellite enables the investigation of temporal variations of stratospheric aerosol particle properties on a global scale [Chu et al., 1989; Thomason et al., 2007]. However, satellite instruments cannot determine particle properties directly. The measured radiance has to be interpreted using radiative transfer simulations. Methods to retrieve stratospheric aerosol extinction from satellite measurements in limb geometry are implemented for the OSIRIS on the Swedish satellite Odin [Bourassa, 2007] and SCIAMACHY on ENVISAT [Ernst et al., 2012] using the optimal estimation approach as described in Rodgers [2000].

In this thesis the onion peeling method is applied to SCIAMACHY measurements at individual wavelengths. The main target is to not only retrieve aerosol extinction profiles but also microphysical properties of aerosol particles using wavelength dependent variation of aerosol extinction. Optimal estimation and onion peeling approach rely on iterating aerosol particle properties provided as input to a radiative transfer model, until the simulated and measured radiance match up. However, the measured radiance is influenced by a number of parameters as summarized in table 6.1. As a result, the problem of finding the correct particle properties is highly underdetermined. Therefore, assumptions are used to reduce the number of free parameters and sensitivity studies help to interpret the result. In the following, general assumptions are listed and explained while important assumptions will be discussed in further detail in section 6.1.

Gaseous Absorbers (e.g. ozone)
Scattering by air molecules (Rayleigh scattering)
Surface albedo
Tropospheric clouds
Stratospheric clouds
Absorbing particles (e.g. soot, ash)
Scattering particles (e.g. H_2SO_4 droplets)

Table 6.1: List of parameters that influence the spectral radiance measured in limb geometry.

Some wavelengths are less affected by gaseous absorbers and thus well suited to reduce the amount of necessary assumptions. The retrieval used in this work operates at 525, 750, 870 and 1090 nm (also used in Savigny et al. [2005]; Taha et al.

[2011]; Bourassa et al. [2012a]). Out of this set of chosen wavelengths only 525 nm is substantially influenced by ozone absorption. Therefore, ozone cross sections from Bogumil et al. [2003] and ozone concentration profiles from the collocated ERA Interim data set provided by the European Center for Medium-Range Weather Forecast (ECMWF) are used. For stratospheric background conditions, i.e. only sulfate aerosol as described in chapter 2, there is also no significant influence of particle absorption for the chosen wavelengths.

Scattering processes on molecules are calculated from the temperature and pressure profiles provided by ECMWF using the collocated ERA Interim data set. For the description of the Rayleigh cross section formulas from Landgraf et al. [2004] are used. In addition to uncertainties of air density, Rayleigh cross section and phase function, the precision of Rayleigh scattering simulations depends on the horizontal and vertical resolution of the radiative transfer model (RTM). For this work the setup of the RTM is two-dimensional with one box in longitudinal direction, a resolution of 1° (about 110 km) in latitudinal direction and 1 km in altitude. For simplification, the chosen grid is not specifically aligned to the line of sight of the satellite instrument. However, for the application on SCIAMACHY limb measurements, the latitudinal direction almost coincides with the line of sight.

Surface albedo and tropospheric clouds are combined to define an effective albedo ω_{eff}. It is derived as the ratio of the reflected radiance measured in nadir geometry I_{nadir} over the incoming solar irradiation E_0 weighted by the cosine of the solar zenith angle SZA:

$$\omega_{\text{eff}} = \frac{I_{\text{nadir}} \cdot \pi}{E_0 \cdot \cos(SZA)} \tag{6.1}$$

The radiance measured in nadir geometry is influenced by surface properties like snow cover, sea surface roughness or regions with high optical thickness like clouds or haze. To get a representative value for the effective albedo, all SCIAMACHY nadir pixels within the horizontal area of sensitivity of the corresponding SCIAMACHY limb measurement are averaged. Typical values for the optical thickness of the atmosphere above the tropopause are in the order of 10^{-3} and at least two orders of magnitude lower than the optical thickness of the troposphere. Here, the optical thickness is usually about 10^{-1} for cloud free cases and much larger than one if clouds are in the field of view. Thus, the effective albedo calculated from those measurements is approximating effects of surface albedo, tropospheric clouds and aerosol layers below the tropopause which influence the measured radiance in limb geometry. This approximation does not hold for events of optically thick particle layers in the stratosphere like PSCs or plumes of volcanic eruptions. However, the retrieval uncertainty for such events is dominated by other effects like saturation as discussed in section 6.1.4.

With the described approximations the model setup now consists of two remaining quantities that can be varied in order to reproduce the measured radiance: Particle scattering and absorption. Both quantities can be described microphysically by refractive index, particle size distribution and number of particles or by their optical

properties, like single scattering albedo, phase function and extinction. Refractive index and particle size distribution are set as shown in table 6.2 leaving the extinction β as a free parameter. Therefore, an agreement between measured and simulated radiances can only be achieved if the extinction profile used in the simulation β_{sim} equals the atmospheric extinction profile $\beta_{\text{atmosphere}}$:

$$I_{\text{meas}} = I_{\text{sim}} \Rightarrow \beta_{\text{atmosphere}} = \beta_{\text{RTM}} = \beta \tag{6.2}$$

For the description of the retrieval β means both $\beta_{\text{atmosphere}}$ and β_{RTM} as used in this equation. Since the main purpose of this retrieval algorithm is to gain information on sulfate aerosol, β is referred to as aerosol extinction in this thesis. However, the retrieval algorithm also applies to extinction caused by other particles like in PSCs or volcanic plumes, with restrictions that arise from the assumptions on microphysical particle properties.

	microphysical		optical properties	
m	$1.405 + 0.000i$		SSA	1.00
$n(r)$	log-normal, unimodal $r_m = 80\,\text{nm}$, $\sigma = 1.6$	➡	$P(\xi)$	Mie$[m, n(r)]$

Table 6.2: The refractive index m is chosen according to in situ measurements by the NASA aircraft ER-2 [Baumgardner et al., 1996], compare section 4.3. The parameters for the aerosol size distribution $n(r)$ are derived from balloon soundings as described in Deshler [2008]. Both parameter sets give a microphysical description of stratospheric aerosol that is sufficient to derive the single scattering albedo (SSA) and phase function $P(\xi)$ (compare figure 4.3b) by applying Mie theory.

The implementation of the retrieval algorithm is explained in section 6.1, followed by consistency and sensitivity studies in section 6.2. Section 6.3 describes how measured radiances are preprocessed for the use in the retrieval algorithm. Also, correction methods for measurement peculiarities like spatial straylight are discussed.

6.1 RETRIEVAL ALGORITHM DESCRIPTION

The assumptions described above lead to a basic algorithm. A short summary of retrieval assumptions is given in figure 6.1. Basic definitions of the RTM grid are given in section 6.1.1 followed by an overview on the general idea of the onion peeling approach in section 6.1.2. In section 6.1.3, a quantity that describes the sensitivity of a measurement to aerosol scattering called radiance-extinction gradient is introduced and the detailed implementation of the retrieval algorithm is discussed. Another method which uses the analyses of photon trajectories simulated by the radiative transfer model to derive sensitivity of measurements in limb geometry to stratospheric aerosol extinction is given in section 6.1.4 .

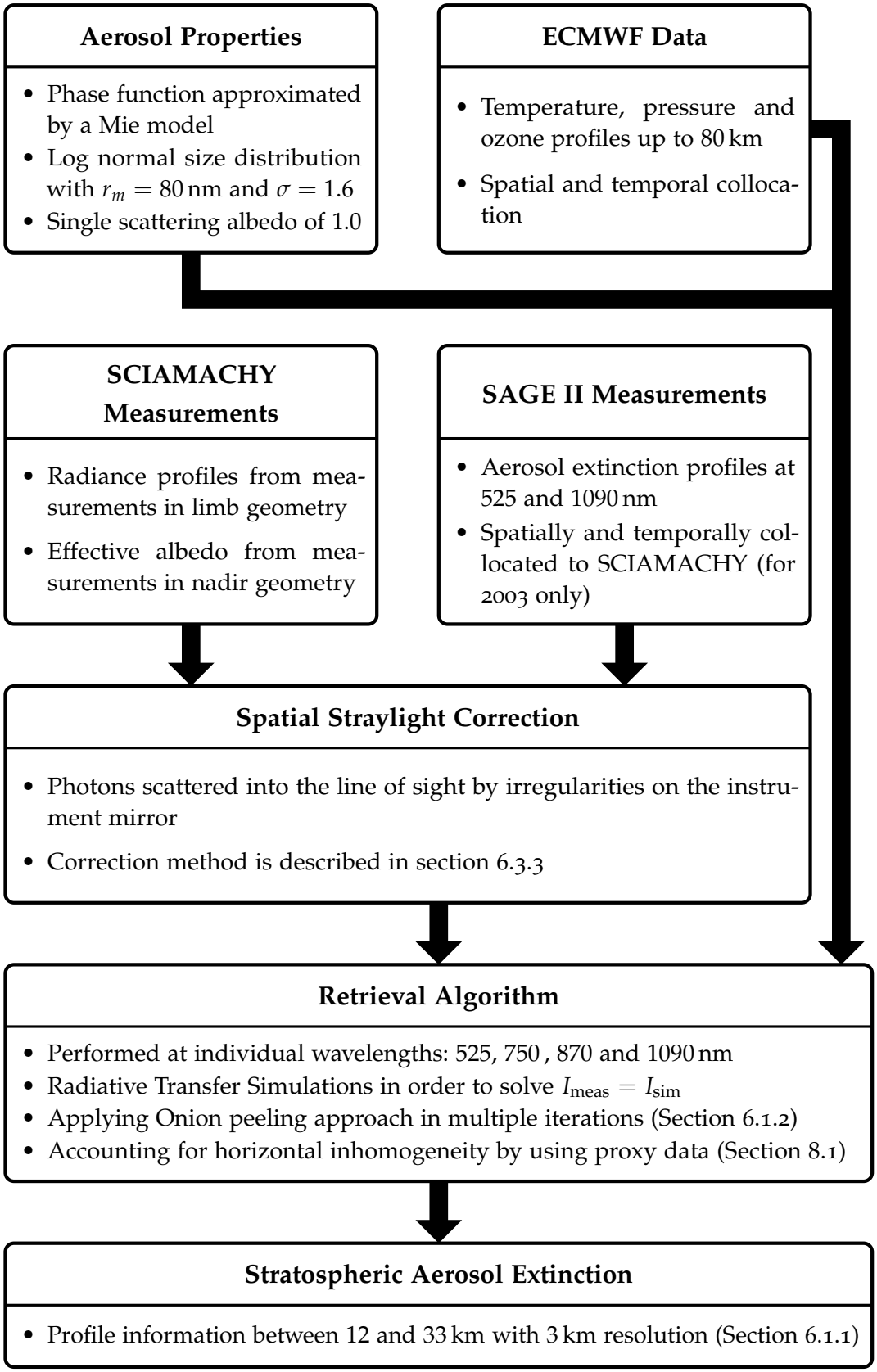

Figure 6.1: Flow chart scheme of the retrieval algorithm developed and used in this thesis.

6.1.1 *Radiative Transfer Model Grid Definition*

For simulations with the radiative transfer model McArtim, horizontal and vertical resolutions of the retrieval domain are defined to optimize computational effort without reducing the capabilities of the retrieval algorithm. Horizontally, the RTM treats the longitudinal dimension a single box and divides the retrieval domain into boxes of 1° in the latitudinal dimension. This resolution is required to handle effects of inhomogeneous aerosol layers in viewing direction (approximately north to south) of the satellite instrument as will be introduced in section 8.1. Vertically, the resolution is set to 1 km for the input of temperature, pressure and ozone profiles. The retrieval of aerosol extinction is performed on clustered 3 km bins according to the measurement resolution of about 3.3 km.

In order to fulfill the assumptions needed for equation 6.4 in section 6.1.3, the upper boundary has to be as high as possible to minimize the influence by aerosol particles on the measured radiance. At the same time the signal to noise ratio worsens with increasing tangent height. As a compromise, the upper boundary of the retrieval domain is chosen to be at 36 km. The lower boundary of the retrieval domain is determined by the increasing optical depth along the line of sight, which eventually results in a shift of the region, where measured photons originate, towards the instrument. This saturation effect is either caused by strong increase of molecular scattering towards shorter wavelengths or by other reasons for enhanced particle scatter, like tropospheric clouds, PSCs or volcanic plumes. The retrieval algorithm will stop as soon as a saturation threshold is reached with the lowest tangent height considered being 13.5 km. This leads to the lower altitude border of the retrieval domain at 12 km. In order to decouple numerical effects caused by interpolation within the RTM, measurements are interpolated to a fix tangent height grid with a resolution of 3 km between 13.5 and 34.5 km, accordingly. The resulting retrieval domain with respect to the tangent point is shown in figure 6.2. From now on h_j describes the model grid box center at an altitude h and TH_i describes the line of sight (LOS) with a tangent height TH. Accordingly index j refers to the retrieval domain and index i refers to the measurement domain. The relation between tangent height and altitude is shown in figure 6.3.

6.1.2 *Onion Peeling Approach*

The method to retrieve information from satellite measurements in limb geometry in an "onion-peeling fashion" without a priori knowledge is being used for over 30 years [Gordley et al., 1981]. This method is applicable if the retrieved quantity from a measurement at a specific tangent height (TH_i) is mainly influenced by the atmosphere at that altitude and above ($h_j \geq TH_i$). Figure 6.3 shows that this is generally true for measurements in limb geometry. Therefore, the aerosol extinction β can be retrieved starting at a reference altitude, above which radiance measurements

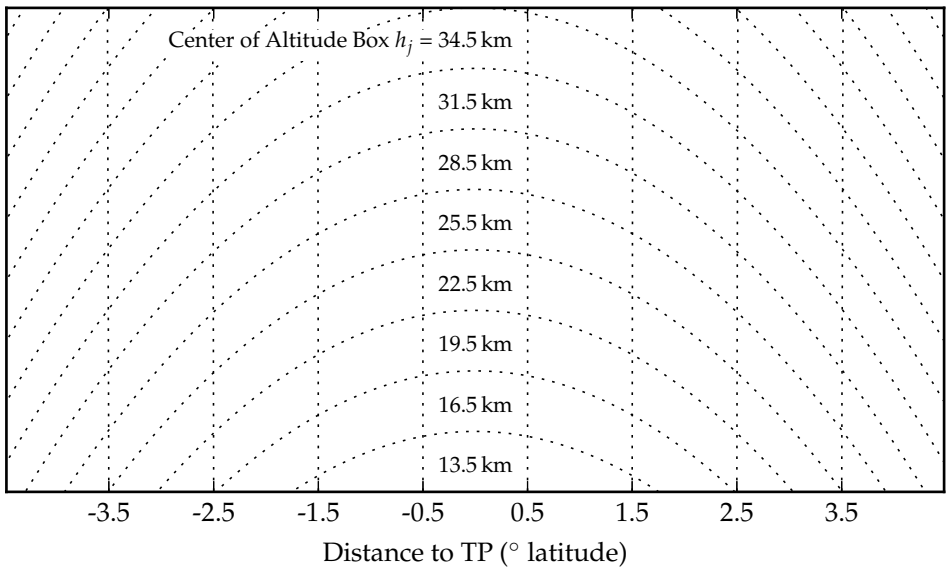

Figure 6.2: The retrieval domain is defined by a latitude grid with 1° resolution and a altitude grid with 3 km resolution. Instead of being of circular shape according to Earth's curvature, altitude grid lines have a parabolic shape and vertical latitude grid lines seem to be in parallel. This results from the aspect ratio of vertical extent (24 km) to horizontal extent (1000 km) of the figure.

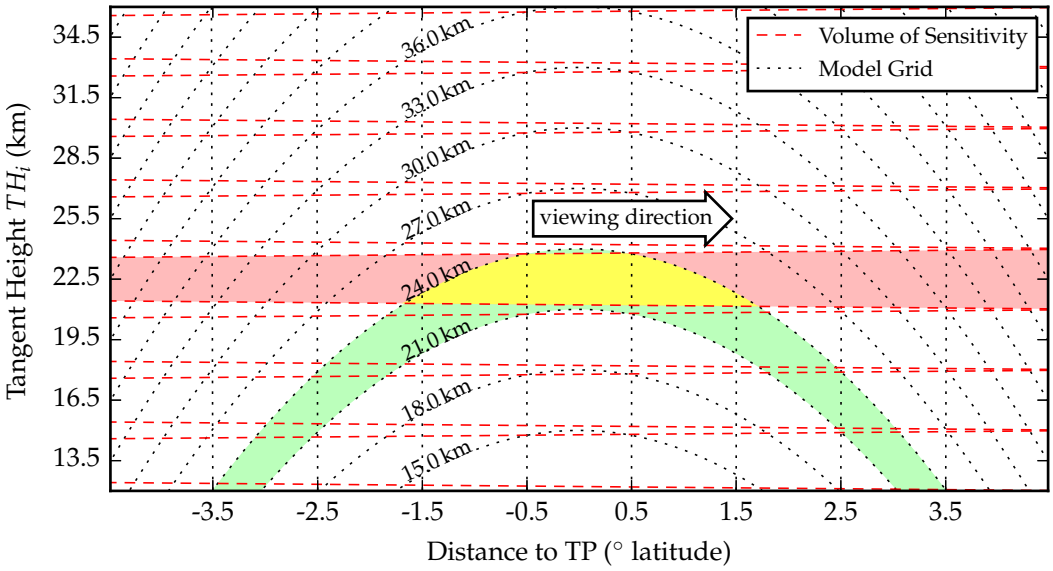

Figure 6.3: Similar to figure 6.2 dotted lines indicate the model grid. The altitude box between 21 and 24 km is indicated by the green area. The red area indicates the volume of sensitivity (VOS) of the LOS with a tangent height of 22.5 km. Measurements at this tangent height are sensitive to the indicated altitude range in an area around the tangent point, as displayed by the yellow area. Additionally, measurements are sensitive to other altitudes above 24 km. The size of the VOS is defined by the aperture of the SCIAMACHY instrument (0.045°).

are not strongly affected by scattering on aerosol particles. For the simulation the extinction profile can then be set to zero above the reference altitude:

$$\beta(h_j > TH_{\text{ref}}) = \beta_{\text{ref}} = 0 \tag{6.3}$$

$$I(TH_{\text{ref}}, \beta(h_j > TH_{\text{ref}})) = I(TH_{\text{ref}}, \beta_{\text{ref}} = 0) \tag{6.4}$$

If chosen assumptions for temperature, pressure and effective albedo in the RTM represent the atmosphere of the measurement, $I_{\text{sim}}(TH_{\text{ref}})$ and $I_{\text{meas}}(TH_{\text{ref}})$ are equal. With β_{ref} being zero, aerosol extinction for each subsequent altitude h_j can be retrieved from measurements with a tangent height of $TH_i = h_j$: The extinction profile in the RTM is varied until simulated and measured radiances match as described by equation 6.2. This method is subsequently applied to all tangent heights above 13.5 km. At this altitude the atmosphere becomes optically thick and the sensitivity to aerosol extinction decreases (see section 6.1.4). If saturation effects occur for measurements above that tangent height, the retrieval will also stop (see section 6.1.5). This retrieval method is summarized by the following flow chart.

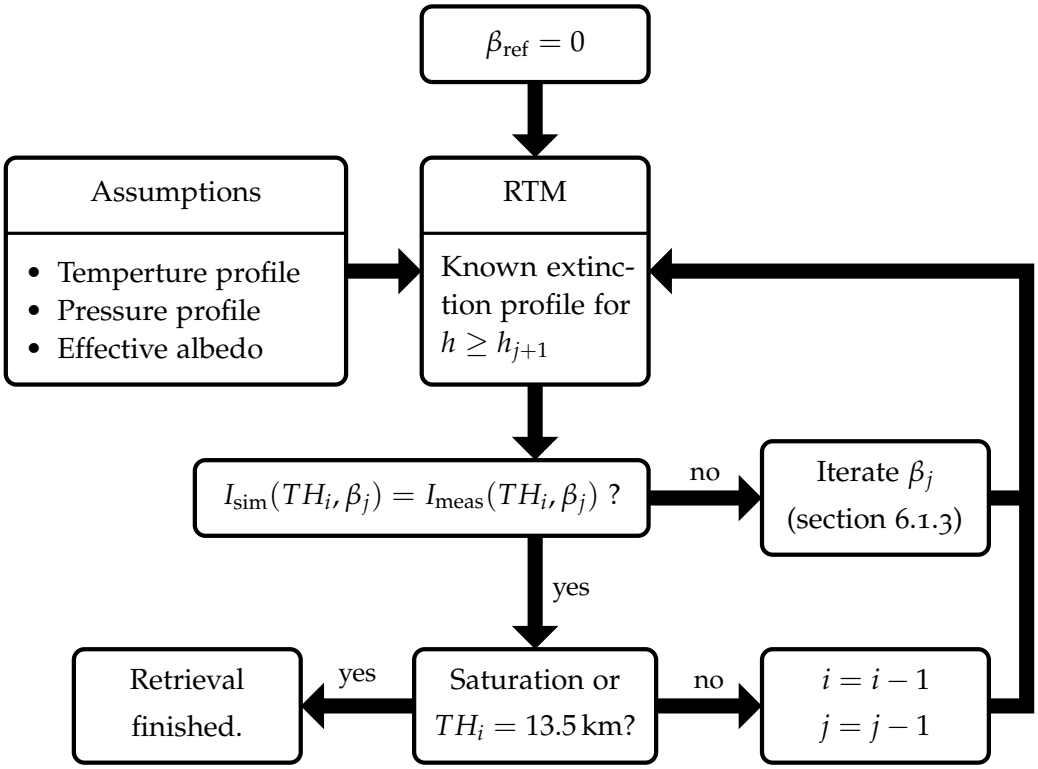

Figure 6.4: Flow chart of the basic onion peeling method for the retrieval of stratospheric aerosol extinction β from measured radiance profiles in limb geometry.

In comparison to the optimal estimation approach [Bourassa et al., 2012a; Ernst et al., 2012] the onion peeling method does not depend on an initial guess for the aerosol extinction profile and is less susceptible to numerical artifacts. On the downside, this method does not directly account for a bottom-up influence of

aerosol extinction on the measured radiance. Bottom-up effects can occur in cases of optically thick aerosol layers within the retrieval domain. To account for this issue, the onion peeling approach is applied in multiple iterations with the resulting aerosol extinction profile of the last iteration used as input for the next iteration.

The uncertainties of effective albedo or instrumental calibration affect the simulations at all tangent heights systematically. The influence of these uncertainties on the retrieval result can be reduced by performing a normalization, using the radiance at a reference tangent height $I(TH_{\text{ref}}, \beta_{\text{ref}} = 0)$ [Ernst et al., 2012]. This normalization modifies equation 6.2 to:

$$\frac{I_{\text{meas}}(TH_i, \beta_j)}{I_{\text{meas}}(TH_{\text{ref}}, \beta_{\text{ref}} = 0)} \stackrel{!}{=} \frac{I_{\text{sim}}(TH_i, \beta_j)}{I_{\text{sim}}(TH_{\text{ref}}, \beta_{\text{ref}} = 0)} \tag{6.5}$$

In this thesis, the tangent height of 34.5 km is used as the reference height. However, measurements with a tangent height of 34.5 km are sometimes still sensitive to aerosol scattering. This matter will be discussed in section 6.3. The following section will describe, how equation 6.5 is solved by the retrieval algorithm.

6.1.3 *Radiance-Extinction Gradient*

Sensitivity to aerosol extinction, i.e. the amount of increase in radiance caused by aerosol extinction, can be investigated using the radiance-extinction gradient

$$\gamma_{i,j} = \gamma(TH_i, h_j) = \frac{\partial I[TH_i, \beta(h_j, \lambda), \lambda]}{\partial \beta(h_j, \lambda)} \tag{6.6}$$

It is calculated by McArtim with the importance sampling method (see section 4.2 in Deutschmann et al. [2011]). An example for simulated radiance-extinction gradients $\gamma_{i,j}$ in an atmosphere with and without an aerosol layer between 21 and 24 km is shown in figure 6.5. As shown in figure 6.3, the simulated radiance is mainly influenced by $\beta(h_j \geq TH_i)$. Therefore, radiance-extinction gradients $\gamma(TH_i = 22.5\,\text{km}, h_j)$ are significantly larger for altitude boxes $h_j \geq 22.5$ km than for boxes below, see figure 6.5b. As a direct result for the simulation with an aerosol layer at 22.5 km, the radiance is increased compared to the simulation without aerosol only for tangent heights $TH_i \leq h_j$ as shown in figure 6.5a.

Decreasing values of the radiance-extinction gradient indicate a dependency on aerosol extinction as displayed in figure 6.5c for a tangent height $TH_i = 22.5$ km at an altitude box $h_j = 22.5$ km. After staying constant up to an extinction of $10^{-4}\,\text{km}^{-1}$, γ rapidly decreases and converges to zero for $\beta \gtrsim 10^{-1}\,\text{km}^{-1}$. In addition, γ depends on any quantity that affects the atmospheric light path, e.g. wavelength, albedo, sun position and aerosol extinction in other altitudes. Examples for this multi-dimensional dependency are given in section A.1.

The sensitivity to particle scattering can be expressed as the change in radiance ΔI with aerosol extinction $d\beta$. This change is calculated by integrating the radiance-

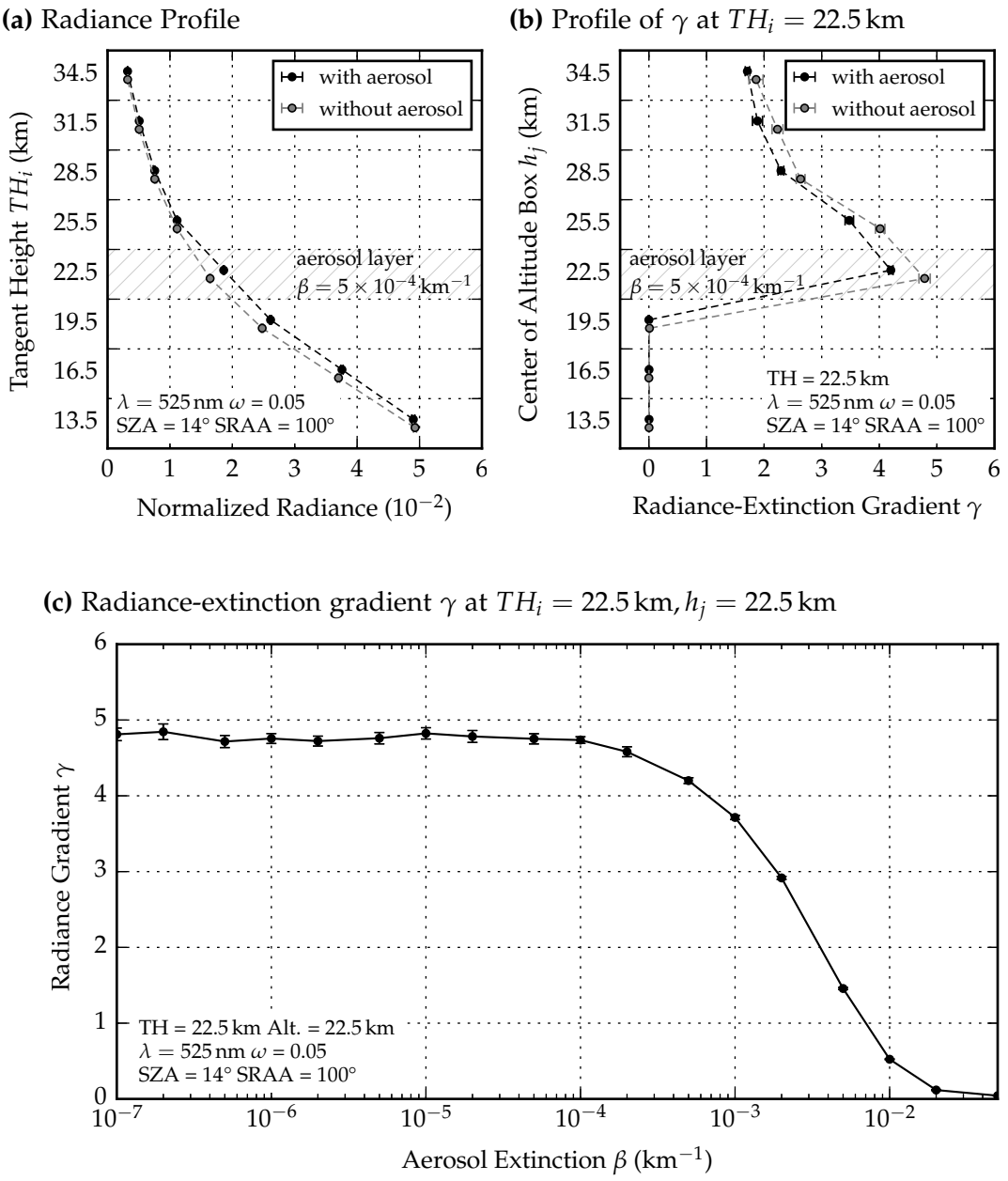

Figure 6.5: (a) Simulated radiance profiles for each tangent height TH_i within the model domain (12 to 36 km) with and without an assumed aerosol layer between altitudes 22 and 25 km. The highest values of the radiance-extinction gradient profile $\gamma(TH_i = 22.5\,\mathrm{km}, h_j)$ in (b) are reached at $h_j = TH_i = 22.5\,\mathrm{km}$ in both cases. However, values are generally higher for the case without the aerosol layer indicating a dependency of γ on the aerosol extinction β. This relation is shown in (c) for $TH_i = 22.5\,\mathrm{km}$ and $h_j = 22.5\,\mathrm{km}$.

extinction gradient γ over $d\beta$ and then adding up the contributions of all altitudes h_j:

$$\Delta I(TH_i) = \sum_j \int_0^{\beta_j} \gamma_{i,j} \cdot d\beta \tag{6.7}$$

Since γ is integrated from zero to an extinction β, small values of γ are not equivalent to small values of $\Delta I(TH_i)$. For the application in the retrieval algorithm the non linear relation between γ and β as shown in figure 6.5c is not known. This limits the possibility to directly interpret γ in terms of aerosol extinction sensitivity.

With γ depending on the aerosol extinction profile β, multiple simulations would be required to derive the functional relation between γ and β for a specific configuration. It turns out, that the computational retrieval performance can be optimized by assuming assume γ to be constant for application in the algorithm:

$$\Delta I(TH_i) \simeq \sum_j \gamma_{i,j} \cdot \beta_j. \tag{6.8}$$

The summation can be separated into three essential parts. For $j < i$ the addend is assumed to be zero, i.e. the intensity measured at a tangent height of TH_i is not influenced by aerosol extinction below the respective altitude as shown in figure 6.3. For $j > i$ the addends are known due to the onion peeling approach. The only unknown addend is therefore:

$$\Delta I'(TH_i, h_j) = \gamma_{i,j} \cdot \beta_j \tag{6.9}$$

In the following $\Delta I'(TH_i, h_j)$ is expressed as $\Delta I'_i$. Reforming this equation in order to determine the extinction β_j yields

$$\beta_j = \gamma_{i,j}^{-1} \cdot \Delta I'_i. \tag{6.10}$$

$\Delta I'_i$ can also be expressed as the difference between simulated and measured radiance, caused by the difference between β_{atm} and β_{sim} at the altitude h_j. For the retrieval algorithm it is defined according to equation 6.5 as

$$\Delta I'_i = I_{\text{meas}}(TH_i, \beta_j) \cdot \frac{I_{\text{sim}}(TH_{\text{ref}}, \beta_{\text{ref}} = 0)}{I_{\text{meas}}(TH_{\text{ref}}, \beta_{\text{ref}} = 0)} - I_{\text{sim}}(TH_i, \beta_j) \tag{6.11}$$

$$\delta\Delta I'_i = |\Delta I_i + 1| \cdot \sqrt{\left(\frac{\delta I_{\text{sim}}(TH_i, \beta_j)}{I_{\text{sim}}(TH_i, \beta_j)}\right)^2 + \left(\frac{\delta I_{\text{sim}}(TH_{\text{ref}}, \beta_{\text{ref}} = 0)}{I_{\text{sim}}(TH_{\text{ref}}, \beta_{\text{ref}} = 0)}\right)^2} \tag{6.12}$$

where $\delta\Delta I'_i$ is the difference uncertainty that results after applying the variance formula with the standard deviation of the radiance simulated by McArtim.

While γ is constant for $\beta \lesssim 10^{-3}\,\text{km}^{-1}$, the simplification is problematic for optically thick aerosol layers. This non-linear problem can be solved iteratively. The iteration formula to determine the extinction β_j that solves equation 6.5 can be written as

$$\beta_{j,k+1} = \beta_{j,k} + \gamma_{i,j,k}^{-1} \cdot \Delta I'_{i,k} \text{ until } \Delta I'_{i,k} < \delta\Delta I'_{i,k} \tag{6.13}$$

With iteration index k. Here, the definition of the difference between measured and simulated radiance in equation 6.11 is extended by the iteration index k: $\Delta I'_{i,k}$. The iteration stops if $\Delta I'_{i,k}$ is smaller then $\delta\Delta I'_{i,k}$.

For the implementation of the onion peeling method it is assumed that aerosol extinction β at altitudes h_j below the respective tangent height TH_i does not influence the radiance measured at tangent height TH_i. However, this assumption is not always valid. In figure 6.7 on page 46 an example for this bottom-up influence is shown. In order to decrease uncertainties caused by this effect, the retrieval algorithm is iterated. After the onion peeling method described in figure 6.4 found an aerosol extinction profile β_j which solves equation 6.5, the retrieval is performed another time, using the resulting aerosol extinction from the last iteration. For the first iteration, the aerosol extinction profile is set to zero for all altitudes.

While the given algorithm yields aerosol extinction profiles from any given radiance profile, the retrieved data have to be interpreted in terms of sensitivity to aerosol scattering and resulting uncertainty in the retrieval result. This will be discussed in the next section.

6.1.4 *Sensitivity to Aerosol Extinction*

In order to describe the sensitivity of a measured radiance at tangent height TH_i to the aerosol extinction in altitude h_j, scatter events of different aerosol configurations are analyzed. Therefore each simulated radiance $I(TH_i)$ is subdivided into radiance originating from scattering on aerosol particles $I_{\text{particle}}(TH_i, h_j)$ and scattering on molecules $I_{\text{molecule}}(TH_i, h_j)$ at the respective altitude h_j:

$$I(TH_i) = \sum_j I_{\text{total}}(TH_i, h_j) = \sum_j \left(I_{\text{particle}}(TH_i, h_j) + I_{\text{molecule}}(TH_i, h_j) \right) \quad (6.14)$$

Figure 6.6 shows $I_{\text{particle}}(TH_i, h_j)$ and $I_{\text{molecule}}(TH_i, h_j)$ for a wavelength of 1090 nm, calculated from simulations with typical background aerosol conditions. The shape of $I_{\text{total}}(TH_i, h_j)$, $I_{\text{particle}}(TH_i, h_j)$ and $I_{\text{molecule}}(TH_i, h_j)$ confirms that the main requirement for the onion peeling approach is fulfilled:

$$I_{\text{total}}(TH_i, h_j) \approx 0 \text{ for } h_j < TH_i \quad (6.15)$$

The full analysis of each simulated scattering event is computational demanding and is therefore not performed within the retrieval algorithm. Instead, the information on retrieval sensitivity to aerosol extinction is approximated using the radiance-extinction gradient $\gamma_{i,j}$ introduced in section 6.1.3

$$\Delta I_{i,j} = \gamma_{i,j} \cdot \Delta\beta_j, \quad (6.16)$$

where $\Delta\beta_j$ can be any assumed aerosol extinction profile that represents variations in the profile β_j of retrieval iteration l. In this thesis $\Delta\beta_j$ is set to 1 % of the aerosol extinction profile β_j with a minimum of $10^{-5}\,\text{km}^{-1}$:

$$\Delta\beta_j = \max\left(0.01 \cdot \beta_j, 10^{-5}\,\text{km}^{-1}\right). \quad (6.17)$$

The resulting $\Delta I_{i,j}$ is then used to find the altitude box h_j for which the radiance simulated at TH_i has the strongest signal and that is not yet being retrieved from the radiance at another tangent height TH_i. In general, a one to one relation between h_j and TH_i is found for stratospheric background conditions. It is also possible to check if the simulation uncertainty is higher than the signal strength $\Delta I_{i,j}$. This threshold is exceeded when the contribution of scattering on molecules becomes large at small wavelengths/low altitudes or when the total aerosol optical thickness (AOT) above the altitude box h_j is too large. In this case lower altitudes are shielded and do not contribute to the measurement at the respective tangent height. An example for an optically thick aerosol layer with $\beta = 10^{-2}\,\mathrm{km}^{-1}$ at 22.5 km is given in figure 6.8.

6.1.5 *Retrieval Uncertainties*

In this section the retrieval uncertainty originating from radiative transfer simulations and measurements will be described and discussed. The retrieval uncertainty due to assumptions will be investigated in section 6.2.2. According to equation 6.13 the retrieval error $\delta\beta_{j,k}$ can be derived from uncertainties defined in the following table.

SIMULATION UNCERTAINTIES	
Aerosol-extinction gradient	$\delta\gamma_{i,j,k}$
Simulated radiance at TH_i	$\delta I_{\mathrm{sim}}(TH_i, \beta_{j,k})$
Simulated radiance at TH_{ref}	$\delta I_{\mathrm{sim}}(TH_{\mathrm{ref}}, \beta_{\mathrm{ref}} = 0)$
MEASUREMENT UNCERTAINTIES (will be described in section 6.3.1)	
Measured radiance at TH_i	$\delta I_{\mathrm{meas}}(TH_i, \beta_{j,k})$

Table 6.3: Definition of quantities used to derive the retrieval uncertainty.

Applying the variance formula yields:

$$\delta\beta_{j,k} = \sqrt{\gamma^2_{\mathrm{err},i,j,k} + I^2_{\mathrm{sim,err},i,k} + I^2_{\mathrm{sim,ref,err}} + I^2_{\mathrm{meas,err},i,k}} \quad \text{, with} \tag{6.18}$$

$$\gamma_{\mathrm{err},i,j,k} = \Delta I_{i,k} \cdot \gamma^{-2}_{i,j,k} \cdot \delta\gamma_{i,j,k} \tag{6.19}$$

$$I_{\mathrm{sim,err},i,k} = \gamma^{-1}_{i,j,k} \cdot \delta I_{\mathrm{sim}}(TH_i, \beta_{j,k}) \tag{6.20}$$

$$I_{\mathrm{sim,ref,err}} = \gamma^{-1}_{i,j,k} \cdot \frac{I_{\mathrm{meas}}(TH_i, \beta_j)}{I_{\mathrm{meas}}(TH_{\mathrm{ref}}, \beta_{\mathrm{ref}} = 0)} \cdot \delta I_{\mathrm{sim}}(TH_{\mathrm{ref}}, \beta_{\mathrm{ref}} = 0) \tag{6.21}$$

$$I_{\mathrm{meas,err},i,k} = \gamma^{-1}_{i,j,k} \cdot \frac{I_{\mathrm{sim}}(TH_{\mathrm{ref}}, \beta_{\mathrm{ref}} = 0)}{I_{\mathrm{meas}}(TH_{\mathrm{ref}}, \beta_{\mathrm{ref}} = 0)} \cdot \delta I_{\mathrm{meas}}(TH_i, \beta_{j,k}) \tag{6.22}$$

using symbols and definitions from equations 6.13 and 6.11.

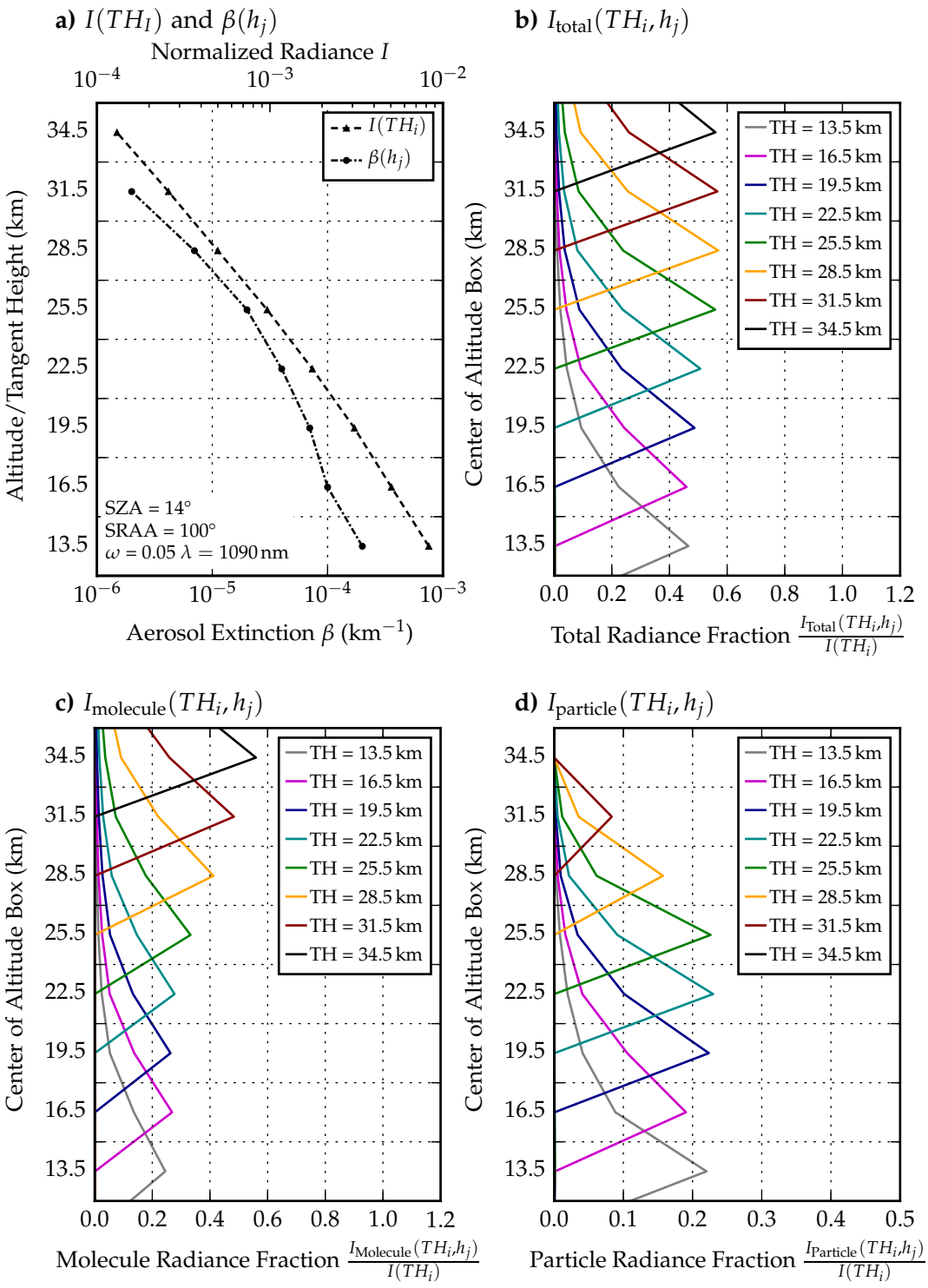

Figure 6.6: (a) Normalized radiance I as a function of tangent height TH_i (triangles). (b) Ratio of normalized radiance as function of h_j. (c) The fraction of molecular scattering to the normalized radiance. (d) The fraction of particle scattering to the normalized radiance. Parameters: aerosol extinction profile β (a, circles), SZA = 14°, SRAA = 100°, albedo = 0.05, wavelength = 1090 nm.

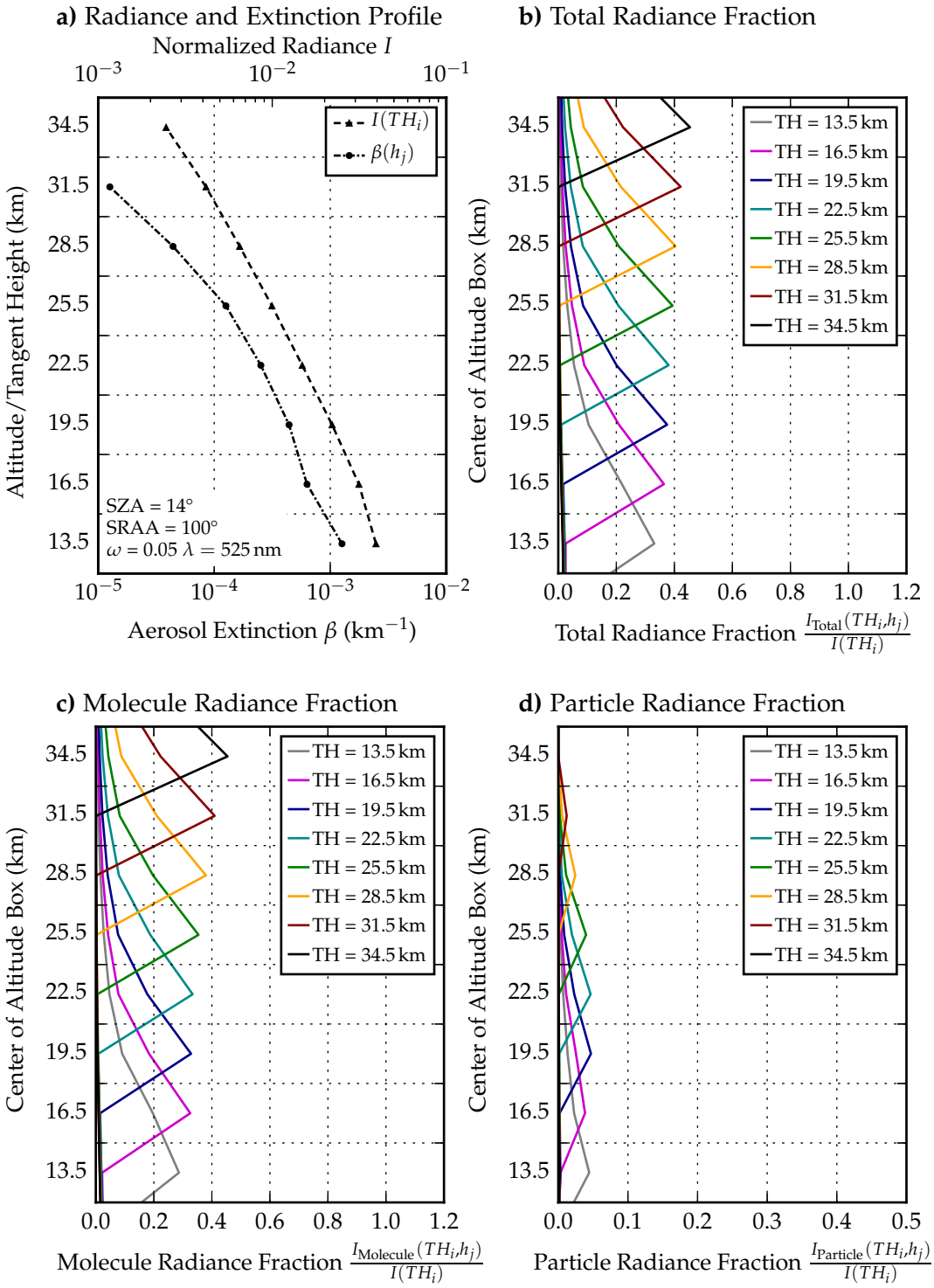

Figure 6.7: Similar to figure 6.6 for a wavelength 525 nm. The aerosol extinction profile is modified with an Ångström coefficient obtained from a Mie model using an aerosol size distribution as defined in section 4.5. The contribution to the radiance caused by scattering on molecules is significantly stronger than the increase in radiance caused by aerosol scattering for the chosen aerosol extinction profile. The maximal signal strength of aerosol scattering stays below 5 % of the total intensity for all tangent heights in all altitude boxes.

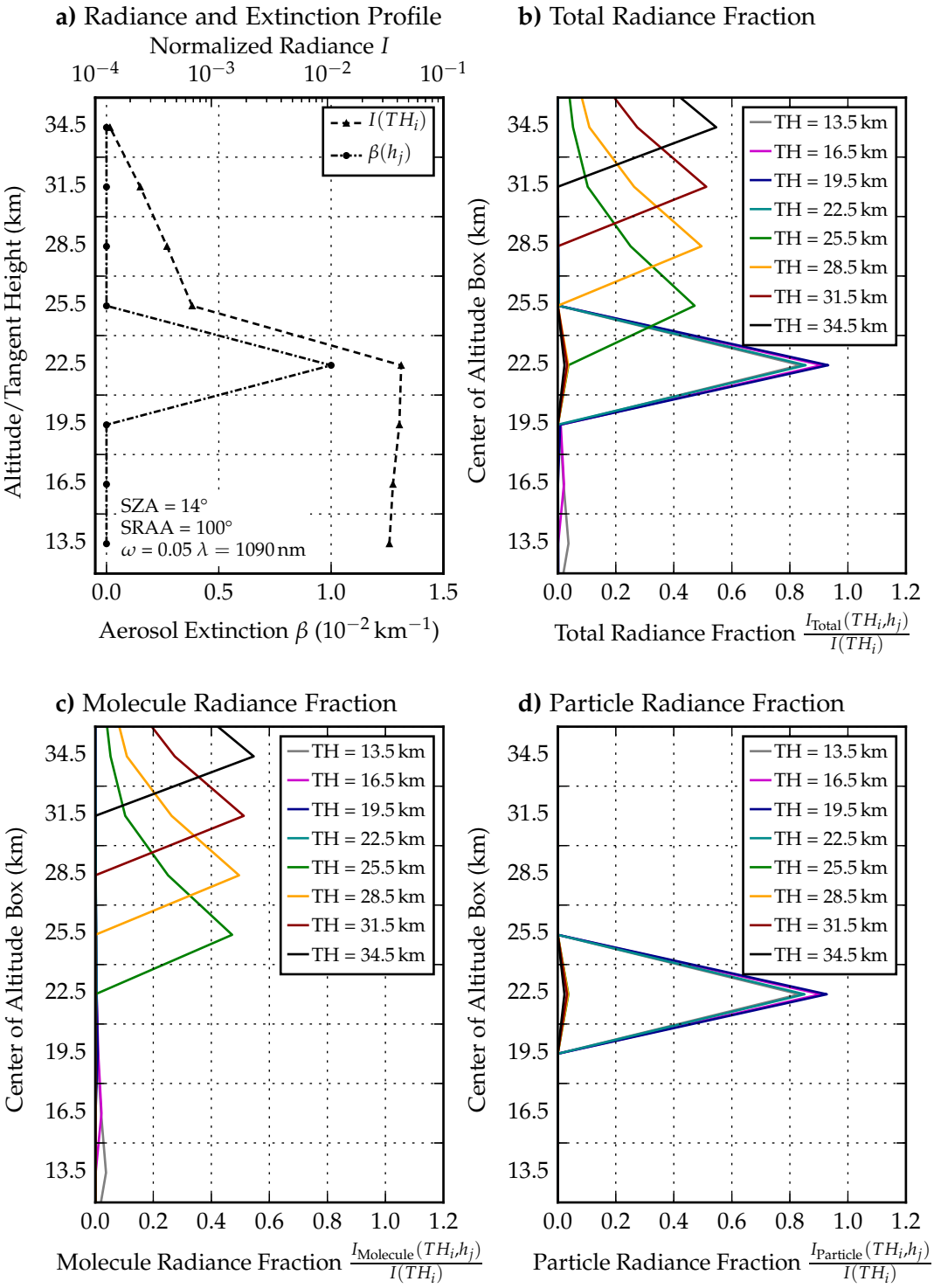

Figure 6.8: Similar to figure 6.6 but for a thick aerosol layer ($\beta = 10^{-2}\,\text{km}^{-1}$) at an altitude of 22.5 km. The aerosol extinction at other altitudes is set to zero as shown in (a). This case demonstrates the shielding effect: The information content on altitude boxes below the aerosol layer is significantly reduced for all simulated radiances at tangent heights between 13.5 and 34.5 km. Furthermore, the aerosol layer at 22.5 km affects simulated radiances at tangent heights above that altitude (d).

For the determination of the retrieval error, uncertainties in the radiance-extinction gradient are assumed to be independent from uncertainties in the measured radiance. The absolute error of the retrieved aerosol extinction $\delta\beta_{j,k}$ (Eqn. 6.18) is governed by uncertainties in the radiance-extinction gradient (Eqn. 6.19) which increases for shorter wavelengths and lower altitudes as sensitivity decreases (see Section 6.1.4). The terms $I_{\text{sim,err},i,k}$ (Eqn. 6.20) and $I_{\text{sim,ref,err}}$ (Eqn. 6.21) are usually small since the RTM will continue the simulation until the uncertainty of the simulated radiances is below 0.5 %. This changes when the sensitivity to scattering by aerosol particles decreases. This is typically the case if the contribution of aerosol scatter to the total radiance is weak compared to contribution of molecular scatter, compare figure 6.7. When the change in radiance caused by aerosol extinction is in the same order as the RTM noise, the contributions of $I_{\text{sim,err},i,k}$ and $I_{\text{sim,ref,err}}$ to the total error become more significant. The contribution of the measured radiance uncertainty $I_{\text{meas,err},i,k}$ (Eqn. 6.22) for wavelengths considered in this thesis is usually in the same order of magnitude as the uncertainty of simulated radiances. It will be described in further detail after introducing the application of measurement data to the retrieval algorithm, see section 6.3.

6.2 CONSISTENCY AND SENSITIVITY STUDIES

In order to evaluate the consistency of the retrieval algorithm and its sensitivity to uncertainties of input parameters, the retrieval method is applied to simulated radiance profiles. Therefore, aerosol extinction profiles typical for stratospheric background conditions β_{input} are added to a pristine model atmosphere without trace gases, clouds or other scattering particles. This configuration is used to simulate a radiance profile that is serves as I_{meas} for the retrieval. Deviations between the resulting aerosol extinction profile β_{output} and β_{input} will show if the retrieval and the RTM are consistent and evaluate the performance at various wavelengths, relative sun position (SZA and SRAA) and albedo values. In a second step, the sensitivity to uncertainties of input parameters is tested.

6.2.1 *Retrieval Algorithm Consistency*

As in the last section a typical stratospheric background aerosol extinction profile is chosen and modified using an Ångström coefficient calculated by Mie theory ($r_m = 80\,\text{nm}$, $\sigma = 1.6$) for the chosen wavelengths 525, 750, 870, 1090 nm as described in section 4.5. Retrieval results for 525 and 1090 nm at SZA $= 14°$, SRAA $= 100°$ and albedo $\omega = 0.05$ are compared in the following figure.
Analyses of radiative transfer simulations in section 6.1.4 showed that the sensitivity of the radiance, measured at a specific tangent height, to aerosol extinction is increasing with wavelength. As a result the retrieval uncertainty and consequently deviations between β_{input} and β_{output} are higher at a wavelength of 525 nm in figure 6.9a than for 1090 nm in figure 6.9b. For this setup aerosol extinction cannot be

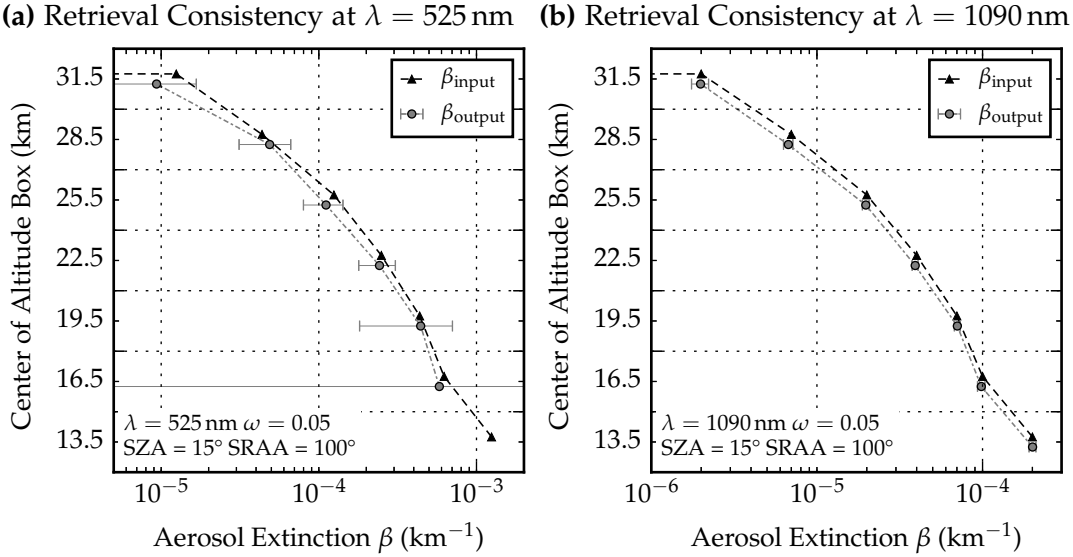

Figure 6.9: The comparison between β_{input} and β_{output} for wavelengths 525 nm (a) and 1090 nm (b) is used to characterize the retrieval consistency. Error bars are derived according to equation 6.18. The retrieval algorithm was not able to retrieve aerosol extinction β_{output} at $h_j = 13.5\,\text{km}$ for $\lambda = 525\,\text{nm}$ due to a low sensitivity at this wavelength.

retrieved by the algorithm for the lowest altitude $h_j = 13.5\,\text{km}$ at 525 nm due to the low sensitivity at this wavelength as shown in figure 6.7 on page 46.

Results for other wavelengths used in this thesis are summarized in figure 6.10. The algorithm is capable of retrieving aerosol extinction profiles which solve equation 6.5 for all wavelengths. Compared to the input extinction profile β_{input} deviations are smaller than 5 % for all wavelengths except $\lambda = 525\,\text{nm}$. The found extinction profiles β_{output} do not perfectly match the input profiles β_{input} due to uncertainties in the RTM. These uncertainties become more significant if the sensitivity to aerosol scattering decreases. At altitudes close to the lower and upper boundary of the retrieval domain at 33 km the retrieval uncertainties are increasing. Near the upper boundary the absolute aerosol extinction is in the order of $10^{-6}\,\text{km}^{-1}$. Here, ratio of aerosol scattering signal to RTM noise worsens as described in section 6.1.5. At the lower boundary the sensitivity to aerosol scattering decreases as shown in section 6.1.4. The best performance of the retrieval algorithm is achieved between 18 and 27 km for all wavelengths. For $\lambda = 525\,\text{nm}$ the sensitivity to aerosol extinction at an altitude of 13.5 km is too low for the retrieval application.

In order to investigate the consistency of the retrieval algorithm for a greater range of SZAs, SRAAs, albedo values and wavelengths, the retrieval performance can be characterized by the average absolute value of the relative difference

$$D = \overline{\left| \frac{\beta_{\text{out},j} - \beta_{\text{in},j}}{\beta_{\text{in},j}} \right|}. \tag{6.23}$$

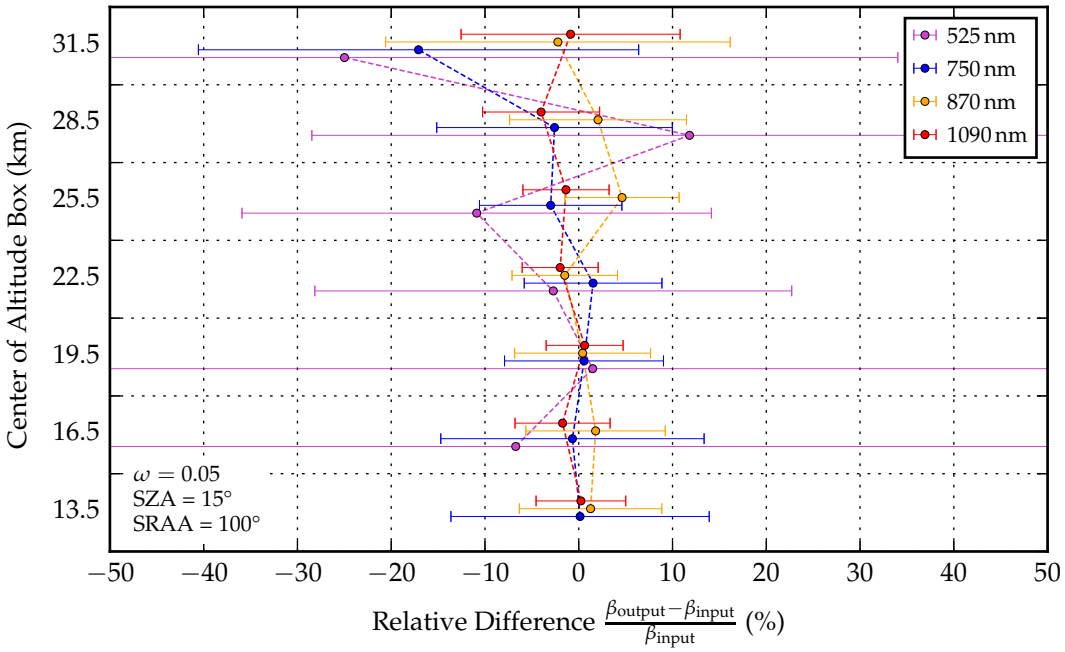

Figure 6.10: Relative deviations of the retrieval algorithm for all wavelengths used in this study at each altitude box. Data points are slightly shifted in altitude to prevent error bars from overlapping. The error bars indicate the retrieval uncertainty as described in section 6.1.5. The dashed line should only increase the visual appearance and does not represent profile information.

According to this definition the retrieval quality is better if the average absolute value of the relative difference D is small. For this investigation solar zenith angle and solar relative azimuth angle are summarized by the single scattering angle ξ as introduced in equation 4.3. Figure 6.11a shows a general decrease of D for increasing wavelengths. In three characteristic scenarios of different surface albedo values ($\omega = 0.05$, 0.5 and 0.95) shown in figure 6.11, D tends to increase with increasing single scattering angles ξ. This indicates that the retrieval performance worsens for a backscatter geometry caused by a reduced sensitivity. Accordingly, these findings are strongly connected to the fraction of radiance made up by particle scattering. Due to the respective scattering phase functions, the aerosol signal strength is decreasing for backscatter geometries, see figure 4.3b. This effect is less pronounced if the wavelength is large compared to the particle radius. The chosen geometries are typical for SCIAMACHY measurements. Especially at $\lambda = 525\,\text{nm}$ possible issues are to be expected for performing the retrieval in southern hemisphere, where the single scattering angle ξ is larger than 90° as shown in figure 3.5c on page 17.

In addition to the probability that direct sunlight is scattered into the line of sight (LOS) of the instrument, for an enhanced surface albedo, light can be scattered into the LOS after being reflected by the Earth's surface. Therefore, an increasing albedo reduces the mean retrieval deviation for most scattering angles by increasing

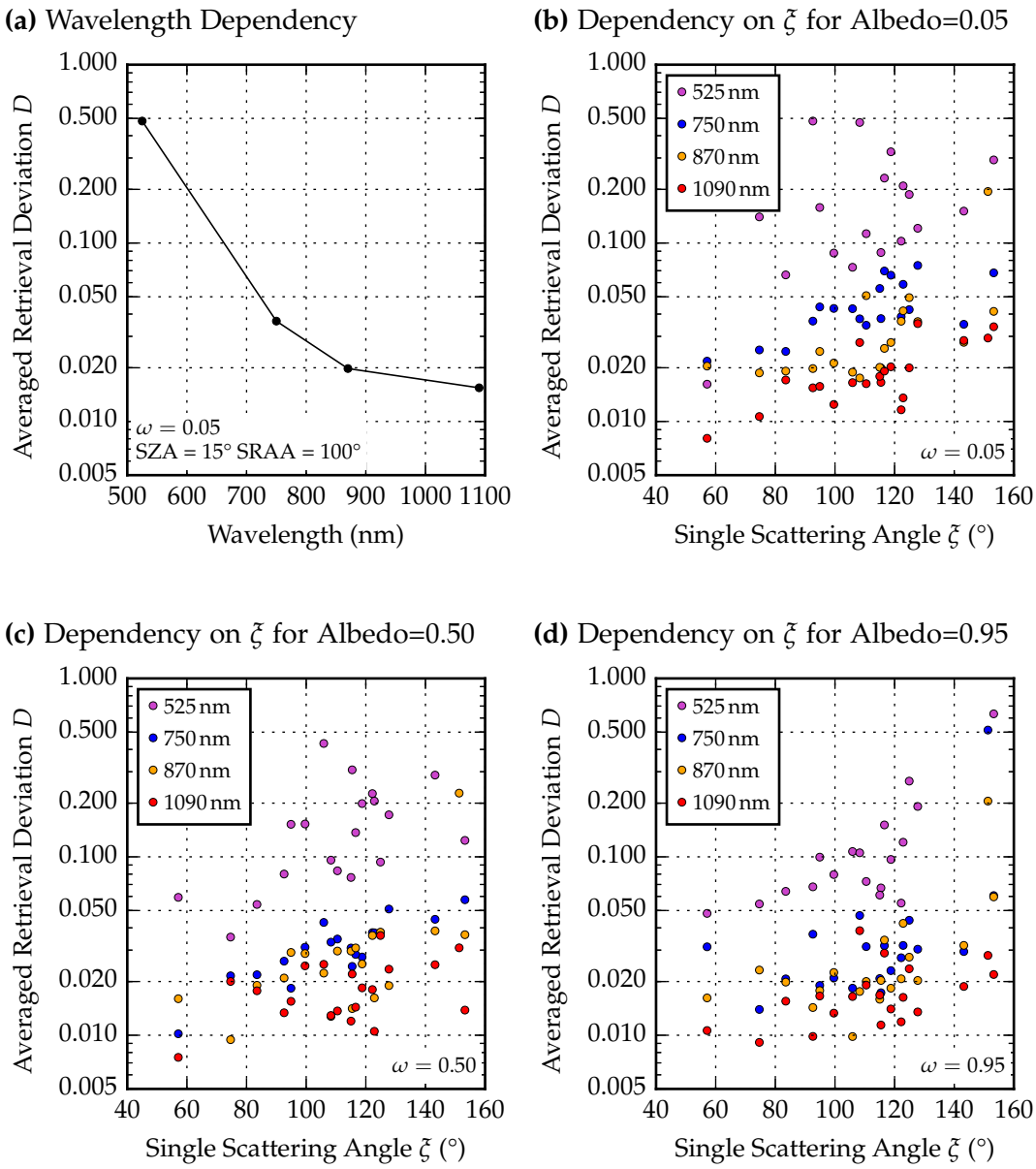

Figure 6.11: (a) shows the relation between D, as defined in equation 6.23, and wavelength for SZA $= 14°$, SRAA $= 100°$ and albedo $\omega = 0.05$. In addition the correlation between D and single scattering angle ξ is investigated for different values of the albedo ω: 0.05 (b), 0.5 (c) and 0.95 (d). D is shown on a logarithmic scale.

the probability of photons to be scattered from the atmosphere below into the line of sight of the instrument.

6.2.2 *Sensitivity to Uncertainties of Input Parameters*

Assumptions of input parameters described in the beginning of this chapter 6 might not be appropriate for each measurement. Therefore, it is necessary to quantify the influence of variations in the assumed parameters on the retrieval output. Variations in pressure, temperature and effective albedo are investigated using one set of parameters that is representative for SCIAMACHY measurements: wavelength $\lambda = 1090\,\text{nm}$, albedo $\omega = 0.5$, aerosol mean radius $r_m = 80\,\text{nm}$ and distribution width $\sigma = 1.6$, SZA = 14°, SRAA = 100°. For the extinction a typical stratospheric background aerosol profile is chosen as shown in figure 6.9b. The radiance profile $I(TH_i)$ which is simulated using this configuration, is then used as retrieval input, while pressure, temperature of the air and effective albedo ω_{eff} are being varied in the retrieval algorithm.

The sensitivity to the aerosol size distribution significantly changes for different solar geometries and wavelengths. The investigation for this dependency is performed for all wavelengths used in the retrieval algorithm for characteristic scattering angles observed by SCIAMACHY.

6.2.2.1 *Albedo Variation*

Although SCIAMACHY provides information on the effective surface albedo using nadir measurements, uncertainties remain, especially in the presence of clouds. Figure 6.12a shows the influence of the effective albedo ω_{eff} on the retrieval results. By using the normalization described in section 6, varying the effective albedo between 0.3 and 0.7 results in deviations of the retrieved aerosol extinction profile of up to $\pm 5\,\%$. Values in black show the result for running the retrieval with the same configuration as used for the simulation of the input radiance profile. In agreement with the consistency study in section 6.2, the retrieval uncertainties are increasing towards the upper boundary of the retrieval domain. Variations in effective albedo and deviations of the aerosol extinction profile are anti-correlated. This results from the retrieval algorithm trying to counterbalance an underestimation in radiance due to an underestimation in surface albedo by an overestimation of the retrieved aerosol extinction.

6.2.2.2 *Air Density Variation*

Figure 6.12b shows that variations in the air density profile derived from pressure and temperature are propagated through the retrieval algorithm only for altitudes where they occur. According to the proportionality in the ideal gas law, overestimation in temperature (underestimation in air density) leads to overestimation in aerosol extinction while overestimation in pressure (overestimation in air density)

leads to underestimation in aerosol extinction. Since these variations affect molecular scattering, this effect is wavelength dependent.

6.2.2.3 *Aerosol Size Variation*

While the chosen aerosol size distribution (log-normal, $r_m = 80\,\text{nm}$, $\sigma = 1.6$) is a good representation of stratospheric aerosol moderately disturbed by volcanic eruptions [Deshler, 2008], particle size varies with altitude and time and is heavily influenced by volcanic SO_2 injections. Figure 6.13 compares the scattering phase function $P(\xi)$ for a variety of aerosol size distributions to $P(\xi)$ for the size distribution used in this thesis at 525, 750, 870 and 1090 nm. In case of single-scattering, an overestimation of $P(\xi)$ leads to an underestimation of the retrieved aerosol extinction and vice versa since a smaller amount of aerosol extinction is required to achieve the same change in radiance.

For stratospheric background conditions, scattering processes can be described by assuming single-scattering, i.e. the single scattering angle ξ at the tangent point and the scattering phase function $P(\xi)$ determine how much light is scattered towards the instrument. This approximation allows to estimate the influence of uncertainties in the aerosol size distributions. In order to investigate the retrieval algorithm response to uncertainties in the scattering phase function, radiance profiles are simulated for a confined aerosol layer between 18 and 21 km. The aerosol size distribution is described by a log-normal distribution with a mean radius $r_m = 80\,\text{nm}$ and a distribution width $\sigma = 1.6$. The simulated radiance profile is used as input for the retrieval algorithm which is performed for varying combinations of mean radius and distribution width. An example for a wavelength of $\lambda = 1090\,\text{nm}$ is given in figure 6.14. At this wavelength, an overestimation in particle size leads to an underestimation in the retrieved aerosol extinction for a forward scattering geometry and vice versa for an underestimation of the particle size ranging from $-10\,\%$ to $50\,\%$. This effect is reversed for the sideward and backward scattering geometry. For a sideward scattering geometry, the sensitivity to uncertainties in the aerosol size distribution is generally smaller ranging from $-20\,\%$ to $20\,\%$. For a backward scattering geometry the sensitivity is highest ranging from $-50\,\%$ to $40\,\%$. The same investigation was also performed for 525, 750 and 870 nm with similar results, see section A.2 in the appendix.

6.3 APPLICATION TO SCIAMACHY MEASUREMENT DATA

In the previous section, precision, consistency and sensitivity of the retrieval algorithm were investigated within a controlled model environment. This section discusses the necessary adjustments to account for additional uncertainties introduced when using of measurement data. Section 6.3.1 describes the calibration used for the SCIAMACHY data set and section 6.3.2 discusses minor adjustments needed for the reference tangent height. More complex changes to the retrieval algorithm in order to account for spatial straylight and inhomogeneous aerosol layers are explained in sections 6.3.3 and 8.1, respectively.

(a) Sensitivity to Variations in Albedo

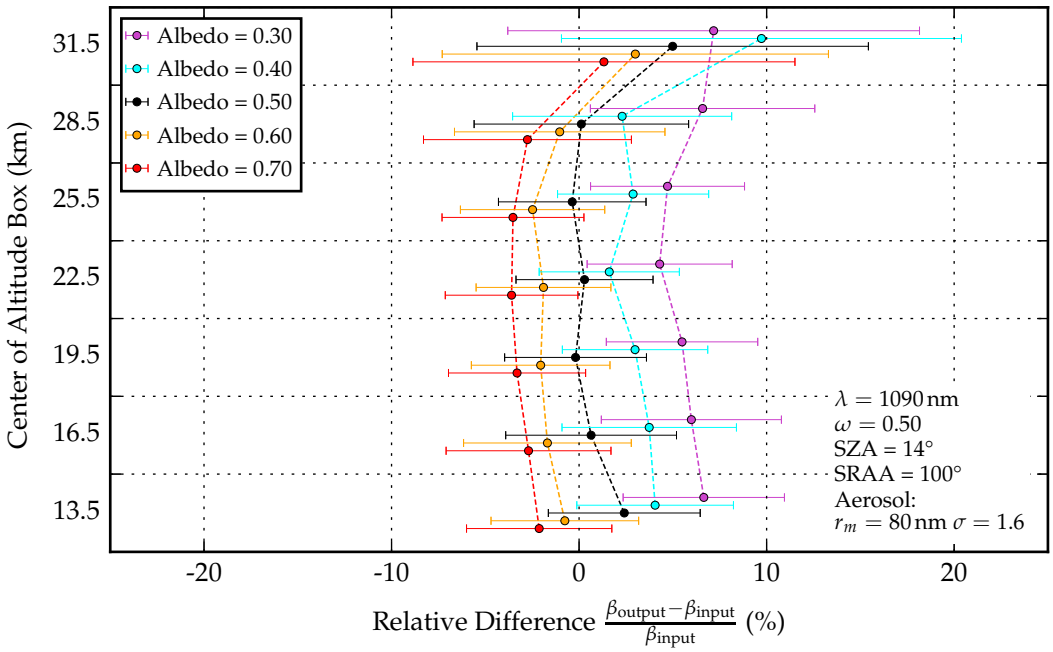

(b) Sensitivity to Variations in Temperature and Pressure

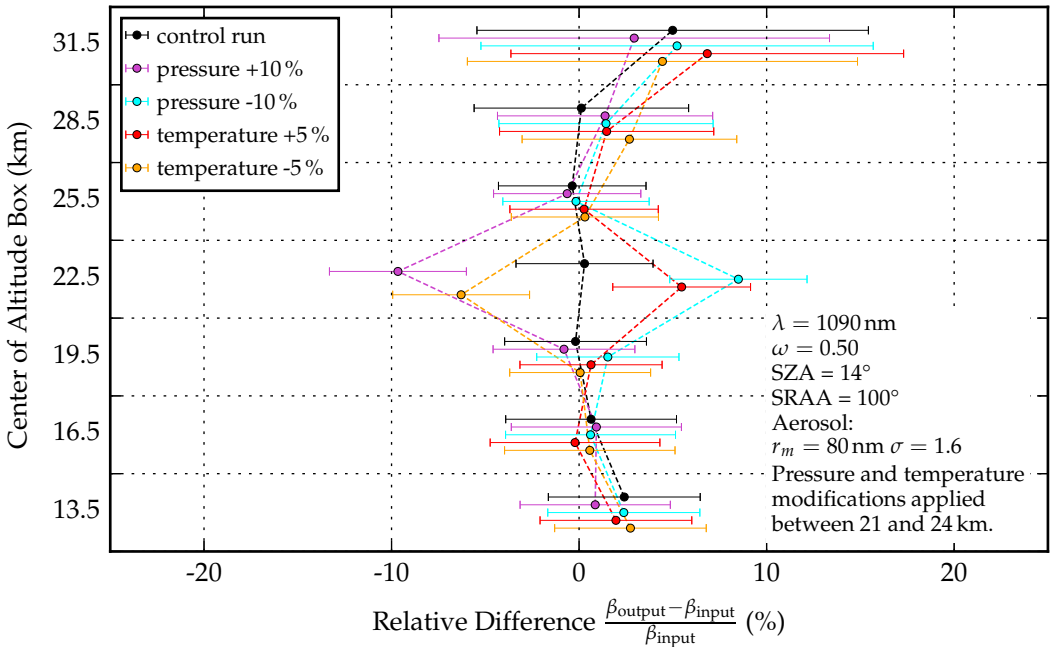

Figure 6.12: Influence of variations in surface albedo (a), temperature and pressure (b) on the retrieved aerosol extinction profile at a wavelengths of 1090 nm for a SZA of 14° and a SRAA of 100°. Data points and error bars are depicted in the same way as in figure 6.10. The black line shows results for running the retrieval with the same configuration used in the simulation of the input radiance profile.

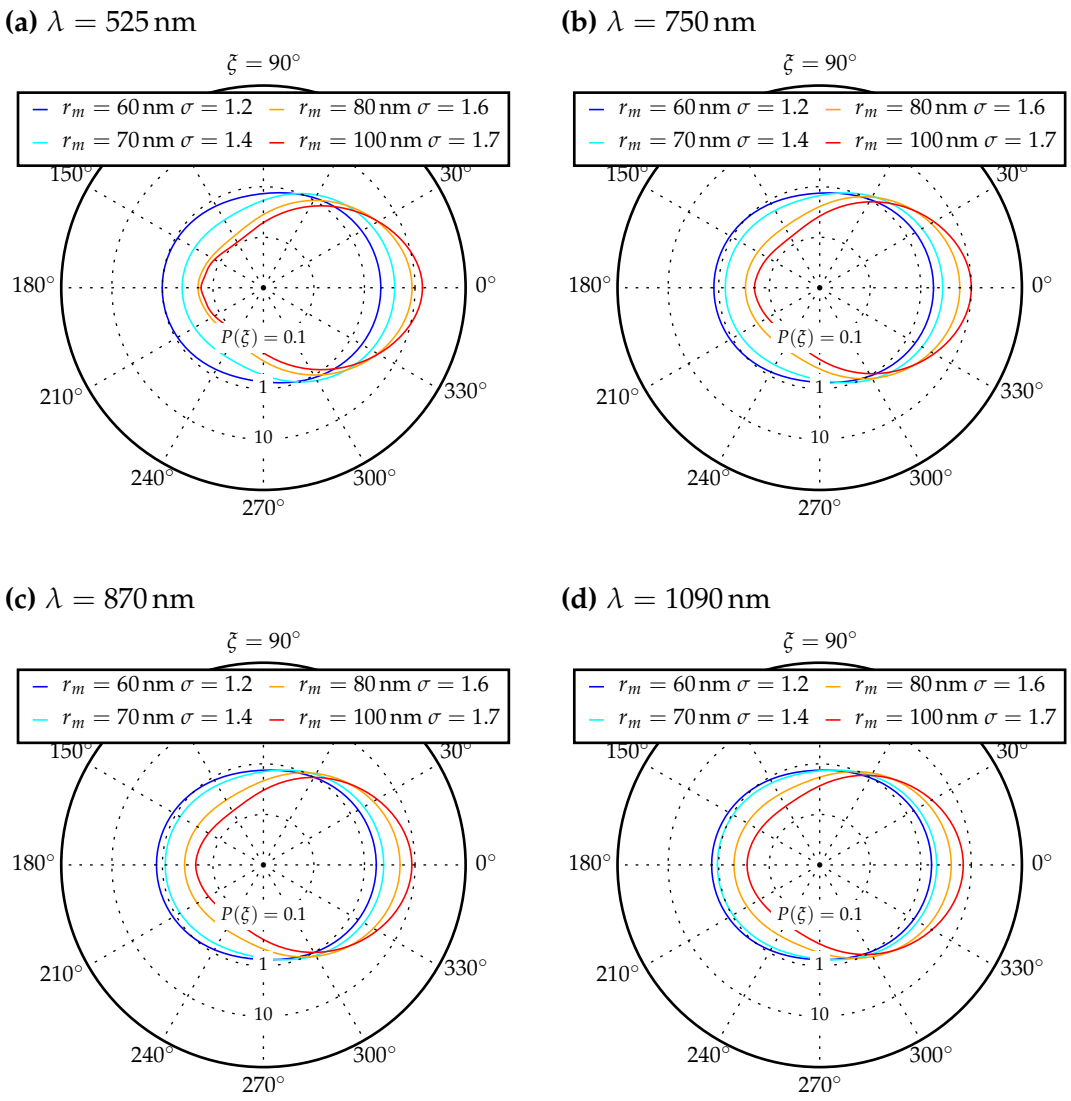

Figure 6.13: Variation of the scattering phase function on a logarithmic scale for different typical aerosol size distributions at four wavelengths: 525, 750, 870 and 1090 nm. The orange line represents the phase function that results from the aerosol sizes distribution with a radius mean $r_m = 80\,\text{nm}$ and a distribution width of $\sigma = 1.6$ as used in this thesis.

(a) Forward scattering geometry: $\xi = 44°$

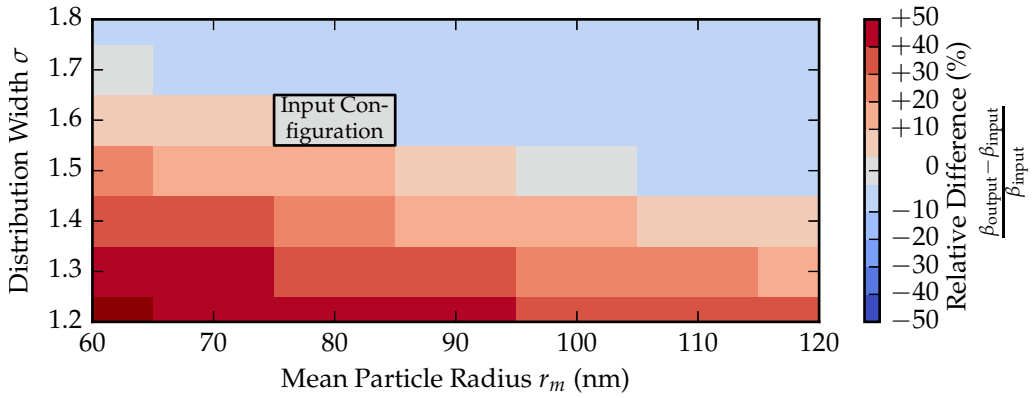

(b) Sideward scattering geometry: $\xi = 92°$

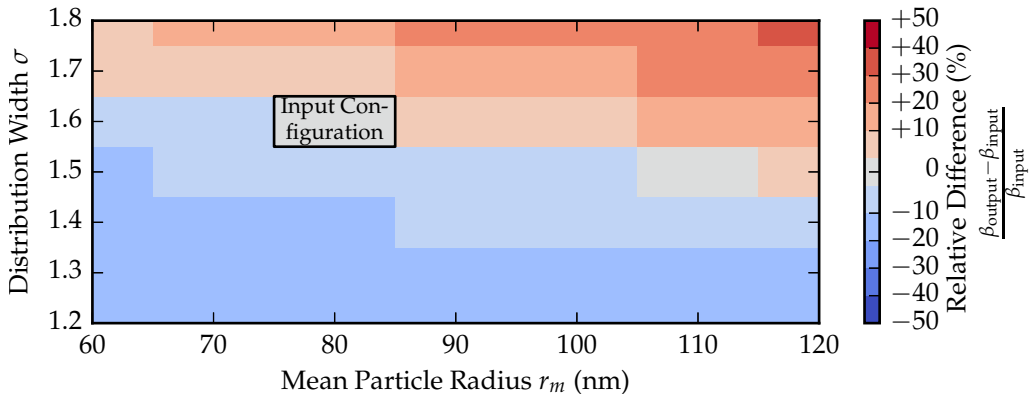

(c) Backward scattering geometry: $\xi = 143°$

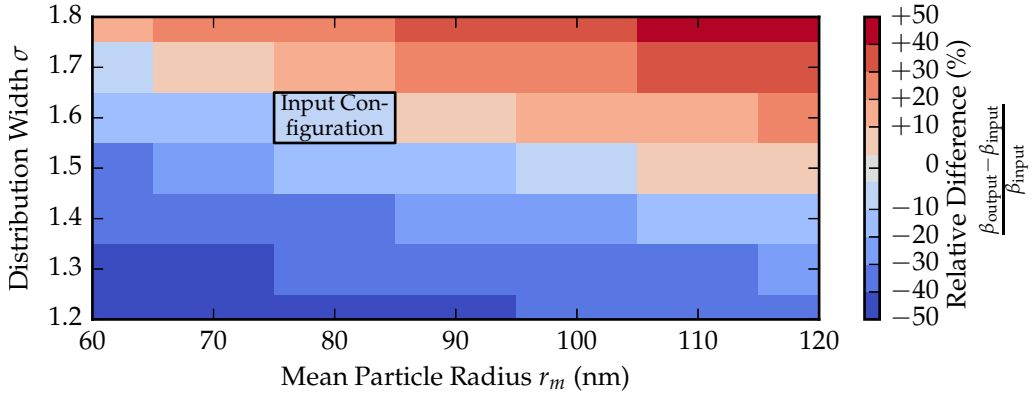

Figure 6.14: Sensitivity to uncertainties in the aerosol size distribution for $\lambda = 1090\,\text{nm}$ at different single-scattering angles ξ: 44°, 92° and 143°. The center of each bin represents the size distribution that was used for the retrieval algorithm. For the simulation of the input radiance profile a size distribution with a mean radius of $r_m = 80\,\text{nm}$ and a distribution width $\sigma = 1.6$ was used as indicated by the input configuration box. Colors indicate the deviation between β_{input} and β_{output} with red for an overestimation and blue for an underestimation with respect to the input extinction profile β_{input}.

6.3.1 *Measured Radiance and Data Version*

SCIAMACHY level 1c data, acquired using configurations shown in table 6.4, are preprocessed for the use in the aerosol extinction retrieval algorithm in two ways:

- To improve the signal to noise ratio, the measured radiances are averaged for an interval of $\pm 2.5\,\mathrm{nm}$ around a target wavelength. The standard deviation of the averaged radiance is used as measurement error for equation 6.22. This becomes especially important for high tangent heights and long wavelengths, where the measured radiance can be close to the noise level of the instrument.
- The possibility of numerical artifacts within the radiative transfer simulations caused by interpolation is being reduced by linearly interpolating the measured radiance profile to a fixed tangent height grid as described in section 6.1.1 before radiative transfer simulations are applied.

The measured radiance profile at high tangent heights or long wavelengths sometimes has a characteristic zig-zag shape as shown in figure 6.15b. This effect directly results from the scanning scheme of SCIAMACHY in limb geometry. Here, only measurement pixels of every other tangent height are horizontally aligned as shown in figure 6.15a. The zig-zag shape of vertically corresponding pixels, e.g. the left most pixels in each row, results from combining horizontal aperture angle and integration time, while the scanning mirror is constantly moving from one elevation to the next. This effect is however not corrected by the calibration and can affect retrieval results for individual cases.

6.3.2 *Aerosol Extinction at the Reference Tangent Height*

Calibration issues that are not fully corrected, like the memory effect, and uncertainties of atmospheric properties, like effective albedo, affect measurements at all tangent heights similarly. These sources of uncertainty are strongly reduced by normalizing the radiance profile with the radiance at the reference tangent height $I(TH_{\mathrm{ref}})$ where the measurement is not significantly affected by the aerosol scattering as discussed in section 6.1.2. Since SCIAMACHY measurements at high tangent heights are significantly influenced by spatial straylight as will be discussed in section 6.3.3, $TH_{\mathrm{ref}} = 34.5\,\mathrm{km}$ is used as a reference tangent height. However, measurements for this tangent height are sensitive to aerosol scattering in the respective altitude region and above. Therefore, the aerosol extinction at the reference altitude and above needs to be known. In this thesis, climatologically averaged aerosol extinction profiles derived from SAGE II measurements are used for altitudes above 33 km. The climatology is averaged longitudinally and seasonally over two years (2003 and 2004) of SAGE II data in latitudinal bins with a resolution of 5°. During the development of the retrieval algorithm, other methods to estimate the aerosol extinction at the reference altitude were tested. Viable approaches like linear or exponential extrapolation or even without the normalization lead to strong numerical instabilities and could therefore not be applied.

Level 1b data version	7.03	
Calibration tool version	1.2 (from 06.08.2008)	
Calibration flags	Memory effect	no
	Leakage current	yes
	Pixel-to-pixel gain	yes
	Etalon Correction	yes
	Straylight Correction	yes
	Wavelength Calibration	yes
	Polarization Correction	no
	Radiometric Calibration	yes
	PMD Sun Normalization	no

Table 6.4: Configuration used to calibrate SCIAMACHY level 1b data in order to generate the level 1c data set. This data set is used for the retrieval of aerosol extinction profiles in limb geometry and for information on effective albedo in nadir geometry. A detailed description of each calibration can be found in chapter 5 of Gottwald and Bovensmann [2010].

(a) SCIAMACHY scanning scheme

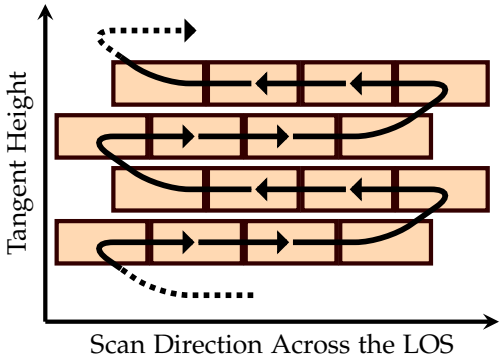

(b) Measurement Example

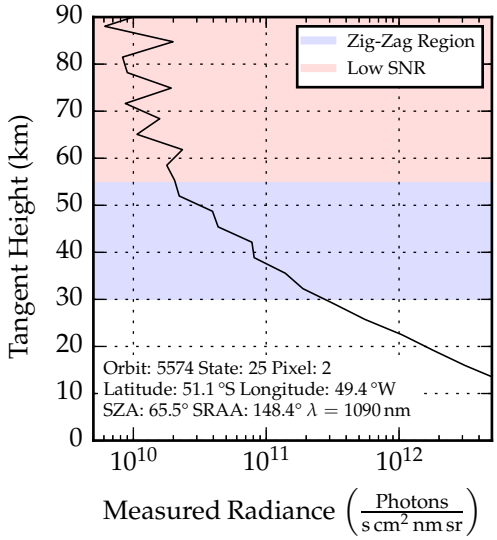

Figure 6.15: (a) Scanning scheme of SCIAMACHY measurements in limb geometry. The field of view (FOV) of a single measurement pixel is shown as a orange box. The arrows indicate how the FOV is moved by the scanning mirror starting at the lowest tangent height. The shifted pixel rows can result in a zig-zag shape of the measured radiance profile. (b) shows an example where the zig-zag becomes noticeable above 30 km and is affected by instrument noise above 55 km.

6.3.3 *Spatial Straylight Correction*

Light diffracted on residual grooves on the telescope mirror causes an increase in the measured radiance called spatial straylight [Gottwald and Bovensmann, 2010]. The following figure gives a qualitative view on the spectral structure of spatial straylight for measurements with a small angular distance between line of sight and the Sun. Light originating from relatively bright parts of Earth's lower atmosphere

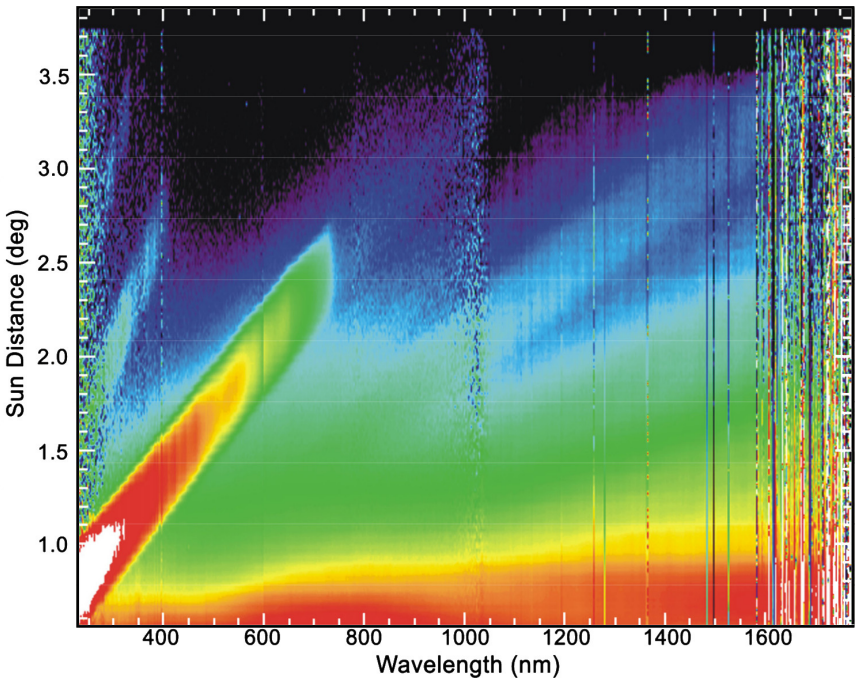

Figure 6.16: The qualitative effects of spatial straylight as a function of LOS distance from the Sun. Generally a continuous contamination is found close to the sun which increases with wavelength. Structural features which are correlated to the wavelength are strongest for the UV range. This picture is adopted from Gottwald and Bovensmann [2010], where it was provided by the DLR-IMF.

are the major source of spatial straylight for all parts of the SCIAMACHY orbit. In general spatial straylight becomes more significant for small measured radiances at high tangent heights or longer wavelengths. In Soest [2005] spatial straylight is characterized by comparing simulated and measured radiance profiles. In this section their method is developed further in order to determine a general correction algorithm for spatial straylight at various wavelengths.

For a comparison of measured and simulated radiance, the same assumptions as discussed in the beginning of this chapter are used to define atmospheric properties. The comparison is performed for SCIAMACHY measurements that can be collocated to SAGE II measurements of aerosol extinction: The distance between the tangent points of both measurements has to be smaller than 250 km and both profiles have to be measured within 24 hours. SAGE II aerosol extinction profiles do not suffer from spatial straylight issues due to the high SNR typical for occultation

measurements. Thus, this data set is used as input for radiative transfer simulations in order to account for scattering on particles in altitude regions between 20 and 40 km. Above 40 km aerosol extinction is extrapolated exponentially using a scale height that is derived between 35 and 40 km. The mean radius of the particle size distribution is derived from SAGE II aerosol extinction at 525 nm and 1090 nm using the Ångström exponent as defined in equation 4.9. Simulated radiances are scaled to the measurement at the adaptation tangent height TH_{ad} which is chosen to be around 27 km, where the aerosol extinction is given by SAGE II and the contribution of spatial straylight is comparably low. The scaled radiance $I'_{\mathrm{sim}}(TH_i)$ is defined as:

$$I'_{\mathrm{sim}}(TH_i) = I_{\mathrm{sim}}(TH_i) \cdot \frac{I_{\mathrm{meas}}(TH_{\mathrm{ad}}) - S(TH_{\mathrm{ad}})}{I_{\mathrm{sim}}(TH_{\mathrm{ad}})} \tag{6.24}$$

with radiance $I_{\mathrm{sim}}(TH_i)$ and spatial straylight $S(TH_i)$. The method of how to approximate the spatial straylight at the adaptation altitude $S(TH_{\mathrm{ad}})$ is explained in the following.

Figure 6.17 shows a comparison for measurements on 26$^{\mathrm{th}}$ May 2003 at 525 and 1090 nm. At 1090 nm the shapes of $I'_{\mathrm{sim}}(TH_i)$ and $I_{\mathrm{meas}}(TH_i)$ agree for tangent heights between 20 and 30 km. This indicates that SAGE II aerosol extinction values, used for the simulation, fit to this SCIAMACHY measurement. Above a tangent height of 40 km simulated radiances keep decreasing while the measured radiance profile becomes almost constant. The influence of uncertainties in the aerosol extinction profile, particle size distribution and air density becomes negligible in this altitude range. Accordingly, spatial straylight becomes the most probable explanation for the positive bias of measured radiance profiles. For the comparison at a wavelength of 525 nm similar effects are observed at higher THs. Two essential conclusions for the properties of spatial straylight S can be drawn:

- The absolute amount of S is higher if the field of view is closer to the bright light source, i.e. parts of Earth's lower atmosphere. In terms of atmospheric brightness this means S is increasing with decreasing tangent height. This boundary condition is applied in the blue shaded tangent height range of figure 6.17, called adjustment range. The absolute radiance at the upper boundary of the adjustment range has to be large enough to not be significantly influenced by uncertainties caused by measurement noise. The lower boundary is chosen to be the lowest tangent height that is only affected by altitudes where aerosol information from SAGE II is still available. In this case this leads to an adjustment range between 22 and 40 km. Accordingly, the straylight contribution at the adaptation altitude $S(TH_{\mathrm{ad}})$ in equation 6.24 is increased until the absolute spatial straylight profile $S(TH_i)$ is monotonously increasing with decreasing tangent height. This is shown in the blue shaded area of figure 6.17c.

- As the air becomes more dense for lower altitudes, the gradient of the atmospheric brightness decreases. Therefore, the increase of absolute spatial straylight will be smaller at lower tangent heights. This allows to extrapolate the relative amount of S below about 20 km, where information on aerosol

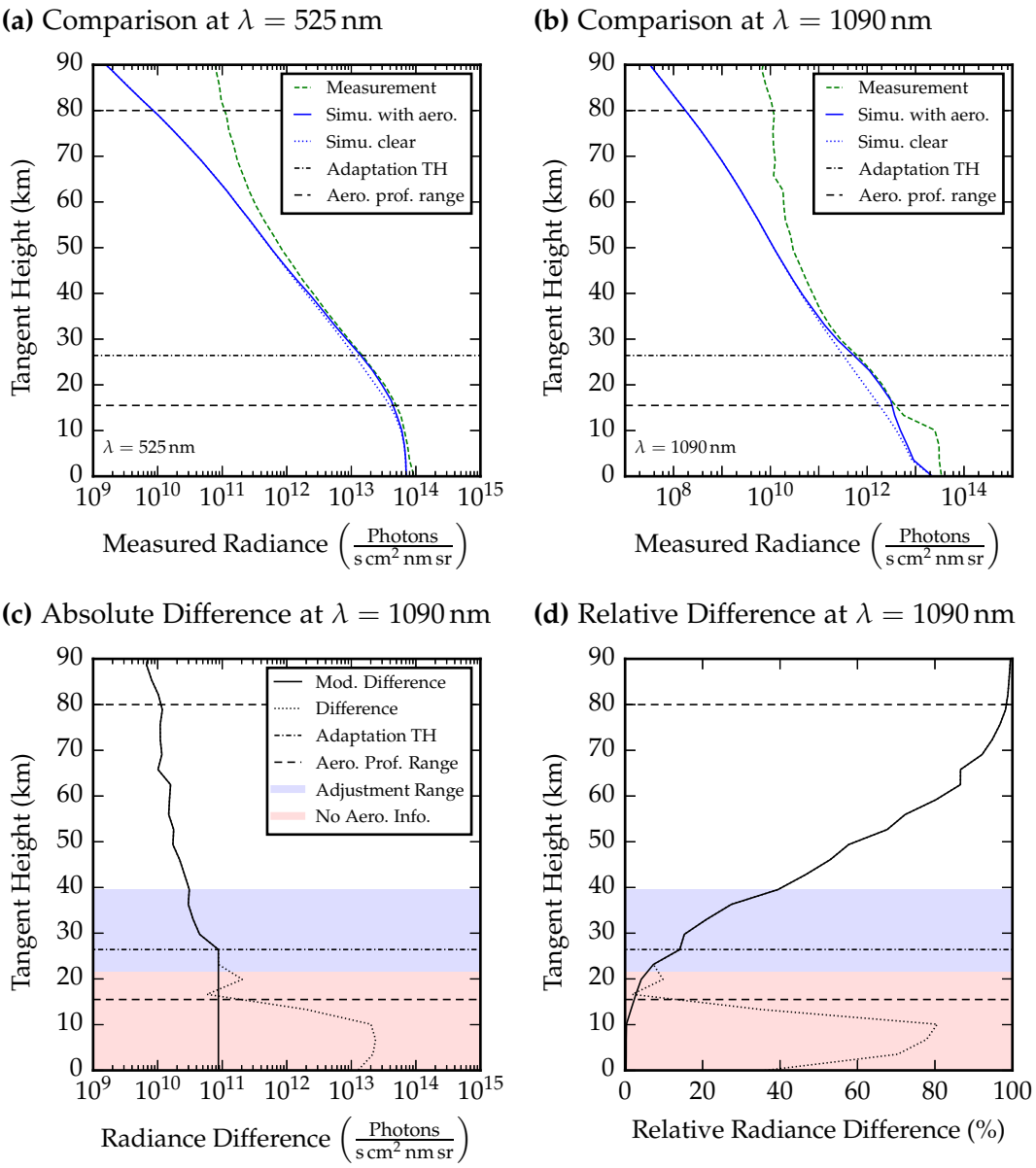

Figure 6.17: Simulated (blue) and measured (green) radiance profiles for a SCIAMACHY measurement in limb geometry at wavelengths 525 nm (a) and 1090 nm (b) on 26th May 2003 (Orbit 6464, State 15, Pixel 3) in the northern hemisphere at 38.8 °N, 86.0 °W. The single scattering angle ξ at the tangent point is 80°. Simulation results are scaled to match the measurement accounting for spatial straylight at a adaptation tangent height of about 27 km. For the comparison at $\lambda = 1090$ nm, absolute (c) and relative (d) differences between simulated and measured radiance are calculated. These differences are representing the altitude dependency of spatial straylight in SCIAMACHY measurements. Values are extrapolated to the altitude region where no information on aerosol extinction from SAGE II is available by keeping the absolute amount of spatial straylight constant.

extinction is not available in the SAGE II data set, as depicted by a red shaded area in figure 6.17d. The relative amount of S converges to zero as shown by the modified radiance difference profile in figure 6.17d. This is independent from the choice of extrapolation, either keeping $S(TH_i \lesssim 20\,\mathrm{km})$ constant or keeping the gradient of $S(TH_i \lesssim 20\,\mathrm{km})$ constant. In figure 6.17c, $S(TH_i)$ is constant below about 20 km.

For the retrieval algorithm based on equation 6.5, normalized correction factors $c(TH_i)$ for each tangent height are derived from the relative spatial straylight profile using equation 6.24:

$$S(TH_i) = I'_{\mathrm{sim}}(TH_i) - I_{\mathrm{meas}}(TH_i) \tag{6.25}$$

$$c(TH_i) = \frac{S(TH_i) \cdot I_{\mathrm{meas}}(TH_{\mathrm{ref}})}{S(TH_{\mathrm{ref}}) \cdot I_{\mathrm{meas}}(TH_i)} \tag{6.26}$$

Analogous to the general retrieval approach explained in section 6.1.2, the normalization used to derive the correction factor c reduces the dependency on effective albedo and linear measurement uncertainties. The correction factor c is determined for all SCIAMACHY measurements for which a SAGE II collocation is available. Normalized correction values are binned by single scattering angle and effective albedo. The binning is optimized to obtain a sufficient number of measurements for each bin. All correction factors in a bin are averaged to derive $\bar{c}(TH_i, \xi, \omega)$. This quantity is then used as a look up table (LUT) to correct for effects of spatial straylight at all tangent heights. Measured radiances in equation 6.5 are replaced by their corrected values according to the following equation:

$$\left(\frac{I_{\mathrm{meas}}(TH_i)}{I_{\mathrm{meas}}(TH_{\mathrm{ref}})}\right)_{\mathrm{corrected}} = \frac{I_{\mathrm{meas}}(TH_i)}{I_{\mathrm{meas}}(TH_{\mathrm{ref}})} \cdot \bar{c}(TH_i, \xi, \omega_{\mathrm{eff}}) \tag{6.27}$$

with the averaged correction factor $\bar{c}$ for scattering angle ξ and effective albedo ω_{eff}.

Figure 6.18 shows general characteristics of the correction factor: It's dependency on effective albedo is much more pronounced for $\xi > 90°$ (backscatter). For measurements above bright surfaces the absolute amount of spatial straylight $S(TH_i)$ is increasing. This increase results in a smaller difference between $S(TH_{\mathrm{ref}})$ and $S(TH_i < TH_{\mathrm{ref}})$ and therefore in smaller a correction factor. For $\xi \lesssim 100°$, light scattering by aerosol towards to instrument is enhanced as shown by the scattering phase function in figure 4.3b. Therefore, the influence of the effective albedo on the correction factor is generally smaller. Correction factors for single scattering angles between 80 and 100° are difficult to interpret due to sparse measurement data. For single scattering angles smaller than 45° the correction factor increases significantly. For SCIAMACHY, this scattering geometry occurs for the first few measurement states after entering the day-side of the orbit in the northern hemisphere. The distance between LOS and the Sun is still much larger than what is shown in figure 6.17, so that the influence of direct sunlight might not be the explanation of these results. Since the precise characterization of spatial straylight is not known, further investigations are necessary especially for the scattering angle range $\xi < 45°$.

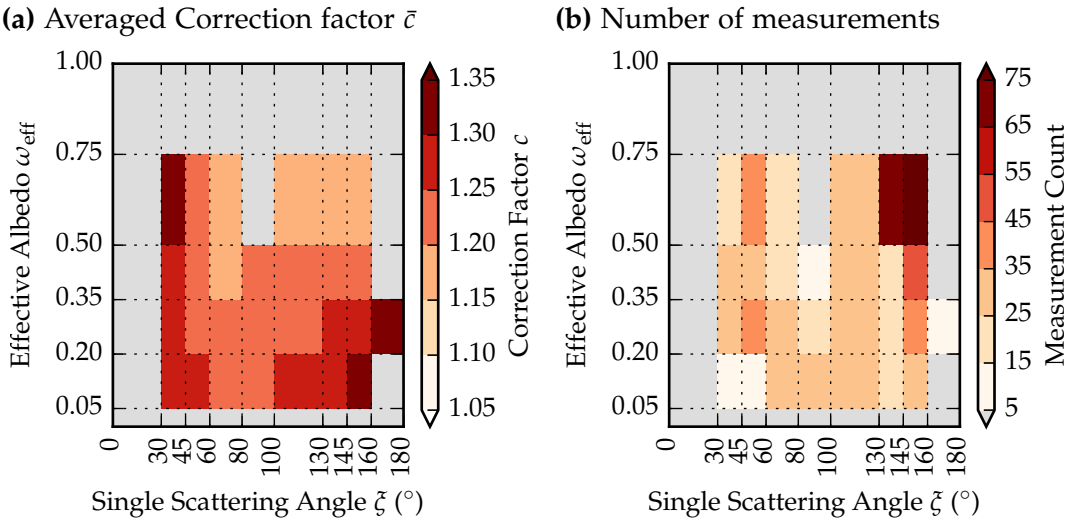

Figure 6.18: Averaged correction factor LUT for tangent height $TH_i = 22.5\,\text{km}$ and wavelength $\lambda = 1090\,\text{nm}$ (a) and the number of measurements taken into account to determine this correction factor (b). Dotted lines mark the bins of single scattering angle ξ and effective albedo ω_{eff}. Gray areas mark bins where less than five measurements were found. Here, statistics are insufficient for the determination of $\bar{c}$.

However, increasing absolute values of the spatial straylight with decreasing tangent height can result in an overcompensation for spatial straylight. Such an example is given in figure 6.19b: Here, the shape of the simulated radiance profile does not match the shape of the measured radiance profile. Uncertainties in the assumption of temperature, pressure profiles or effective albedo cannot explain these findings since they affect the simulated radiance at all tangent heights similarly. This is different for the aerosol size distribution that assumed to be constant for these simulations. If the mean radius of aerosol particles is decreasing with altitude, the aerosol size used for the simulation is overestimated for higher altitudes. According to figure 6.14c this results in an overestimation of the simulated radiance. As a result the contribution of spatial straylight at the adjustment altitude $S(TH_{\text{ad}})$ is also overestimated. Figure 6.19d shows that this overestimation also affects the relative spatial straylight profile and therefore the correction factor c. In addition, uncertainties in SCIAMACHY and SAGE II data sets and differences in the volume of sensitivity for both instruments can cause similar issues.

Cases, where the simulated radiance profile does not fit the measured radiance profile, can be identified by unrealistically high amounts of relative straylight at the adaptation tangent height TH_{ad}. Therefore, the available collocations are filtered using an empirical threshold:

$$\frac{S(TH_{\text{ad}})}{I(TH_{\text{ad}})} \overset{!}{<} 0.1 \tag{6.28}$$

Collocations for which this threshold is exceeded are not considered for the calculation of $\bar{c}$.

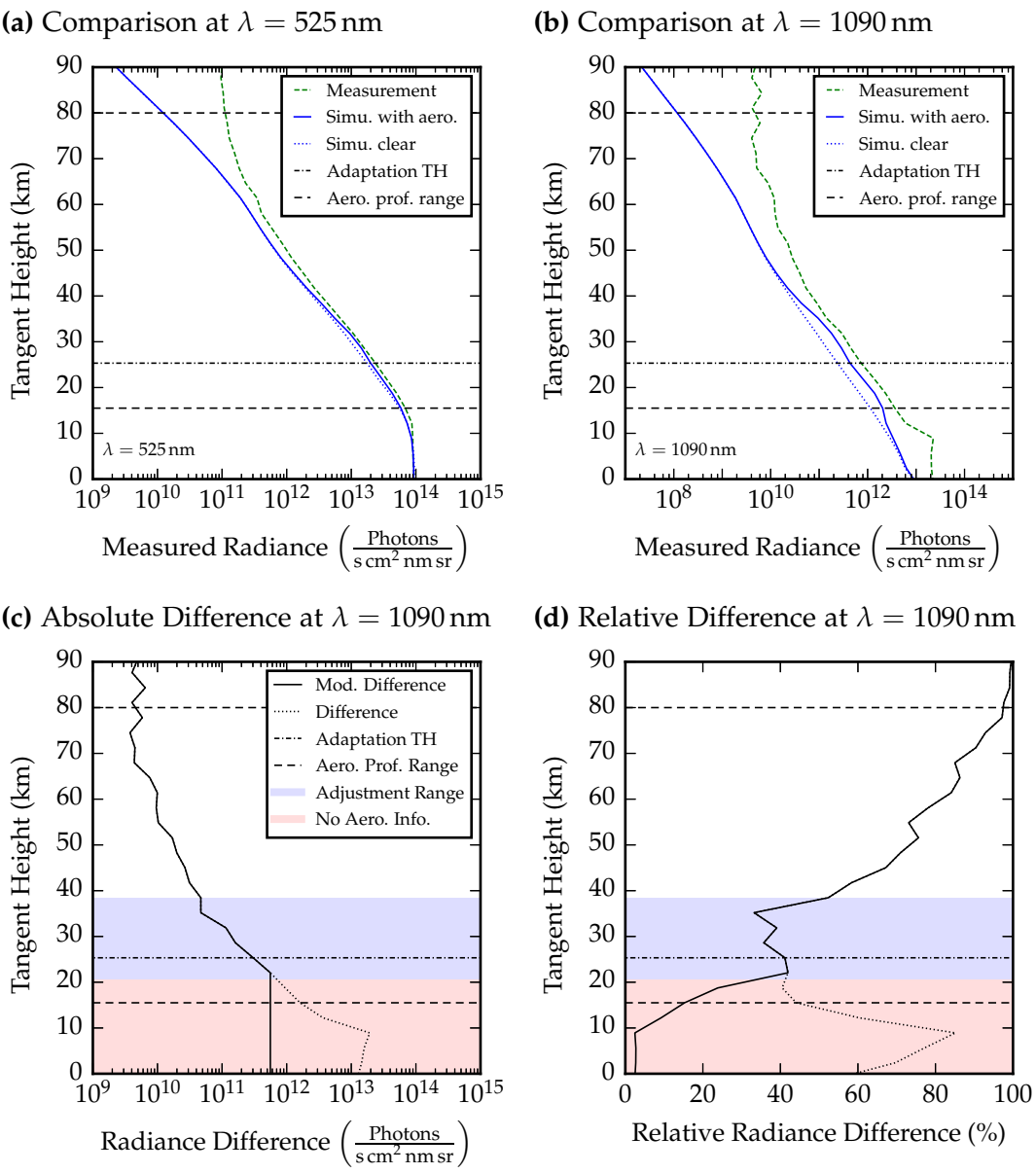

Figure 6.19: Same as figure 6.17c for a measurement on the 10th June 2003 (Orbit 6677, State 25, Pixel 1) in the southern hemisphere at 34.9 °S, 65.5 °W. The single scattering angle ξ at the tangent point is 153°. In this case, the shape of the simulated radiance profile does not match the shape of the measured radiance profile. This results in an overestimation of the relative spatial straylight with values around 40 % for tangent heights between 20 and 35 km.

Figure 6.20 shows that correction factors $\bar{c}$ derived from filtered collocations after applying equation 6.28. Values of $\bar{c}$ are significantly smaller than in the unfiltered case. The number of remaining collocations in each bin is strongly reduced. In addition to the removal of failed radiance comparisons like in figure 6.19b, the filter

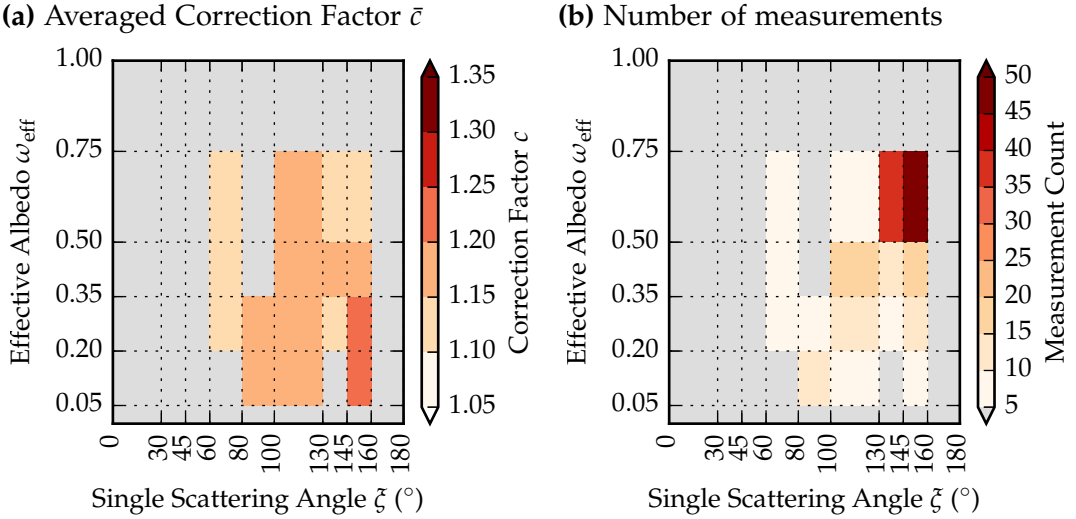

Figure 6.20: After filtering the available data as described in equation 6.28, correction factors are binned by single scattering angle and effective albedo and then averaged similar to figure 6.18.

removes profiles for which a relative spatial straylight fraction of 10 % or higher is probably reasonable. Especially for single scattering angles below 60° the filter is probably not representative since all collocations are filtered. Considering the issues of filtered and unfiltered straylight correction factors, three different correction methods can be applied to the retrieval algorithm:

UNFILTERED SPATIAL STRAYLIGHT CORRECTION: Averaged correction factors $\bar{c}$ shown in figure 6.18a are used in the retrieval algorithm without filtering. According to the findings in this section, this correction is expected to overcompensate the effects of spatial straylight.

CONSTANT SPATIAL STRAYLIGHT CORRECTION: The number of measurements for each bin is strongly reduced after filtering the available collocations according to equation 6.28. As a result, the remaining information on albedo and scattering angle dependence is questionable due to bad statistics. Instead of using the LUT as shown in figure 6.20a, one averaged correction factor profile can be used for all configurations. The correction factor profile for ale wavelengths used in this thesis are shown in figure 6.22.

$$\bar{c}(TH_i, \xi, \omega_{\text{eff}}) \rightarrow \bar{c}(TH_i) \tag{6.29}$$

EXTRAPOLATED SPATIAL STRAYLIGHT CORRECTION: While statistics for each LUT bin are reduced, similar dependencies on effective albedo and single scattering angle of the correction factor $\bar{c}$ can be found in figure 6.18. Therefore, values can be interpolated and extrapolated in order to get a full coverage of all single scattering angle and effective albedo combinations as shown in figure 6.21a.

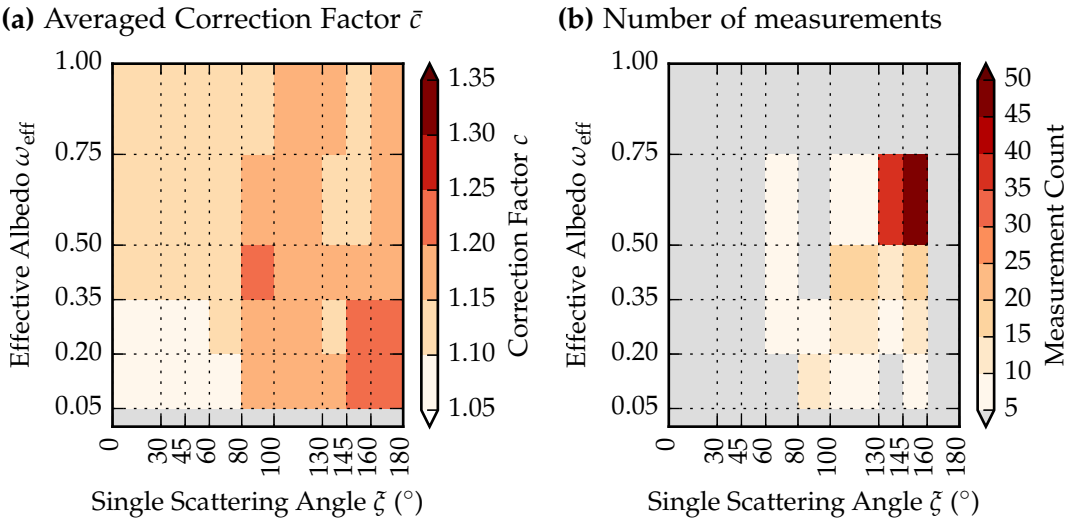

Figure 6.21: In addition to filtering and binning as shown in figure 6.18, values are interpolated and extrapolated for bins with insufficient statistics.

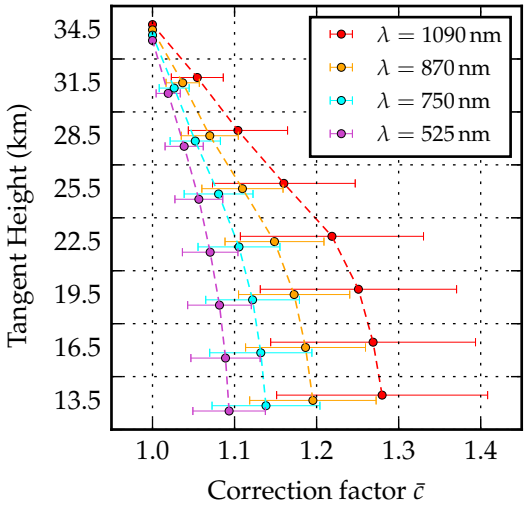

Figure 6.22: Averaged correction factor profile $\bar{c}(TH)$ according to equation 6.29 for all wavelengths used in this thesis. Mean value and standard deviation are derived from all correction factor values that remained after the filtering according to the constant spatial straylight correction method.

Advantages and disadvantages of all three methods are discussed in a comparison study with SAGE II, see section 7.1.

6.3.4 *Limitations of the Retrieval Algorithm*

Despite the use of approximations, assumptions and corrections described in the previous sections, the retrieval does not always find an aerosol extinction β that fulfills equation 6.5. Known issues that prevent the retrieval from converging, are described and discussed in this section. For the onion peeling approach described in

section 6.1.2 aerosol extinction at an altitude h_j can only be retrieved, if the aerosol extinction profile above this altitude $\beta(h > h_j)$ is known. Therefore, the retrieval algorithm stops at an altitude h_{flag} and results are flagged accordingly, if the aerosol extinction could not be retrieved. An overview on all known retrieval issues, their influence on the aerosol extinction profile and how the algorithm treats it is given in the following table.

Retrieval Issue	Influencing Aerosol Extinction at	Issue Type
Failed iteration convergence	h_{flag} and to a smaller extent $h_j < h_{\text{flag}}$	warning
No Sensitivity	h_{flag}	warning
Below Detection Limit	h_{flag}	warning
AOT along the LOS reaches Saturation Threshold	$h_j \leq h_{\text{flag}}$	retrieval stop
Negative Aerosol Extinction	$h_j \leq h_{\text{flag}}$	retrieval stop
Negative Measured Radiance	all h_j	retrieval stop
Simulation Timeout	all h_j	retrieval stop

Table 6.5: List of possible retrieval results that yield no information on aerosol extinction. These issues are detected by the retrieval algorithm and flagged accordingly. If an issue results in missing information on aerosol extinction at an altitude h_j, the retrieval algorithm is stopped. h_{flag} marks the altitude where an issues occurred.

FAILED ITERATION CONVERGENCE The iteration described in equation 6.13 does not always converge: If the sensitivity for aerosol extinction is low, the retrieval result tends to alternate between two values of aerosol extinction that both are not fulfilling the stop criterion of the iteration as defined in 6.13. In any case the calculation is stopped after a arbitrarily chosen maximum number of iterations $k_{\text{max}} = 15$. If k_{max} is reached the results at the current altitude h_{flag} are flagged accordingly. The retrieved aerosol extinction is marked with the same warning flag for all altitudes below h_{flag} as they are affected by uncertainties at h_{flag}.

NO SENSITIVITY This flag is set if a tangent height is only sensitive to altitudes outside of the retrieval domain or if an altitude box cannot be retrieved by any tangent height. This issue can only occur for the application of a three-dimensional correction that will be introduced in section 8.1. Table 8.1 on page 94 shows an example of this issue. The flag does not result in a retrieval stop and is used to interpret an aerosol extinction result of $0\,\text{km}^{-1}$.

BELOW DETECTION LIMIT If the aerosol extinction is below the detection limit, equation 6.5 is fulfilled within the simulation uncertainties an aerosol extinction of $\beta = 0\,\mathrm{km}^{-1}$. This issue is only flagged at h_{flag}.

SATURATION THRESHOLD If the aerosol optical thickness (AOT) along the LOS becomes too large, further increases in aerosol extinction do not change the measured radiance. In this case the retrieval reaches the saturation threshold. An example for such a case is given in figure 6.8 on page 47. For the retrieval algorithm described in this thesis the upper boundary of measurable aerosol extinction is set to $10^{-1}\,\mathrm{km}^{-1}$. For an aerosol extinction in that order of magnitude, the AOT along the LOS reaches values of at least 30. This is comparable to a thick tropospheric cloud. Consequently, the retrieved aerosol extinction is underestimated for the altitude h_{flag} and cannot be retrieved for altitudes $h < h_{\mathrm{flag}}$. The retrieved aerosol extinction is flagged and the retrieval is stopped.

NEGATIVE AEROSOL EXTINCTION For cases where the measured values of the normalized radiance are smaller than the simulated values for a model atmosphere without aerosol ($\beta = 0\,\mathrm{km}^{-1}$), the retrieval algorithm would result in a negative extinction in order to fulfill equation 6.5. This case usually indicates an issue in the assumption of the input parameters, used for retrieving the aerosol extinction. However, sensitivity studies show that the effect of reasonable variations in effective albedo and air density are too small to account for this problem. Measurement uncertainties like the zig-zag effect shown in figure 6.15b can also cause this issue. By accounting for aerosol extinction at the reference tangent height and above as introduced in section 6.3.2 and applying a spatial straylight correction as discussed in section 6.3.3 the occurrence of this issue is significantly reduced as will be shown in section 7.1. Since the aerosol extinction cannot be retrieved at h_{flag}, the retrieval algorithm is stopped and all altitudes below are flagged.

NEGATIVE MEASURED RADIANCE For higher tangent heights and longer wavelengths, the measured radiance at the reference tangent height can be in the same order of magnitude as the noise level of the SCIAMACHY instrument. Thus, calibrated radiance values can be below zero. In that case the retrieval algorithm is not able to retrieve the aerosol extinction profile.

SIMULATION TIMEOUT This issue occurs mainly in the northern hemisphere for SCIAMACHY measurements where the solar zenith angle at the instrument is above 90°. Measurements are possible for this viewing geometry since the solar zenith at the tangent point is around 70° for these locations. However, in some cases the RTM requires long calculation times to achieve the precision required for the application of the aerosol extinction retrieval. For performance reasons the calculation time for a single simulation is limited to 60 s. Simulations which require a longer calculation time are discarded. The retrieval algorithm is interrupted and the resulting profile is flagged accordingly.

7

COMPARISON TO SAGE II AND BALLOON SOUNDINGS

In this chapter, results of the stratospheric aerosol extinction retrieval described in chapter 6 are compared to the long term data set of SAGE II and balloon soundings. This comparison is used to evaluate the accuracy of the retrieval method and the influence of assumptions and approximations made in the algorithm.

7.1 SAGE II OCCULTATION MEASUREMENTS

The second generation of the second Stratospheric Aerosol and Gas Experiment (SAGE II) on board of the Earth Radiation Budget Satellite (ERBS) provides stratospheric aerosol extinction profiles at 525 nm and 1020 nm for more than 20 years between October 1984 and August 2005. In order to directly compare this long term data set with aerosol extinction profiles retrieved from SCIAMACHY measurements in limb geometry, the SAGE II data set was reprocessed as follows:

- SAGE II aerosol extinction profiles are interpolated to the altitude grid defined in section 6.1.1. The vertical resolution is reduced from the initial 0.5 km (SAGE II) to 3 km (SCIAMACHY).
- The Ångström exponent derived from SAGE II extinctions at 525 nm and 1020 nm is used to calculate the aerosol extinction profile at 1090 nm as explained in section 4.5.
- For temporal collocation, measurements of the same day (UTC) were chosen allowing time differences of up to 24 h.
- For spatial collocation, tangent points of both measurements have to be within 250 km.

In general, line of sight (LOS) and volume of sensitivity (VOS) differ between both instruments. SAGE II generally looks to the east or west where the sun is located at the time of sunrise or sunset, while the viewing direction of SCIAMACHY is approximately north to south on the descending node of the ENVISAT orbit as shown in figure 7.1. These different viewing geometries might cause deviations in aerosol extinction despite the application of temporal and spatial collocation criteria since different parts of the atmosphere are sampled. In addition, the SCIAMACHY data set is susceptible to uncertainties in the assumed aerosol size distribution and refractive index, especially for measurements with a single scattering angle $\xi > 90$ as shown in section 6.2.2.3. In contrast, SAGE II results are not affected by uncertainties of the aerosol size distribution, as measurements in occultation geometry are dominated by direct sunlight. Therefore, additional systematic deviations are expected that are enhanced in the southern hemisphere.

(a) Northern Hemisphere

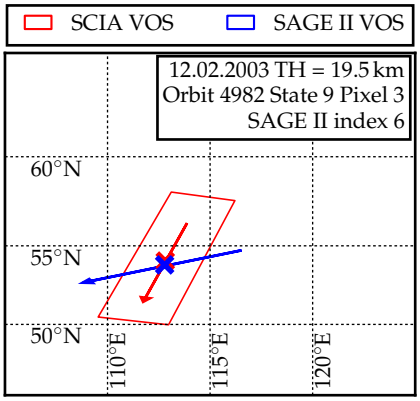

(b) Southern Hemisphere

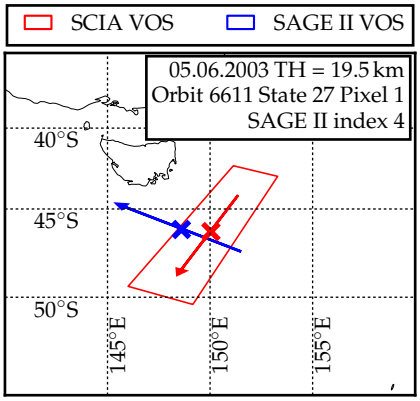

Figure 7.1: Comparison of SCIAMACHY (red) and SAGE II (blue) volume of sensitivity (VOS) in the northern hemisphere (a) and the southern hemisphere (b). The red box indicates the size of SCIAMACHY's VOS which results from line of sight and aperture angle. In comparison, the small VOS of SAGE II, with a width of 2.5 km at the tangent point, is represented by a blue line. Arrows show the viewing direction and crosses mark the respective tangent points.

7.1.1 *Single Measurement Comparison*

An example that fits the collocation criteria for measurements on the 15th October 2003 at about 41 °N is shown in figure 7.2. SCIAMACHY aerosol extinction derived from measured radiance spectra using different spatial straylight corrections, see section 6.3.3, are compared against the SAGE II results. SCIAMACHY results for $\lambda = 525\,\text{nm}$ and $\lambda = 1090\,\text{nm}$ are systematically smaller than the SAGE II results in this example. Applying a spatial straylight correction increases the retrieved aerosol extinction from SCIAMACHY and resulting deviations are smaller. However, results of the different spatial straylight correction methods do not vary significantly in this case. The retrieval uncertainty as displayed by the error bars is larger for the shorter wavelength $\lambda = 525\,\text{nm}$ and for low altitudes at both wavelengths, according to the findings of consistency studies in section 6.2.

7.1.2 *Global Coverage and Retrieval Issues*

Figure 7.3 shows maps of all measurement locations considered in this comparison study. Color and shape of the location markers indicate different retrieval algorithm warnings and errors as defined in section 6.3.4. Systematic simulation problems (simulation timeout) are occurring in the northern most latitudes (above 70 °N) and in a latitude band around 50 °N. All affected locations have a similar solar azimuth angle of around 180°. Saturation issues are mainly found in the tropical regions where strong convective cloud systems can reach up to 18 km and therefore increase the retrieved aerosol extinction. Outside of the tropical region, the occurrence of

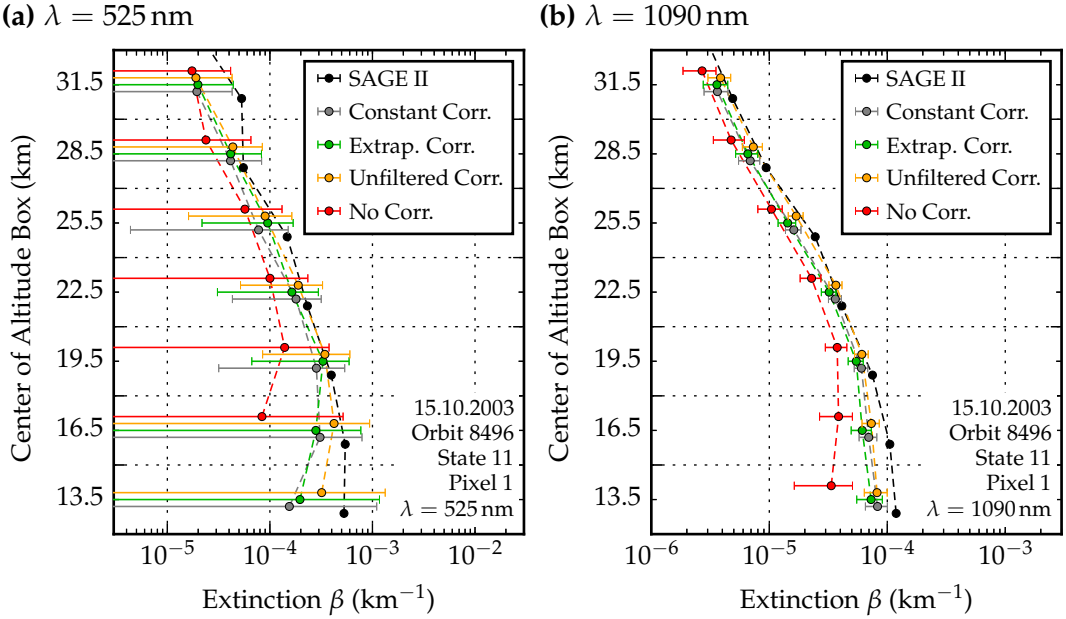

Figure 7.2: Comparison of SAGE II and SCIAMACHY aerosol extinction profiles measured on 15th October 2003 for 525 nm (a) and 1090 nm (b). For SCIAMACHY a variety of spatial straylight correction approaches was applied as described in section 6.3.3. Values of different data sets are slightly shifted within the respective altitude box, depicted by horizontal grid lines, to keep them distinguishable. Large error bars and missing data points indicate retrieval problems for example at altitudes below 18 km.

the negative aerosol extinction flag (red triangles) is increased. With the application of the constant spatial straylight correction, the occurrence rate of this warning decreases by over 50 %.

The number of retrieval problems found for the collocated measurements is further investigated for the retrieval approach with and without spatial straylight correction, see figures 7.4 and 7.5. Here, the three spatial straylight correction methods discussed in section 6.3.3 are compared. Accounting for spatial straylight reduces the measured radiance at the reference tangent height. Therefore, the normalized measured radiance is increased and cases of $I_{\text{sim}}(\beta = 0) > I_{\text{meas}}$, which would result negative β, are less probable. Applying any spatial straylight correction significantly increases the number of measurements for which the retrieval algorithm is capable to derive the aerosol extinction profile without warnings. For all methods, the retrieval algorithm converges successfully at a wavelength of 1090 nm for more than 60 % of the collocations. For the extrapolated spatial straylight correction, the number of collocations flagged with the negative extinction warning is larger than for the other correction methods, especially for latitudes below 50°. This indicates, that the applied extrapolation method appears to be inappropriate.

(a) No correction for spatial straylight

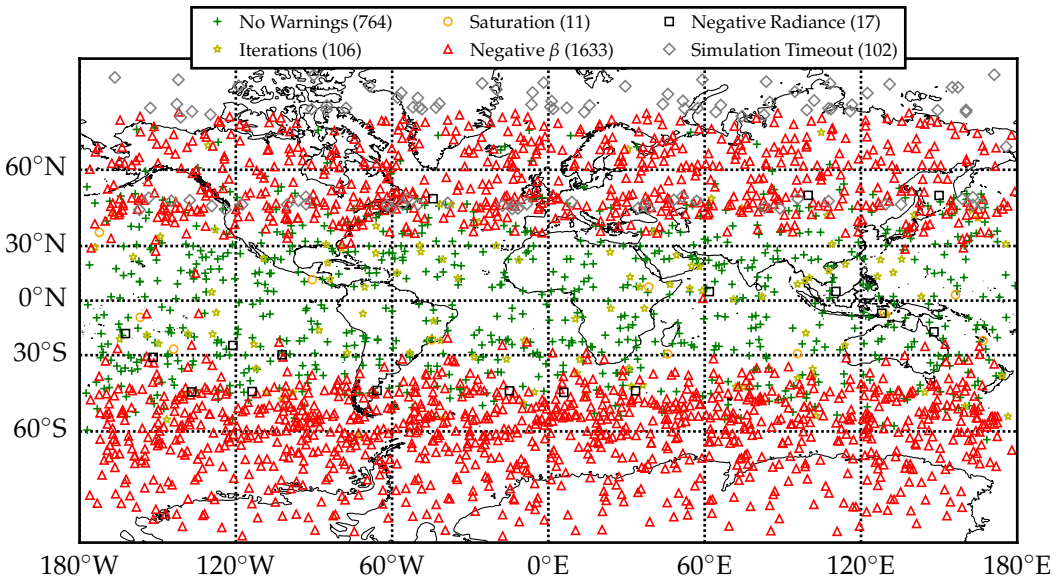

(b) Constant spatial straylight correction

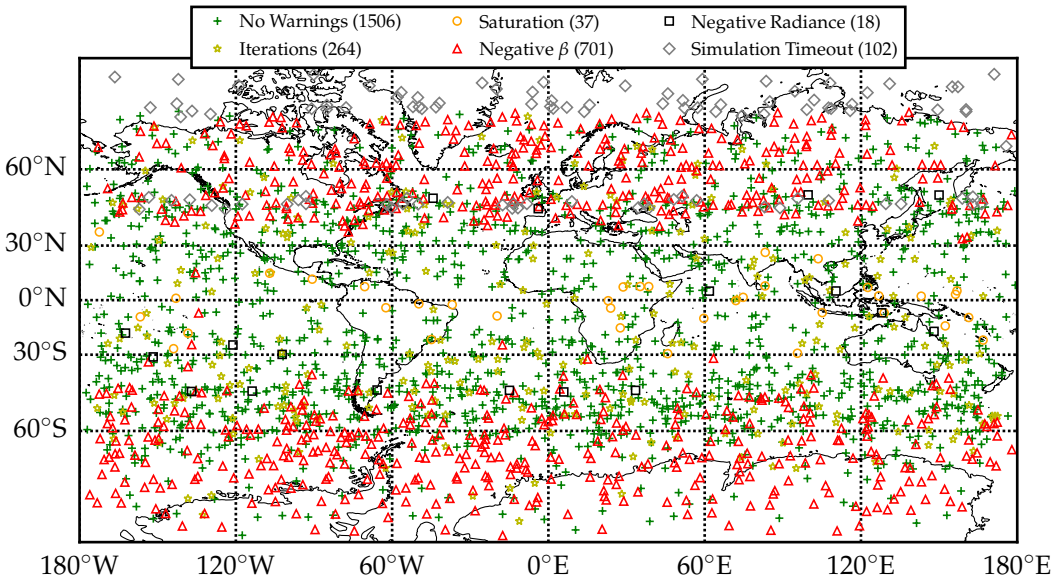

Figure 7.3: Available collocations for SAGE II and SCIAMACHY measurements between January 2003 and April 2005. Green crosses show where the SCIAMACHY retrieval algorithm performed at a wavelength of 1090 nm converged without applying a spatial straylight correction (a) and with using constant spatial straylight correction (b). In addition, different colors indicate the warning flags as introduced in table 6.5. Numbers in the legend indicate how many collocations are found for the respective category.

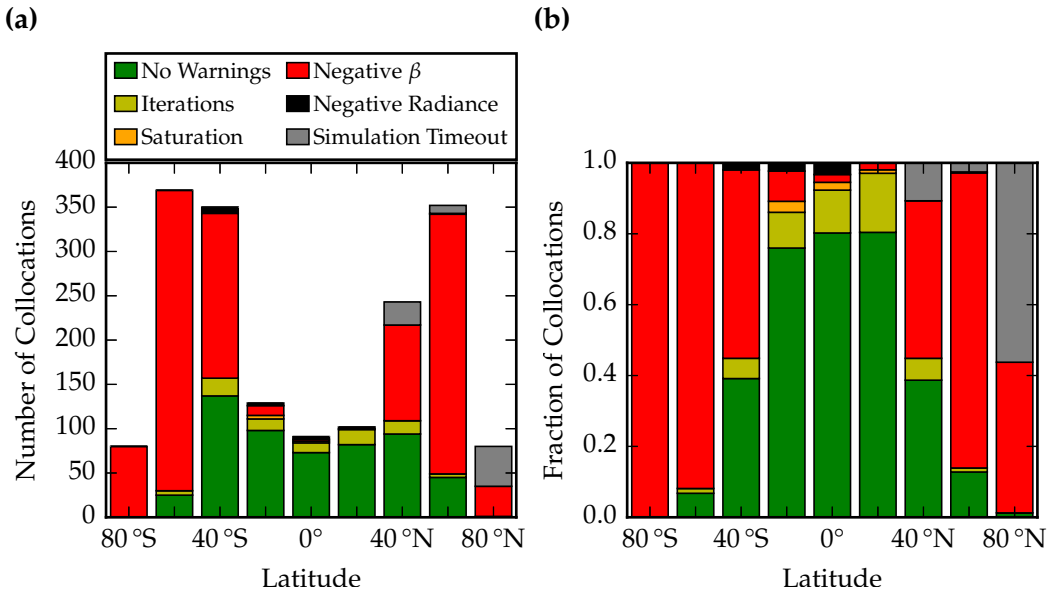

Figure 7.4: The absolute (a) and relative (b) number of collocations shown in figure 7.3a is derived in bins of 20° latitude. Shown occurrence rates of different warning flags result from using the retrieval algorithm without spatial straylight correction at $\lambda = 1090\,\text{nm}$.

Due to varying sensitivity for aerosol extinction, the frequency distribution of warnings is strongly wavelength dependent. The analysis for 525 nm in figure 7.6 shows that the retrieval algorithm was capable of deriving aerosol extinction profiles in about 20 % of the collocations only despite correcting for spatial straylight. All valid measurements are located in the northern hemisphere. With a decreased sensitivity, uncertainties of the retrieval algorithm are higher, as shown in section 6.2. Therefore, this wavelength is susceptible to uncertainties in assumptions like aerosol size distribution or spatial straylight. Collocation maps and error analyses for other wavelengths, i.e. 750 and 870 nm, can be found in the appendix section A.3.

7.1.3 *Comparison of Averaged Aerosol Extinction Profiles*

The spatial straylight correction does not only affect the number of measurements that can be successfully processed by the retrieval algorithm, it also affects the agreement of aerosol extinction profiles from SCIAMACHY and SAGE II as shown in figure 7.7. The chosen time range from January 2004 to April 2005 contains only collocations that were not used to determine the spatial straylight correction. This reduces the influence of SAGE II aerosol extinction profiles on SCIAMACHY results. Collocations are additionally filtered for those measurements where the retrieval algorithm converged with and without applied spatial straylight correction or SAGE II data for the full altitude range are unavailable (203 measurements at

(a) Unfiltered Spatial Straylight Correction

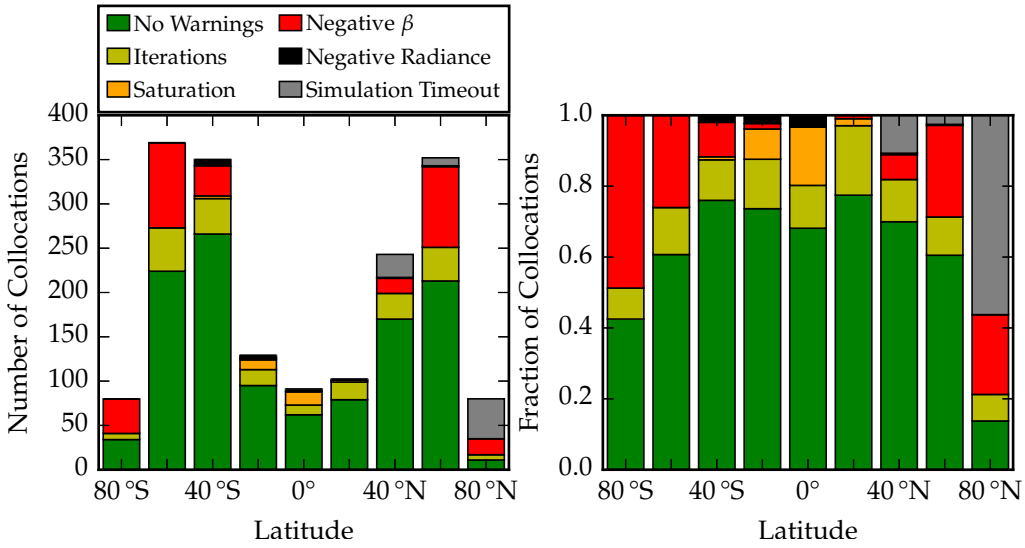

(b) Extrapolated Spatial Straylight Correction

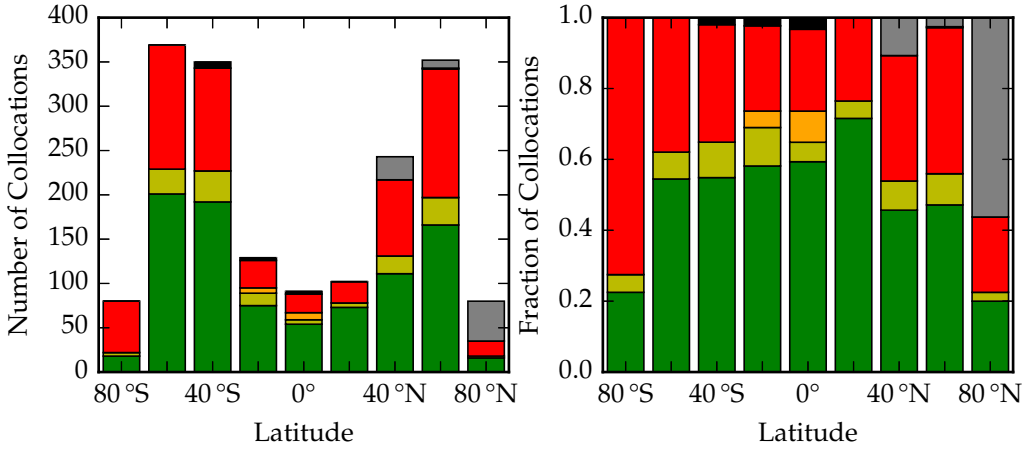

(c) Constant Spatial Straylight Correction

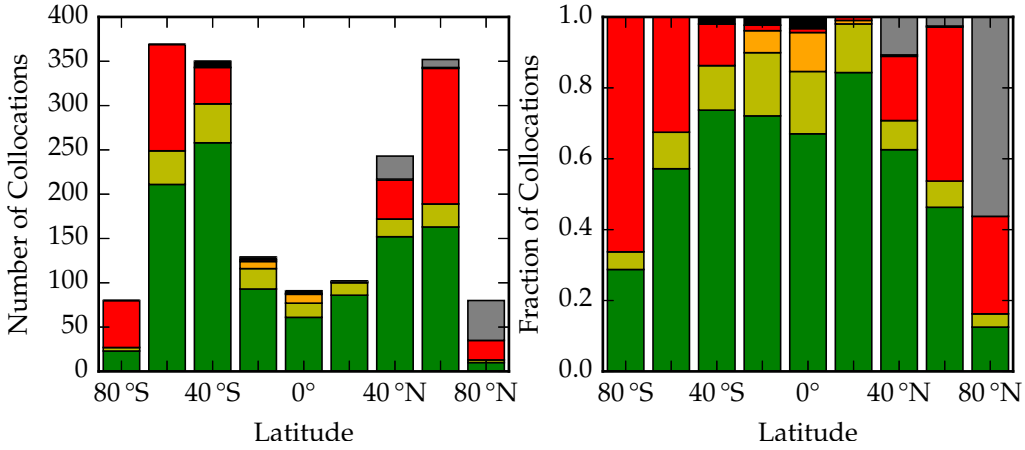

Figure 7.5: The application of a spatial straylight correction generally increases the number of collocations for which the retrieval converged without warnings. Similar to figure 7.4, the occurrence rate of different warning flags is compared for the application of three different spatial straylight corrections described in section 6.3.3: Unfiltered correction factors (a), extrapolated correction factors (b) and constant correction factors (c).

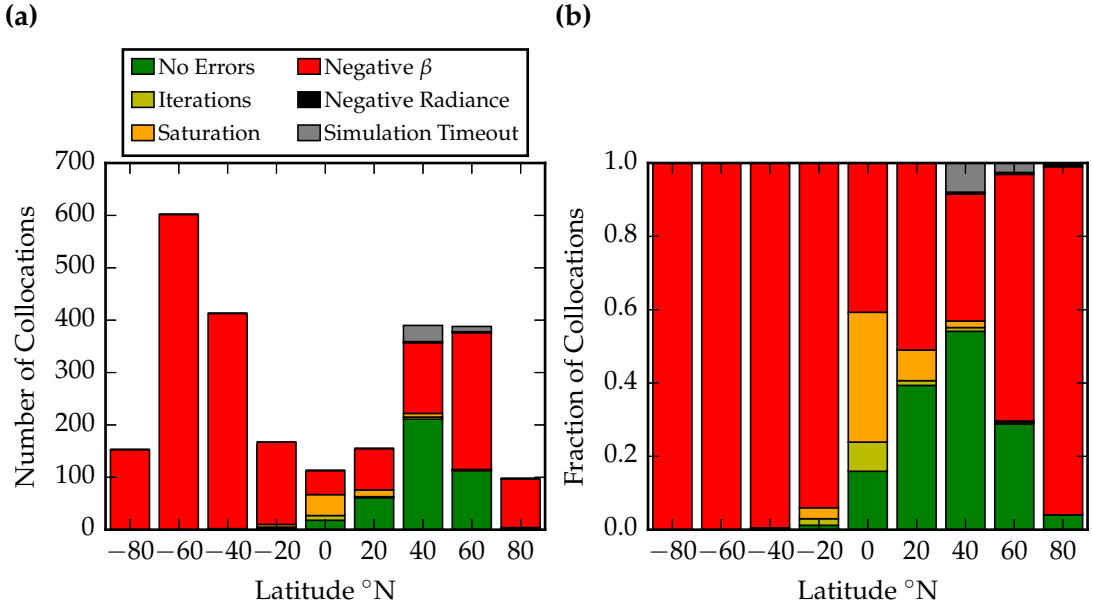

Figure 7.6: For a wavelengths of 525 nm the retrieval algorithm converges in about 20 % of the available collocations. Similar to figure 7.5c absolute (a) and relative (b) values are shown.

1090 nm). Globally averaged retrieval results without spatial straylight correction (red) are low biased by about 30 to 40 % as compared to SAGE II. For unfiltered, extrapolated and constant correction approach, the results of SCIAMACHY aerosol extinction profiles are systematically larger than the SAGE II results. Here, extrapolation and constant correction approach yield similar deviations of about +10 to +20 %, while the results for an unfiltered correction approach are positively biased by about 30 to 50 %. This confirms that the unfiltered correction approach overcompensates for spatial straylight as discussed in section 6.3.3. For an altitude of 19.5 km and below, SCIAMACHY results are generally increasing due to the influence of tropospheric convective cloud systems in the tropical regions.

Uncertainties of the retrieval algorithm are related to the sensitivity to particle scattering. For an optically thin stratosphere that contains mainly sulfate aerosol, the probability for multiple scattering is reduced and the sensitivity to particle scattering can be described the scattering phase function. In the following, the comparison between SCIAMACHY and SAGE II is performed for different ranges of the single-scattering angle ξ. According to figure 3.5c, the single-scattering angle of SCIAMACHY measurements varies with latitude and can be grouped into three regions: The northern hemisphere with $\xi \lesssim 70°$, the tropics with $70° \lesssim \xi \lesssim 110°$ and the southern hemisphere with $\xi \gtrsim 110°$.

SAGE II and SCIAMACHY show the best agreement for a forward scattering geometry using the constant spatial straylight correction method with deviations below 10 % between 19.5 and 28.5 km, as shown in figure 7.8. Similar to the global

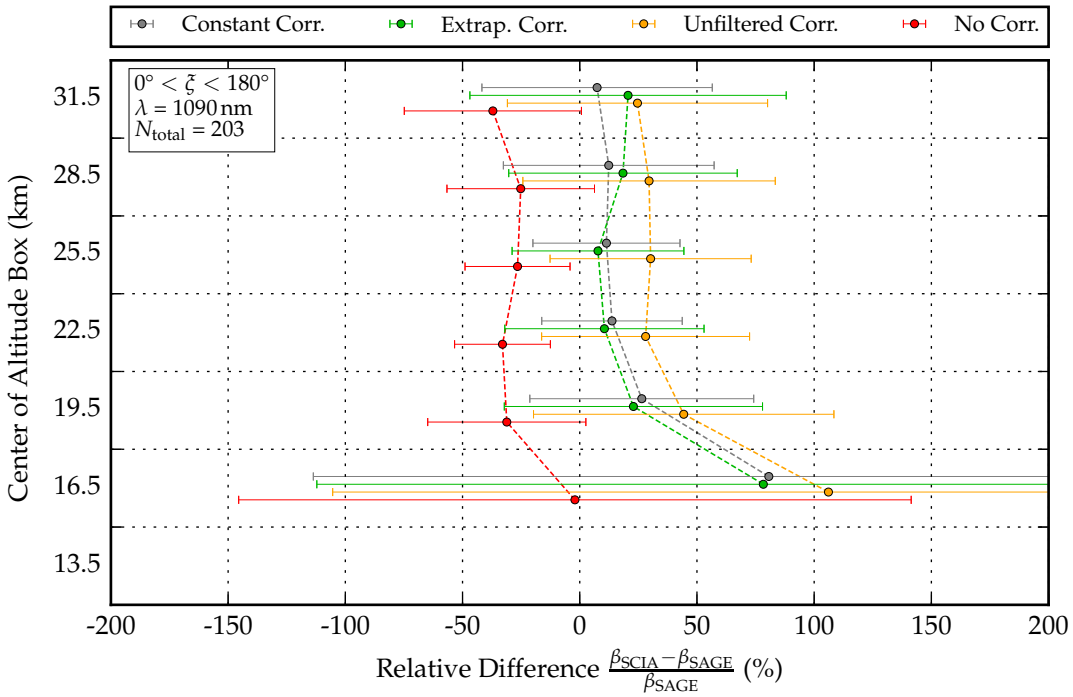

Figure 7.7: Relative differences between SCIAMACHY and SAGE II aerosol extinction profiles averaged for all collocations between January 2004 and April 2005. Values of different data sets are slightly shifted within the respective altitude box, depicted by horizontal grid lines, to keep them distinguishable. Error bars indicate the standard deviation of the differences. Here, only those measurements are used, for which the retrieval algorithm converged with and without spatial straylight correction.

comparison, SCIAMACHY results without spatial straylight correction are around 40 % smaller than SAGE II results. The unfiltered correction method yields deviations of around +20 %, while for the extrapolated correction method deviations of -20 % are found. For all applied correction methods the relative difference between SCIAMACHY and SAGE II is decreasing with increasing altitude due to the influence of the aerosol size distribution assumption. In contrast to SAGE II where this assumption is not required, the aerosol size distribution has to be assumed for the SCIAMACHY retrieval. This causes uncertainties as described in section 6.2.2.3. With respect to figure 4.3b negative differences at high altitudes can be explained by an overestimated particle size for $\xi < 70°$. Accordingly, positive differences at low altitudes can be explained by an underestimated particle size. For scattering angles around 90° shown in figure 7.9, deviations between SCIAMACHY and SAGE II are strongly increasing for altitudes below 22.5 km due to the influence of tropospheric clouds. The results in other altitudes are similar to those of the forward scattering geometry comparison. The sensitivity to particle scattering in both regions is comparable, but according to the phase function of the assumed aerosol size distribution, sensitivity is strongly decreasing for larger values of ξ (backscatter geometry).

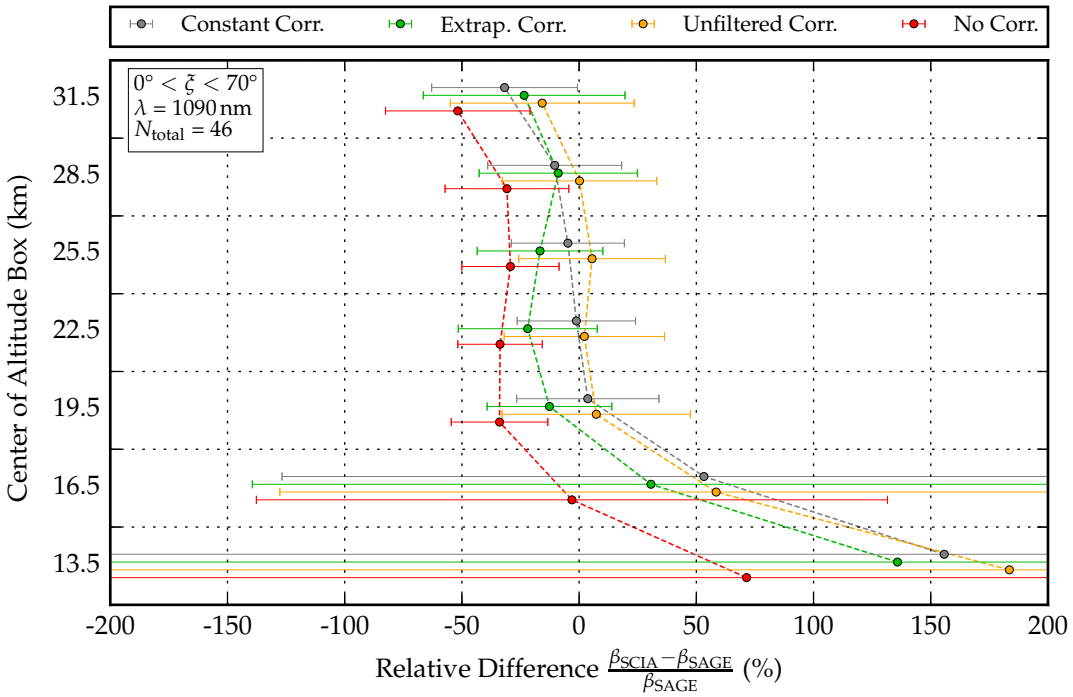

Figure 7.8: Comparison for collocations with a single scattering angle $\xi < 70°$ at the SCIAMACHY tangent point. Values are selected and depicted similar to figure 7.7.

For $\xi > 90°$ shown in figure 7.10, the results for all spatial straylight correction methods are systematically larger than the aerosol extinction of SAGE II: A positive bias of about 50 % for constant and extrapolated correction methods and about 70 to 120 % for the unfiltered correction method is found. Although the effect of uncertainties in aerosol size distribution and refractive index is larger for this scattering geometry, those large differences cannot solely be explained by wrong estimates in the scattering phase function. In addition to the retrieval result, the determination of the correction factor also depends on assumptions in the aerosol size distribution. This could be a reason for an overcorrection of SCIAMACHY radiance profiles. Another possible reason for the overcompensation of spatial straylight is the choice of the filter criterion in equation 6.28. In the northern hemisphere, this filter criterion reduces the overcompensation of spatial straylight as shown by the comparison of unfiltered and constant correction approach, see figure 7.8. For the southern hemisphere however, similar deviations of all three straylight correction methods indicate, that the selected threshold might be to high.

At $\lambda = 525\,\text{nm}$ only a few collocations in the northern hemisphere remain for the comparison study, see figure 7.11. Nevertheless, aerosol extinction profiles of SCIAMACHY and SAGE II show deviations below 10 %. SCIAMACHY results at 19.5 km are probably affected by PSCs which result cause similar deviations as tropospheric convective clouds. The influence of PSCs on the comparison is weaker at $\lambda = 1090\,\text{nm}$ due to an increased statistic.

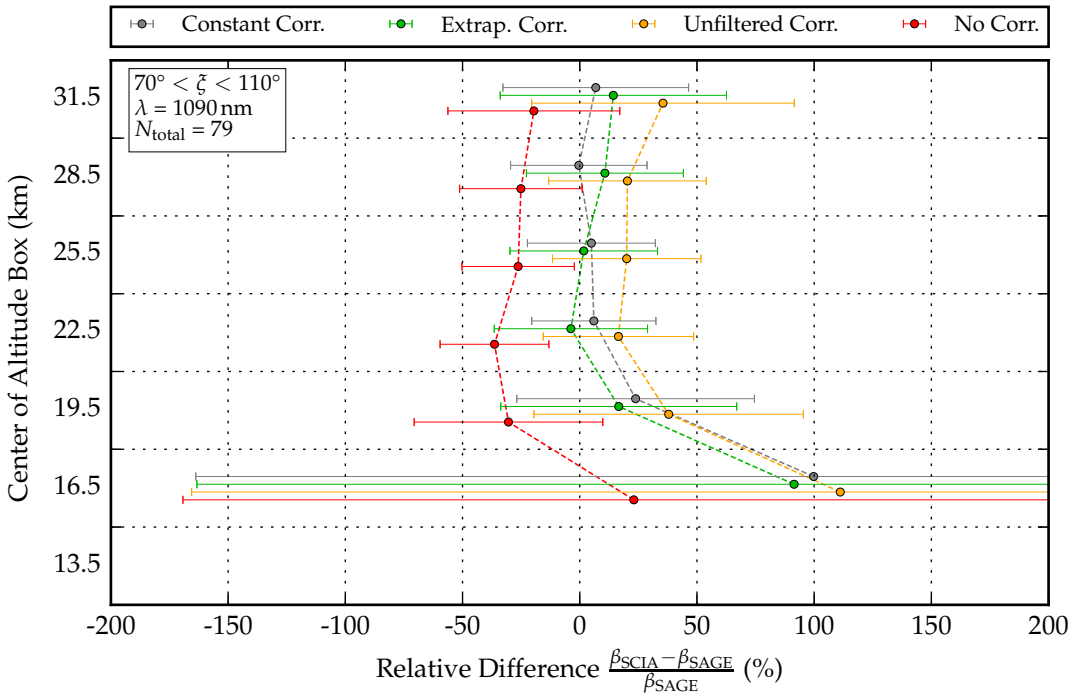

Figure 7.9: As figure 7.7 but for collocations with a single scattering angle $70 < \xi < 110°$ at the SCIAMACHY tangent point.

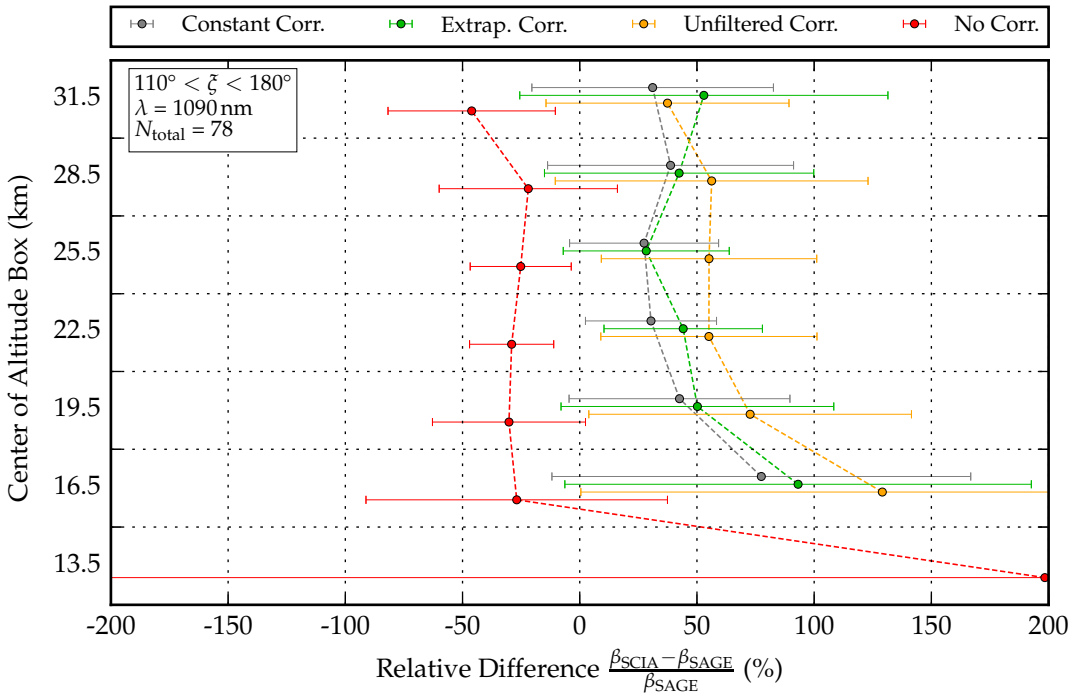

Figure 7.10: As figure 7.7 but for collocations with a single scattering angle $110 < \xi < 180°$ at the SCIAMACHY tangent point corresponding to backward scatter geometry.

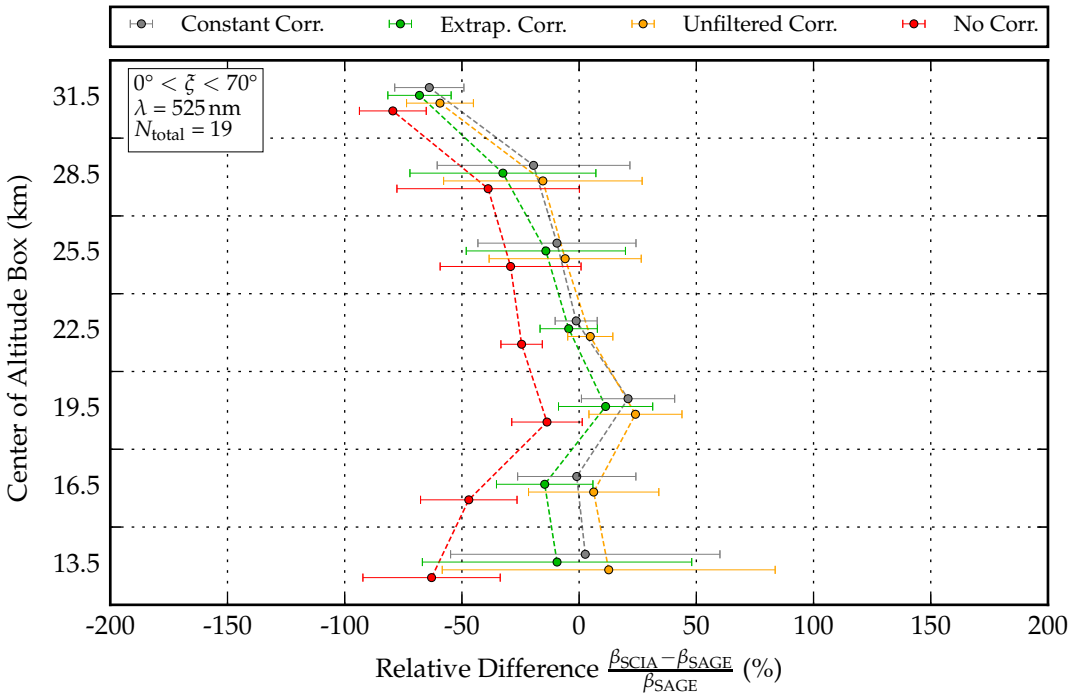

Figure 7.11: Same as figure 7.8 but for a wavelength of 525 nm.

As this study shows, the application of a straylight correction is required to reduce deviations between SAGE II and SCIAMACHY and to increase the number of SCIAMACHY measurements that can be retrieved without warnings. Therefore, statistics of this comparison can be improved by removing the retrieval without applied spatial straylight correction from the selection criteria, see appendix section A.4. However, the general findings for deviations at different single-scattering angles are confirmed.

7.1.4 *Summary and Comparison to Other Retrieval Methods*

Bourassa [2007] introduces an optimal estimation method to derive stratospheric aerosol number densities from radiance spectra. In this thesis, this method is called **Saskatoon** retrieval, referring to the city where it was developed. This retrieval algorithm is applied to measurements in limb geometry by the Optical Spectrograph and InfraRed Imaging System (OSIRIS) on the Swedish satellite Odin. For the comparison with SAGE II, retrieved number density values are multiplied with a scattering cross section for a log-normal aerosol size distribution ($r_m = 80$ nm, $\sigma = 1.6$) at 1020 nm, derived from Mie theory. Since the retrieval is performed for a ratio of radiances at 470 nm and 750 nm, the dependency of the comparison on uncertainties in the aerosol size distribution is increased. A comparison between SAGE II, SAGE III and OSIRIS is performed for measurements on the 5th January 2004 at a latitude of 37.7 °S, that are collocated spatially within 1° latitude and

temporally within 8 hours time difference. For this comparison all three aerosol extinction profiles agree within approximately 15 % for an altitude range between 15 and 30 km.

Ernst [2013] applied a similar method to the SCIAMACHY measurement data set used in this study in order to derive stratospheric aerosol extinction from a ratio of radiances at 450 nm and 800 nm. In this thesis, the method is referred to as **Bremen** retrieval. Aerosol extinction is only derived for cloud free conditions as determined from SCIAMACHY limb measurements. A correction for spatial straylight was not applied. Results are compared to collocated SAGE II aerosol extinction profiles at 525 nm. The aerosol size distribution is described by a log-normal size distribution with $r_m = 110\,\text{nm}$ and $\sigma = 1.37$. Phase functions are derived at $\lambda = 450\,\text{nm}$ and $\lambda = 800\,\text{nm}$ and linearly interpolated to $\lambda = 525\,\text{nm}$. This phase function is used to determine the aerosol extinction profile at $\lambda = 525\,\text{nm}$. For the comparison of collocated data between January 2003 and August 2005, deviations of around 20 % between the Bremen retrieval and SAGE II are found. Especially in the northern hemisphere and the tropics SCIAMACHY results are systematically smaller than results from the SAGE II instrument.

(a) Mie phase function at $\lambda = 525\,\text{nm}$ **(b)** Mie phase function at $\lambda = 1090\,\text{nm}$

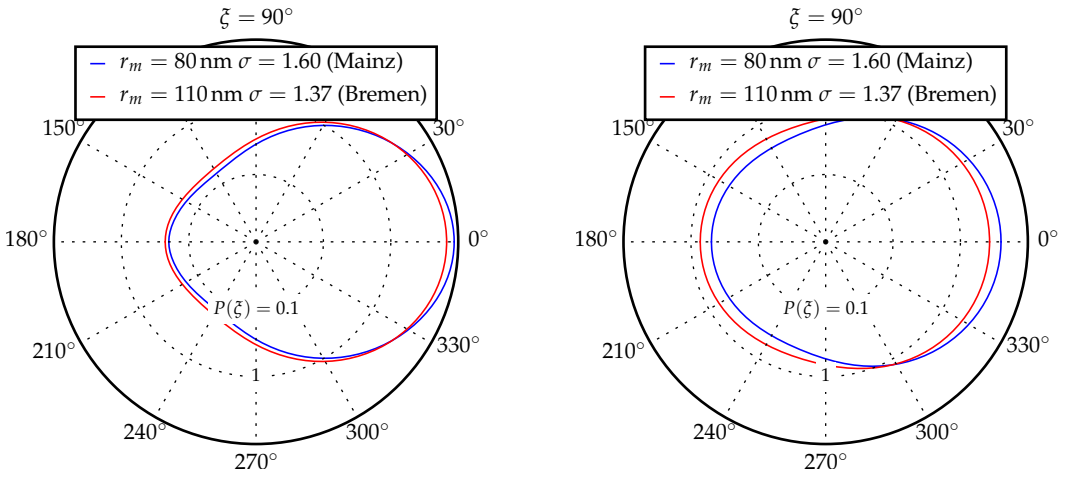

Figure 7.12: (a) Aerosol scattering phase functions $P(\xi)$ for a wavelength of 525 nm as used in the Mainz retrieval (blue) are compared to $P(\xi)$ used in the Bremen retrieval (red) [Ernst, 2013]. (b) shows the deviations at 1090 nm, accordingly. Differences in these phase function can be used to estimate possible deviations between results of the Bremen and the Mainz retrieval algorithm.

From now on the retrieval algorithm described in section 6 is referred to as **Mainz** retrieval. For the northern hemisphere, the agreement between SAGE II and SCIAMACHY is similar for both Bremen and Mainz retrievals at 525 nm. For the corresponding scattering angles $\xi < 70°$, the phase function values used in the Bremen retrievals are slightly larger due to differences in the assumed aerosol size distribution as shown in figure 7.12. This results in smaller aerosol extinction values.

In addition, the spatial straylight correction applied in the Mainz retrieval leads to higher values of the aerosol extinction at all wavelengths. For shorter wavelengths this increase is less significant since the correction factors are smaller, see figure 6.22. An influence of spatial straylight was not found in the Bremen retrieval which could be related to the wavelength normalization or the chosen wavelengths. The problem of negative extinctions is not being reported by Ernst [2013]. It is important to recall that the Bremen retrieval is performed for a wavelength ratio of 450 nm and 800 nm with aerosol extinction at 525 nm being derived thereafter. The sensitivity to particle scattering appears to be high enough at the chosen wavelength ratio for a retrieval application in both hemispheres. In contrast, the Mainz retrieval algorithm derives the aerosol extinction directly at 525 nm and is therefore heavily influenced by sensitivity problems for a backscatter geometry. However, a comparison at a different wavelength, e.g. 1020 nm was not performed for the Bremen retrieval.

7.2 BALLOON SOUNDING AT LARAMIE, WYOMING

Since 1971, vertical profiles of size resolved number concentrations for particle radii between 0.01 and 10 µm are measured by two balloon-borne opticle particle counters (OPCs) at Laramie, Wyoming about two to three times each year [Deshler et al., 2003]. Measured vertical profiles of the number concentration in size bins between 0.15 and 2.0 µm are used to fit vertically resolved single- and bimodal lognormal size distributions. Aerosol extinction profiles with a vertical resolution of 500 m for the wavelengths 521, 758, 869 and 1020 nm are then derived from Mie theory, assuming a spherical shape of the measured aerosol particles [Foster, 2015]. The comparison with aerosol extinction profiles retrieved from SCIAMACHY radiance spectra is performed for measurement locations close to Laramie, Wyoming (41 °N, 105 °W). From balloon soundings within the time frame of SCIAMACHY operations (between 2003 and 2012) specific dates when the retrieval algorithm converged for most of the wavelengths were chosen for the comparison study as listed in table 7.1. Aerosol extinction profiles and size distributions derived from the balloon borne measurements are averaged in 3 km altitude boxes matching the vertical resolution of SCIAMACHY measurements.

The comparisons are shown in figures 7.14 to 7.20. A good qualitative agreement between aerosol extinction profiles retrieved from SCIAMACHY radiance spectra and balloon borne OPC measurements is consistently found for all compared wavelengths and all days. While the profile shape is the same for both data sets and aerosol extinction profiles are within the same order of magnitude, systematic deviations of a factor of two to three are found. Usually, comparisons between local in situ measurements and quantities retrieved from satellite remote sensing measurements with a coarse horizontal resolution are challenging. However, in a typical background scenario, stratospheric aerosol extinction can assumed to be homogeneously spread over hundreds of kilometers reducing spatial sampling issues for this comparison. Similar results of SCIAMACHY measurements at different

Balloon Sounding at Laramie, Wyoming	Availability of SCIAMACHY results			
	525 nm	750 nm	870 nm	1090 nm
20th May 2005	✗	✓	✓	✓
7th July 2005	✓	✓	✓	✓
17th October 2005	✓	✓	✓	✓
13th February 2006	✗	✓	✓	✓
6th May 2006	✗	✗	✗	✓
9th December 2006	✓	✓	✓	✓
3rd July 2007	✓	✓	✓	✓

Table 7.1: List of balloon soundings used for the comparison study with SCIAMACHY aerosol extinction profiles.

locations confirm the horizontal homogeneity for altitudes above 16.5 km. Increasing variations of retrieval results within the lowest altitude box (13.5 km) indicate the presence of clouds. Possible reasons for the deviations between both data sets will be explained and discussed in the following.

The retrieval of stratospheric aerosol extinction profiles from SCIAMACHY measurements in limb geometry is based on a variety of assumptions. Based on sensitivity studies in section 6.2.2, uncertainties in effective surface albedo, temperature and pressure account for differences $\lesssim 10\,\%$. Uncertainties caused by the assumed spatial straylight correction are globally in the order of 30 % as shown in the SAGE II comparison (see section 7.1). For measurements in the northern hemisphere the application of a constant spatial straylight correction leads to smaller uncertainties. The most important remaining assumption is the aerosol size distribution. A sensitivity study for different scattering geometries at $\lambda = 1090\,\text{nm}$ shows that an overestimation of aerosol size, with respect to distribution width and mean radius, leads to an overestimation of 30 to 50 % in retrieved aerosol extinction for scattering angles around 90°, compare figure 6.14b. Since single scattering angles vary between 50 and 80° for the shown comparisons in figures 7.14 to 7.20, the expected overestimation due to aerosol size distribution is even smaller.

Hervig and Deshler [2002] found that results from balloon borne measurements deviated from the results of SAGE II and the Halogen Occultation Experiment (HALOE) by about 50 %. The reason for this deviation is probably a sensitivity bias in volcanic quiescent periods where particles are smaller and less abundant. [Kovilakam and Deshler, 2015] discuss required correction methods for OPC measurements. Their results show a significant increase of aerosol extinction derived from corrected OPC measurements as shown in figure 7.13. This difference can also account for most of the differences between SCIAMACHY an balloon borne measurements. Hence, the found differences between SCIAMACHY and balloon borne measurements can be explained by uncertainties in both methods.

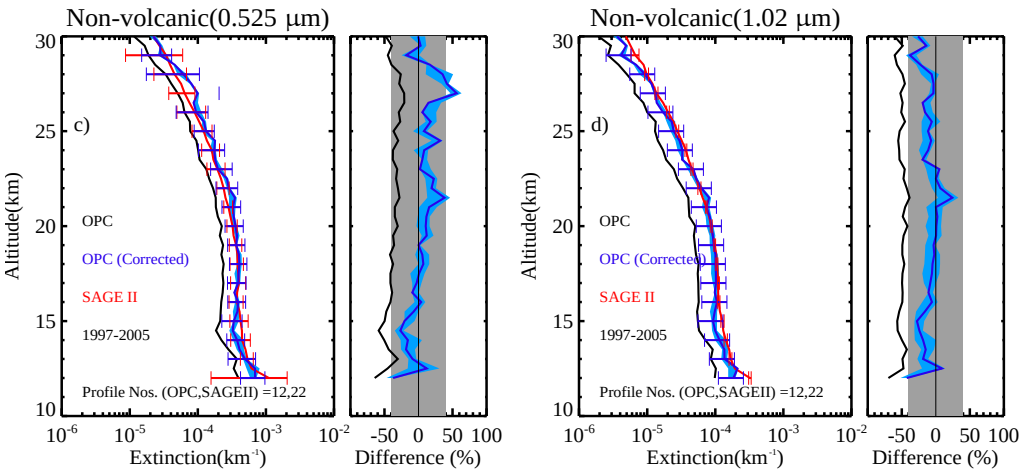

Figure 7.13: Corrected OPC measurements significantly increase average aerosol extinction profiles derived at 525 nm and 1020 nm for the volcanic quiescent period between 1997 and 2004. The difference between SAGE II (red) and OPC measurements (black) is derived as $\frac{\beta_{\mathrm{OCP}}-\beta_{\mathrm{SAGEII}}}{\beta_{\mathrm{SAGEII}}}$. This graphic is provided by Kovilakam and Deshler [2015].

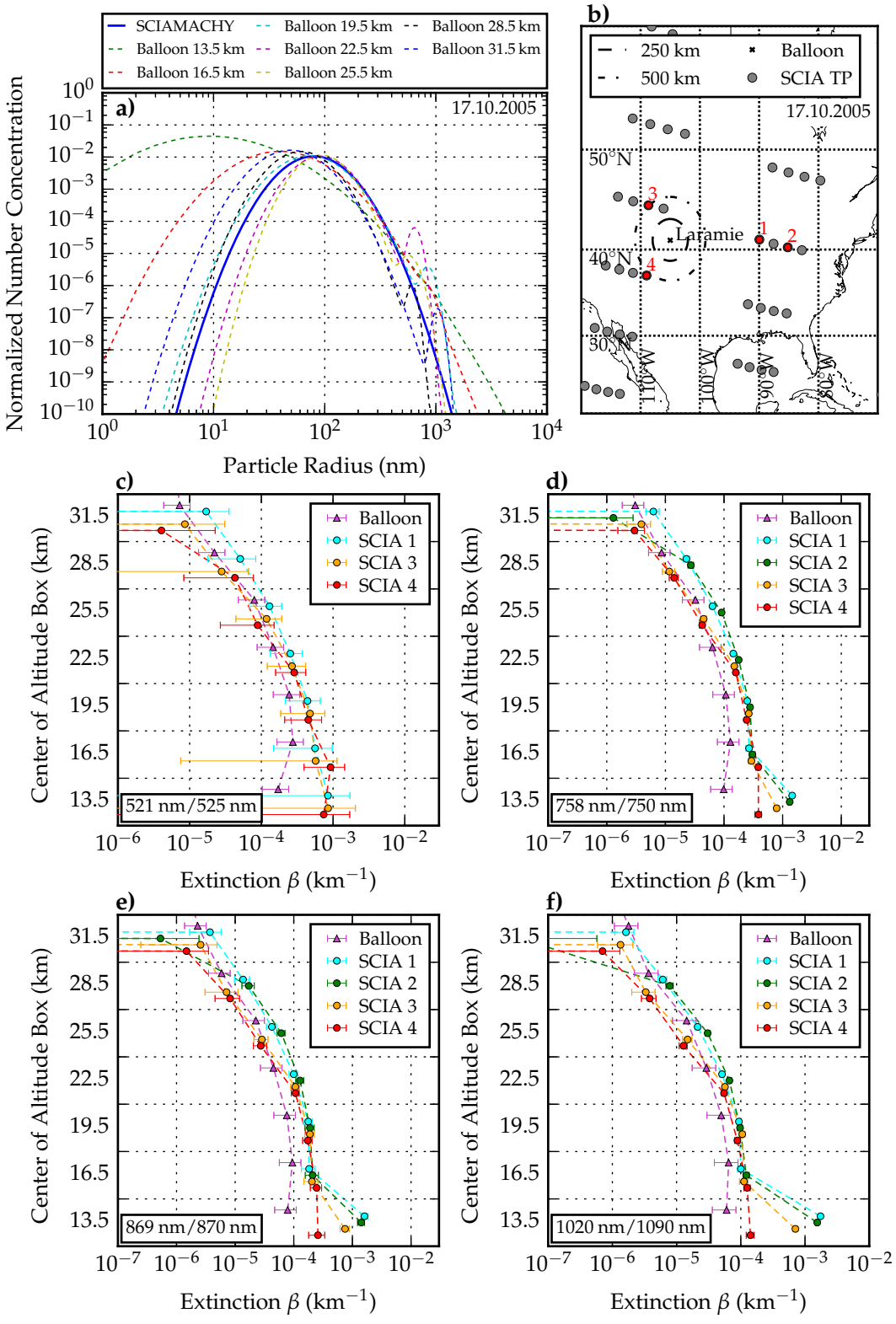

Figure 7.14: Extinction profile comparison as derived from balloon sounding and SCIAMACHY measurements in limb geometry on 17th October 2005. Aerosol size distributions assumed for SCIAMACHY results are compared to balloon borne measurements at various altitudes panel a). Panel b) shows a map of SCIAMACHY tangent points considered in the comparison (red) compared to the balloon sounding location. In panels c) to f), aerosol extinction profiles are compared for the marked locations at the wavelengths 521/525, 758/750, 869/870 and 1020/1090 nm, respectively. Values are slightly shifted in altitude to make them more distinguishable. All values in one grid box belong to the same altitude in the center of that grid box.

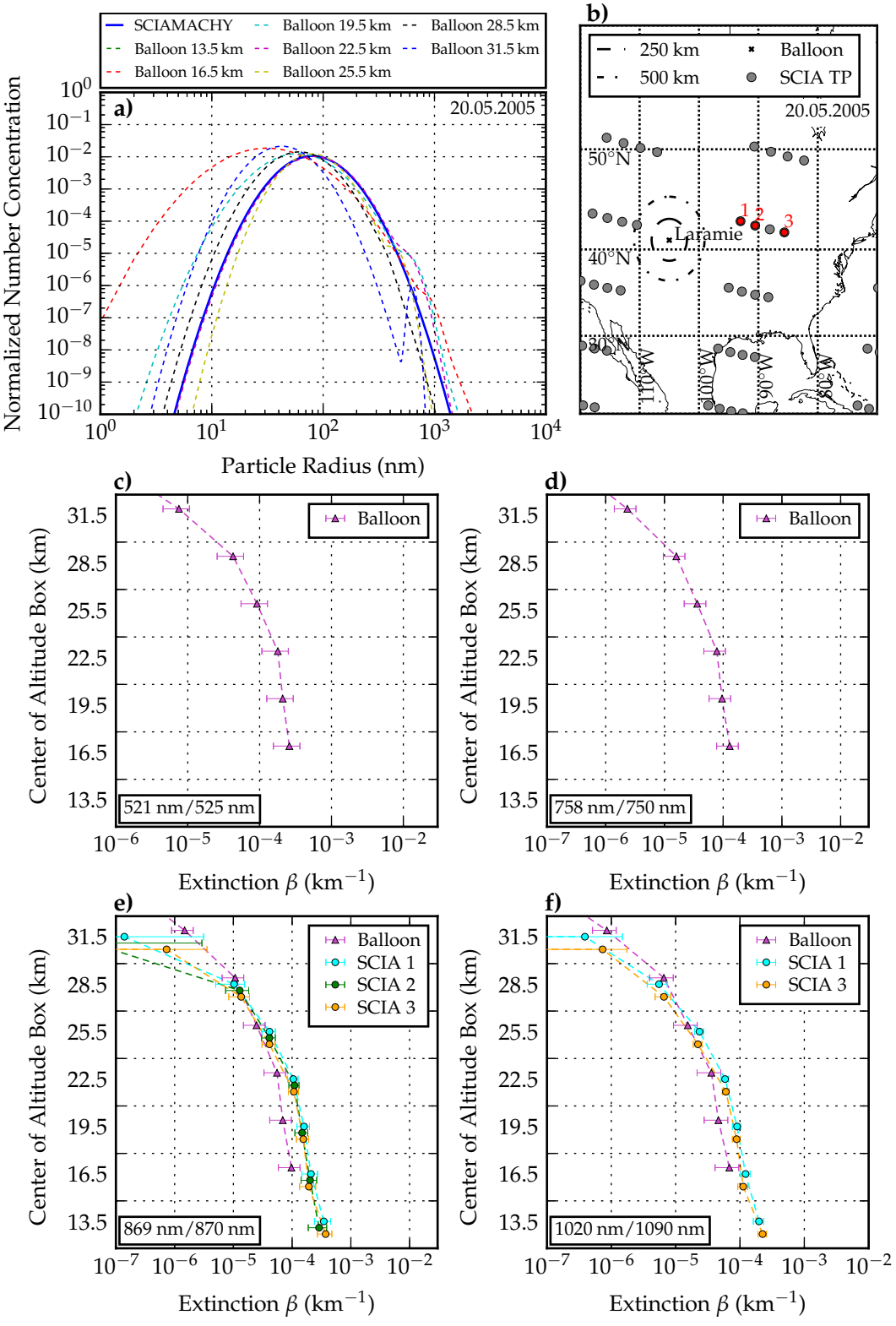

Figure 7.15: Same as figure 7.14 but for the 20th May 2005

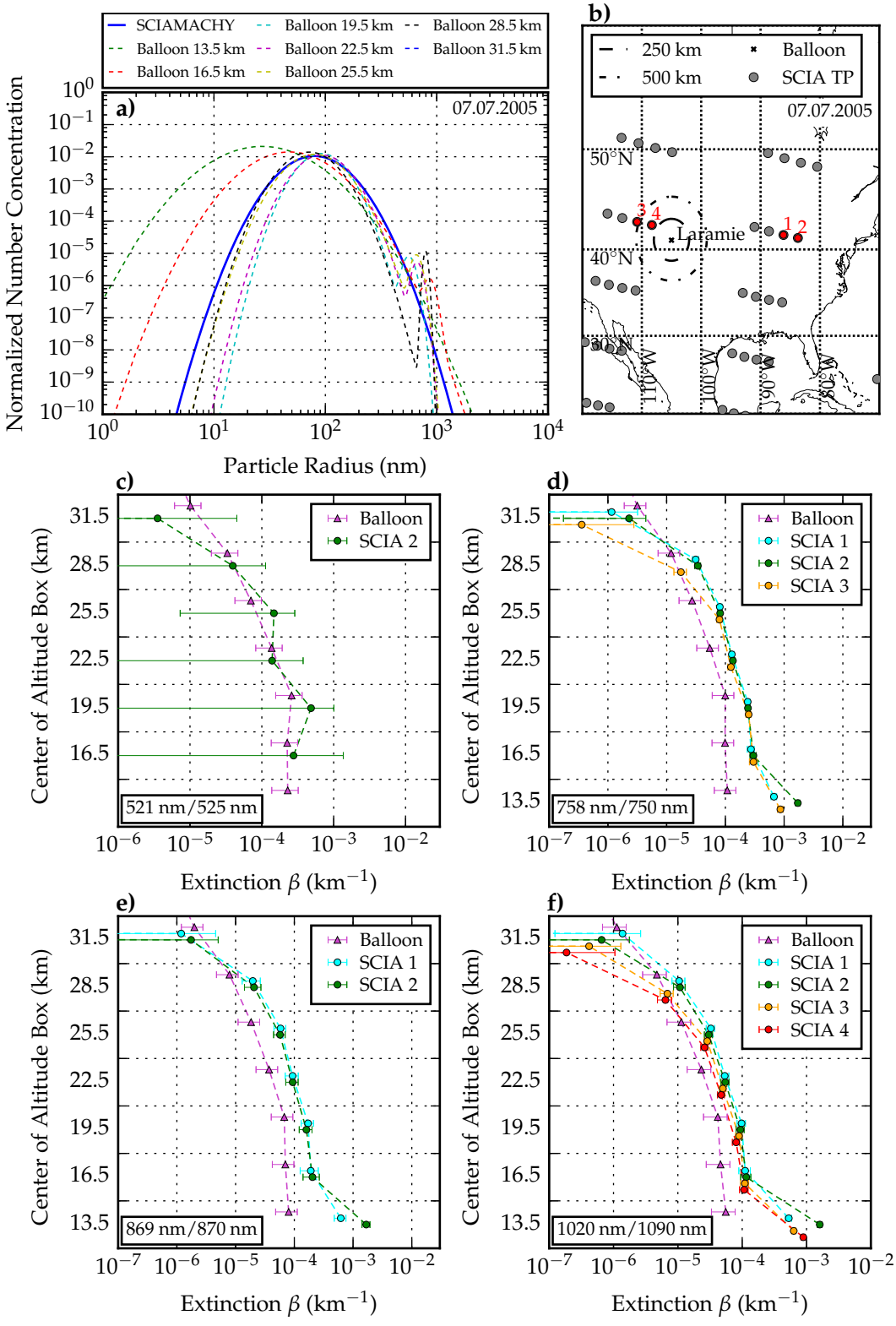

Figure 7.16: Same as figure 7.14 but for the 7th July 2005.

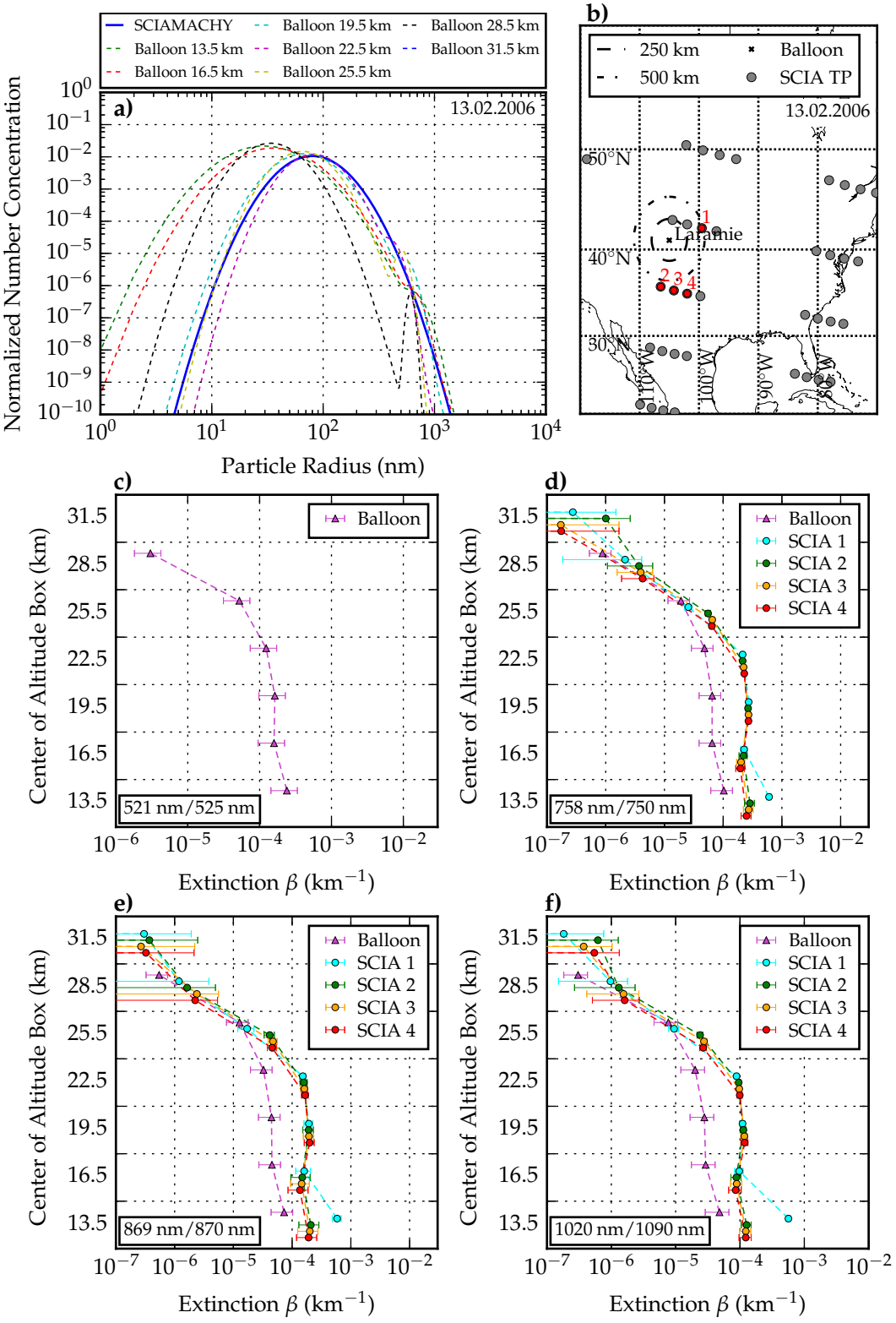

Figure 7.17: Same as figure 7.14 but for the 13th February 2006.

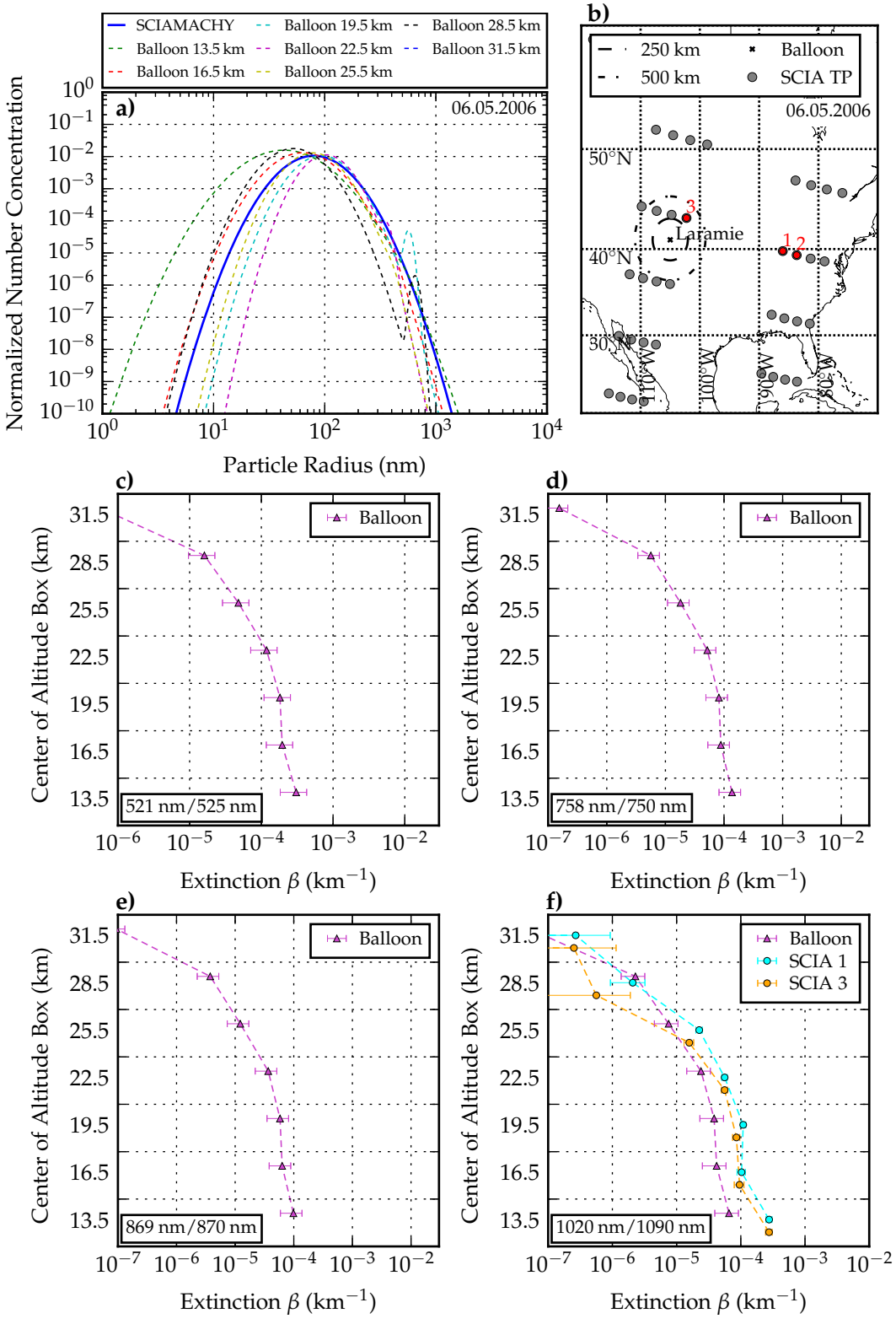

Figure 7.18: Same as figure 7.14 but for the 6th May 2006.

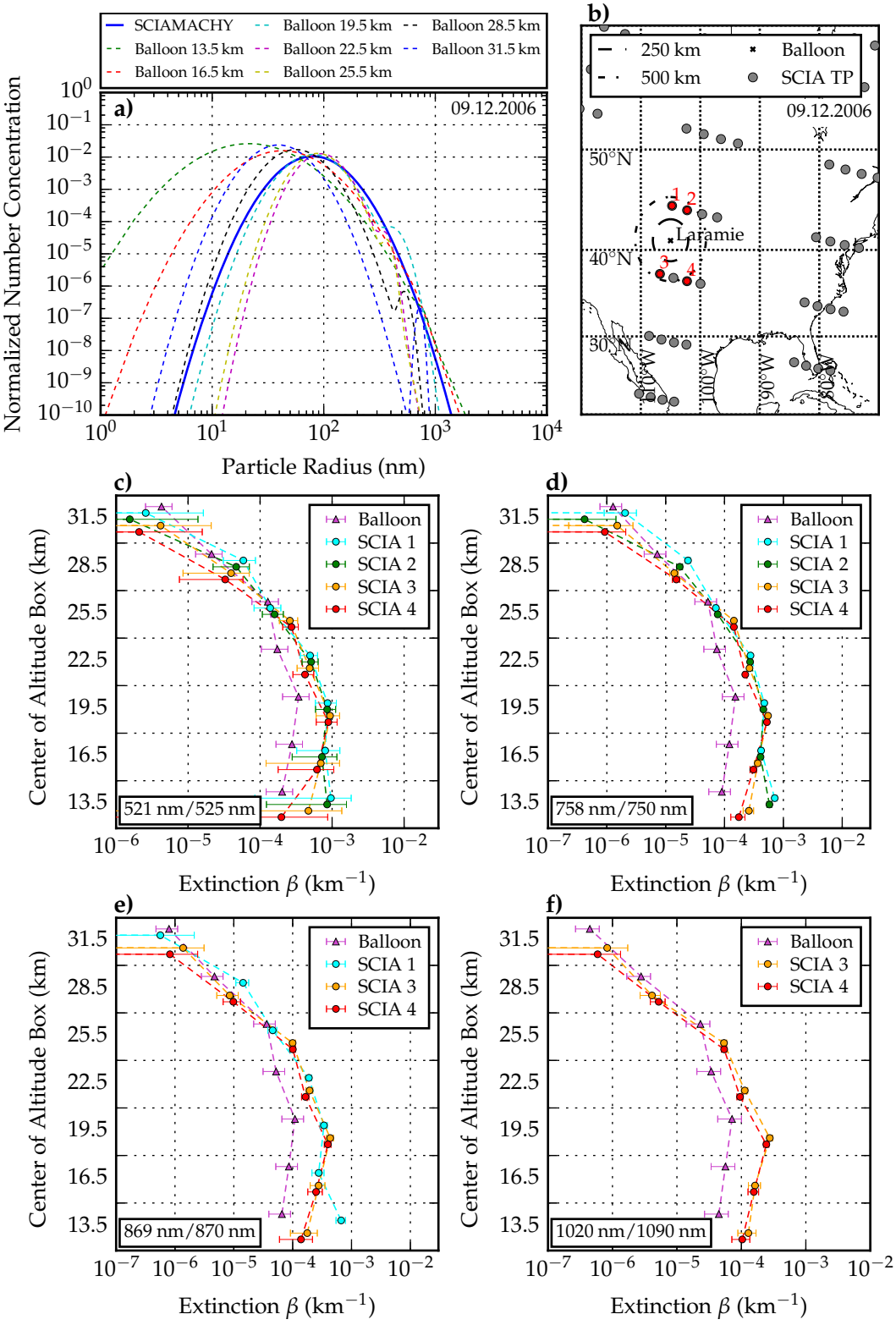

Figure 7.19: Same as figure 7.14 but for the 9th December 2006.

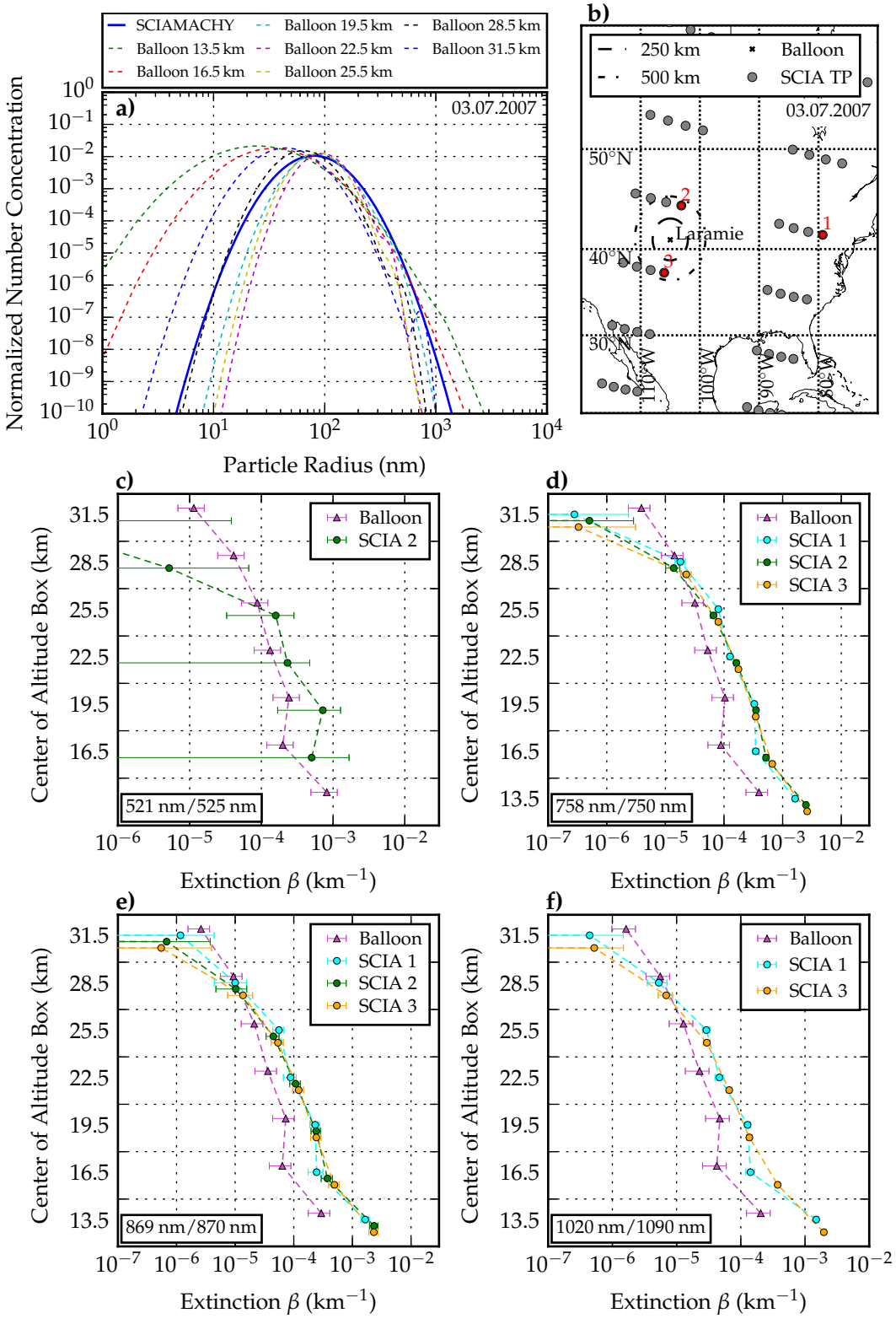

Figure 7.20: Same as figure 7.14 but for the 3rd July 2007.

8

THREE-DIMENSIONAL AEROSOL DISTRIBUTIONS

On the spatial scale of SCIAMACHY measurements (240 km across track, 1000 km along track), variations of stratospheric aerosol abundance are low, motivating the assumption of horizontal homogeneity. However, this assumption does not hold for volcanic plumes, lee wave PSCs or other conditions with strong gradients (e.g. at the polar vortex boundary). This chapter focuses on horizontal inhomogeneities in extinction along the line of sight and its influences on retrieval results. After introducing the correction method, the approach will be applied to measurements of the Nabro volcanic eruption plume in 2011, continuing the work published in Penning de Vries et al. [2014], and to PSCs in the Southern Hemisphere in September 2004.

8.1 METHODOLOGY

The radiative transfer model used in this study supports the input of three dimensional particle distributions. Using the model grid defined in section 6.1.1, latitudinal variations in the particle distribution are represented with a resolution of 1°. In the following model studies, the influence of horizontal inhomogeneities along the LOS is explained. Therefore, the retrieval algorithm is performed with and without a 3D correction to derive the extinction of a particle layer between 18 and 21 km with different characteristic horizontal distributions. Below 18 and above 21 km the extinction profile is set to zero, in order to minimize the influence on other altitude layers. In the following, this profile will be referred to as β_{input}. Similar to section 6.2 a radiance profile is simulated based on the assumed aerosol distribution and then used as input for the retrieval algorithm. β_{input} is compared with the retrieved extinction profile β_{output} in figure 8.1b. The retrieval is capable of retrieving the correct extinction at the aerosol layer as well as an extinction of zero above and below the aerosol layer which confirms the consistency of the implemented three-dimensional correction. However, result uncertainty are increasing below the aerosol layer as indicated by the error bars. This results from the viewing geometry as shown in figure 8.1a: In addition to a tangent height of 19.5 km, the homogeneously distributed aerosol layer also affects simulated radiances at lower tangent heights, that are used for the retrieval of the aerosol extinction at 13.5 km and 16.5 km. As a result, the uncertainty of retrieved aerosol extinction is increasing for altitudes below 18 km. In section 6.2 similar increases of the uncertainties with decreasing altitude are found.

For the next example the horizontal extent of the aerosol distribution is reduced to a width of 1° centered around the tangent point as indicated in figure 8.2a. Assuming horizontal homogeneity for the retrieval of aerosol extinction results

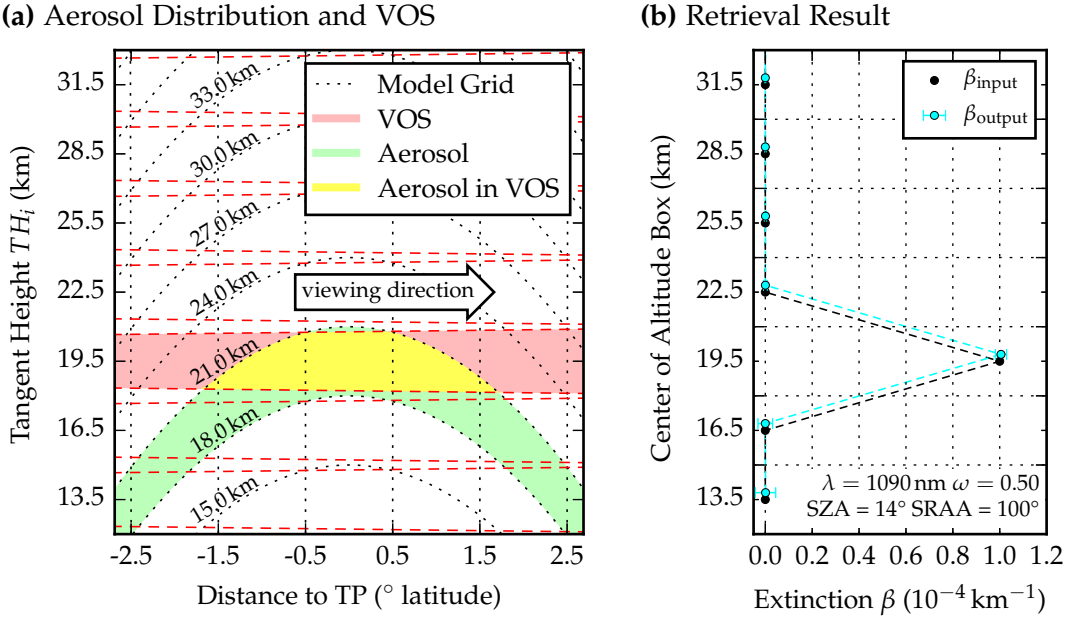

Figure 8.1: (a) displays a homogeneous aerosol layer for an altitude between 18 and 21 km (green area). The edges of the volume of sensitivity (VOS) at each tangent height are marked by dashed red lines. As an example the VOS for $TH_i = 19.5\,\text{km}$ is shown (red area). In the overlap region (yellow area) the measurement at $TH_i = 19.5\,\text{km}$ is sensitive to the aerosol layer. Outside the yellow region the measurement is not affected by particle scattering since the extinction is set to zero for all other altitudes. (b) compares aerosol extinction profiles: Black lines show the assumed aerosol extinction profile β_{input} that is used to simulated the input radiance. Blue lines represent results of the retrieval β_{output} which uses the implementations for three-dimensional corrections.

in an underestimation by about 60 % as shown by the blue curve in figure 8.2b. A comparison of this distribution to the homogeneous layer in figure 8.1a shows, that degree of underestimation is related to the decreased horizontal plume extent. Appropriately, at a tangent height of 19.5 km the volume of sensitivity (VOS) covered by the limited plume (yellow area) is reduced by about 60 % as compared to the homogeneous case. As the measured radiance is correlated to VOS within the aerosol layer, smaller extinction values in a homogeneously spread layer result in the same increase in radiance as higher values of extinction in a more narrow horizontal distribution. Retrieval results agree with β_{input}, if the correct plume extent is used for the three-dimension correction as shown by the orange data points in figure 8.1b. By narrowing the horizontal plume extent, less backscatter signal is received. Hence, the sensitivity for aerosol extinction is reduced which results in slightly higher uncertainties in the retrieval algorithm as indicated by larger error bars.

For an aerosol distribution that shifted by about 200 km to the south of the tangent point, the VOS at a tangent height of 19.5 km is no longer sensitive to scattering by the aerosol plume as shown in figure 8.3a. Thus, assuming horizontal homogeneity

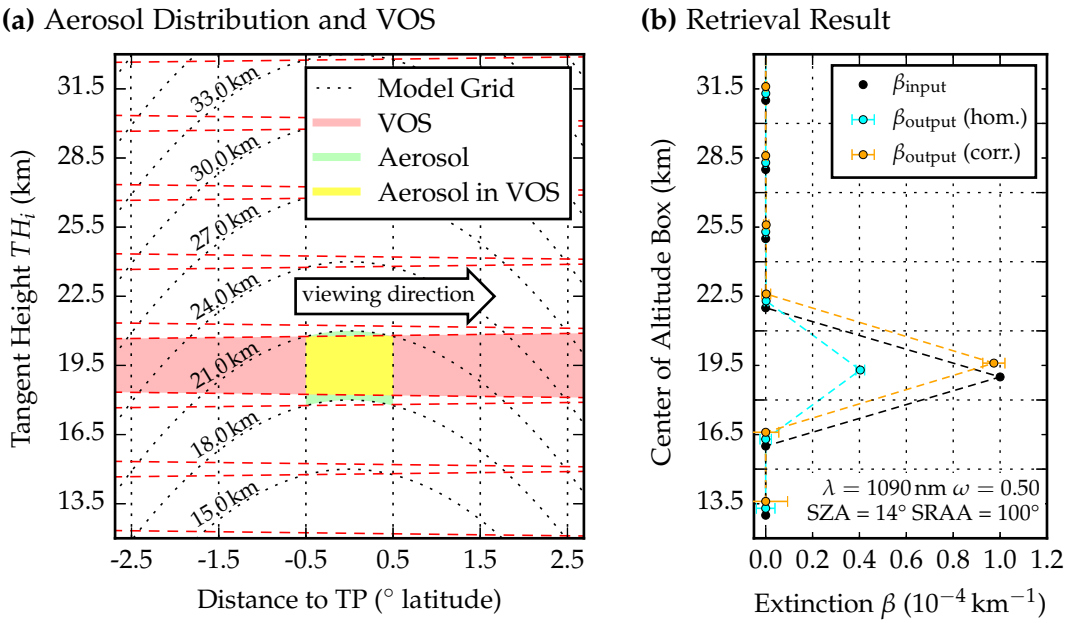

Figure 8.2: (a) shows a centered inhomogeneous aerosol plume between 18 and 21 km altitude similar to figure 8.1. Data points in (b) compare the profiles of β_{input} (black), the results for a homogeneous assumption (blue) and the results for the correct horizontal distribution (orange). The agreement between black and orange data points confirms the consistency of the 3D approach for inhomogeneous aerosol distributions.

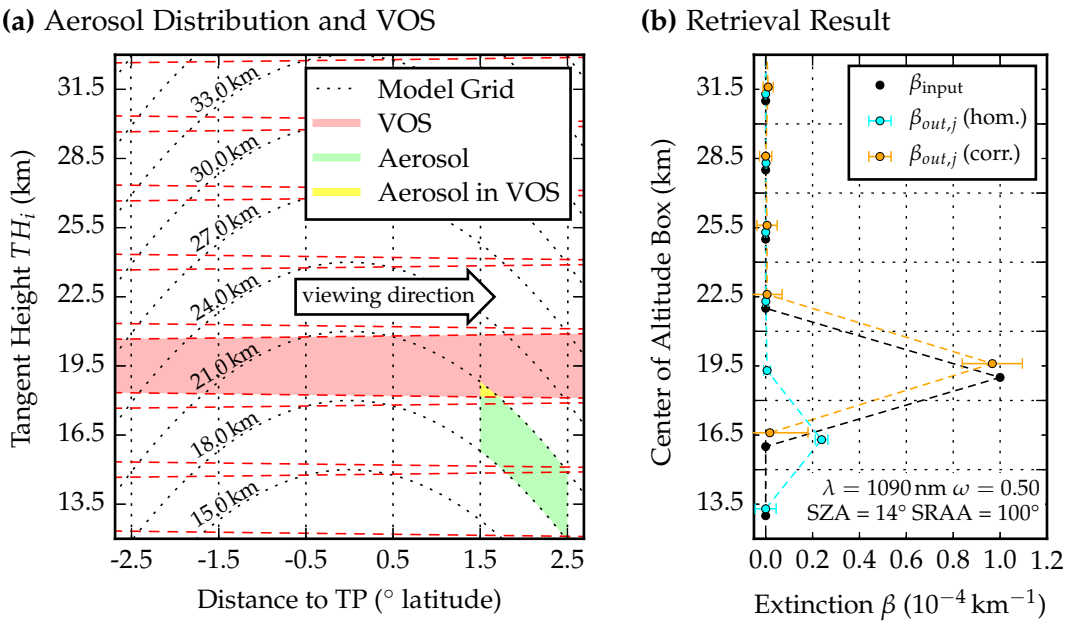

Figure 8.3: Similar to figure 8.2 for a general inhomogeneous aerosol layer between 18 and 21 km altitude that is not centered around the tangent point.

results in underestimated extinction and down-shifted layer altitude, see figure 8.3b. Results of the three-dimensional correction algorithm agree with β_{input} if the correct horizontal aerosol distribution is used. In order to retrieve the correct layer altitude it is important to determine which tangent height TH_i contains enough information to retrieve extinction at an altitude h_j as described in section 6.1.4 using equation 6.17. If each tangent height is sensitive to an altitude box within the retrieval domain (12 to 33 km), a one-by-one relation is found. This is however not the case for the off-centered plume. For an aerosol plume located 200 km south of the tangent point, a measurement at a tangent height of 10.5 km would be required to retrieve information on extinction at 13.5 km, according to figure 8.3a. Therefore, the retrieval algorithm cannot retrieve extinction for this altitude box. At the same time the measurement at a tangent height of 31.5 km is sensitive to altitude boxes outside of the retrieval domain above 33 km. As a result, this measurement is not used in the retrieval. The following table summarizes the relation between tangent height and altitude box found for this off-centered aerosol distribution.

Tangent Height of the measurement	Corresponding altitude (according to sensitivity)
31.5 km	-
28.5 km	31.5 km
25.5 km	28.5 km
22.5 km	25.5 km
19.5 km	22.5 km
16.5 km	19.5 km
13.5 km	16.5 km

Table 8.1: Relation between tangent height and altitude box for the case of off-centered horizontal inhomogeneity as depicted in figure 8.3. The relation is found using equation 6.17 as described in section 6.1.4.

This retrieval technique is applicable if the horizontal location of a plume can be retrieved from proxy data. For example, shortly after volcanic eruptions enhanced abundances of sulphate aerosol are correlated with its precursor SO_2. In this case, SO_2 vertical column densitys (VCDs), derived from SCIAMACHY measurements in nadir geometry, can be used as a proxy for the horizontal position of the fresh volcanic plume. In addition, an aerosol extinction profile under background conditions, i.e. without the plume, has to be assumed for the retrieval. Therefore, nearby measurements outside of the plume can be used, since stratospheric background aerosol is generally homogeneously distributed within a few hundreds of km. For the comparison of retrieval implementations of 1D and 3D approach, the aerosol extinction profile is derived in three different ways:

1D APPROACH: The retrieval algorithm implementation is used as described in section 6 assuming horizontal homogeneity.

3D APPROACH WITHOUT PROXY (HOMOGENEOUS): A background measurement is evaluated using the 1D approach. The resulting background aerosol extinction profile $\beta_{\text{background}}$ is then included into the RTM simulations as an additional scatterer with the same particle properties ($m = 1.405 + 0.000i$, $r_m = 80\,\text{nm}$, $\sigma = 1.6$). Now, the retrieval algorithm with three-dimension correction is applied assuming an infinite horizontal width which represents a homogeneous distribution. Accordingly, the algorithm will find $0\,\text{km}^{-1}$ extinction for all altitude boxes except for those where the measurement is affected by a plume. For the tangent heights which correspond to these altitudes, the measured radiance differs significantly from the background case and a extinction is retrieved. The retrieved extinction corresponds to a particle plume β_{plume}. The total extinction profile β is derived as the sum of $\beta_{\text{background}}$ and β_{plume}.

3D APPROACH WITH PROXY: For this method, after adding the background aerosol to the RTM calculation, the remaining particles are limited to the horizontal position determined by proxy information (e.g. SO_2 VCD). This results in an increased extinction for altitude boxes affected by the plume and might shift the sensitivity relation between tangent heights and altitude as shown in table 8.1, depending on the distance between plume and tangent point. As in the 3D approach without proxy, the total extinction β is the sum of $\beta_{\text{background}}$ and β_{plume}.

8.2 VOLCANIC AEROSOL: NABRO ERUPTION

During the night between 12$^{\text{th}}$ and 13$^{\text{th}}$ June 2011 the Nabro volcano (13.37 °N, 41.70 °E) started erupting. Besides CO_2, significant amounts of SO_2 and water into were injected the stratosphere [Theys et al., 2013]. One of the first investigations on perturbations in the stratospheric aerosol layer caused by this eruption shows the influence of the Asian monsoon transport on altitudes affected by the eruption [Bourassa et al., 2012b]. This work gave rise to a discussion on initial injection altitude and amount of early formed/injected stratospheric aerosol particles as reviewed by a variety of instruments, e.g. [Vernier et al., 2012a; Clarisse et al., 2014], and by using trajectory calculations [Fairlie et al., 2014]. SCIAMACHY was the first instrument providing height resolved information on the eruption plume about twelve hours after the eruption. Preliminary results of the retrieval technique introduced in section 8.1 are shown in Penning de Vries et al. [2014]. Figure 8.4 shows SCIAMACHY measurements in limb (color index, reddish colored dots) and nadir geometry (SO_2 VCD, gray shaded area) that were affected by the Nabro eruption between 13$^{\text{th}}$ and 16$^{\text{th}}$ June 2011. In the following, extinction profiles are used to track optical thickness and layer altitude of the volcanic plume.

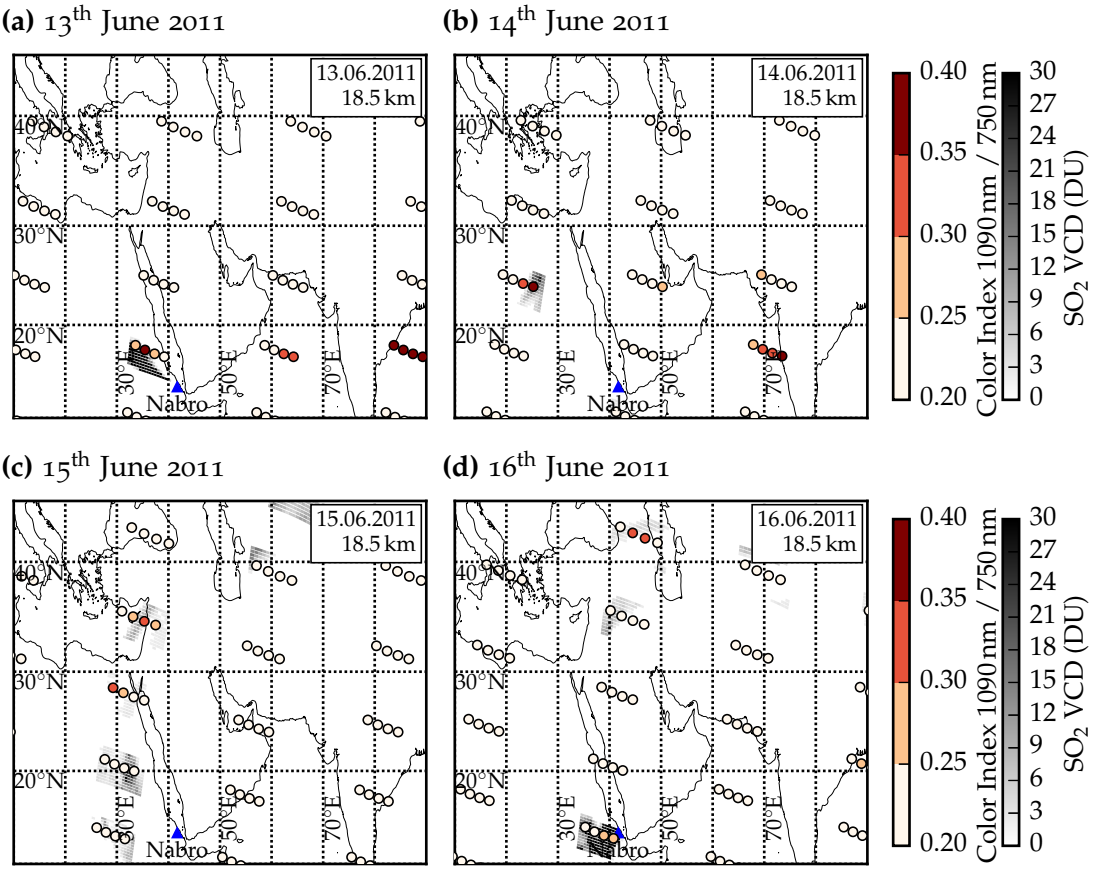

Figure 8.4: Color index and SO_2 vertical column density (VCD) derived from SCIAMACHY measurements in limb and nadir geometry for the region affected by the initial Nabro eruption plume between the 13th and 16th June 2013.

This case is very well suited for the application of the 3D correction method for various reasons: Due to the unique limb-nadir matching capability of SCIAMACHY, air masses measured in limb geometry are very well collocated with a measurement in nadir geometry taken only about 60 seconds later. Thus, SO_2 vertical column densities can be used as a proxy for the horizontal position and extent of the plume. For the first measurements of the volcanic plume on 13th June 2011, ice particles significantly contribute to the scattering signal as detected by MODIS IR cloud data [Fromm et al., 2012] and SEVIRI data [Vernier et al., 2012b] making the plume visible from space as shown in figure 8.5a. At the same time negative values of the UV Aerosol Index indicate that the plume does not contain strongly absorbing particles like volcanic ash [Penning de Vries et al., 2014]. On the 14th June, one day after the eruption, the plume is not visible in MODIS data which indicates that the ice particles vanished, see figure 8.5b. This is confirmed by an increased aerosol fine mode fraction without significant depolarization features measured at the joint MPLNET/AERONET (MicroPulse Lidar NETwork, Welton et al. [2001] and AErosol RObotic NETwork, Holben et al. [1998]) in Sede Boker,

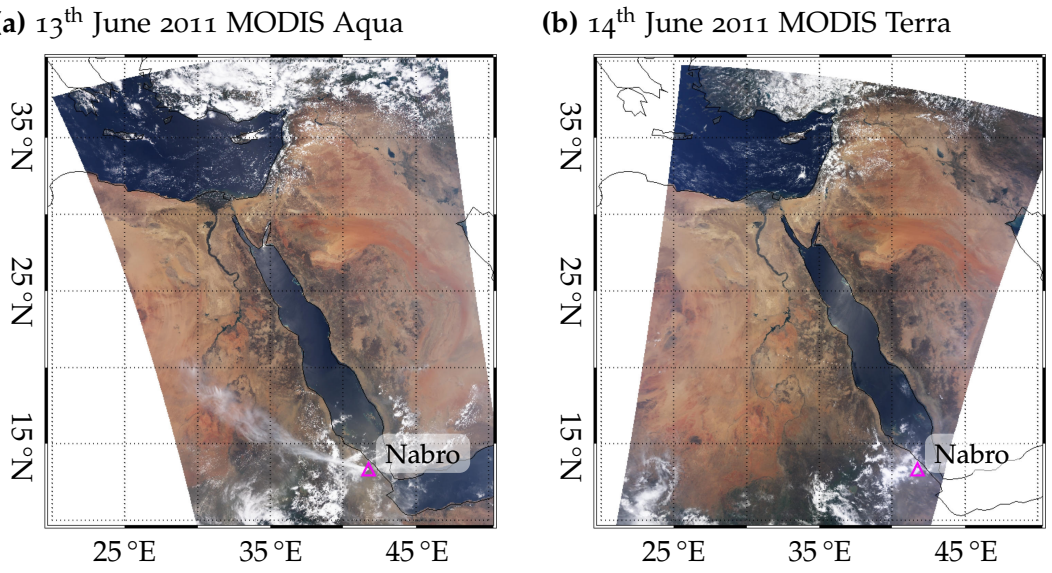

Figure 8.5: True color images from MODIS Aqua on 13th June 2011 8.5a and MODIS Terra on 14th June 2011 8.5b. Calibrated RGB data is provided by LAADS [2015].

Israel on 15th June. Therefore assumptions on particle shape and refractive index, defined in section 6, fit to particle properties that are expected for the volcanic plume. Aerosol size distributions derived from measurements with a balloon borne OPC [Deshler, 2008] indicate that, in general, the aerosol size distribution of sulphuric acid particles freshly formed after volcanic eruptions are usually represented by a two log-normal modes. While the first mode is similar to assumptions made in this thesis ($r_m = 80\,\text{nm}$, $\sigma = 1.6$), the second mode with radii around 200 nm is not represented in the SCIAMACHY retrieval algorithm. Since balloon borne measurements are not available for the Nabro plume, the assumed aerosol size distribution remains unchanged. The underestimation in particle size leads to underestimations of the extinction as shown in section 6.2.2.3.

In figure 8.6 results are compared for 1D approach, 3D approach assuming horizontal homogeneity (consistency check) and 3D approach using the horizontal distribution of the SO_2 VCD proxy as defined in section 8.1. In order to determine the region affected by the volcanic plume, the horizontal projection of the SCIAMACHY limb volume of sensitivity (VOS) at a tangent height of 19.5 km is overlaid by SCIAMACHY nadir measurements that show SO_2 VCDs above 2 DU, compare black outlined boxes in the left panel of figure 8.6a. Regions without significant enhancements in SO_2 VCD are displayed as gray boxes. Regions without gray or black boxes are not covered by SCIAMACHY nadir measurements on that day. Red shaded areas show the altitude of the LOS with a tangent height of 19.5 km within the model domain between 12 and 33 km, compare figure 6.3.

For the three-dimensional correction an aerosol extinction profile retrieved from a SCIAMACHY measurement on the 12th June is used as the background aerosol

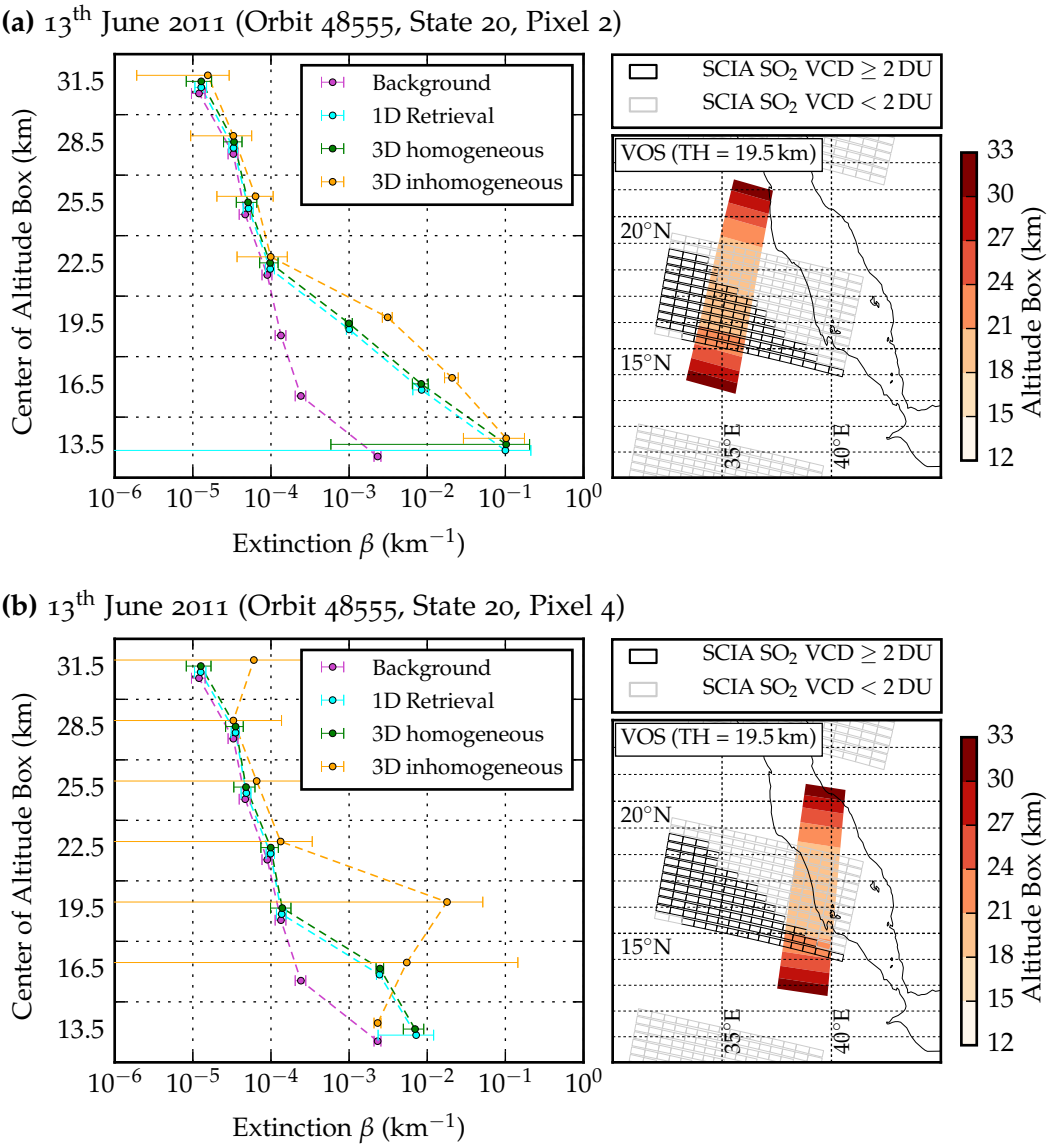

Figure 8.6: (left) Application of the 3D retrieval correction method that accounts for aerosol layer inhomogeneities along the LOS for two SCIAMACHY measurements on the 13th June 2011 compared to the 1D approach. (right) The horizontal distribution is determined by the overlap region of enhanced SO_2 VCD and volume of sensitivity of the measurement.

extinction profile (violet data points). The agreement between results of 1D approach (blue) and 3D approach using horizontal homogeneity (green) in figure 8.6 confirm that the background aerosol extinction profile is suitable for both measurements. In addition, the consistency of the implemented 3D correction algorithm is confirmed, according to the findings in section 8.1.

For the 3D correction method the aerosol particles are assumed to be homogeneously spread within the region marked by enhanced SO_2 VCDs. The aerosol

plume region covers the VOS south of the tangent point for latitude boxes from 14 °N to 17 °N for the first measurement, i.e. total plume width of about 300 km. Thus, the retrieved extinction profile shown in figure 8.6a (orange) is increased for altitudes between 15 and 21 km by about a factor of about two.

In the second measurement (Orbit 48555, State 20, Pixel 4) the volcanic plume only covers the southern most edge of the VOS from 12 °N to 14 °N. Following the color coding of the VOS, the plume only affects a measurement at a tangent height of 19.5 km, if it reaches higher than 21 km. Accordingly, enhanced values of aerosol extinction cannot be found at 19.5 km for the 1D approach in figure 8.6b. Using the horizontal distribution gained from SO_2 VCD proxy data, the retrieval results look similar to the first measurement in terms of plume altitude and integrated optical thickness. Here, the 3D approach with proxy yields similar results of the same plume for both pixels, in contrast to the 1D approach. This is a clear indication that the 3D correction method constitutes an improvement with respect to the 1D approach.

This correction method is highly susceptible to horizontal grid resolution and threshold value for the SO_2 VCD. However, the implementation of finer grid resolutions (in longitude and latitude) and/or a weighting algorithm for the horizontal aerosol distribution will be discussed in chapter 10. In addition it should be kept in mind that the retrieval results for this measurement may be heavily influenced by ice particles. Therefore values below the first box affected by the plume (18 km) are probably suffering from saturation problems and should be treated with care. However, the method to detect effects of saturation as defined in section 6.3.4 is only applicable for spherically shaped particles. Although saturation effects are not detected by the retrieval algorithm in this case, they cannot be ruled out.

One day after the eruption the plume tail is seen by SCIAMACHY measurements in limb and nadir above northern Africa (Fig. 8.7). The extinction for both measurements has decrease significantly compared to the previous day. This indicates that the majority of ice particles seen on 13th June has disappeared and the remaining signal mainly consists of sulfate aerosol.
While the plume spreads across the full VOS for the first measurement (Orbit 48570, State 19, Pixel 4) leaving the retrieved extinction unchanged with respect to the 1D approach, the SO_2 plume only covers about 60 % of the VOS in the second example (Orbit 48570, State 19, Pixel 3). In figure 8.7b, the enhancement of the retrieved extinction using the 3D approach would stronger for a longitudinally resolved plume distribution. For the latitudinal direction the plume extent and the underestimation of aerosol extinction are linearly correlated. If this finding can be applied to the longitudinal direction, the underestimation of aerosol extinction can be approximated to be roughly a factor of two in this case, since about 50 % of the VOS are covered by the plume in longitudinal direction. Applying this factor on the 3D corrected aerosol extinctions between 12 and 21 km, further improves the agreement between the retrieval results of both measurements, compare orange data points in figures 8.7a and 8.7b. Pixels 1 and 2 of state 19 west of pixel 3 are

(a) 14th June 2011 (Orbit 48570, State 19, Pixel 4)

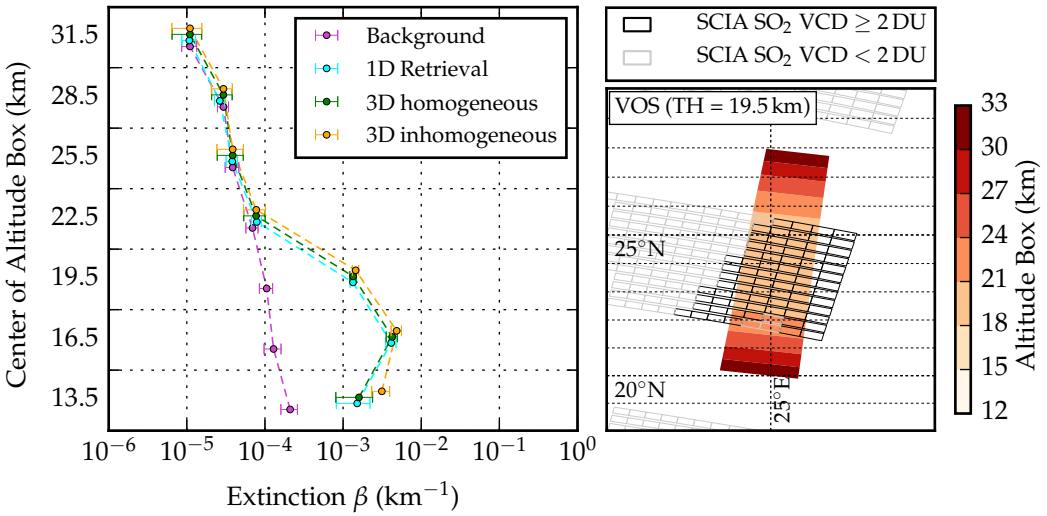

(b) 14th June 2011 (Orbit 48570, State 19, Pixel 3)

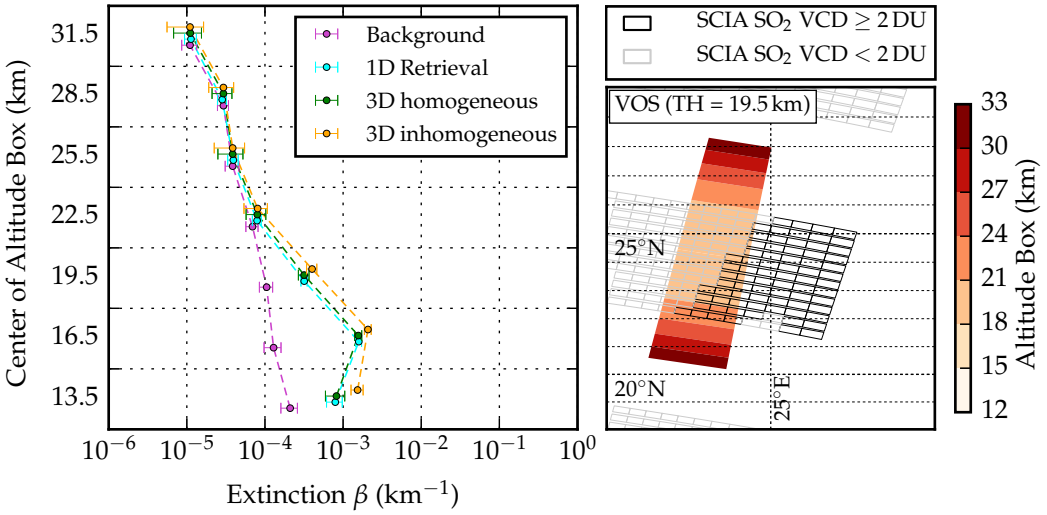

Figure 8.7: Two SCIAMACHY measurements on the 14th June 2011, as figure 8.6.

not affected by the volcanic plume according to the SO_2 data and therefore used as background aerosol profile.

On 15th June global pictures of SO_2 VCDs show a separation of the Nabro eruption plume into a fast moving northern branch at a higher altitude and a slow moving southern branch at a lower altitude [Penning de Vries et al., 2014]. This separation can also be seen for SO_2 VCDs in figure 8.8a. For the 3D correction, a measurement on the same day east of the plume was selected as background.

Similar to measurements on 14th June, the plume is homogeneously spread over the VOS for the first example (Orbit 48584, State 17, Pixel 4) and covers about 60 % of the VOS latitude range in the second example (Orbit 48584, State 17, Pixel 2), compare figure 8.8. However, trajectory analyses and ground based measurements

(a) 15th June 2011 (Orbit 48584, State 17, Pixel 4)

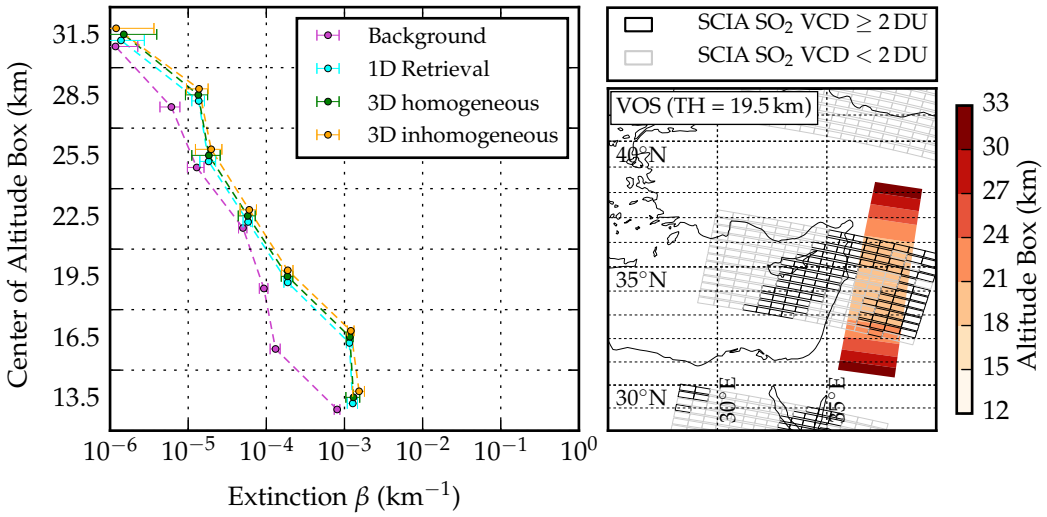

(b) 15th June 2011 (Orbit 48584, State 17, Pixel 2)

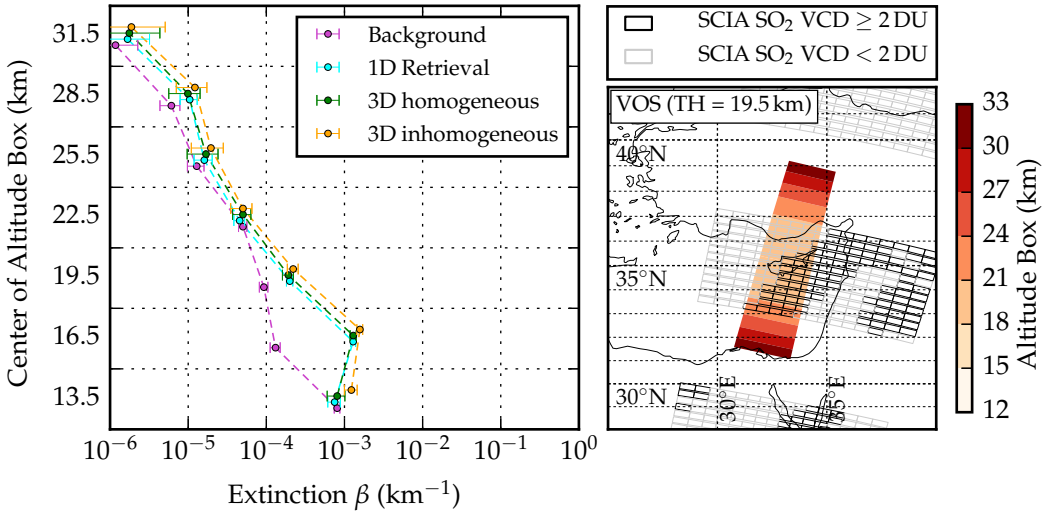

Figure 8.8: As figure 8.6 but for two SCIAMACHY measurements on the 15th June 2011.

at Sede Boker indicate that the southern plume is located at a much lower altitude. Therefore, using all latitude boxes within the area of enhanced SO_2 concentration might not be justified in this case. This shows the limitations of this proxy data set for cases where SO_2 plumes at different altitudes overlap horizontally.

In the following days the plume is picked up by strong westerly winds in the northern mid latitudes. The subsequent stretching of the plume leads to the reduction of its north-south extension to about 100 km as shown in figure 8.9.
With the plume stretching from west to east while remaining at the same latitude, the the plume can be assigned to one latitudinal grid box. The background aerosol extinction profile is the same as that used in figure 8.8. Figure 8.9a shows for the first case (Orbit 48598, State 16, Pixel 3) that the plume is almost centered around the

(a) 16th June 2011 (Orbit 48598, State 16, Pixel 3)

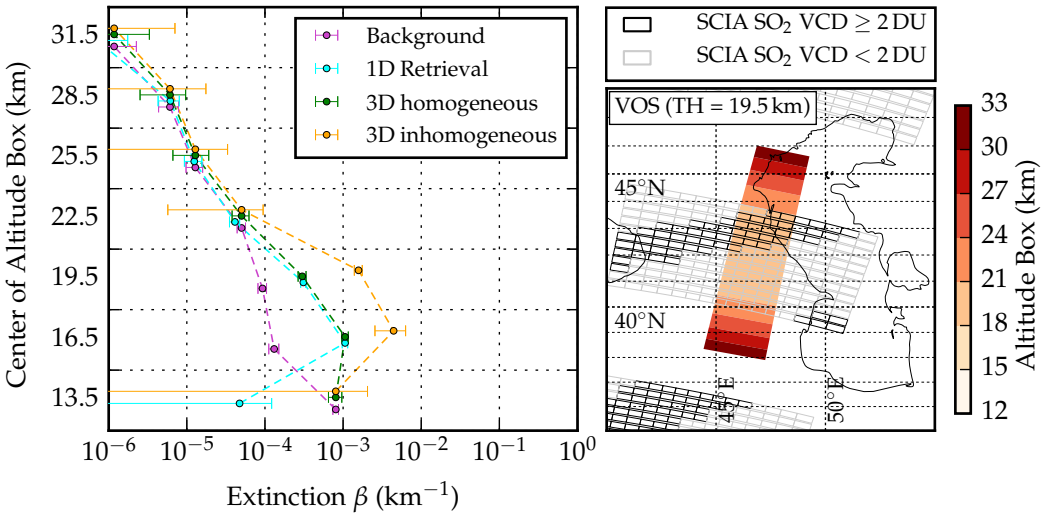

(b) 16th June 2011 (Orbit 48598, State 16, Pixel 4)

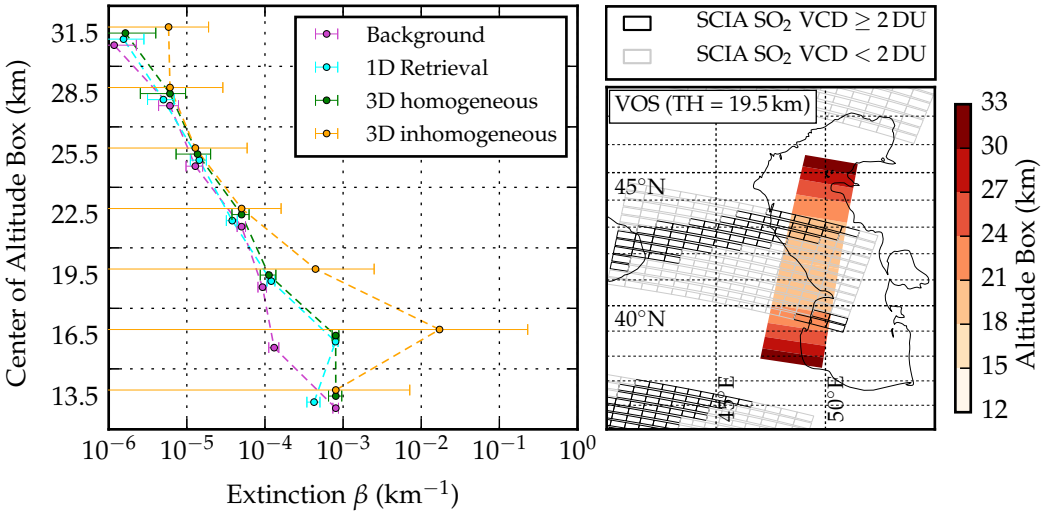

Figure 8.9: As figure 8.6 but for two SCIAMACHY measurements on the 16th June 2011 (Orbit 48598).

tangent point. As a result the plume altitude remains unchanged while the aerosol optical thickness increases by a factor of six after applying the 3D correction, similar to the example in figure 8.2. For the second case shown in figure 8.9b (Orbit 48598, State 16, Pixel 4) the plume is shifted to the north of the tangent point resembling the case study in figure 8.3. In comparison with the 1D approach, the plume altitude is shifted and the extinction increases for the altitude around 19.5 km. 3D corrected aerosol extinction profiles are comparable with results on the 14th with respect to plume altitude and aerosol optical thickness.

8.3 POLAR STRATOSPHERIC CLOUDS

In the southern polar region stratospheric temperatures around 20 km reach values below 188 K consistently in each winter season, creating environmental conditions for the formation of polar stratospheric clouds (PSCs), as introduced in section 2.3. At the end of the winter season in the southern hemisphere, the sun reaches further south which enables SCIAMACHY measurements of the polar stratosphere. Here, these measurements can be influenced by polar stratospheric clouds. Savigny et al. [2005] introduced a qualitative method of detecting PSCs that makes use of the color index method, as shown in section 5. In this section, the extinction retrieval algorithm is applied to measurements affected by polar stratospheric clouds (PSCs). As particle micro-physics vary significantly between different PSC types results of both methods have to be treated with care. While extinction profiles are heavily influenced by uncertainties in the scattering phase function, uncertainties in the identification of PSC altitude are generally not expected. Figure 8.10 shows that the color index is enhanced for some measurements close to the temperature contour at which PSCs can exist according to the scheme in section 2.3. Depending on the PSC type the temperature threshold is either 193 K for a supercooled ternary solution (STS, type Ib) or 195 K for nitric acid trihydrate (NAT, type Ia). Water ice PSCs are not considered for the shown measurements. If the temperature threshold is appropriate for the PSC detected in this case, strong gradients in particle abundance can be expected within the volume of sensitivity (VOS) of the SCIAMACHY measurement. This motivates the application of the 3D correction algorithm.

(a) Antarctic 12th September 2004, $T_{PSC} = 195\,K$

(b) Antarctic 12th September 2004, $T_{PSC} = 193\,K$

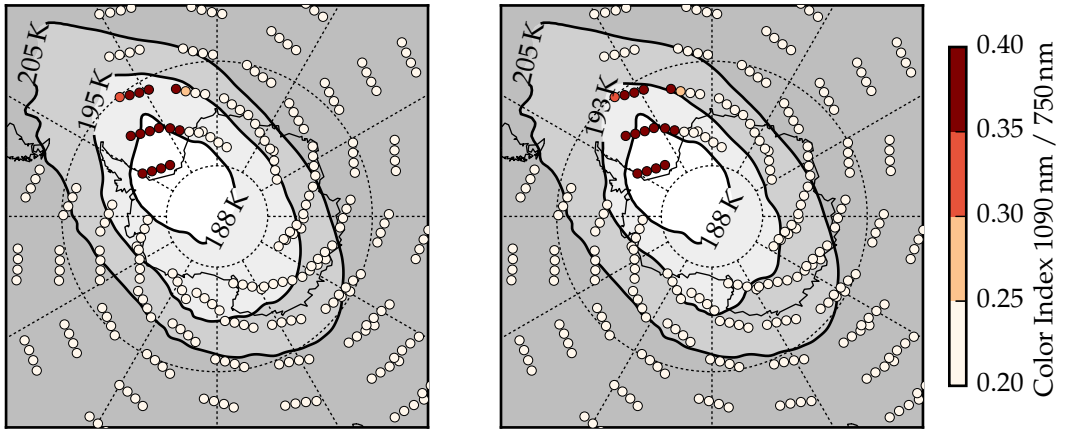

Figure 8.10: Color index values in the southern polar region derived from SCIAMACHY measurements with a tangent height of 18.5 km (circles) on 12th September 2004. ECMWF temperatures at an altitude of 18.5 km are displayed as gray contours. Area of possible PSC formation is indicated by the $T_{PSC} = 195\,K$ contour (a) and the $T_{PSC} = 193\,K$ (b), alternatively.

The following case studies focus on a comparison between a SAGE II measurement and three measurements of SCIAMACHY within the region of expected horizontal inhomogeneity. The background aerosol extinction profile used for all three cases was derived from a measurement at the same latitude region on the 16th September that is presumably not affected by PSCs. Effects of the 3D correction are investigated using ECMWF temperature contours at 193 K (PSC type Ib) and 195 K (PSC type Ia) as a proxy for the horizontal distribution. Similar to volcanic plumes in section 8.2, it is assumed that PSC properties like altitude and optical thickness do not vary significantly for neighboring measurements as long as they remain in the area of possible existence.

Results for the SCIAMACHY measurement with a tangent point (TP) location within a 250 km distance (collocation criterion used in section 7.1) of the SAGE II TP are shown in figure 8.11. SAGE II and SCIAMACHY extinction profiles show strongly enhanced values between 15 and 24 km as compared to the background profile. Above 24 km both data sets agree with the background profile.

If the 195 K contour is used as a proxy, the 3D correction does not affect the retrieved aerosol profile since most of the VOS is almost fully covered by the region of possible PSC existence. Using the 193 K contour for the horizontal distribution results in slightly increased extinctions for altitudes between 12 and 18 km. However, in both cases SAGE II and SCIAMACHY extinctions deviate significantly for altitudes up to 24 km. This may be due to uncorrected 3D effects on SAGE II retrieval results, but can also be caused by uncertainties in assumptions of aerosol properties for the SCIAMACHY results. According to figure 8.2 a 3D correction of the SAGE II results would enhance extinction values for all altitudes affected by the PSC further. This would further increase the deviations for altitudes below 21 km while deviations at 24 km would decrease. In terms of aerosol properties, figure 6.14b shows that underestimations in the assumed aerosol size distribution significantly decrease the SCIAMACHY retrieval result. However, the description of an appropriate aerosol size distribution for PSC particles requires much more detailed information on the PSC type. In addition, the Mie model used in the retrieval algorithm only applies to spherically shaped particles (PSC Type Ib). Following PSC properties described in section 2.3, PSC particles are generally larger than sulfate aerosol. Consequently, SCIAMACHY retrieval results, with the assumed properties of sulfate aerosol particles, underestimate the particle size. This results in an underestimation of the retrieved extinction by more than 50 %. Considering these uncertainties, both measurement results are in reasonable agreement.

In the next example the comparison study is performed for a measurement to the east where the influence of the 3D correction is expected to be stronger, since the VOS is not as much covered by the area of possible PSC existence, see figure 8.12b. Results are compared to the same SAGE II extinction profile as before. Extinction profiles retrieved from SCIAMACHY measurements using the 1D approach show increased values relative to the background profile up to an altitude of 21 km. When the 195 K contour is used as proxy for the horizontal distribution, the 3D correction only slightly affects the lowermost altitudes. After using the 3D correction method

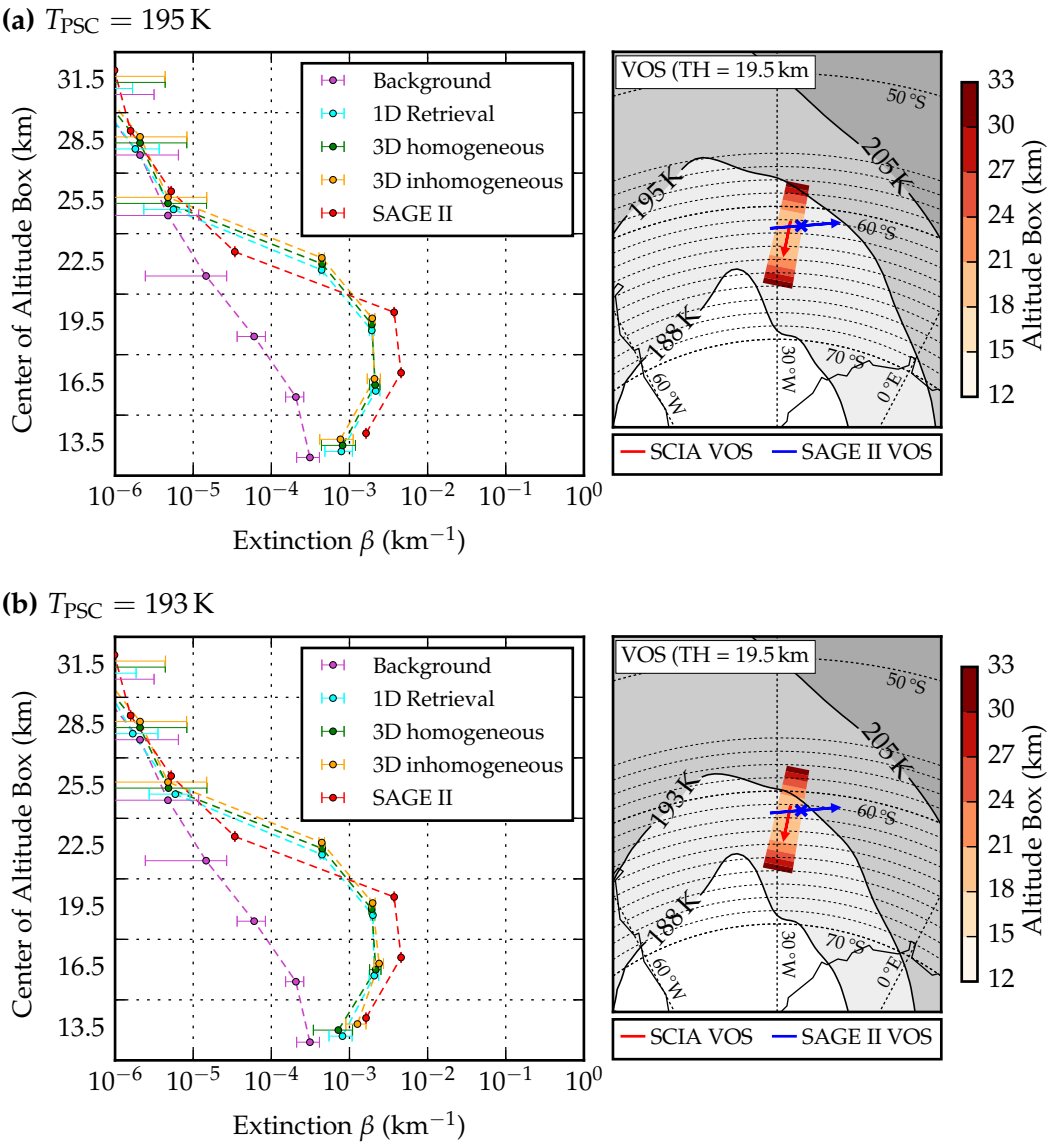

Figure 8.11: (left) Detection of increased extinction in the southern polar region on 12th September 2004 by SAGE II and SCIAMACHY indicating possible polar stratospheric clouds. (right) Different ECMWF temperatures at 19.5 km are used as proxy for the horizontal extent of the layer: 8.11a $T_{PSC} = 195\,K$ and 8.11b $T_{PSC} = 193\,K$. Blue colors indicate the volume of sensitivity (VOS) of SAGE II and red colors indicate the VOS of SCIAMACHY in a similar fashion as figure 7.1. Different shades of red depict the altitude of the SCIAMACHY VOS.

for a different proxy threshold of 193 K (2° further south), the results for profile shape and highest affected altitude are in much better agreement to the findings in figure 8.11.

For the third example shown in figure 8.13 the temperature contour is located even further to the south. Effects of the 3D correction are visible for using the 195 K

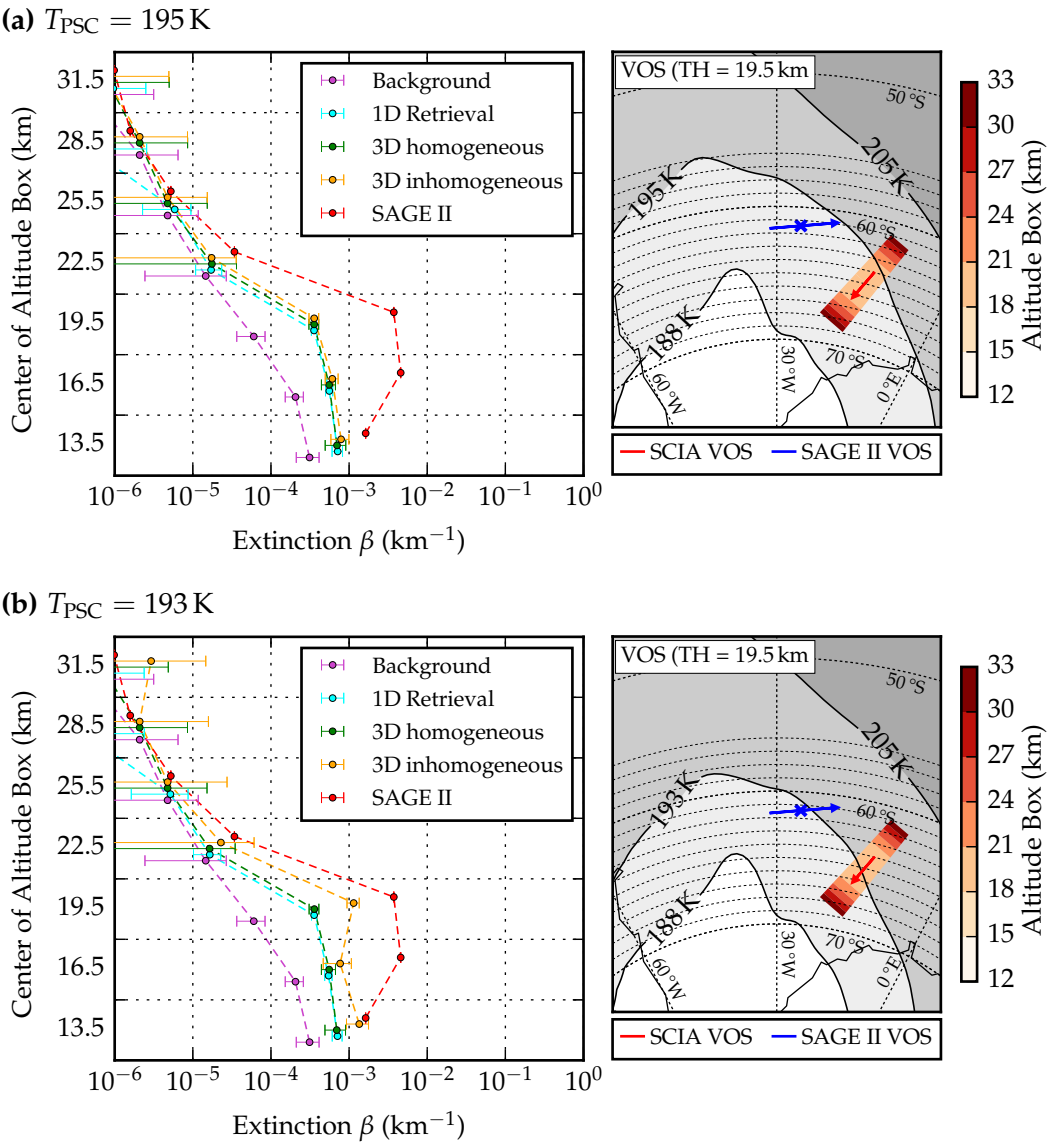

Figure 8.12: Same as figure 8.11 but for another measurement east of the SAGE II TP location where the temperature contour is further south increasing the importance of a three dimensional correction.

contour proxy, but still insufficient to create comparable results with the measurements in figures 8.11 and 8.12. This changes when applying the 3D correction using the 193 K temperature contour: Only the southern most edge of the VOS is within the assumed PSC area introducing a significant shift in altitude of the retrieved extinction profile. This results comparable to the extinction profile in figure 8.11 above 18 km. Below an altitude of 18 km the 3D correction failed since there is no measurement with information on the extinction of this altitude region—similar to the theoretical case discussed in figure 8.3.

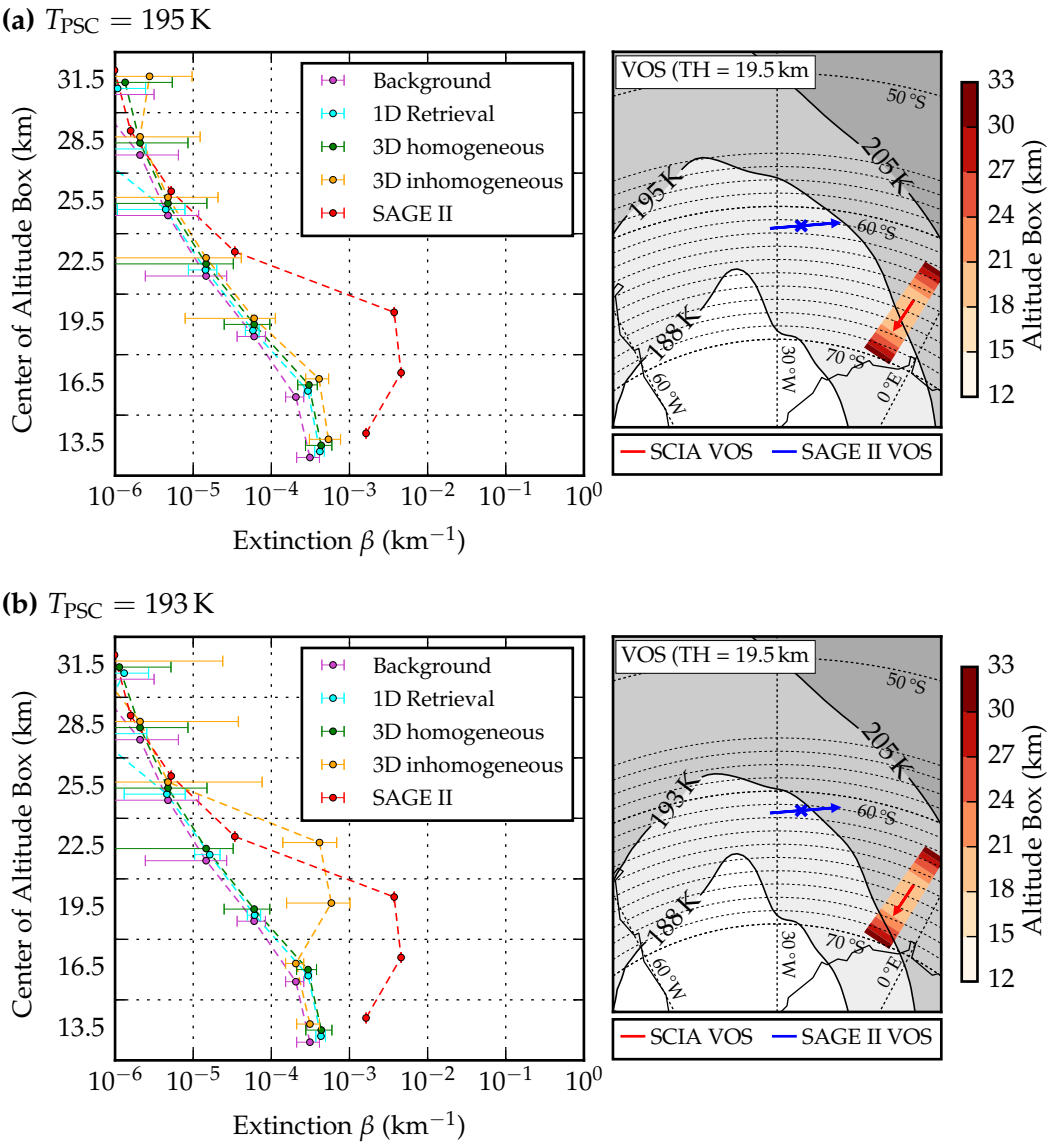

Figure 8.13: Same as figure 8.11 but for another measurement east of the SAGE II TP location where the temperature contour is at the edge of the SCIAMACHY VOS.

According to the PSC scheme described in figure 2.2 and to the temperature values from the ECMWF Interim model, the findings of this case study suggest a PSC of type Ib (STS). Considering the assumptions and uncertainties of the retrieval algorithm further investigations are needed to confirm this finding. Modifications on the retrieval algorithm in order to determine particle size and to account for particle sizes variations depending on altitude would provide a more consistent data set for such an investigation. This will be discussed in chapter 10.

8.4 SUMMARY

Horizontal inhomogeneities are neglected in all existing retrievals of aerosol extinction. However, measurements of volcanic plumes (narrow plume) and PSCs (strong gradient) show that horizontally resolved distributions need to be considered. The information gained from the 3D correction approach can also raise interesting questions: For the PSC case, with different assumptions for the proxy data, information on the PSC type can be obtained. Although it does not substantially affect the results for other retrievals of stratospheric aerosol extinction for the typical background case (e.g. Bourassa [2007] and Ernst [2013]), a proper representation of inhomogeneities within the VOS can be essential for the determination of the top altitude and optical thickness of particle layers with a small horizontal extent. However, it is important to recall that the vertical resolution of the SCIAMACHY instrument is limited. Even with a full 3D correction approach the layer altitude can only be determined with an uncertainty of up to 3 km. The availability of proxy data for the horizontal distribution is essential for performing a 3D correction. Especially when this method is applied to measurements of other instruments, which do not have collocated nadir and limb measurements, e.g. for OSIRIS or SAGE II.

9

SUMMARY AND CONCLUSIONS

This thesis introduces an algorithm for the retrieval of stratospheric aerosol extinction profiles at individual wavelengths from satellite measurements in limb geometry. The retrieval algorithm is developed for the SCanning Imaging Absorption spectroMeter for Atmospheric CHartographY (SCIAMACHY) on the ENVIronmental SATellite (ENVISAT), but may be adopted for the use with similar limb-viewing instruments, such as the Optical Spectrograph and InfraRed Imaging System (OSIRIS) and the Ozone Mapping and Profile Suite (OMPS). The algorithm utilizes the onion peeling method to iteratively retrieve aerosol extinction profiles with a vertical resolution of 3 km by comparing simulated and measured radiance profiles. For the simulations with a radiative transfer model, physical and especially optical properties of the atmosphere have to be assumed. Temperature, pressure and ozone profiles are provided by the ERA Interim simulations data set from the European Center for Medium-Range Weather Forecast (ECMWF). For information on surface albedo and tropospheric clouds, SCIAMACHY measurements in nadir geometry are used (Chapter 6).

Sensitivity studies are performed for the wavelengths 525, 750, 870 and 1090 nm for an altitude range between 12 and 33 km. It is shown that the retrieval of aerosol extinction becomes more challenging towards shorter wavelengths and lower altitudes. The sensitivity to scattering aerosol particles reduces for shorter wavelengths due to the strongly increasing contribution of scattering by molecules, in agreement with findings by Taha et al. [2011]. For lower altitudes the increase in air density enhances the radiance fraction that originates from scattering by molecules and therefore reduces the fraction that originates from scattering on aerosol particles. In consistency studies, aerosol extinction profiles are assumed for the simulation of radiance profiles which are then used as input for the retrieval algorithm. Deviations between input and retrieved extinction profiles are used to quantify the performance of the retrieval method. These tests show that the algorithm retrieves the synthetic aerosol extinction profile with deviations below 3 % for a wavelength of 1090 nm. For a wavelength of 525 nm deviation stay below 15 % in case of forward scattering and increase up to 50 % for backward scattering.

The application of the retrieval method to measurement data outlines strengths and limitations of the developed retrieval algorithm. Bourassa [2007] showed that the use of a normalization for measured radiances reduces the influence of uncertainties of the surface albedo and the effect of instrumental calibration issues. Accordingly, in the presented algorithm, the measured radiance profile is normalized by a measurement at a reference tangent height of 34.5 km. However, first applications to SCIAMACHY data showed that measured radiances at this tangent height are affected by scattering on aerosol particles. In addition, with increasing tangent height

the signal to noise ratio decreases and spatial straylight contributions increase which restricts the reference tangent height to 34.5 km. Accordingly, aerosol extinction for altitudes above 33 km cannot be retrieved from the measurement data. The required aerosol extinction at the reference tangent height is taken from a climatology derived from measurements by the second Stratospheric Aerosol and Gas Experiment (SAGE II) between January 2003 and December 2004.

SCIAMACHY measurements suffer from the contamination by spatial straylight which originates from imperfections on the scanning mirror [Gottwald and Bovensmann, 2010]. Initiated by the findings of their work, correction methods for the tangent height dependent effects of spatial straylight are developed and investigated in this thesis. For the spatial straylight correction method, SAGE II measurements in 2003 are used as shown in section 6.3.3. For these reasons, the presented retrieval results are not completely independent from SAGE II.

SCIAMACHY results are compared to SAGE II and balloon borne measurement in order to evaluate the performance of the retrieval algorithm. The comparison with SAGE II is performed at the wavelengths $\lambda = 525$ and $\lambda = 1090$ nm for a data set between January 2004 and April 2005. The time range is complementary to the data used for the spatial straylight correction. For measurements in the northern hemisphere, a good agreement between SAGE II and SCIAMACHY is found with deviations up to 10 % at $\lambda = 1090$ nm and up to 20 % at $\lambda = 525$ nm for altitudes between 18 and 27 km. These deviations are comparable to the results of other retrieval methods developed by Bourassa [2007] and Ernst [2013] and can partially be explained by altitude dependent variations of the aerosol size distribution.

In the southern hemisphere SCIAMACHY's viewing geometry leads to single-scattering angles above 90°. Here, the effect of uncertainties in the aerosol size distribution on SCIAMACHY results is much stronger. As a result deviations between SAGE II and SCIAMACHY increase to about 40 % at $\lambda = 1090$ nm in this hemisphere. For a wavelength of $\lambda = 525$ nm the retrieval does not converge at all for measurements with this scattering geometry due to a strong decrease in sensitivity to scattering on aerosol particles, see section 7.1.

For the comparison of SCIAMACHY retrieval results with aerosol extinction profiles derived from in-situ balloon borne measurements, a good qualitative agreement of the stratospheric aerosol profile shape is found. Satellite measurements are found to be systematically larger than the in-situ results by a factor of 2 to 3. A recent study shows that balloon borne measurement underestimate the aerosol extinction by about a factor of 2 [Kovilakam and Deshler, 2015]. Taking this into account, the results agree well within the uncertainties of the SCIAMACHY retrieval results.

While simple methods like the Color Index show that satellite measurements in limb geometry are in principle sensitive to particle scattering in the stratosphere, the quantification of the aerosol amount remains a challenging task. Aerosol extinction varies between 12 and 33 km over three orders of magnitude for background conditions and can increase by another two order of magnitude in the presence of polar stratospheric clouds or volcanic plumes. Comparisons to measurements from SAGE II show that the results of different retrieval methods that are applied

to limb measurements deviate by less than 60 %. These deviations are in the same order of magnitude as uncertainties caused by the assumptions of aerosol size, refractive index, tropospheric clouds, surface albedo, etc. used in these inversions. This indicates that the available spectral information should be used to its full extent in order to reduce the number of required assumptions, especially in terms of aerosol size distribution. A recent study by Rieger et al. [2014] shows first promising results for the retrieval of size information from measurements in limb geometry by the Optical Spectrograph and InfraRed Imaging System (OSIRIS).

Up to now retrieval algorithms for stratospheric aerosol extinction assumed a horizontally homogeneous particle distribution. This is a well justified assumption in a stratosphere that contains only background aerosol, but in the presence of polar stratospheric clouds or volcanic plumes strong gradients can occur. Simulations of horizontally inhomogeneous particle distributions suggest that the total amount of particles and the layer height are significantly underestimated if homogeneity is assumed. Therefore, a three-dimensional correction method is introduced and used for the investigations of volcanic plumes and polar stratospheric clouds. Results show that for the determination of plume altitude and particle abundance of volcanic plumes, the application of the three-dimensional correction is essential. However, the correction method strongly depends on the availability of information on horizontal gradients. In the given example, SO_2 vertical column densities measured in nadir geometry are used as proxy for the horizontal distribution of the volcanic plume. Running the three-dimensional correction greatly improves the consistency of retrieved extinction profiles in most cases. For the investigations of polar stratospheric clouds (PSCs) close to the edge of the polar vortex, typical temperature thresholds that indicate the existence of PSCs are chosen as proxy for the horizontal distribution. Here, the results of the three-dimensional correction were most consistent if a temperature threshold of 193 K was chosen. This indicates that the detected PSC probably consists of a supercooled ternary solution. For this investigation, uncertainties in the used temperature profile from the ECMWF ERA Interim data set and the altitude dependency of the formation temperature of PSCs, however, limit the accuracy three-dimensional correction method.

The general concept of a three-dimensional correction can be applied to any measurement in limb geometry as long as additional information on the horizontal distribution can be obtained. The application is more difficult for instruments like OSIRIS or the Ozone Mapping and Profile Suite (OMPS), since it depends on the availability of simultaneous measurements in nadir geometry. The PSC study showed that other data sets can also be used to define the horizontal distribution of an enhanced particle abundance.

Investigations and results of this thesis confirm, that SCIAMACHY measurements in limb geometry are well suited for the retrieval of vertically resolved information of aerosol extinction. Results of the applied onion peeling method are comparable to measurements of an balloon borne opticle particle counter and to SAGE II. For the presented retrieval algorithm a correction for spatial straylight is essential. Correction approaches are developed and compared in this thesis. In addition, a

correction method for three-dimensional effects was developed, which allows to retrieve the correct extinction and altitude of volcanic plumes and PSCs.

10

OUTLOOK AND RECOMMENDATIONS

The 8th of April 2012 marks the end of the SCIAMACHY measurements due to a loss of communications with the ENVISAT satellite after being in space for over ten years. Nowadays, the Optical Spectrograph and InfraRed Imaging System (OSIRIS) on the Odin satellite and the Ozone Mapping and Profile Suite (OMPS) on the Suomi National Polar-orbiting Partnership (Suomi NPP) satellite provide the only measurements in limb geometry but do not cover the full spectral range of the SCIAMACHY instrument. Future satellite missions covering this geometry are not planned, endangering the availability of a continuous record on vertically resolved stratospheric profiles of trace gases and particles. At the same time, more and new questions on the interactions between stratospheric dynamics and climate change arise, e.g. regarding recently found systematic changes in the concentration of trace gases like SF_6 and other sulfur containing species [WMO, 2014] and the stratospheric aerosol particle abundance [Solomon et al., 2011].

With this uncertain future of satellite measurements in limb geometry it becomes even more important to make the best use of available data. Perhaps surprisingly, even after ten years of operational SCIAMACHY measurements, fundamental problems like spatial straylight are still not fully understood and characterized. This results in large potential uncertainties especially for measurements at longer wavelengths and higher altitudes. This thesis shows that retrieving information on stratospheric aerosol particles from satellite remote sensing in limb geometry is a challenging task due to several assumptions and approximations. However, satellite measurements ranging from the UV to the NIR spectral range provide valuable information to reduce the number of assumptions: For example, the wavelength dependency of aerosol extinction as retrieved from SCIAMACHY measurements contains information on the aerosol size distribution and thus on the phase function. Further refinements can improve the consistency of this data set as needed for a well founded discussion on scientific questions. In case of the Nabro volcano a few kilometer difference in initial injection height are relevant to decide if a new process of lifting aerosol particles into the stratosphere by the Asian monsoon as suggested by Bourassa et al. [2012b] is necessary to explain the observed abundances of sulfate aerosol in the stratosphere or if known processes are sufficient to explain this observation.

Possible improvements of the retrieval algorithm will be discussed in section 10.1. Section 10.2 will describe possible applications of the retrieval results.

10.1 IMPROVEMENTS OF THE RETRIEVAL ALGORITHM

This section discusses optimizations of existing features like the spatial straylight correction. In addition, possible new features resulting from the findings in this thesis, will be discussed.

10.1.1 *Aerosol Size Distribution*

In the current version of the retrieval algorithm scattering phase functions are calculated for a spatially and temporally constant log-normal aerosol size distribution with a mean radius of 80 nm and a distribution width of 1.6. In section 7.2 the variability of the aerosol size obtained from balloon borne measurements with an optical particle counter are shown for the background aerosol during volcanic quiescent periods. Deshler [2008] suggests an even stronger variation for phases of increased volcanic disturbance. Especially in the northern hemisphere where SAGE II and SCIAMACHY results mostly agree as shown in figure 7.8, remaining deviations can be explained by an altitude dependence of the aerosol size distribution. The retrieval algorithm would greatly benefit from the use of height resolved aerosol size distributions. It was not implemented in the current version, since the required climatologies are insufficiently known.

Retrieving aerosol extinction at various wavelengths (525, 750, 870 and 1090 nm) provides information on the aerosol size distribution, e.g. by the derivation of the Ångström exponent. In section 6.2.2.3, detailed studies on the assumed size distribution indicate a certain ambiguity of this information: Multiple different aerosol size distributions can lead to similar retrieval results. However, a method to retrieve aerosol particle size parameters was investigated and successfully implemented for OSIRIS measurements for single mode log-normal distributions with a constant distribution width of $\sigma = 1.6$ [Rieger et al., 2014]. The authors of that work suggest that the use of measurements in the near infra red around 1.5 µm are needed for a robust retrieval of particle size parameters. The retrieval algorithm presented in this thesis is only restricted to wavelengths that are not influenced by atmospheric absorbers. Also, SCIAMACHY's spectral range reaches wavelengths of up to 2.4 µm. Therefore, the full retrieval of size parameters, at least for a single mode log-normal distribution should be possible.

10.1.2 *Spatial Straylight Correction*

In section 6.3.3 a method is introduced to correct for light that is being diffracted into the field of view of the SCIAMACHY instrument by residual grooves on the telescope mirror. This kind of straylight is referred to as spatial straylight. With the Sun and the Earth as possible sources for spatial straylight, a dependency on tangent height, solar zenith angle and effective albedo, i.e. surface albedo and cloud influence, is expected. However, the statistics for the time range used for

the determination of a spatial straylight correction (January to December 2003) are merely sufficient to derive the elevation angle (tangent height) dependency of spatial straylight. Only about 20 % of the available measurements in 2003 fulfilled the criteria to be considered for the straylight analysis. Therefore, filter criteria as well as the intensity comparison between simulation and SCIAMACHY measurement should be re-investigated. Height resolved size distributions, as discussed in section 10.1.1, will affect these comparisons. A possible improved spatial straylight correction should make use of information from other data sources like for example model simulations.

10.1.3 *3D Correction Method*

So far the 3D correction method is only implemented for horizontal variations in latitudinal direction. Depending on the available proxy data used to define the horizontal extent of an aerosol layer, the calculation grid used for the retrieval algorithm needs to be refined in order to implement a full 3D retrieval. This can be achieved without changing the basic approach of the correction method. A case study investigating the plume of the Nabro eruption showed that the 3D correction method would also greatly benefit from the use of weighting functions for the aerosol distribution. For example, instead of using a SO_2 threshold to decide which regions are affected by a volcanic plume, the SO_2 distribution can be used to derive a 2D weighting function for the horizontal distribution of the aerosol.

In addition, this correction is not constraint to the retrieval of aerosol extinction SCIAMACHY measurements. The incorporation of a correction for the effects of horizontal inhomogeneity would also benefit other instruments like SAGE II, OSIRIS or OMPS.

10.1.4 *Computational Efficiency Optimization*

Radiative transfer simulations for the retrieval algorithm are performed by the full spherical 3D Monte Carlo radiative transfer model McArtim (see section 4). While the use of the Monte Carlo method enables the use of three-dimensional distributions of trace gases and scatterers, it is computationally demanding. In this thesis the retrieval algorithm was run in parallel on a computer cluster at the Max Planck Institute for Chemistry using up to 40 cores. With this setup the algorithm needed about 36 h to derive aerosol extinction for about 2500 SCIAMACHY measurements at four wavelengths corresponding to all collocations found between SCIAMACHY and SAGE II between January 2003 and April 2005 (see section 7.1). With the current set up, the retrieval would need about 8 years to evaluate the full SCIAMACHY data set. Methods to optimize computational efficiency, like the use of look up tables, have not yet been tested and might not be viable due to the strong non-linearity of the problem. It could however be reasonable to derive and apply look up tables for cases of an undisturbed stratospheric background aerosol profile with extinctions

below $10^{-3}\,km^{-1}$. Here, the retrieval can be linearized as shown in section 6.1.3. Cases of increased aerosol extinction can be identified using the color index method explained in section 5 and run with online calculations. This way the full data set could be evaluated within a more realistic time frame. For 1D applications other RTM like SCIATRAN [Rozanov et al., 2014] or LIDORT [Spurr, 2008] might be used.

10.2 FURTHER APPLICATIONS

There are two main applications for the retrieved stratospheric aerosol extinction retrieval:

- Information on the variability of stratospheric aerosol concentration and its microphysical properties is interesting in itself, e.g. for the determination of radiative effects and effects on heterogeneous chemistry in the stratosphere.
- Knowledge on aerosol properties and extinction along the line of sight of a SCIAMACHY measurement in limb geometry can be used to improve existing trace gas retrievals of NO_2, BrO and OClO that use those measurements [Kühl et al., 2004, 2008; Puķīte, 2010].

Detailed knowledge on the aerosol distribution does not only improve trace gas retrievals, it is can also improve climate models. Case studies in sections 8.2 and 8.3 show that the results of this thesis contribute to the understanding of formation processes of sulfate aerosol and polar stratospheric clouds. Extinction profiles derived from limb observations are also well suited for gaining information on the altitude of plumes which originated from volcanic eruptions or biomass burning. The knowledge on the temporal development of the global stratospheric aerosol distribution can also be used to draw conclusions for dynamic properties of the stratosphere like the Brewer Dobson circulation or the variation of stratospheric transport barriers, like shown in Puķīte [2010]. The investigation on how sulfate aerosol distributions in the stratosphere might affect the ozone chemistry is especially important for discussions on geo-engineering. Recent studies show, that chemical species known as very short lived substances which do not greatly affect ozone chemistry under current conditions, can have a much larger impact in a scenario of increased sulfate aerosol abundance [Tilmes et al., 2009]. Therefore, it is necessary to monitor variations in the stratospheric aerosol abundance continuously with a good spatial and temporal coverage.

Part III

APPENDIX

APPENDIX

A.1 SENSITIVITIES OF THE RADIANCE-EXTINCTION GRADIENT

In this section example of the multi-dimensional dependency of the radiance-extinction gradient γ are given.

Figure A.1: The radiance-extinction gradient γ for tangent height of 22.5 km at an altitude of 22.5 km ($\beta = 0\,\mathrm{km}^{-1}$, referred to as γ_0) is affected by aerosol layers above 24 km (reddish, dashed) depending on the respective aerosol extinction. Aerosol layers below 21 km (blueish, solid) do not affect γ significantly.

(a) Albedo Dependency

(b) Wavelength Dependency

Figure A.2: Dependency of the radiance-extinction gradient γ on effective albedo (a) and wavelength (b).

Figure A.3: Dependency of the radiance-extinction gradient γ on the single scattering angle ξ.

A.2 EXTENDED ANALYSIS OF SENSITIVITY TO AEROSOL SIZE DISTRIBUTION

(a) Forward scattering geometry: $\xi = 44°$

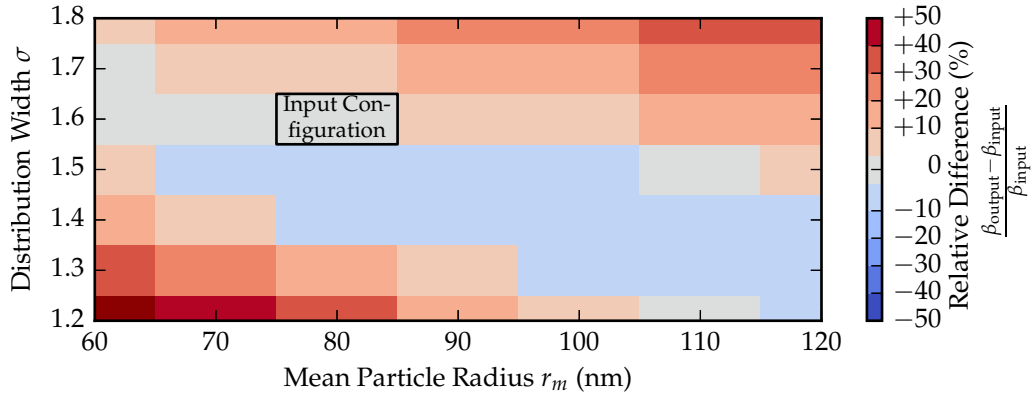

(b) Sideward scattering geometry: $\xi = 92°$

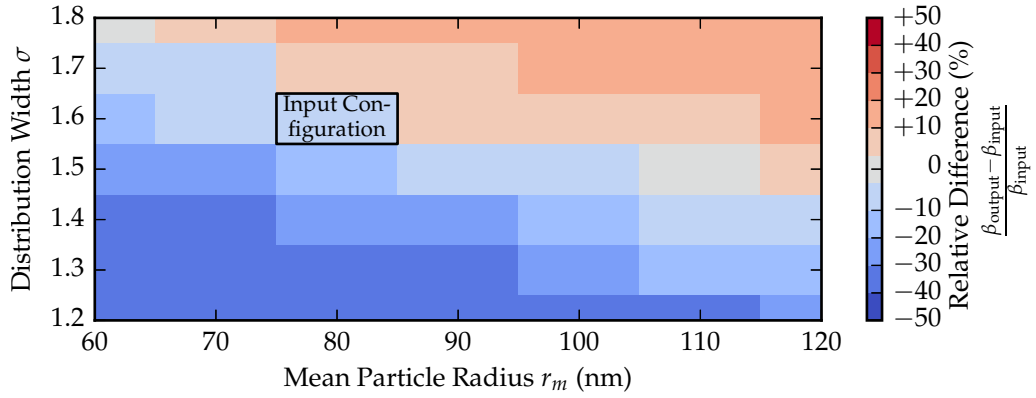

(c) Backward scattering geometry: $\xi = 143°$

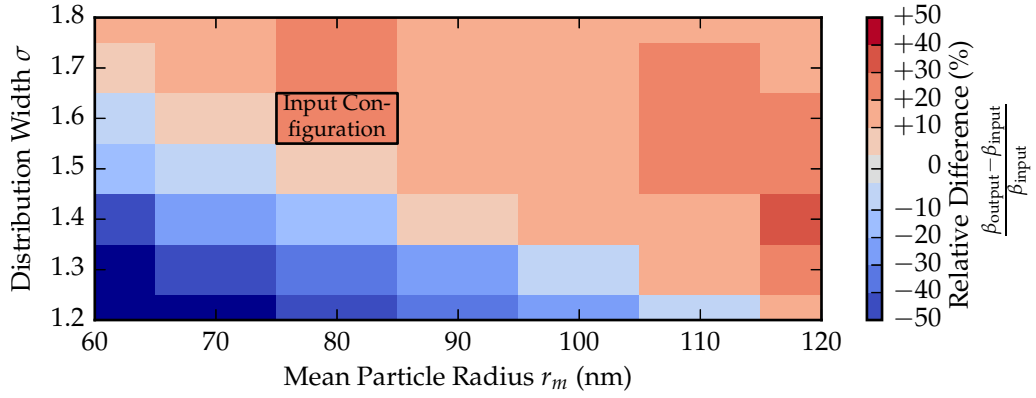

Figure A.4: Figure description was moved to figure A.5 due to lack of vertical space. This figure shows the same but for a of wavelength $\lambda = 525\,\text{nm}$.

(a) Forward scattering geometry: $\xi = 44°$

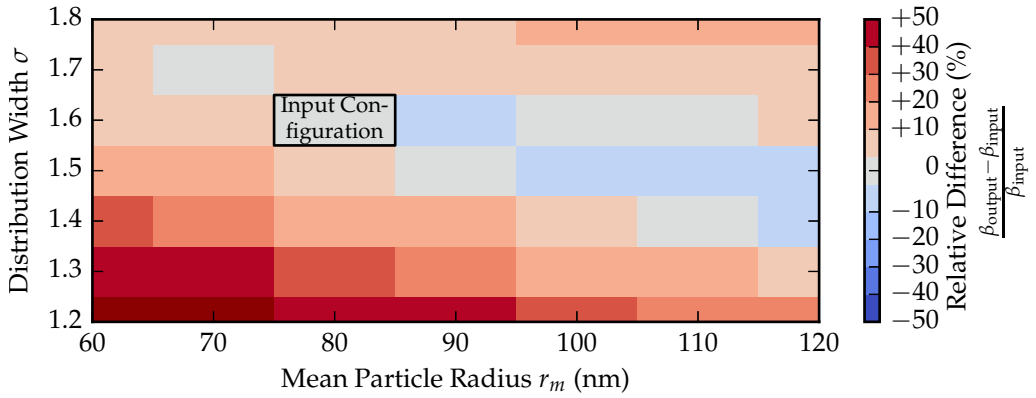

(b) Sideward scattering geometry: $\xi = 92°$

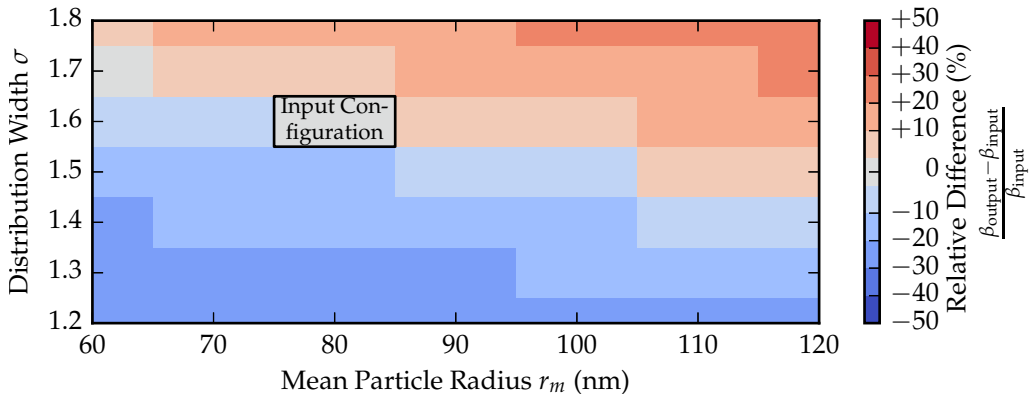

(c) Backward scattering geometry: $\xi = 143°$

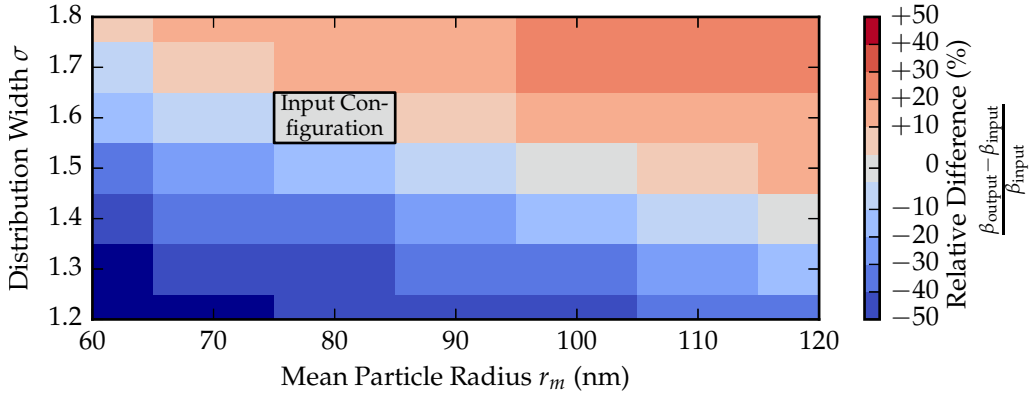

Figure A.5: Sensitivity to uncertainties in the aerosol size distribution for $\lambda = 750\,\text{nm}$ for different single-scattering angles ξ: 44°, 92° and 143°. The center of each bin represents the size distribution that was used for the retrieval algorithm. For the simulation of the input radiance profile a size distribution with a mean radius of $r_m = 80\,\text{nm}$ and a distribution width $\sigma = 1.6$ was used as indicated by the input configuration box. Colors indicate the deviation between β_{input} and β_{output} with red for an overestimation and blue for an underestimation with respect to the input extinction profile β_{input}. In some cases input configuration box is not gray, which indicates that deviation between β_{input} and β_{output} is not zero despite using the input configuration in the retrieval algorithm. Here, the retrieval algorithm is not consistent. These cases are discussed in section 6.2.

(a) Forward scattering geometry: $\xi = 44°$

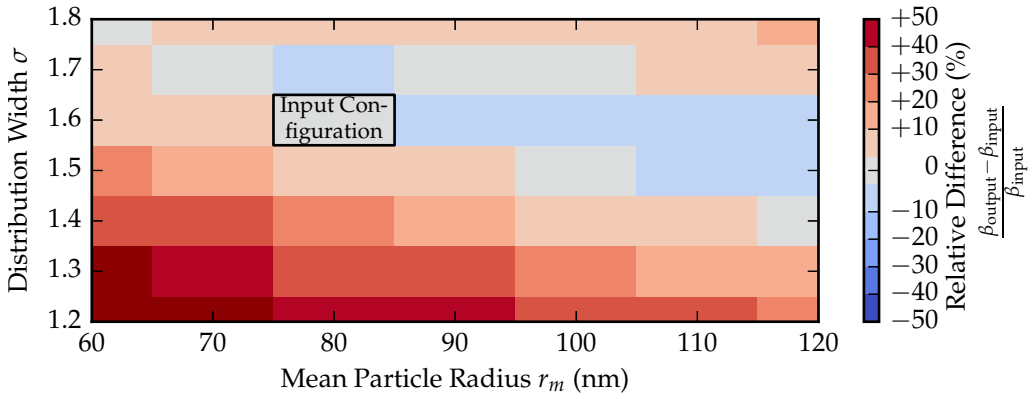

(b) Sideward scattering geometry: $\xi = 92°$

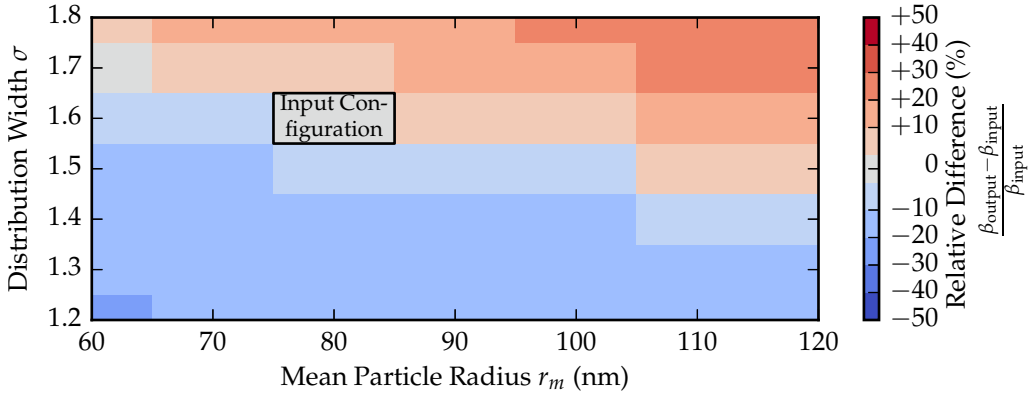

(c) Backward scattering geometry: $\xi = 143°$

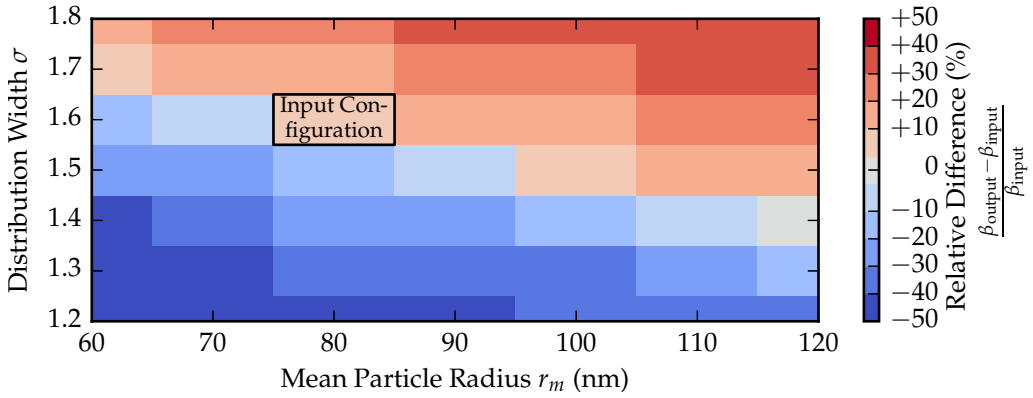

Figure A.6: As figure A.5, but for a of wavelength $\lambda = 870\,\text{nm}$.

A.3 SAGE II COLLOCATIONS - ERROR ANALYSIS

The following maps of SAGE II and SCIAMACHY collocations describe the occurrence of retrieval flags, as defined in section 6.3.4, for the wavelengths 525, 750 and 870 nm after applying a constant correction factor. According to findings of the comparison between SCIAMACHY and SAGE II in section 7.1, the number of measurements influenced by the problem of negative extinctions decreases with increasing wavelength. In general, higher wavelengths are less susceptible to uncertainties in the assumption of spatial straylight correction, aerosol extinction at the reference tangent height and scattering phase function, due to a increasing sensitivity to aerosol extinction. Errors caused by negative measured radiance or simulation timeout are consistent for all wavelengths. The maps are summarized in figure A.10.

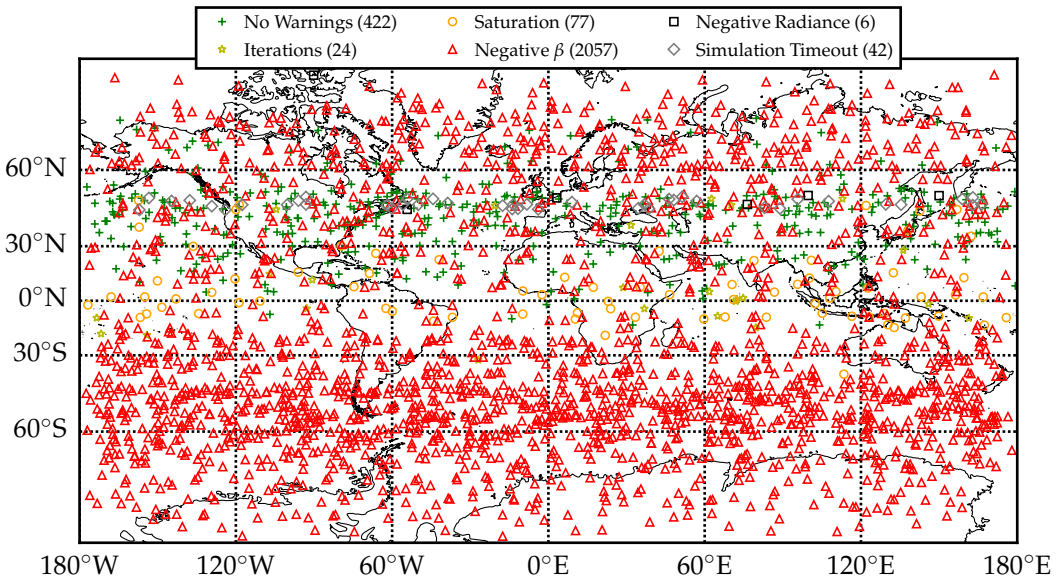

Figure A.7: As figure 7.3a after applying a constant spatial straylight correction profile for measurements at 525 nm.

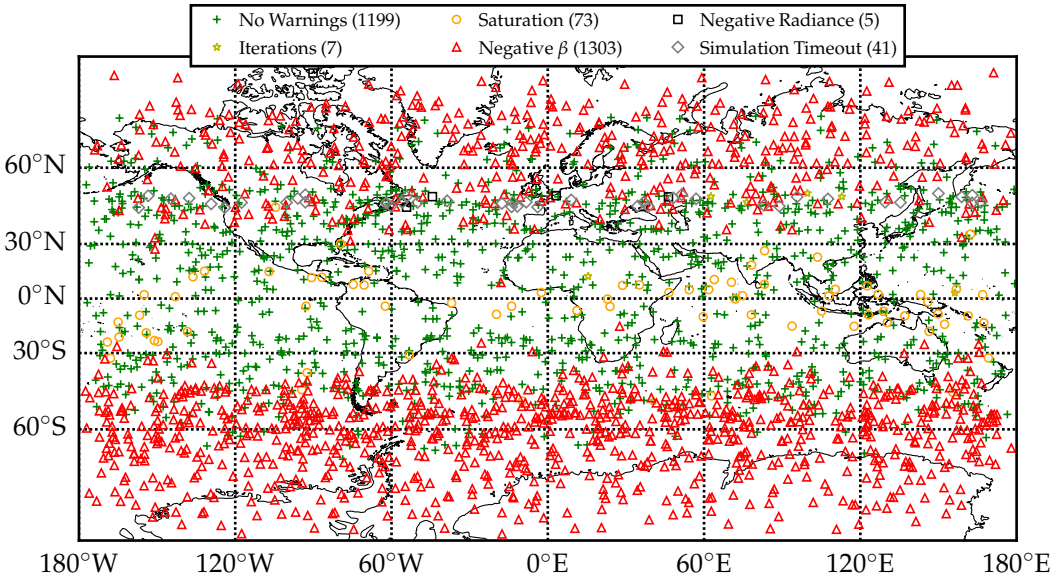

Figure A.8: As figure 7.3a after applying a constant spatial straylight correction profile for measurements at 750 nm.

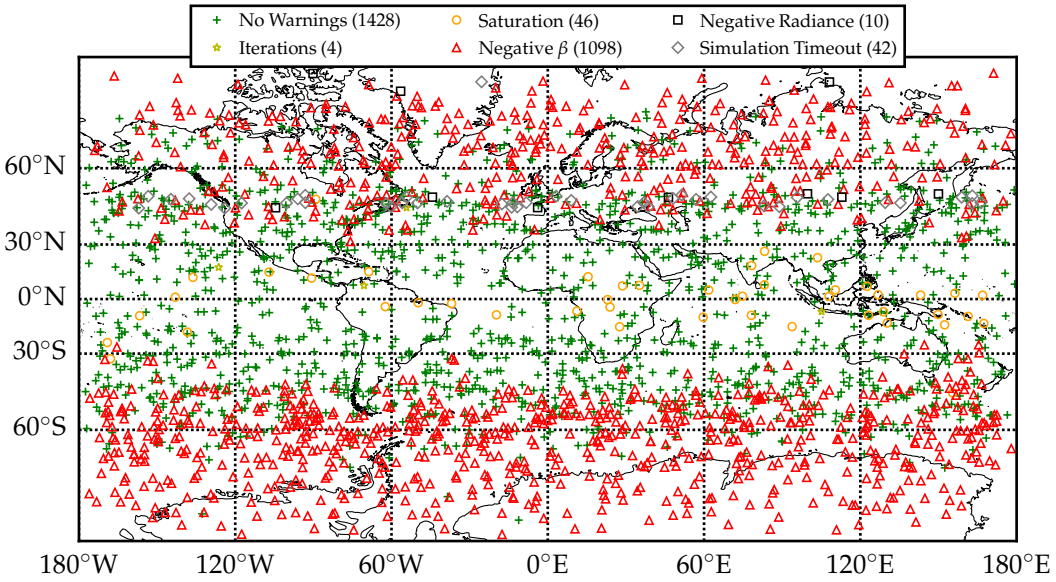

Figure A.9: As figure 7.3a after applying a constant spatial straylight correction profile for measurements at 870 nm.

(a) Unfiltered Spatial Straylight Correction

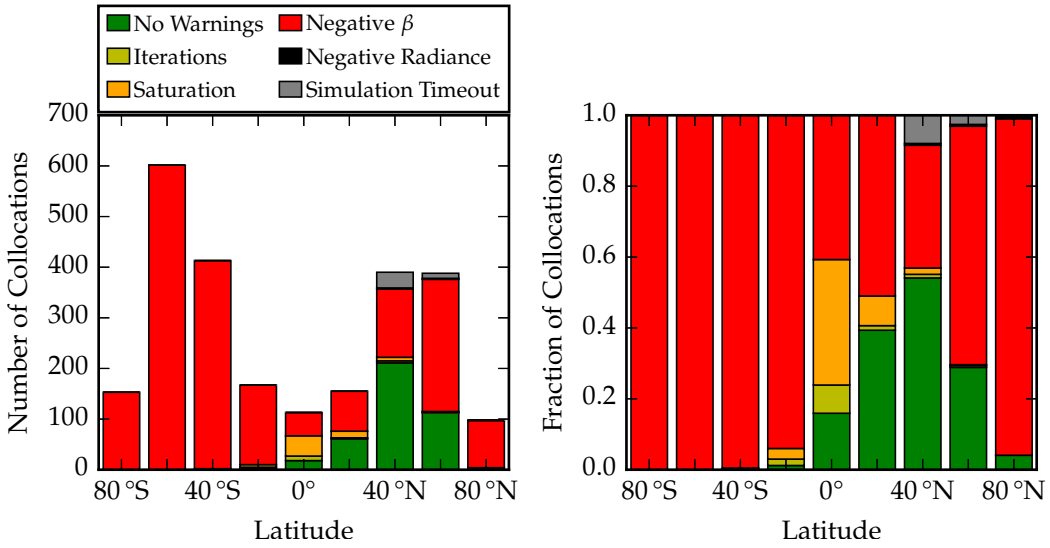

(b) Extrapolated Spatial Straylight Correction

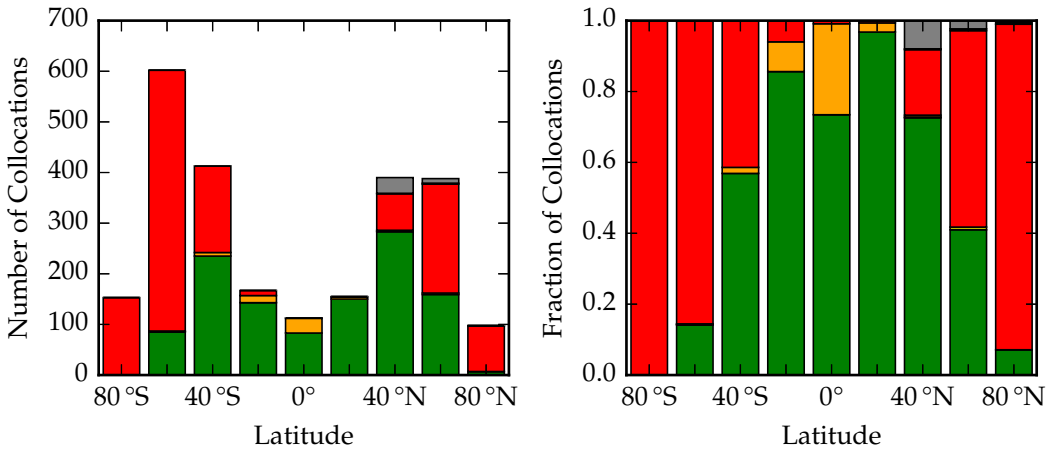

(c) Constant Spatial Straylight Correction

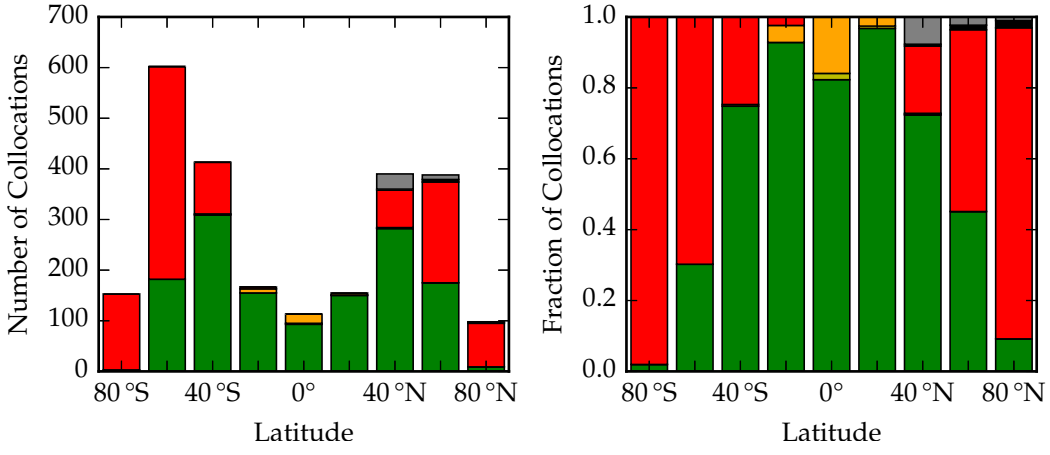

Figure A.10: Same as figure 7.6, but in addition for the wavelengths $\lambda = 750\,\text{nm}$ and $\lambda = 870\,\text{nm}$.

A.4 EXTENDED SAGE II COMPARISON

In order to improve statistics for the comparison between SAGE II and SCIAMACHY aerosol extinction performed in section 7.1, results without spatial straylight correction are removed. While the number of collocations without retrieval errors or warnings significantly increases, found deviations are comparable to findings in figures 7.8 to 7.11.

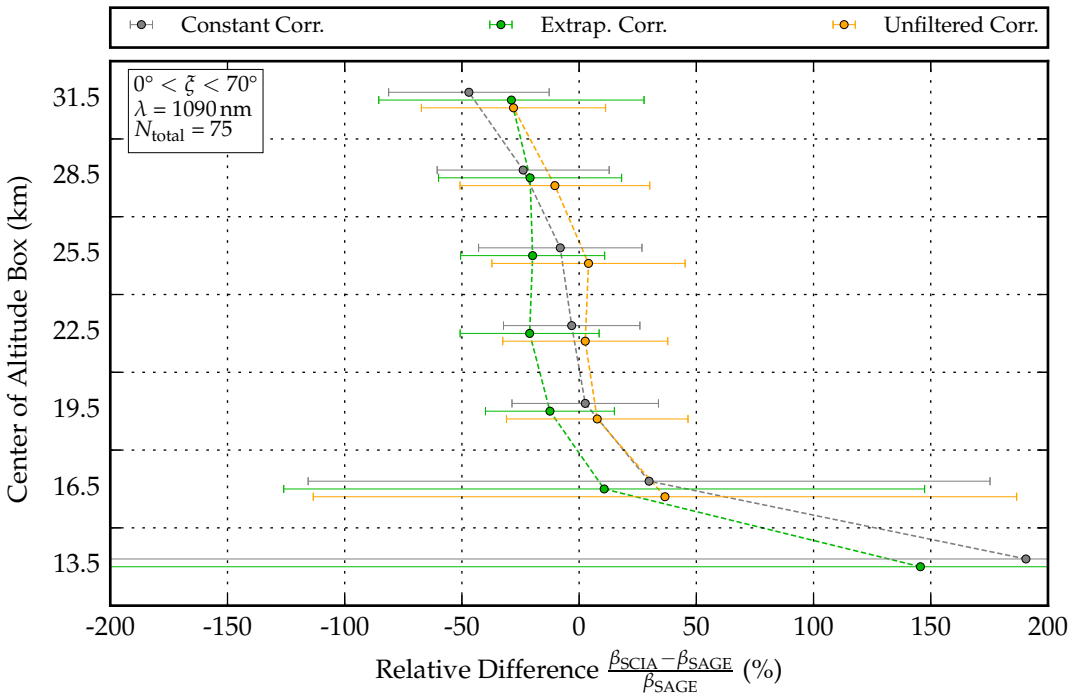

Figure A.11: Same as figure 7.8 but for $\xi < 70°$ and $\lambda = 1090\,\text{nm}$ and measurements without spatial straylight correction are not considered in order to increase the number of remaining collocations.

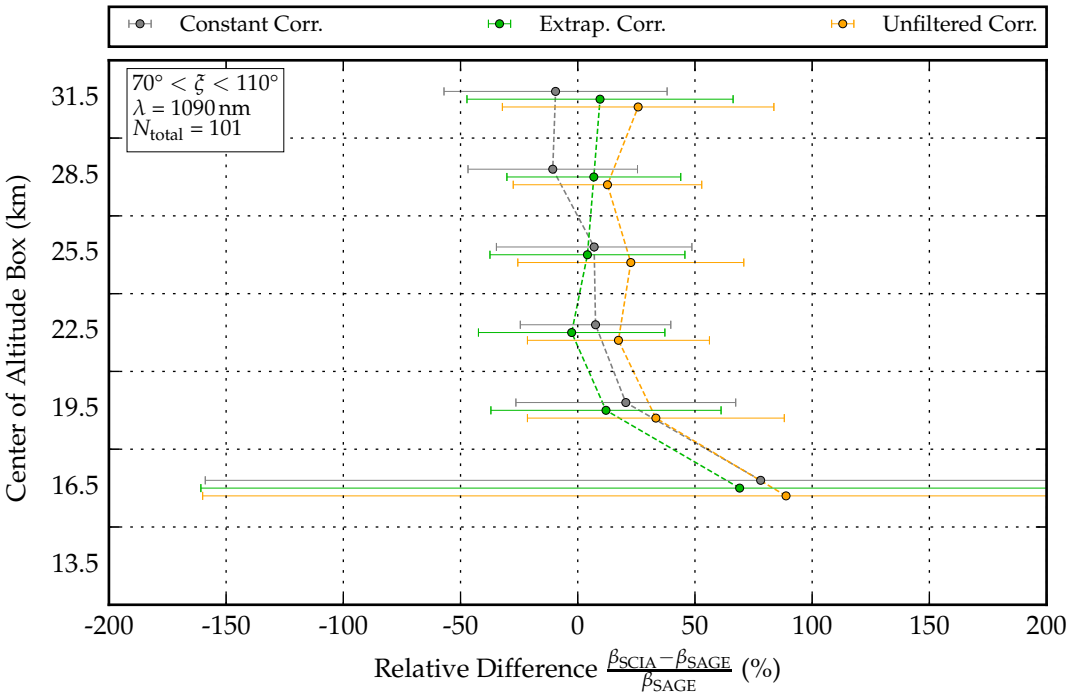

Figure A.12: Same as figure A.11 but for $70° < \xi < 110°$ and $\lambda = 1090\,\text{nm}$.

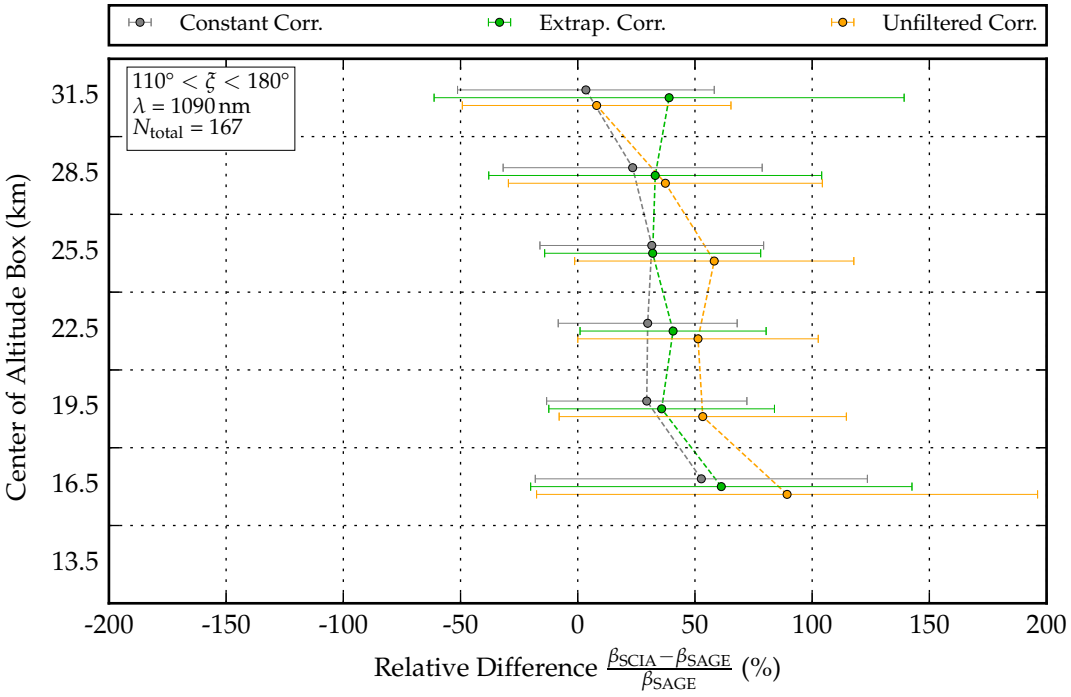

Figure A.13: Same as figure A.11 but $\xi > 110°$ and $\lambda = 1090\,\text{nm}$.

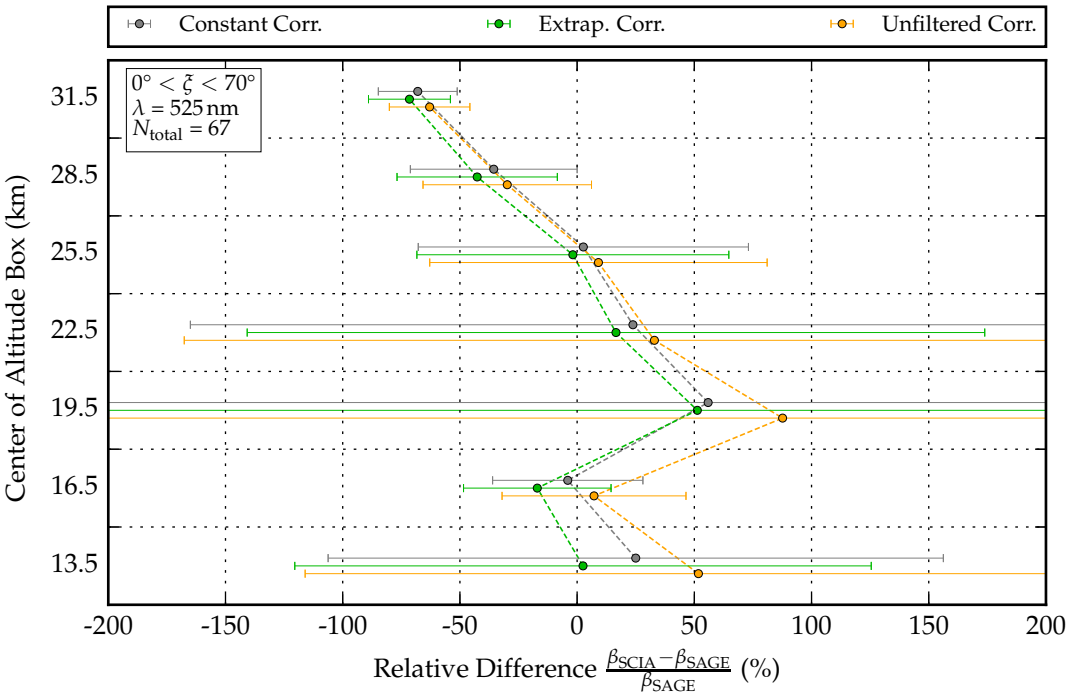

Figure A.14: Same as figure A.11 but for $\xi < 70°$ and $\lambda = 525\,\text{nm}$.

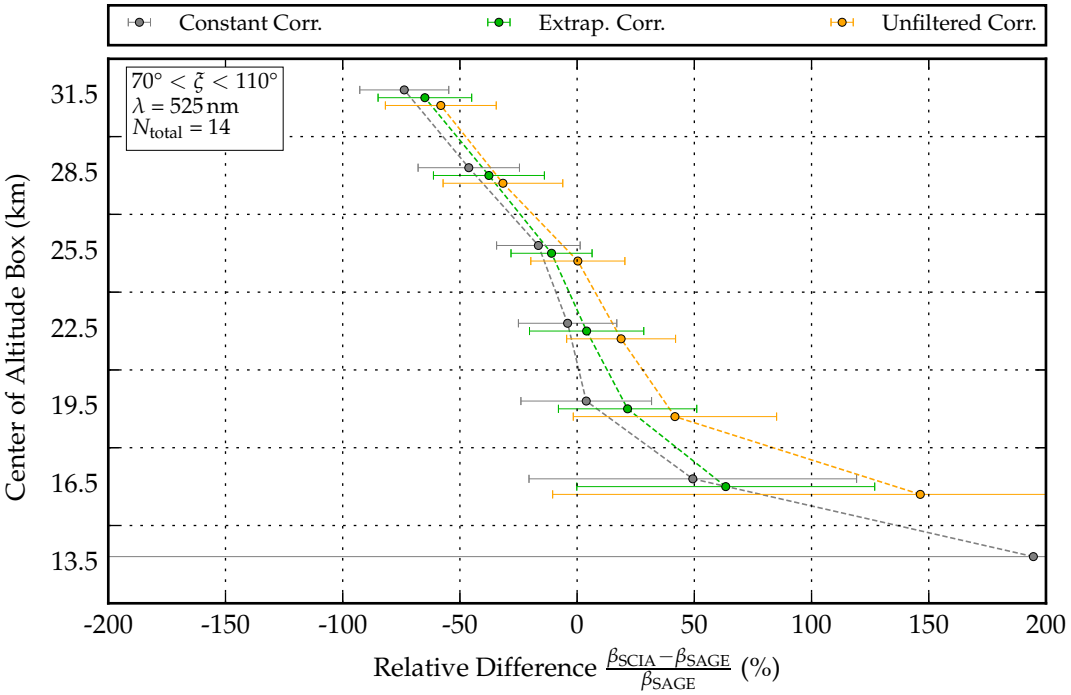

Figure A.15: Same as figure A.11 but for $70° < \xi < 110°$ and $\lambda = 525\,\text{nm}$.

BIBLIOGRAPHY

Ångström, A.: On the atmospheric transmission of sun radiation. II., Geografiska Annaler, pp. 130–159, 1930.

Baumgardner, D., Dye, J. E., Gandrud, B., Barr, K., Kelly, K., and Chan, K. R.: Refractive indices of aerosols in the upper troposphere and lower stratosphere, Geophysical research letters, 23, 749–752, 1996.

Beirle, S., Kühl, S., Wagner, T., et al.: Retrieval of tropospheric column densities of NO_2 from combined SCIAMACHY nadir/limb measurements, Atmospheric Measurement Techniques, 3, 283–299, 2010.

Berger, M., Moreno, J., Johannessen, J. A., Levelt, P. F., and Hanssen, R. F.: ESA's sentinel missions in support of Earth system science, Remote Sensing of Environment, 120, 84–90, 2012.

Bertram, A. K., Patterson, D. D., and Sloan, J. J.: Mechanisms and temperatures for the freezing of sulfuric acid aerosols measured by FTIR extinction spectroscopy, The Journal of Physical Chemistry, 100, 2376–2383, 1996.

Bogumil, K., Orphal, J., Homann, T., Voigt, S., Spietz, P., Fleischmann, O., Vogel, A., Hartmann, M., Kromminga, H., Bovensmann, H., et al.: Measurements of molecular absorption spectra with the SCIAMACHY pre-flight model: instrument characterization and reference data for atmospheric remote-sensing in the 230–2380 nm region, Journal of Photochemistry and Photobiology A: Chemistry, 157, 167–184, 2003.

Bourassa, A. E.: Stratospheric aerosol retrieval from OSIRIS limb scattered sunlight spectra, Ph.D. thesis, Department of Physics and Engineering Physics, University of Saskatchewan, 2007.

Bourassa, A. E., Rieger, L. A., Lloyd, N. D., and Degenstein, D. A.: Odin-OSIRIS stratospheric aerosol data product and SAGE III intercomparison, Atmospheric Chemistry and Physics, 12, 605–614, 2012a.

Bourassa, A. E., Robock, A., Randel, W. J., Deshler, T., Rieger, L. A., Lloyd, N. D., Llewellyn, E. J. T., and Degenstein, D. A.: Large volcanic aerosol load in the stratosphere linked to Asian monsoon transport, Science, 337, 78–81, 2012b.

Brock, C. A., Hamill, P., Wilson, J. C., Jonsson, H. H., and Chan, K. R.: Particle formation in the upper tropical troposphere: A source of nuclei for the stratospheric aerosol, Science, 270, 1650–1653, 1995.

Cadle, R. D. and Kiang, C. S.: Stratospheric Aitken particles, Reviews of Geophysics, 15, 195–202, 1977.

Chu, W. P., McCormick, M. P., Lenoble, J., Brogniez, C., and Pruvost, P.: SAGE II inversion algorithm, Journal of Geophysical Research: Atmospheres (1984–2012), 94, 8339–8351, 1989.

Clarisse, L., Coheur, P.-F., Theys, N., Hurtmans, D., and Clerbaux, C.: The 2011 Nabro eruption, a SO_2 plume height analysis using IASI measurements, Atmospheric Chemistry and Physics, 14, 3095–3111, 2014.

Conover, J. H.: Cloud and terrestrial albedo determinations from TIROS satellite pictures, Journal of Applied Meteorology, 4, 378–386, 1965.

Curtius, J., Weigel, R., Vössing, H.-J., Wernli, H., Werner, A., Volk, C.-M., Konopka, P., Krebsbach, M., Schiller, C., Roiger, A., et al.: Observations of meteoric material and implications for aerosol nucleation in the winter Arctic lower stratosphere derived from in situ particle measurements, Atmospheric Chemistry and Physics, 5, 3053–3069, 2005.

Deshler, T.: A review of global stratospheric aerosol: Measurements, importance, life cycle, and local stratospheric aerosol, Atmospheric Research, 90, 223–232, 2008.

Deshler, T., Hervig, M. E., Hofmann, D. J., Rosen, J. M., and Liley, J. B.: Thirty years of in situ stratospheric aerosol size distribution measurements from Laramie, Wyoming (41°N), using balloon-borne instruments, Journal of Geophysical Research: Atmospheres (1984–2012), 108, 2003.

Deshler, T., Anderson-Sprecher, R., Jäger, H., Barnes, J., Hofmann, D. J., Clemesha, B., Simonich, D., Osborn, M., Grainger, R. G., and Godin-Beekmann, S.: Trends in the nonvolcanic component of stratospheric aerosol over the period 1971–2004, Journal of Geophysical Research: Atmospheres (1984–2012), 111, 2006.

Deutschmann, T.: On Modeling Elastic and Inelastic Polarized Radiation Transport in the Earth Atmosphere with Monte Carlo Methods, Ph.D. thesis, University of Leipzig, Germany, 2014.

Deutschmann, T., Beirle, S., Frieß, U., Grzegorski, M., Kern, C., Kritten, L., Platt, U., Prados-Román, C., Wagner, T., Werner, B., et al.: The Monte Carlo atmospheric radiative transfer model McArtim: Introduction and validation of Jacobians and 3D features, Journal of Quantitative Spectroscopy and Radiative Transfer, 112, 1119–1137, 2011.

Drdla, K., Tabazadeh, A., Turco, R. P., Jacobson, M. Z., Dye, J. E., Twohy, C., and Baumgardner, D.: Analysis of the physical state of one Arctic polar stratospheric cloud based on observations, Geophysical Research Letters, 21, 2475–2478, 1994.

Engel, I., Luo, B. P., Pitts, M. C., Poole, L. R., Hoyle, C. R., Grooß, J.-U., Dörnbrack, A., and Peter, T.: Heterogeneous formation of polar stratospheric clouds–Part 2: Nucleation of ice on synoptic scales, Atmospheric Chemistry and Physics, 13, 10 769–10 785, 2013.

Ernst, F.: Stratospheric aerosol extinction profile retrievals from SCIAMACHY limb-scatter observations, Ph.D. thesis, University of Bremen, 2013.

Ernst, F., Savigny, C. v., Rozanov, A., Rozanov, V., Eichmann, K.-U., Brinkhoff, L. A., Bovensmann, H., and Burrows, J. P.: Global stratospheric aerosol extinction profile retrievals from SCIAMACHY limb-scatter observations, Atmospheric Measurement Techniques Discussions, 5, 5993–6035, 2012.

European Space Agency: earthnet online, URL `http://earth.esa.int`, 2010.

Fairlie, T. D., Vernier, J.-P., Natarajan, M., and Bedka, K. M.: Dispersion of the Nabro volcanic plume and its relation to the Asian summer monsoon, Atmospheric Chemistry and Physics, 14, 7045–7057, 2014.

Foster, A. K.: personal communication, 2015.

Fromm, M., Bevilacqua, R., Servranckx, R., Rosen, J., Thayer, J. P., Herman, J., and Larko, D.: Pyro-cumulonimbus injection of smoke to the stratosphere: Observations and impact of a super blowup in northwestern Canada on 3–4 August 1998, Journal of Geophysical Research: Atmospheres (1984–2012), 110, 2005.

Fromm, M., Nedoluha, G., and Charvàt, Z.: Comment on: "Large volcanic aerosol load in the stratosphere linked to Asian monsoon transport", Science, 339, 647 pp., doi:10.1126/science.1228605, 2012.

Gobbi, G. P., Kaufman, Y. J., Koren, I., and Eck, T. F.: Classification of aerosol properties derived from AERONET direct sun data, Atmospheric Chemistry and Physics, 7, 453–458, 2007.

Gordley, L. L., Russell III, J. M., et al.: Rapid inversion of limb radiance data using an emissivity growth approximation, Applied optics, 20, 807–813, 1981.

Gottwald, M. and Bovensmann, H.: SCIAMACHY - Exploring the Changing Earth's Atmosphere, Springer Science & Business Media, 2010.

Hervig, M. and Deshler, T.: Evaluation of aerosol measurements from SAGE II, HALOE, and balloonborne optical particle counters, Journal of Geophysical Research: Atmospheres, 107, AAC 3–1–AAC 3–12, doi:10.1029/2001JD000703, URL `http://dx.doi.org/10.1029/2001JD000703`, 2002.

Heue, K.-P., Richter, A., Bruns, M., Burrows, J. P., Friedeburg, C. v., Platt, U., Pundt, I., Wang, P., and Wagner, T.: Validation of SCIAMACHY tropospheric NO_2-columns with AMAXDOAS measurements, Atmospheric Chemistry and Physics, 5, 1039–1051, 2005.

Hilboll, A., Richter, A., Rozanov, A., Hodnebrog, Ø., Heckel, A., Solberg, S., Stordal, F., and Burrows, J. P.: Improvements to the retrieval of tropospheric NO_2 from satellite – stratospheric correction using SCIAMACHY limb/nadir matching and comparison to Oslo CTM2 simulations, Atmospheric Measurement Techniques, 6, 565–584, 2013.

Holben, B. N., Eck, T. F., Slutsker, I., Tanre, D., Buis, J. P., Setzer, A., Vermote, E., Reagan, J. A., Kaufman, Y. J., Nakajima, T., et al.: AERONET - A federated instrument network and data archive for aerosol characterization, Remote sensing of environment, 66, 1–16, 1998.

Hoyle, C. R., Engel, I., Luo, B. P., Pitts, M. C., Poole, L. R., Grooß, J.-U., and Peter, T.: Heterogeneous formation of polar stratospheric clouds–Part 1: Nucleation of nitric acid trihydrate (NAT), Atmospheric Chemistry and Physics, 13, 9577–9595, 2013.

Humphreys, W.: Physics of the Air, Dover, Mineola, NY, USA, 1940.

Hunten, D. M., Turco, R. P., and Toon, O. B.: Smoke and dust particles of meteoric origin in the mesosphere and stratosphere, Journal of the Atmospheric Sciences, 37, 1342–1357, 1980.

Junge, C. and Manson, J.: Stratospheric aerosol studies, Journal of Geophysical Research, 66, 2163–2182, 1961.

Kirner, O., Ruhnke, R., Buchholz-Dietsch, J., Jöckel, P., Brühl, C., and Steil, B.: Simulation of polar stratospheric clouds in the chemistry-climate-model EMAC via the submodel PSC, Geoscientific Model Development, 4, 169–182, 2011.

Koop, T., Luo, B., Tsias, A., and Peter, T.: Water activity as the determinant for homogeneous ice nucleation in aqueous solutions, Nature, 406, 611–614, 2000.

Kovilakam, M. and Deshler, T.: On the accuracy of stratospheric aerosol extinction derived from in situ balloon borne size distribution measurements and surface area derived from SAGE II extinction measurements, submitted to Journal of Geophysical Research, 2015.

Kühl, S., Wilms-Grabe, W., Beirle, S., Frankenberg, C., Grzegorski, M., Hollwedel, J., Khokhar, F., Kraus, S., Platt, U., Sanghavi, S., et al.: Stratospheric chlorine activation in the Arctic winters 1995/96-2001/02 derived from GOME OClO measurements, Advances in Space Research, 34, 798–803, 2004.

Kühl, S., Puķīte, J., Deutschmann, T., Platt, U., and Wagner, T.: SCIAMACHY limb measurements of NO_2, BrO and OClO. Retrieval of vertical profiles: Algorithm, first results, sensitivity and comparison studies, Advances in Space Research, 42, 1747–1764, 2008.

LAADS: MODIS Granule Browser, URL `http://ladsweb.nascom.nasa.gov/browse_images/granule_browser.html`, 2015.

Landgraf, J., Hasekamp, O. P., Van Deelen, R., and Aben, I.: Rotational Raman scattering of polarized light in the Earth atmosphere: a vector radiative transfer model using the radiative transfer perturbation theory approach, Journal of Quantitative Spectroscopy and Radiative Transfer, 87, 399–433, 2004.

Larden, W.: The Sky-Glows, Nature, 30, 488 pp., 1884.

Lowe, D. and MacKenzie, A. R.: Polar stratospheric cloud microphysics and chemistry, Journal of Atmospheric and Solar-Terrestrial Physics, 70, 13–40, 2008.

McGarragh, G.: Mie Scattering Routines, URL http://eodg.atm.ox.ac.uk/MIE/, 2015.

Meilinger, S. K., Koop, T., Luo, B. P., Huthwelker, T., Carslaw, K. S., Krieger, U., Crutzen, P. J., and Peter, T.: Size-dependent stratospheric droplet composition in Lee wave temperature fluctuations and their potential role in PSC freezing, Geophysical research letters, 22, 3031–3034, 1995.

Mie, G.: Beiträge zur Optik trüber Medien, speziell kolloidaler Metallösungen, Annalen der Physik, 330, 377–445, 1908.

Mohn, H.: Irisierende Wolken, Met. Zeit, 1893.

Neu, J. L. and Plumb, R. A.: Age of air in a "leaky pipe" model of stratospheric transport, Journal of Geophysical Research: Atmospheres (1984–2012), 104, 19 243–19 255, 1999.

Newman, P., Nash, E., and Long, C.: Annual NCEP Data, URL http://acdb-ext.gsfc.nasa.gov/Data_services/met/ann_data.html, 2015.

Noël, S., Bovensmann, H., Burrows, J. P., Frerick, J., Chance, K. V., and Goede, A. H. P.: Atmospheric trace gas sounding with SCIAMACHY, Physics and Chemistry of the Earth, Part C: Solar, Terrestrial & Planetary Science, 24, 427–434, 1999.

Noël, S., Bovensmann, H., Wuttke, M., Burrows, J., Gottwald, M., Krieg, E., and Mager, R.: SCIAMACHY nominal operations and special features, in: Proc. ERS-ENVISAT symposium Gothenburg, cDROM (SP-461), 2000.

OSCAR: Observing Systems Capability Analysis and Review Tool, URL http://www.wmo-sat.info/oscar/instruments/, 2015.

Penning de Vries, M. J. M., Dörner, S., Puķīte, J., Hörmann, C., Fromm, M. D., and Wagner, T.: Characterisation of a stratospheric sulfate plume from the Nabro volcano using a combination of passive satellite measurements in nadir and limb geometry, Atmospheric Chemistry and Physics, 14, 8149–8163, 2014.

Puķīte, J.: Retrieval of vertical profiles of stratospheric trace gases from limb observations of the SCIAMACHY instrument on ENVISAT, Ph.D. thesis, Ruprecht-Karls University of Heidelberg, Germany, 2010.

Puķīte, J., Kühl, S., Deutschmann, T., Platt, U., and Wagner, T.: Accounting for the effect of horizontal gradients in limb measurements of scattered sunlight, Atmos. Chem. Phys., 8, 3045–3060, 2008.

Rieger, L. A., Bourassa, A. E., and Degenstein, D. A.: Stratospheric aerosol particle size information in Odin-OSIRIS limb scatter spectra, Atmospheric Measurement Techniques, 7, 507–522, 2014.

Rodgers, C. D.: Inverse methods for atmospheric sounding - Theory and Practice, vol. 2 of *Series on Atmospheric Oceanic and Planetary Physics*, World Scientific Publishing Co. Pte. Ltd., 2000.

Rozanov, V. V., Rozanov, A. V., Kokhanovsky, A. A., and Burrows, J. P.: Radiative transfer through terrestrial atmosphere and ocean: software package SCIATRAN, Journal of Quantitative Spectroscopy and Radiative Transfer, 133, 13–71, 2014.

Savigny, C. v., Ulasi, E. P., Eichmann, K.-U., Bovensmann, H., and Burrows, J. P.: Detection and mapping of polar stratospheric clouds using limb scattering observations, Atmospheric Chemistry and Physics, 5, 3071–3079, 2005.

Schuster, G. L., Dubovik, O., and Holben, B. N.: Ångström exponent and bimodal aerosol size distributions, Journal of Geophysical Research: Atmospheres (1984–2012), 111, 2006.

SCIAMACHY Operations Support Team: SCIAMACHY, URL `http://atmos.caf.dlr.de/projects/scops`, 2010.

Shia, R.-L., Ko, M. K. W., Weisenstein, D. K., Scott, C., and Rodriguez, J.: Transport between the tropical and midlatitude lower stratosphere: Implications for ozone response to high-speed civil transport emissions, Journal of Geophysical Research: Atmospheres (1984–2012), 103, 25 435–25 446, 1998.

Soest, G. v.: Investigation of SCIAMACHY limb spatial straylight, Tech. rep., SRON-Eos-rp-05-006, SRON, 2005.

Solomon, S., Daniel, J. S., Neely, R. R., Vernier, J.-P., Dutton, E. G., and Thomason, L. W.: The persistently variable "background" stratospheric aerosol layer and global climate change, Science, 333, 866–870, 2011.

SPARC/ASAP: WMO/SPARC Assessment of Stratospheric Aerosol Properties (ASAP) SPARC Report No. 4, WCRP-124 WMO/TD No. 1295, World Climate Research Program, 2006.

Spurr, R.: LIDORT and VLIDORT: Linearized pseudo-spherical scalar and vector discrete ordinate radiative transfer models for use in remote sensing retrieval problems, in: Light Scattering Reviews 3, pp. 229–275, Springer, 2008.

Tabazadeh, A., Turco, R. P., Drdla, K., Jacobson, M. Z., and Toon, O. B.: A study of type I polar stratospheric cloud formation, Geophysical Research Letters, 21, 1619–1622, 1994.

Taha, G., Rault, D. F., Loughman, R. P., Bourassa, A. E., and Savigny, C. v.: SCIAMACHY stratospheric aerosol extinction profile retrieval using the OMPS/LP algorithm, Atmospheric Measurement Techniques, 4, 547–556, 2011.

Theys, N., Campion, R., Clarisse, L., Brenot, H., Van Gent, J., Dils, B., Corradini, S., Merucci, L., Coheur, P.-F., Van Roozendael, M., et al.: Volcanic SO2 fluxes derived from satellite data: a survey using OMI, GOME-2, IASI and MODIS, Atmospheric Chemistry and Physics, 13, 5945–5968, 2013.

Thomason, L. W., Pitts, M. C., and Winker, D. M.: CALIPSO observations of stratospheric aerosols: a preliminary assessment, Atmospheric Chemistry and Physics, 7, 5283–5290, 2007.

Tilmes, S., Garcia, R. R., Kinnison, D. E., Gettelman, A., and Rasch, P. J.: Impact of geoengineered aerosols on the troposphere and stratosphere, Journal of Geophysical Research: Atmospheres (1984–2012), 114, 2009.

Trentmann, J., Luderer, G., Winterrath, T., Fromm, M. D., Servranckx, R., Textor, C., Herzog, M., Graf, H.-F., and Andreae, M. O.: Modeling of biomass smoke injection into the lower stratosphere by a large forest fire (Part I): reference simulation, Atmospheric Chemistry and Physics, 6, 5247–5260, 2006.

Trepte, C. R. and Hitchman, M. H.: Tropical stratospheric circulation deduced from satellite aerosol data, Nature, 355, 626–628, 1992.

Vernier, J.-P., Barnes, J. E., Berkoff, T. A., Welton, E. J., Alados-Arboledas, L., Navas-Guzmán, F., Pappalardo, G., Mona, L., Madonna, F., et al.: Stratospheric AOD after the 2011 eruption of Nabro volcano measured by lidars over the Northern Hemisphere, Environmental Research Letters, 7, 034 013, 2012a.

Vernier, J.-P., Thomason, L. W., Fairlie, T. D., Minnis, P., Palikonda, R., and Bedka, K. M.: Comment on: "Large volcanic aerosol load in the stratosphere linked to Asian monsoon transport", Science, 339, 647pp., doi:10.1126/science.1227817, 2012b.

Wagner, T., Burrows, J. P., Deutschmann, T., Dix, B., Friedeburg, C. v., Frieß, U., Hendrick, F., Heue, K.-P., Irie, H., Iwabuchi, H., et al.: Comparison of box-air-mass-factors and radiances for Multiple-Axis Differential Optical Absorption Spectroscopy (MAX-DOAS) geometries calculated from different UV/visible radiative transfer models, Atmospheric Chemistry and Physics, 7, 1809–1833, 2007.

Welton, E. J., Campbell, J. R., Spinhirne, J. D., and Scott III, V. S.: Global monitoring of clouds and aerosols using a network of micropulse lidar systems, in: Second

International Asia-Pacific Symposium on Remote Sensing of the Atmosphere, Environment, and Space, pp. 151–158, International Society for Optics and Photonics, 2001.

Wendisch, M. and Yang, P.: Theory of atmospheric radiative transfer, John Wiley & Sons, 2012.

WMO: Scientific Assessment of Ozone Depletion: 2014, Report No. 55, World Meteorological Organization Global Ozone Research and Monitoring Project, 2014.

ACKNOWLEDGMENTS

DECLARATION

I hereby declare that I wrote the dissertation submitted without any unauthorized external assistance and used only sources acknowledged in the work. All textual passages which are appropriated verbatim or paraphrased from published and unpublished texts as well as all information obtained from oral sources are duly indicated and listed in accordance with bibliographical rules. In carrying out this research, I complied with the rules of standard scientific practice as formulated in the statutes of Johannes Gutenberg-University Mainz to insure standard scientific practice.

Mainz, March 2015

Steffen Dörner